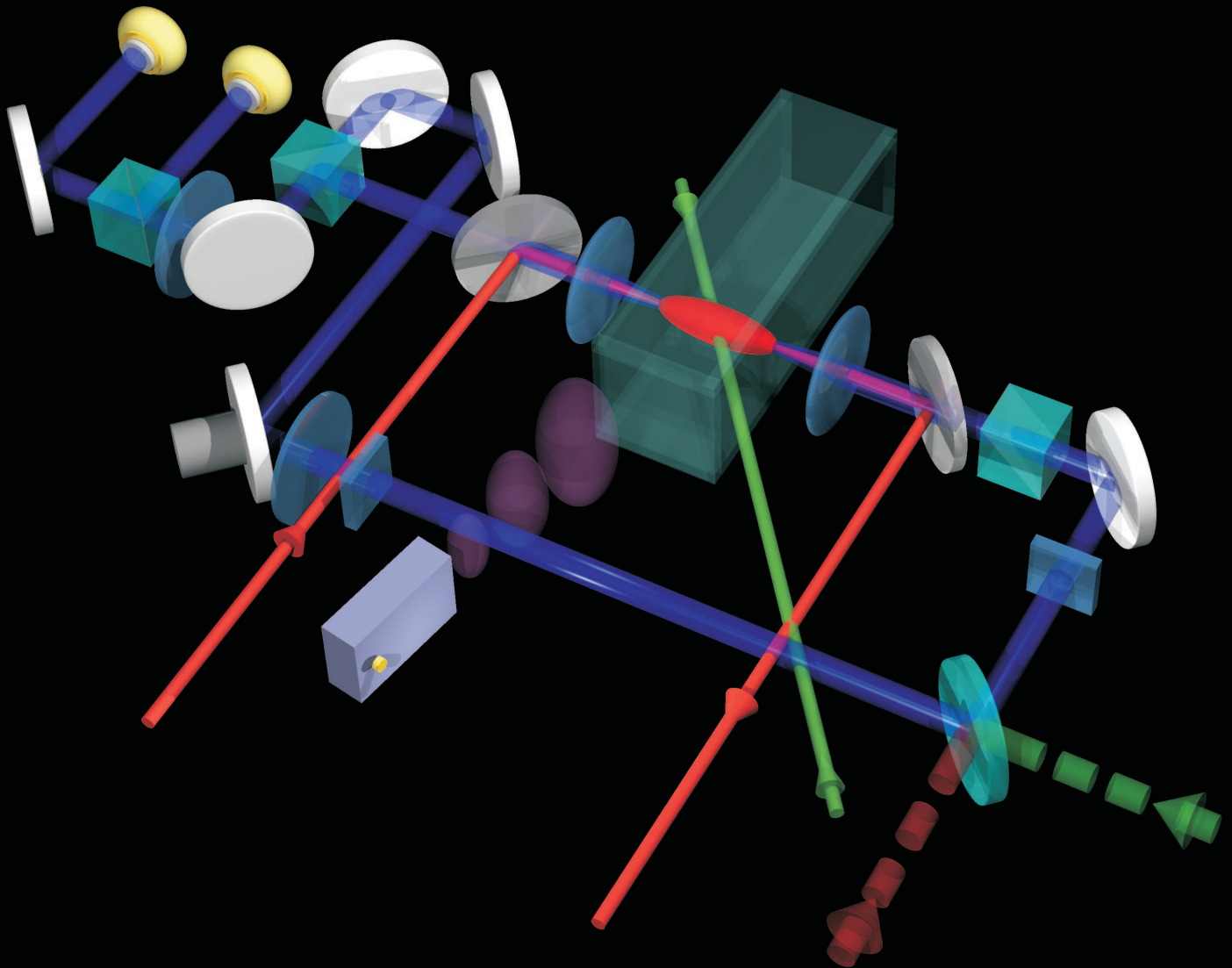




**CENTER FOR QUANTUM OPTICS**  
**NIELS BOHR INSTITUTE**  
FACULTY OF SCIENCE  
UNIVERSITY OF COPENHAGEN



# Non-destructive quantum state measurements and Quantum noise squeezing



Patrick J. Windpassinger

Ph.D. Thesis



**Non-destructive quantum state measurements  
and  
Quantum noise squeezing**

---

*What are you going to do?  
Learn to love the cold.  
(The memory of water)*

**Patrick J. Windpassinger**

Ph.D. Thesis  
Danish National Research Foundation  
Center for Quantum Optics (QUANTOP)  
Niels Bohr Institute  
Faculty of Science  
University of Copenhagen  
October 2008

Academic supervisors: *Prof. Eugene S. Polzik*  
*Assoc. Research Prof. Niels Kjergaard*

Evaluation committee:

NBI local head: *Prof. Andrew Jackson*

External referees: *Prof. Elisabeth Giacobino*  
*Prof. Dieter Meschede*

Thesis submitted: *October 20, 2008*

Disputation: *December 17, 2008*





# Summary

A method for non-destructive probing of the clock state population of laser-cooled, dipole trapped Cs atoms at the standard quantum limit is presented. To that end, we couple light off-resonantly to the atomic ensemble and determine the phase shift imposed onto a probe laser beam with a Mach Zehnder interferometer.

The non-destructive probing allows us to follow the evolution of the population difference of the Cs-atom clock states when subjected to microwave fields in real time. This way, Rabi oscillations on the clock transition can be observed non-destructively over an extended period of time. We apply microwave spectroscopy techniques to characterize the evolution of the quantum state in the trap and especially focus on the effect of probe induced inhomogeneous dephasing and of probe induced spontaneous photon scattering on the atomic ensemble.

Finally, we push the population readout precision to the quantum mechanical limits. We demonstrate that the precision of the population difference measurement of the two clock states has reached a level where it is only limited by the quantum noise of the probe light (shot noise) and of the atoms in the ensemble (projection noise). At this standard quantum limit we are able to observe correlations between consecutive non-destructive measurements on the same ensemble. We demonstrate that these correlations are non-classical and that therefore an entangled state of atoms has been created in the ensemble. The correlations allow us to infer a quantum noise reduction of 72%, i.e.,  $-5.4$  dB of remaining noise and  $-3.5$  dB of spectroscopically relevant pseudo spin squeezing. Applying these results to a state of the art atomic clock should significantly increase its precision.

# Sammendrag

Nærværende afhandling beskriver ikke-destruktive målinger af populationen af kvantetilstande for laserkølede Cs atomer i en dipolfælde nær den såkaldte standardkvantegrænse. Sådanne målinger udføres ved at lade et atomart ensemble vekselvirke med ikke-resonant laserlys og bestemme det resulterende faseskift af lyset med et Mach Zehnder interferometer.

Den ikke-destruktive målemetode gør det muligt at følge udviklingen i populationsforskellen mellem de såkaldte ur-tilstande i Cs, alt imens ur-overgangen drives med et resonant mikrobølgefelt. Således kan Rabi-oscillationer på ur-overgangen observeres over en længere tidsperiode, uden at observationen leder til destruktion af det atomare systems koherens. Vi anvender metoder fra mikrobølgespektroskopi til at karakterisere udviklingen i atomernes kollektive kvantetilstand med særligt henblik på at kortlægge effekter som inhomogen fasespredning fra dispersiv vekselvirkning og dekoherens fra spontan spredning af fotoner i forbindelse med den ikke-destruktive målemetode.

Sluttelig presser vi udlæsningen af populationsforskellen mellem de atomare ur-tilstande til den kvantemekaniske grænse. Vi påviser at have opnået en præcision, hvor målingen af denne forskel kun begrænses af den kvantemekaniske støj fra henholdsvis lyset (shot støj) og atomerne (projektionsstøj). Ved denne standardkvantegrænse har vi været i stand til at observere korrelationer mellem to på hinanden følgende målinger på et atomart ensemble. Vi påviser at disse korrelationer er ikke-klassiske (kvantemekaniske), og at der således er blevet skabt en kvantemekanisk sammenfiltrering af ensembles atomer. Korrelationerne muliggør en reduktion af den kvantemekaniske støj på 72% og på -3.5 dB for det spektroskopisk betydende atomare pseudo-spin. Disse resultater kan potentielt anvendes til at forbedre præcisionen for nutidens bedste atomure.





# Preface

The work presented in this theses has been performed in one of Eugene S. Polzik’s labs at the Danish National Research Foundation Center for Quantum Optics — QUANTOP — located at the Niels Bohr Institute, University of Copenhagen and covers the experimental progress between October 2005 and September 2008. The experimental apparatus on which part of the work is based has been the subject of an earlier Master’s [1] and a Ph.D. thesis [2]. Technical details which have been reported previously are therefore only included where they are necessary to ensure a certain level of completeness. For further reading interested subjects are referred to these documents. Due to the family planning of my co-worker Daniel Oblak, the temporal and in consequence the overlap in respect of contents with his Ph.D. thesis [3] will be noticeable. However, an attempt has been made to mainly report results where a large amount of originality can be claimed. Parts of the presented work have been or will be published as [4, 5, 6, 7, 8, 9]. Although political motivations cannot be denied, in some cases the author lists represent an attempt to ascribe the contributions to names.

The presented work is the result of a group effort – with varying number of contributors over time. Starting out as a tripod together with Daniel Oblak and Niels Kjærgaard in the lab, many long nights were spent in trusted togetherness with my most favorite Postdoc “Nielsky” during Daniel’s leaves. Some of the results during the final stage would probably not have been achieved in the same fashion without the energetic contributions of Jürgen Appel and the helping hands of Ulrich Busk Hoff.

Numerous other long and short term members of the QUANTOP group did their part to complete the work as presented here. Their contributions are greatly acknowledged.

The work has been funded by the Danish national research council through a Forskeruddannelsesråd (FUR) stipend and by QUANTOP. Additional funding, especially for traveling was provided by the European projects QAP and QUROPE.



# Contents

<b>Summary</b>	<b>iii</b>
<b>Preface</b>	<b>vii</b>
<b>1 Introduction</b>	<b>1</b>
<b>2 General remarks</b>	<b>7</b>
2.1 The players . . . . .	7
2.1.1 Quantum state of an atomic ensemble . . . . .	8
2.1.2 Coherent light states . . . . .	12
2.2 Reduction of population number uncertainty . . . . .	12
2.2.1 Quantum non-demolition measurements . . . . .	13
2.2.2 Squeezing criteria . . . . .	15
2.2.3 Spin squeezing via QND interaction . . . . .	16
2.3 Light – atom interaction . . . . .	17
2.3.1 Specialization to caesium atoms . . . . .	19
2.4 Mach Zehnder interferometer . . . . .	20
2.4.1 Single color interferometer . . . . .	21
2.4.2 Interaction Hamiltonian in QND form . . . . .	23
2.5 Experimental proposal . . . . .	26
<b>3 Experimental techniques</b>	<b>27</b>
3.1 Generation of cold Cs atoms . . . . .	27
3.1.1 Layout of setup . . . . .	27
3.1.2 Magneto-Optical Trap . . . . .	28
3.1.3 Optical dipole trap . . . . .	32
3.2 Interferometer setup . . . . .	35
3.2.1 Probe laser setup . . . . .	37
3.2.2 White light alignment and interferometer locking . . . . .	38
3.2.3 Noise properties of the interferometer . . . . .	40
3.3 Experiment control . . . . .	44
3.3.1 Fast pulse sequence generation . . . . .	45
3.3.2 Data readout and postprocessing . . . . .	47
3.4 Non-destructive probing of dipole trapped sample . . . . .	48
3.4.1 General measurement procedure . . . . .	49
3.4.2 Lifetime of atoms in the trap . . . . .	50
3.4.3 The problem with the atom number . . . . .	51
3.4.4 Longitudinal oscillations . . . . .	53
3.4.5 Direct observation of trap induced light shift on probe transition . . . . .	53

<b>4</b>	<b>Differential, integrating photo detector</b>	<b>57</b>
4.1	Principle of operation . . . . .	58
4.1.1	Detector layout based on Amptek amplifiers . . . . .	61
4.1.2	Detector based on CREMAT modules . . . . .	62
4.1.3	Detector test setup . . . . .	62
4.2	DC operation and noise measurements . . . . .	63
4.3	Pulsed detector operation and noise analysis . . . . .	67
4.3.1	Shot noise limited performance and optimization . . . . .	68
4.3.2	Baseline pulling and offset subtraction . . . . .	70
4.4	Comparison of performances . . . . .	72
<b>5</b>	<b>Microwave spectroscopy</b>	<b>75</b>
5.1	Light–atom coupling applied to the clock transition . . . . .	76
5.1.1	Theoretical background . . . . .	76
5.1.2	Loss of coherence in ensembles of atoms . . . . .	79
5.1.3	Rabi oscillations and state rotations . . . . .	80
5.2	Generation of microwave pulses . . . . .	82
5.3	Quantum state preparation . . . . .	84
5.3.1	General measurement procedure . . . . .	84
5.3.2	Sample initialization to the clock states . . . . .	85
5.4	Non–destructive observation of Rabi oscillations . . . . .	90
5.4.1	Spontaneous photon scattering . . . . .	91
5.4.2	Experimental observation of Rabi oscillations . . . . .	91
5.4.3	Two color probing of Rabi oscillations . . . . .	95
5.5	Inhomogeneous light shift effects on Rabi oscillations . . . . .	95
5.5.1	Theoretical model . . . . .	97
5.5.2	Application to Rabi oscillations . . . . .	99
5.6	Rabi spectroscopy - transition line shape . . . . .	101
5.7	Ramsey spectroscopy . . . . .	102
5.7.1	Principle of Ramsey spectroscopy . . . . .	104
5.7.2	Inhomogeneous dephasing due to differential light shift of the dipole trap . . . . .	105
5.7.3	Running a Cs atomic clock . . . . .	107
5.7.4	Inhomogeneous light shift of probe pulses . . . . .	109
5.8	Sample rephasing – Spin echo techniques . . . . .	112
5.8.1	Rephasing the dipole trap shift effects . . . . .	112
5.9	Re-phasing the inhomogeneous light shift from probe pulses . . . . .	114
5.10	Spontaneous photon scattering probability and trap oscillations . . . . .	116
5.10.1	Effect of trap motion on reversibility of inhomogeneous phase imprints . . . . .	116
5.10.2	Estimation of photon scattering probability . . . . .	119
5.11	Two color light shift cancelation . . . . .	120

<b>6 Atomic projection noise measurements and quantum noise squeezing</b>	<b>123</b>
6.1 Condition for optimal squeezing . . . . .	124
6.2 Noise measurements with two color – single port interferometer . . . . .	125
6.2.1 The two–sample variance and the issue of timescales . . . . .	125
6.2.2 Stability requirements . . . . .	130
6.2.3 Projection noise measurements . . . . .	134
6.2.4 Experimental observation of projection noise . . . . .	140
6.3 Noise measurements with two color – two port interferometer setup	144
6.3.1 Remarks on the technical realization . . . . .	144
6.3.2 Shot noise limited performance . . . . .	147
6.3.3 Projection noise and squeezing measurements . . . . .	147
6.3.4 Experimental observation of projection noise . . . . .	151
6.3.5 Quantum noise squeezing . . . . .	153
<b>7 Conclusion and Outlook</b>	<b>157</b>
7.1 Where do we stand? . . . . .	157
7.2 Further developments . . . . .	158
<b>A Light atom interaction</b>	<b>163</b>
A.1 Atomic light phase shift and absorption . . . . .	163
A.2 Matrix elements . . . . .	165
<b>B D1 line laser</b>	<b>169</b>
<b>C Wiener–Khinchin theorem and detector circuit layouts</b>	<b>173</b>
C.1 Wiener–Khinchin theorem . . . . .	173
C.2 Detector circuit layouts . . . . .	175
<b>List of publications</b>	<b>177</b>
<b>Coauthor statements</b>	<b>179</b>
<b>Bibliography</b>	<b>183</b>



---

# Introduction

Atomic clocks are the most accurate instruments developed in human history. In these devices, one derives time from the frequency of an extremely narrow atomic transition. To this end, one defines the transition frequency between two atomic levels as fixed and it is up to the experimentalist to spectroscopically measure the frequency with the best accuracy and precision possible. The frequency oscillator generating the necessary electromagnetic radiation then serves as the time basis for the signals broadcasted throughout the world. Such highly precise clocks are for example also implemented on the satellites transmitting the signals for the global positioning system (GPS). The precision of the clock determines the accuracy with which the position of the receiver can be determined. A magnetic hyperfine transition in caesium has been singled out to serve as the standard of time; officially, the second is defined as “the duration of 9,192,631,770 periods of the radiation corresponding to the transition between the two hyperfine levels of the ground state of the caesium 133 atom”.

Since the atomic two level system being used to define a standard of time is intrinsically quantum mechanical, quantum mechanics imposes restrictions on the precision with which the transition frequency can be determined: When we consider a two level system with energy eigenstates  $|\uparrow\rangle$  and  $|\downarrow\rangle$ , the state of the system is described by the state vector  $|\psi\rangle = a|\uparrow\rangle + b|\downarrow\rangle$ , where  $a$  and  $b$  are the complex probability amplitudes characterizing the state. In a spectroscopy setup one typically initializes the system into one of the two states, e.g., the  $|\downarrow\rangle$  state, and applies a radiation field. Depending on the duration and the frequency of the field, the state of the atomic system is changed by the atom–field interaction and the final state of the system can be used to extract information on the frequency difference between the external oscillator and the atomic transition frequency. Figure 1.1(a) illustrates the clock measurement principle, the so-called Ramsey spectroscopy sequence. We illustrate the evolution of the atomic state under the influence of electromagnetic radiation in the so-called Bloch sphere picture where the atomic state is mapped onto the position of a point on a sphere. The theoretical background will be discussed in detail in chapter 5. In a nutshell, the single steps of the clock protocol are: The sequence starts by creating an atomic superposition state  $|\Psi\rangle = \frac{1}{\sqrt{2}}(|\downarrow\rangle + i|\uparrow\rangle)$  from the initial  $|\downarrow\rangle$  state. After the clock atoms have been

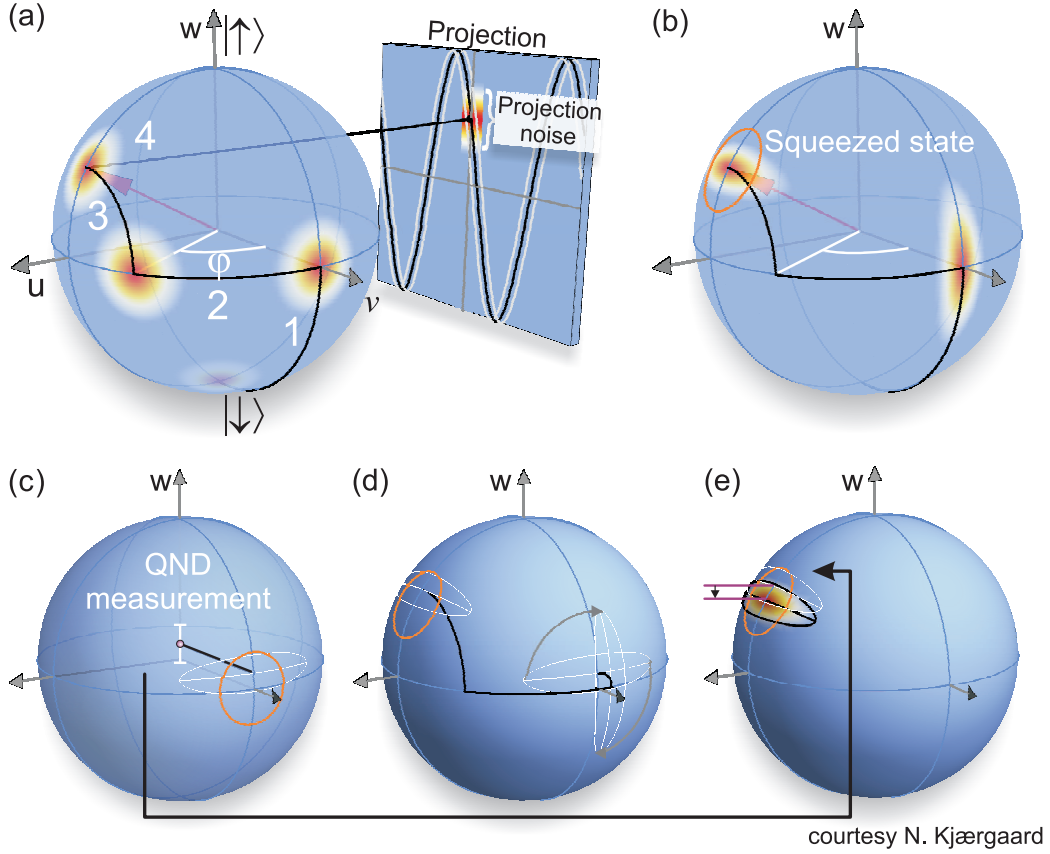


**FIGURE 1.1:** Illustration of the Ramsey clock measurement sequence and the influence of the quantum mechanical measurement uncertainty on the measurement precision. The atomic state  $|\psi\rangle = a|\uparrow\rangle + b|\downarrow\rangle$  is mapped onto a sphere where the position on the sphere depends on the probability amplitudes  $|a|^2, |b|^2$  and the complex phase difference  $\phi = \arctan \frac{\text{Im } b}{\text{Re } b} - \arctan \frac{\text{Im } a}{\text{Re } a}$ . (a) In Ramsey spectroscopy, a superposition state (step 1) is produced and allowed to evolve freely (step 2). The evolution of the state, i.e., the angle  $\phi$ , depends on the frequency difference between the transition frequency of the two level system and the reference oscillator. By mapping the phase shift  $\phi$  onto the population number difference  $\Delta N_{|\uparrow\rangle-|\downarrow\rangle} = |b|^2 - |a|^2$  (step 3), the frequency difference can be extracted and used to stabilize the reference oscillator. The quantum mechanical measurement uncertainties are indicated as noise discs and it is obvious that the measurement uncertainties compromise the precision of the atomic clock. (b) Using a phase uncertainty squeezed state in the clock protocol reduces the measurement uncertainty and thereby increases the precision of the clock. (c)–(e) Applying a QND measurement to the superposition state reduces the population number uncertainty. The population squeezed state has to be rotated into a phase squeezed state which is then used to complete the Ramsey cycle.

transferred into the superposition state, the state precesses along the equator by an angle  $\phi$  (step 2) which is determined by the frequency offset between the atomic transition frequency and the microwave oscillator. In step 3, this angle is mapped onto a difference between  $\Delta N_{|\uparrow\rangle-|\downarrow\rangle} = |b|^2 - |a|^2$  the populations in the two clock states  $|\uparrow\rangle$  and  $|\downarrow\rangle$  and becomes measurable (step 4). The measurement signal can be used to stabilize the frequency of the oscillator to the atomic transition frequency. The final state of the atomic system is described by the final state probability amplitudes  $a$  and  $b$ . Since quantum mechanics only predicts the probability  $|a|^2, |b|^2$

of obtaining the associated measurement results  $|\uparrow\rangle$  or  $|\downarrow\rangle$ , the measurement outcome is intrinsically probabilistic. The Poissonian nature of the measurement process leads to a fundamental, statistical uncertainty of the measurement result. It should be obvious from figure 1.1(a) that the quantum mechanical measurement uncertainty, indicated by the density discs associated with the states, limits the precision with which the precession angle  $\phi$  and thereby the difference between the reference oscillator and the atomic transition can be determined. Due to the probabilistic nature of the measurement process, the measurement precision, the certainty with which one can assume that a measurement outcome actually corresponds to the real value, depends on the the number of systems being measured on. In the specific case of caesium atomic clocks, this is the number of atoms used in the spectroscopy setup. The precision of state-of-the-art caesium fountain clocks has reached the “quantum projection noise limit” [10], which is the fundamental limit, given a fixed number of atoms. Interestingly enough, quantum mechanics itself proposes a way out of the misery it creates [11].

When an ensemble of atoms is considered, the projection postulate of a quantum mechanical measurement only demands that the ensemble state is projected into an ensemble eigenstate. It is therefore possible to devise a so-called quantum non-demolition (QND) measurement scheme on a multi particle system, where the single atom wave function can still represent a quantum mechanical superposition state after the measurement. This allows one to extract information on the state multiple times without considerably altering it. When a first measurement on the system is already quantum projection noise limited, it is obvious that combining it with the outcome of a second measurement allows one to reduce the measurement uncertainty below the standard quantum limit [12]. This entirely quantum mechanical effect is called *quantum noise squeezing*. Creating such a squeezed state in the clock sequence as indicated in figure 1.1(b) obviously increases the precision of the population readout and in consequence the precision of the atomic clock. As we shall learn in chapter 2, the QND measurement scheme we apply produces a population uncertainty squeezed state. Subfigures 1.1(c)–(e) illustrate how a population uncertainty squeezed state can be used in the clock sequence by transferring the population squeezing into phase uncertainty squeezing.

The achievement of quantum uncertainty squeezing in an atomic clock configuration has been a long standing goal. To the best of our knowledge, this work, the corresponding publication [8] and the complementary work of the Vuletic group [13] are the first reports in this direction.

Quantum non-demolition probing of a collective atomic (pseudo)-spin is a powerful instrument in quantum information processing and control in itself. It is obvious that the ability to extract information on a quantum state without altering at least the variable one is interested in, opens various ways of optimal quantum state estimation and control. So reaching the quantum limit in a non-destructive probing scheme is an important milestone in itself. It is furthermore a prerequisite to being able to use the setup for quantum memory applications. Clearly, only when a control of the system on the quantum level has been achieved and quantum mechanical effects dominate the evolution and the measurements on the system, the transfer of quantum information can be demonstrated.

The first proposal of our experimental configuration can be found in [14] where first efforts on applying quantum non-demolition measurements to demonstrate quantum noise squeezing are reported. Further results have been summarized in [1, 2, 15]. In the present thesis work we shall take the non-destructive probing of an atomic ensemble as demonstrated in [2] to the next level. While the former work considered atomic ensembles with each atom prepared in one of the energy eigenstates  $|\uparrow\rangle$  or  $|\downarrow\rangle$ , we shall now focus on intrinsically quantum mechanical states  $|\psi\rangle = a|\uparrow\rangle + b|\downarrow\rangle$ , their coherent evolution under external microwave fields and the influence of dispersive probing. Finally, we consider the noise properties of the system and push the system to the standard quantum limit of measurement precision and beyond.

After this introductory chapter, the basic principles behind the measurements are given in chapter 2. We introduce the two main players in our setup, the atomic ensemble and the probe light field. After briefly discussing the essence of quantum noise, quantum non-demolition measurements and quantum noise squeezing, we look at the light-atom interaction. We are particularly interested in the light phase shift imposed onto a probe beam by the atomic ensemble, since this dispersive part of the interaction can be used to obtain a non-demolition character of the interaction. Finally, we introduce the actual measurement setup for the light phase shift, a Mach Zehnder interferometer, and discuss some corresponding theory. The chapter concludes with the experimental proposal – quantum noise limited measurements in a cold atomic ensemble. Chapter 3 discusses the experimental setup and the basic experimental techniques applied. Here we briefly recall the principles of cooling and trapping of cold atoms and discuss the technical realization of the Mach Zehnder interferometer setup. After a short excursion to the control of the equipment used in the experiment, we consider experimental data characterizing the cold sample in the dipole trap. We measure the lifetime of the atoms in the trap in a non-destructive way and observe density oscillations. Chapter 4 reports on the development of a new set of low noise differential photo detectors which are used in the experiment. The characterization of the detector deserves its own chapter because the understanding of the detector itself and the quality of the detector is one of the main reasons for the huge experimental progress starting mid 2007. The main focus of the thesis lies on chapter 5, the non-destructive measurement of quantum states during their evolution. First, the theory and basic principles of microwave spectroscopy are introduced. We then turn to the observation of Rabi oscillations on the two level system of the caesium clock states and investigate the effect of dispersive light-atom interaction on the coherent evolution of the states. Ramsey and spin echo techniques are thereafter applied to gain further information on the atomic ensemble, the effect of probing and the motion of the atoms in the trap. The tedious way towards a quantum noise limited performance of the measurement apparatus is outlined in chapter 6. We discuss the noise properties of two different interferometer setups and the obtained projection noise results. The highlight of the chapter is the observation of quantum noise limited performance of the setup in general and the demonstration of projection noise squeezing on the caesium clock transition in particular.

The presented work is the result of mainly experimental efforts. One of the main foci of the daily work in the lab has been to develop a machine which performs in

a deterministic way and according to self-introduced standards on a daily basis. A lot of time has been spent to “clean up” the technical, engineering and especially electronics side of the setup. Another focus of the work was to create a well controllable experiment where all the key control parameters can be accessed remotely via software interfaces. The realization and implementation of these controls have made many of the systematic studies presented in the main experimental chapters possible in the first place. Although perfection has not (yet) been reached, in the end, we can confidently claim that the achievement of some of these ambitious goals have been very fruitful and produced very satisfactory results. Some of them can be found in [4, 5, 6, 7, 8, 9, 16]. Of course, the work has also been presented at conferences by different members of the work group in form of talks and posters on almost every continent.



---

## General remarks

To set the stage and to get a theoretically founded approach to the experimental work presented in the later chapters, we start with some mathematical descriptions of the physical systems, their interaction focussed towards the main goal: atomic projection noise limited, quantum non-demolition measurements. In general, the work reported on in this thesis is an experimental one and this section is therefore fitted to the needs of an experimentalist to understand the experiment and the data, and we shall try not to wander off onto the meandering trails of theory too much. This theory section is meant as an introduction to the subject and motivation for the work.

We will first introduce the two main players involved in our efforts – an atomic ensemble for which we desire to measure the population of internal state and coherent light states which we use to extract information on the atomic system. For both we look at the intrinsic quantum mechanical uncertainties. We then introduce the main goal of our undertakings: reaching and beating the standard quantum limit. The light–atom interaction is formalized and we derive the interaction Hamiltonian used to obtain a non-destructive atomic state readout and population uncertainty squeezing. The chapter concludes with the experimental proposal we then implement in the later chapters.

### 2.1 The players

The experimental work is focussed on the implementation of a non – destructive measurement scheme for the *quantum* state of an atomic ensemble with a coherent light beam at the standard quantum limit. That is, we want to achieve a stability of the measurement setup, where the accuracy of the measurement outcome is limited only by the quantum mechanical uncertainties of the states involved. We will introduce the so-called projection noise of an atomic two level system and the fundamental photon number fluctuations in a coherent light state.

First we define the quantum mechanical atomic and light states, atomic pseudo-spin operators and then describe the quantum mechanical noise properties.

### 2.1.1 Quantum state of an atomic ensemble

#### Energy eigenstate description

In a quantized picture the state of an atom is characterized by a linear combination of possible (orthogonal) energy states. If we denote these states by  $|i\rangle$ , where  $\hbar\omega_i$  is their energy and  $i$  collects all relevant quantum numbers to describe the state, it is useful to define the atom transition operators [17]:

$$\hat{\sigma}_{ij} = |i\rangle\langle j| \quad (2.1)$$

For a general atomic input state,  $|\psi\rangle = \sum_l c_l |l\rangle$ , the symmetric atomic operator  $\hat{\sigma}_{ii}$  maps out the probability distribution across the energy states:  $\langle \hat{\sigma}_{ii} \rangle \equiv \langle \psi | \hat{\sigma}_{ii} | \psi \rangle = |c_i|^2$ . The non-diagonal matrix elements  $\hat{\sigma}_{ij}, i \neq j$ , are especially useful when writing down the dipole-transition operator:

$$\mathbf{er} = \sum_{i,j} |i\rangle\langle i | \mathbf{er} | j \rangle \langle j| = \sum_{i,j} \hat{\mathbf{d}}_{ij} \hat{\sigma}_{ij}, \quad \hat{\mathbf{d}}_{ij} \equiv \langle i | \mathbf{er} | j \rangle \quad (2.2)$$

For an ensemble of  $N$  identical, independent particles, the collective atomic operator  $\hat{\Sigma}_{ij}$  can be naturally introduced through:

$$\hat{\Sigma}_{ij} = \sum_{k=1}^N \hat{\sigma}_{ij}^k = \sum_k (|i\rangle\langle j|)^k \quad (2.3)$$

For a collective state, where all  $N \gg 1$  particles have been prepared in the same state,  $|\Psi\rangle = |\psi\rangle^{\otimes N} = (\sum_l c_l |l\rangle)^{\otimes N}$  the mean of the collective operators  $\langle \hat{\Sigma}_{ij} \rangle$  basically gives the not normalized ensemble average of  $N \langle \hat{\sigma}_{ij} \rangle$ .

The total energy of the system is then given by:

$$\hat{H}_A = \sum_i \hbar\omega_i \hat{\Sigma}_{ii} = \sum_k \sum_i \hbar\omega_i (|i\rangle\langle i|)^k \quad (2.4)$$

By construction, the states  $|i\rangle$  are eigenstates of the Hamiltonian.

The energy eigenstates we shall consider are the ground and excited states of the  $^{133}\text{Cs}$  D2 line transition. Figure 2.1 shows the state manifold. The single energy state is characterized by  $n L_{J=L+S}(F, m_F)$ , where  $n = 6$  is the principal quantum number of the ground and first excited states,  $L \in \{0, 1\} \equiv \{\text{S}, \text{P}\}$  is the angular momentum quantum number of the (only) valence electron, and  $S = 1/2$  its spin.  $\mathbf{J} = \mathbf{L} + \mathbf{S}$  gives the combined spin-angular momentum with quantum numbers  $J = 1/2, 3/2$ .  $F$  are the quantum numbers of the combined electron-nucleus spin  $\mathbf{F} = \mathbf{J} + \mathbf{I}$ , where  $I = 7/2$  for the caesium isotope we are considering. When we are only concerned with the states indicated in figure 2.1, the state can be sufficiently described by  $(J, F, m_F)$ ; usually we omit  $J$  and refer to the excited state quantum number as  $(F', m'_{F'})$ . We will be mentioning the corresponding transitions of the D1 line,  $6S_{1/2} \rightarrow 6P_{1/2}$  at some stage. A full level diagram can be found in [18].

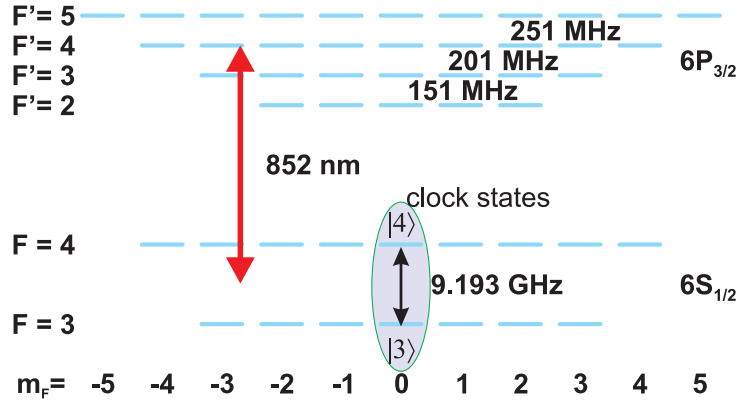


**FIGURE 2.1:** Ground and  $D2$  line excited levels of caesium. The relevant quantum numbers are the combined spin angular momentum of the electron  $\mathbf{J} = \mathbf{L} + \mathbf{S}$ ,  $J = \{1/2, 3/2\}$ , the combined angular momentum of the electron and the nucleus  $F$  and the magnetic substate quantum number  $m_F$ .

### Angular momentum representation

Let us for the moment restrict the discussion to the two magnetic hyperfine sub-levels of the caesium atom  $6S_{1/2}(F = 3, m_F = 0) \equiv |3\rangle$  and  $6S_{1/2}(F = 4, m_F = 0) \equiv |4\rangle$  – the so-called clock levels.

The two level system  $\{|3\rangle, |4\rangle\}$  is equivalent to a spin-1/2 system. This connection is made obvious by spelling out the single atom  $k$  angular momentum operators  $\hat{\mathbf{j}}^k = (\hat{j}_x^k, \hat{j}_y^k, \hat{j}_z^k)$  in the spin-1/2 operator algebra basis [19, 20]:

$$\hat{j}_x^k = \frac{1}{2}(\hat{\sigma}_{43}^k + \hat{\sigma}_{34}^k) = \frac{1}{2}(|4\rangle\langle 3|^k + |3\rangle\langle 4|^k) \quad (2.5)$$

$$\hat{j}_y^k = -\frac{i}{2}(\hat{\sigma}_{43}^k - \hat{\sigma}_{34}^k) = -\frac{i}{2}(|4\rangle\langle 3|^k - |3\rangle\langle 4|^k) \quad (2.6)$$

$$\hat{j}_z^k = \frac{1}{2}(\hat{\sigma}_{44}^k - \hat{\sigma}_{33}^k) = \frac{1}{2}(|4\rangle\langle 4|^k - |3\rangle\langle 3|^k) \quad (2.7)$$

$\hat{\mathbf{j}}^k$  is an angular momentum operator in the sense that its components span an angular momentum algebra through the commutator relation  $[\hat{j}_x^k, \hat{j}_y^k] = i\hat{j}_z^k$ , cyclic. A collective spin operator for an ensemble of  $N$  atoms can naturally be defined by  $\hat{\mathbf{J}} = \sum_{k=1}^N \hat{\mathbf{j}}^k$ .

The physical meaning of  $\hat{J}_z$  is quite obvious: Its mean value for a general collective input state  $|\Psi\rangle = \prod_l (c_3^l|3\rangle + c_4^l|4\rangle)$  gives half the mean population number difference:  $\langle \hat{J}_z \rangle = \frac{1}{2} \sum_l (|c_4^l|^2 - |c_3^l|^2)$ . The orthogonal  $x$  and  $y$  projections are the coherences of the state. Their meaning becomes clear when comparing their mean values for

- a coherent superposition state  $|\Psi\rangle_{\text{coh}} = \left( \frac{|3\rangle + e^{i\phi}|4\rangle}{\sqrt{2}} \right)^{\otimes N}$  where all single atom states are added up coherently with the same phase  $\phi$
- to a fully decohered ensemble state  $|\Psi\rangle_{\text{decoh}} = \prod_{l=1}^N \left( \frac{|3\rangle_l + e^{i\phi_l}|4\rangle_l}{\sqrt{2}} \right)$  with a flat, random distribution of the phases  $\phi_l$

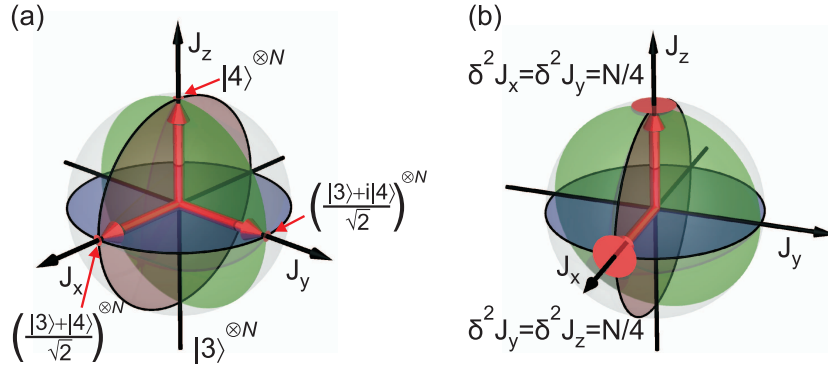


**FIGURE 2.2:** (a) Illustration of collective angular momentum vector for different ensemble states. (b) Uncertainties of the projections for two different states. A minimum uncertainty state – coherent or coherent superposition state – has been assumed.

- and an incoherent mixture  $|\Psi\rangle_{\text{mix}} =$  where  $N/2$  atoms are prepared in the  $|3\rangle$  state and  $N/2$  atoms reside in the  $|4\rangle$  state

All three states have  $\langle \hat{J}_z \rangle = 0$ . While  $\sqrt{\langle \hat{J}_x \rangle^2 + \langle \hat{J}_y \rangle^2} = \frac{N}{2}$  for  $|\Psi\rangle_{\text{coh}}$ , both  $\langle \hat{J}_x \rangle = \langle \hat{J}_y \rangle = 0$  for the fully decohered state  $|\Psi\rangle_{\text{decoh}}$  and the statistical mixture  $|\Psi\rangle_{\text{mix}}$ <sup>1</sup>. The length of the collective spin vector  $|\langle \hat{\mathbf{J}} \rangle| = \sqrt{\langle \hat{J}_x \rangle^2 + \langle \hat{J}_y \rangle^2 + \langle \hat{J}_z \rangle^2}$  is zero for fully decohered states and can therefore be used to distinguish between fully coherent superpositions and systems with less or no coherence.

The vector  $\hat{\mathbf{J}}$  can be conveniently illustrated in a Bloch sphere like picture. The Bloch vector  $\mathbf{U}$  will be introduced more formally in section 5.1.1, but it deviates from  $\hat{\mathbf{J}}$  only by a factor of 2 in the normalization. For a given state and without decoherence, the components of  $\langle \hat{\mathbf{J}} \rangle = (\hat{J}_x, \hat{J}_y, \hat{J}_z)$  form a vector with fixed length. The length of  $\langle \hat{\mathbf{J}} \rangle$  is fixed since  $\langle \hat{\mathbf{J}} \rangle^2$  has to be a constant eigenvalue as for a spin variable. For a coherent atomic state of  $N$  atoms, can therefore be mapped onto a sphere with radius  $|\langle \hat{\mathbf{J}} \rangle| = \frac{N}{2}$ . The state corresponds to a point on the sphere – the tip of the vector. The evolution of the ensemble under the influence of an interaction Hamiltonian can then be described as a trajectory on the surface of the sphere. Decohering terms in the Hamiltonian can change the length of the vector. Figure 2.2(a) illustrates some of the states discussed above.

### Angular momentum uncertainties

Let us consider an ensemble superposition state  $|\Psi\rangle = \left(\frac{1}{\sqrt{2}}(|3\rangle + |4\rangle)\right)^{\otimes N}$  and calculate the first two moments of the collective spin operator  $\hat{\mathbf{J}}$ , the mean values

<sup>1</sup>Note that *in general* the fully decohered state with a random, flat phase distribution  $\phi_n \in [0, 2\pi]$  cannot be distinguished from a statistical mixture.

$\langle \hat{J}_i \rangle$  and the variances  $\delta^2 \hat{J}_i = \langle \hat{J}_i^2 \rangle - \langle \hat{J}_i \rangle^2$ :

$$\langle \hat{J}_x \rangle = \frac{N}{2} \quad , \quad \delta^2 \hat{J}_x = 0 \quad (2.8)$$

$$\langle \hat{J}_y \rangle = 0 \quad , \quad \delta^2 \hat{J}_y = \frac{N}{4} \quad (2.9)$$

$$\langle \hat{J}_z \rangle = 0 \quad , \quad \delta^2 \hat{J}_z = \frac{N}{4} \quad (2.10)$$

The uncertainties for non-commuting quantum mechanical variables can also be directly derived from the Heisenberg uncertainty principle, which for a general set of two operators reads [21]:

$$\delta^2 \hat{o}_1 \delta^2 \hat{o}_2 \geq \frac{1}{4} |\langle [\hat{o}_1, \hat{o}_2] \rangle|^2 \quad (2.11)$$

For the above combination,  $\delta^2 \hat{J}_y \delta^2 \hat{J}_z \geq \frac{1}{4} \frac{N^2}{4}$ , we see that for an ideally prepared superposition state the uncertainty relation is met with an equal sign. The atomic ensemble state is thus a minimum uncertainty state. For reasons which will become clear later, such states are often termed coherent spin states (CSS). In the particular case of coherently added single atom superposition states  $|\Psi\rangle = \left( \frac{|3\rangle + |4\rangle}{\sqrt{2}} \right)^{\otimes N}$ , the term coherent superposition state is also common.

As mentioned,  $\hat{J}_z$  is proportional to the population number difference operator. A set of measurements of this operator returns  $\langle \hat{J}_z \rangle$ . Due to the uncertainty relations (2.8) – (2.10) the variance of the measurement results for a given number of atoms has a lower bound. Since the uncertainties are basically due to the probabilistic nature of quantum mechanics and the projection postulate, these uncertainties are also known as *projection noise*.

In figure 2.2(b) the uncertainty discs are illustrated for a coherent spin state  $|\Psi\rangle = |4\rangle^{\otimes N}$  and a coherent superposition state  $|\Psi\rangle = \left( \frac{|4\rangle + |3\rangle}{\sqrt{2}} \right)^{\otimes N}$ . When  $|3\rangle$  and  $|4\rangle$  correspond to the two caesium hyperfine levels as discussed above, one only has direct (experimental) access to the population number difference  $\sim \langle \hat{J}_z \rangle$ , so the quantum mechanical uncertainties only manifest themselves when a superposition state is considered. When considering a real spin variable as in [22], the projections can be directly observed by choosing the right measurement basis.

To derive the uncertainty relations in a slightly different approach, which is often used in textbooks as a illustration for the probabilistic nature of quantum mechanics, one combines the measurement probabilities for an ensemble of  $N$  atoms (or a collection of measurement results from  $N$  independent systems) according to the binomial distribution. The probability  $P_3$  of measuring  $N_3$  atoms in state  $|3\rangle$  for an initial state  $|\Psi\rangle = \prod_l (c_3^l |3\rangle_l + c_4^l |4\rangle_l)$  is ( $c_3^l \equiv c_3, c_4^l \equiv c_4$ ) [20]:

$$P_3 = \frac{N!}{N_3!(N - N_3)!} |c_3|^{2N_3} (1 - |c_3|^2)^{(N - N_3)} \quad (2.12)$$

with the well known variance of  $\sigma^2 = N/4$  for  $|c_3|^2 = 1/2$ .

Note that we *in general* associate the term “noise” with the variance  $\delta^2 s$  of a statistical variable  $s$ ; usually measurement precision or uncertainty is associated with the standard deviation  $\sigma = \sqrt{\delta^2 s} \equiv \delta s$ .

Operationally, when we want to determine if a measurement is indeed limited by the projection noise of the atomic ensemble we are measuring on, a linear scaling of the signal variance of the population number difference with atom number in the coherent superposition state, is the signature of quantum mechanics.

### 2.1.2 Coherent light states

To determine the population number difference between the quantum states of the atomic ensemble, we couple coherent laser light pulses to it. The coupling itself will be discussed in section 2.3. For now we shall only consider the quantum mechanical uncertainties in the photon number of a coherent light pulse. From the quantization of the electromagnetic field [23] it is known that the closest quantum mechanical description of a classical, monochromatic laser light field is a coherent state  $|\alpha\rangle$  [24]:

$$|\alpha\rangle = \exp\left(-\frac{1}{2}|\alpha|^2\right) \sum_{n=0}^{\infty} \frac{\alpha^n}{\sqrt{n!}} |n\rangle \quad (2.13)$$

which is an eigenstate of the field annihilation operator  $\hat{a}$ :

$$\hat{a}|\alpha\rangle = \alpha|\alpha\rangle \quad (2.14)$$

For the coherent state, the mean photon number is  $\langle\alpha|\hat{a}^\dagger\hat{a}|\alpha\rangle = |\alpha|^2 = \bar{n}$  and the second moment  $\delta^2(\hat{a}^\dagger\hat{a}) = \bar{n}$ . Using a coherent light state in a measurement, where the measurement signal is proportional to the number of photons in the pulse (or the intensity of the beam), the measurement accuracy will be fundamentally limited by the intrinsic uncertainty of the photon number in the coherent state. Operationally, this limit is achieved, when the variance of the measured signal scales linearly with the applied mean photon number. In this case, the measurement is light shot noise limited. The determination of light shot noise is discussed in detail in section 4 where we consider the operation principle and characterization of photo detectors. The linear scaling of the variance with “particle” number justifies the term coherent state for the atomic superposition state discussed above. In amplitude  $X_L = \frac{1}{2}(\hat{a} + \hat{a}^\dagger)$  and phase  $P_L = \frac{1}{2i}(\hat{a} - \hat{a}^\dagger)$  quadratures,  $[X_L, P_L] = i/2$ , the coherent state is a minimum uncertainty state  $\delta^2 X_L \delta^2 P_L = 1/16$ . This is the motivation for calling a minimum atomic uncertainty state a coherent state.

## 2.2 Reduction of population number uncertainty

One of the main goals in our experiment is to reach a precision of the measurement of the population number difference  $\sim \hat{J}_z$  of two energy eigenstates of atoms in an atomic ensemble only bounded by the above introduced quantum limits: A measurement uncertainty which is limited only by the projection noise of the atomic ensemble and the shot noise of the probe light. We want to reach this limit in a quantum non-demolition (QND) measurement. In this type of measurement scheme, the eigenvalue of the operator  $\hat{J}_z$  we are interested in is determined without destroying the quantum nature of the system. The disturbance on the quantum system due to the measurement is channeled into a variable we are (at first glance)

not interested in. Assume, we have reached the standard quantum limit in such a measurement. In this case it is possible to measure a second time on the same ensemble and look for correlations between the two measurements. If such correlations are observed, the first measurement allows to predict the second measurement to an accuracy better than the standard quantum limit. The first measurement has projected the atomic state onto a new state with reduced uncertainty – a squeezed state – and this squeezing is verified with the second measurement.

To understand the process better, we shall first take a closer look at QND measurements and then see what squeezing is all about.

### 2.2.1 Quantum non-demolition measurements

The general notion of quantum non-demolition (QND) measurements was first introduced by Braginsky [25]. In general, a quantum mechanical measurement process is described by the interaction Hamiltonian  $\hat{H}_{\text{int}}$  of the measurement apparatus  $\mathcal{S}$  and the system to be measured on  $\mathcal{J}$ . The objective of the measurement on system  $\mathcal{J}$  is to extract the eigenvalues  $\gamma_n$  of the observable  $\hat{J}_z$ . The time evolution of an operator  $\hat{O}$  (in the Heisenberg picture, where the time dependence is in the operators and not in the states as for the Schrödinger picture), is as usual governed by the Heisenberg equation of motion:

$$\frac{\partial}{\partial t}\hat{O}(t) = \frac{i}{\hbar}[\hat{H}, \hat{O}(t)] \quad (2.15)$$

It is obvious that if the observable  $\hat{J}_z$  commutes with the total Hamiltonian of the system  $\hat{H} = \hat{H}_{\mathcal{J}} + \hat{H}_{\mathcal{S}} + \hat{H}_{\text{int}}$ , i.e.,  $[\hat{H}, \hat{J}_z] = 0$ , it is left unchanged throughout the evolution.  $\hat{J}_z$  is a QND observable. The condition can be relaxed to the sufficient condition [26, 27]:

$$[\hat{H}_{\text{int}}, \hat{J}_z] = 0 \quad (2.16)$$

where the observable has to commute with the interaction Hamiltonian, only.

From a theorists point of view, the goal is now to construct an interaction Hamiltonian which commutes with the  $\hat{J}_z$  operator of our spin system as introduced in section 2.1.1. Let us consider a Hamiltonian which couples the  $z$ -components of two spins  $\hat{\mathbf{J}}, \hat{\mathbf{S}}, [\hat{S}_x, \hat{S}_y] = i\hat{S}_z, [\hat{J}_x, \hat{J}_y] = i\hat{J}_z$ , cyclic:

$$\hat{H}_{\text{int}} = \kappa\hbar\delta(t)\hat{S}_z\hat{J}_z \quad (2.17)$$

where  $\kappa$  parameterizes the measurement strength during the instantaneous interaction –  $\delta(t)$  is the Dirac delta function. Clearly,  $\hat{J}_z$  and  $\hat{S}_z$  are constants of motion; integrating the Heisenberg equation we get:

$$\hat{S}_x^{\text{out}} = \hat{S}_x^{\text{in}} - \kappa\hat{S}_y^{\text{in}}\hat{J}_z^{\text{in}} \quad \hat{J}_x^{\text{out}} = \hat{J}_x^{\text{in}} - \kappa\hat{J}_y^{\text{in}}\hat{S}_z^{\text{in}} \quad (2.18)$$

$$\hat{S}_y^{\text{out}} = \hat{S}_y^{\text{in}} + \kappa\hat{S}_x^{\text{in}}\hat{J}_z^{\text{in}} \quad \hat{J}_y^{\text{out}} = \hat{J}_y^{\text{in}} + \kappa\hat{J}_x^{\text{in}}\hat{S}_z^{\text{in}} \quad (2.19)$$

$$\hat{S}_z^{\text{out}} = \hat{S}_z^{\text{in}} \quad \hat{J}_z^{\text{out}} = \hat{J}_z^{\text{in}} \quad (2.20)$$

Due to the symmetry of the Hamiltonian, the input – output relations are also fully symmetric in  $\hat{\mathbf{J}}$  and  $\hat{\mathbf{S}}$ . Looking at the equations, it is obvious that by choosing the

$\hat{S}_x$  or the  $\hat{S}_y$  component of system  $\hat{\mathbf{S}}$  as a meter variable, we can extract information on the desired  $\hat{J}_z$  component. The correlation strength between the two systems is given by  $\kappa$ .

In such an indirect measurement [26, 28], the eigenvalues  $\gamma_n$  of the observable  $\hat{J}_z$  of the atomic system  $\mathcal{J}$  are inferred by coupling  $\mathcal{J}$  to a second quantum system  $\mathcal{S}$ . The total system  $\mathcal{J} + \mathcal{S}$  prior to the measurement is described by  $|\psi^{\mathcal{J}}\rangle \otimes |\psi^{\mathcal{S}}\rangle$  where  $|\psi^{\mathcal{J}}\rangle$  and  $|\psi^{\mathcal{S}}\rangle$  are the states of the systems prior to the measurement. At the measurement time  $t_0$ , the systems interact and form an entangled state:

$$|\psi^{\mathcal{J}}\rangle \otimes |\psi^{\mathcal{S}}\rangle \rightarrow |\psi^{\mathcal{J},\mathcal{S}}\rangle \quad (2.21)$$

In a second step, information on the state of the system  $\mathcal{J}$ , i.e., a meter for the eigenvalue  $\gamma_n$  of  $\hat{J}_z$  is obtained in the eigenvalue  $\sigma_n$  of  $\hat{S}_y$  in a direct measurement on the system  $\mathcal{S}$ . The correlation strength between  $\gamma_n$  and  $\sigma_n$  is given by the interaction strength  $\kappa$ . If there are correlations between the two eigenvalues, the systems must have been correlated, i.e., the combined wave function  $|\psi^{\mathcal{J},\mathcal{S}}\rangle \neq |\psi^{\mathcal{J}}\rangle \otimes |\psi^{\mathcal{S}}\rangle$  cannot have been separable, and thus the system must have been in an entangled state.

Since the destructive measurement is done on the secondary system, the wave function of  $\mathcal{J}$  does still exist. In the case of  $\kappa \rightarrow \infty$ , the correlations between the two systems are perfect. Unless it was prepared in an eigenstate, the system  $\mathcal{J}$  has been projected into an eigenstate of  $\hat{J}_z$  with eigenvalue  $\gamma_n$  in by the measurement. Repeated measurements on  $\mathcal{J}$  of  $\hat{J}_z$  in the same indirect fashion will thus yield the same measurement outcome  $\sigma_n \rightarrow \gamma_n$ . When the correlations are finite,  $\kappa \approx 1$ , the system  $\mathcal{J}$  is projected into a subset of eigenstates and a second measurement has to return an outcome compatible with this reduced set.

After a perfect and completely projective QND measurement, the observed variable  $\hat{J}_z, \gamma_n$  is known,  $\delta^2 \hat{J}_z \rightarrow 0$ . At first glance one would expect that due to the lower bound in the uncertainty product of equation (2.11), the conjugate observable  $\hat{J}_y$  becomes undetermined,  $\delta^2 \hat{J}_y \rightarrow \infty$ . This is unphysical since the possible values for  $\hat{J}_y$  are bounded by the size of the Bloch sphere, figure 2.2 and the variance of a flat random distribution  $\langle \hat{J}_y \rangle \in [-\frac{N}{2}, \frac{N}{2}]$  is  $\delta^2 \hat{J}_y = \frac{N^2}{3}$ . To resolve the mystery, one has to take into account that the  $\hat{J}_x$  and  $\hat{J}_y$  components are not decoupled. An increase in the width of the distribution in  $\hat{J}_y$  direction changes the mean value of  $\hat{J}_x$  as well. For a state with randomly distributed phases in the  $\hat{J}_x - \hat{J}_y$  plane (the fully decohered state as discussed above),  $\langle \hat{J}_x \rangle = 0$ , so the uncertainty relation is trivial. In that sense, the lower bound in the uncertainty relation changes and it stays fulfilled. Since the mean length of the vector  $\langle \mathbf{J} \rangle$  is proportional to the maximum signal amplitude in a spectroscopic measurement, a perfectly squeezed state is useless for spectroscopical applications.

In general, a QND measurement will not be perfect, i.e., there are terms in the interaction Hamiltonian which do not commute with the observable. These terms change or destroy the quantum state during the measurement and correlations between consecutive measurements will be reduced. In this context, we call anything that reduces the mean length of the  $\hat{J}_x$  component beyond the back action from the ideal QND measurement “state destruction”. In the case of a non-ideal QND measurement, the coupling strength has to be chosen such that the destruction

inflicted by the measurement is less than the information gain. The measurement will then only be weakly projective, i.e., the system will be projected into a subset of the allowed eigenvalues [29, 30, 31, 32]. The outcome of a second measurement on the same system can only be predicted with limited certainty. The projection into the subset of eigenvalues acts as a truncation of the initial probability distribution of the eigenvalues, it decimates the possible states and therefore the variance of the remaining state (or rather the width of the eigenvalue distribution) will be reduced.

### 2.2.2 Squeezing criteria

#### Kitagawa and Ueda squeezing criterion

The above discussion makes clear that the “change of the uncertainty relation” by the measurement has to be taken into account when claiming a useful noise reduction for the output state. To be able to talk about a squeezed state, the variance  $\delta^2 \hat{J}_z^{\text{out}}$  has to be reduced below the bound in the uncertainty product of the states *after* the measurement. When the measurement reduces the mean value of  $\langle \hat{J}_x \rangle^{\text{in}} \rightarrow \langle \hat{J}_x \rangle^{\text{out}} = (1 - \eta) \langle \hat{J}_x \rangle^{\text{in}}$ , the variance  $\delta^2 \hat{J}_z^{\text{reduced}}$  has to be compared to the *new* standard quantum limit. To obtain squeezing we therefore need to demand [33]:

$$\begin{aligned} \delta^2 \hat{J}_z^{\text{out}} &< \frac{1}{2} \langle \hat{J}_x \rangle^{\text{out}} = (1 - \eta) \frac{\langle \hat{J}_x \rangle^{\text{in}}}{2} \\ \Leftrightarrow \delta^2 \hat{J}_z^{\text{out}} &< (1 - \eta) \delta^2 \hat{J}_z^{\text{in}} \end{aligned} \quad (2.22)$$

Here we have merged all the destruction effects into the *decoherence* parameter  $\eta$ . This squeezing limit is known as the Kitagawa and Ueda criterion. It is often cited as the criterion relevant for claiming entanglement between the atoms but even in the original paper they state that it is in general not sufficient [33, 34, 35].

#### Wineland et al. squeezing criterion

A more stringent criterion has been put up by Wineland *et al.* [34, 36]. In spectroscopy it is the angular uncertainty of the state vector:

$$\delta\alpha = \arcsin \frac{\sqrt{\delta^2 \hat{J}_z}}{|\langle \hat{J}_x \rangle|} \quad (2.23)$$

which has to be reduced for the state to decrease the uncertainty in the spectroscopy signal. We therefore get the relation:

$$\begin{aligned} \frac{\delta^2 \hat{J}_z^{\text{out}}}{|\langle \hat{J}_x \rangle^{\text{out}}|^2} &< \frac{\delta^2 \hat{J}_z^{\text{in}}}{|\langle \hat{J}_x \rangle^{\text{in}}|^2} \\ \Leftrightarrow \delta^2 \hat{J}_z^{\text{out}} &< (1 - \eta)^2 \delta^2 \hat{J}_z^{\text{in}} \end{aligned} \quad (2.24)$$

as squeezing criterion. It can be shown that the atoms in the sample have to be non-classically correlated to fulfil this relation [34].

### 2.2.3 Spin squeezing via QND interaction

The essence of squeezing did already become clear in the previous section: In a QND measurement, the state of the system is projected into an eigenstate of the observable. If the measurement is only weak, the system is projected into a eigenstate subset of the observable. Two consecutive measurements  $m_1, m_2$  will therefore be correlated,  $\delta^2(m_1 + m_2) \neq \delta^2 m_1 + \delta^2 m_2$  and the conditional variance  $\delta^2(m_2 - km_1) < \delta^2 m_2$  will be reduced below the variance of a single measurement result, where  $k$  is the correlation strength. At the quantum limit, one is therefore able to predict the outcome of a second measurement to better than the projection noise limit. This, in return, means that the atoms in the ensemble can no longer be independent and thus have to be correlated or entangled [33, 34, 35]. The squeezing criterion in equation (2.22) and equation (2.24) further tells us that the back action onto the system has to be taken into account, especially when large squeezing or imperfect QND measurements are considered.

Let us formalize the reduction of the variance  $\delta^2 J_z$  by QND measurements a bit more: After the measurement, described by an interaction Hamiltonian like in equation (2.17), the output state is described by equations (2.18) – (2.20). Let us assume (we will substantiate this claim later) that the second spin variable used as measurement system  $\hat{\mathbf{S}}$  is also in a superposition state with mean values and variances as for the atomic state  $\hat{\mathbf{J}}$  in equations (2.8) – (2.10), ( $N \rightarrow \bar{n}$  will be associated with the mean photon number in the measurement apparatus later on):

$$\langle \hat{S}_x \rangle = \frac{\bar{n}}{2} \quad , \quad \delta^2 \hat{S}_x = 0 \quad (2.25)$$

$$\langle \hat{S}_y \rangle = 0 \quad , \quad \delta^2 \hat{S}_y = \frac{\bar{n}}{4} \quad (2.26)$$

$$\langle \hat{S}_z \rangle = 0 \quad , \quad \delta^2 \hat{S}_z = \frac{\bar{n}}{4} \quad (2.27)$$

With these values the variance of the atomic output state  $\hat{J}_y^{\text{out}}$  is found from equation (2.19):

$$\begin{aligned} \delta^2 \hat{J}_y^{\text{out}} &= \delta^2 \hat{J}_y^{\text{in}} + \kappa^2 \delta^2 (\hat{J}_x^{\text{in}} \hat{S}_z^{\text{in}}) \\ &= \frac{N}{4} (1 + \kappa^2 \frac{N}{4} \frac{\bar{n}}{4}) \equiv \frac{N}{4} (1 + \tilde{\kappa}^2) \end{aligned} \quad (2.28)$$

where we have used that  $\delta^2 (\hat{J}_x^{\text{in}} \hat{S}_z^{\text{in}}) = \langle \hat{J}_x^{\text{in}} \rangle^2 \delta^2 \hat{S}_z^{\text{in}} + \langle \hat{S}_z^{\text{in}} \rangle^2 \delta^2 \hat{J}_x^{\text{in}}$ . Since the state we started out in was a minimum uncertainty state and the product of the variances stays constant under the action of a unitary interaction Hamiltonian [37], i.e.,  $\delta^2 \hat{J}_y^{\text{in}} \delta^2 \hat{J}_z^{\text{in}} = \delta^2 \hat{J}_y^{\text{out}} \delta^2 \hat{J}_z^{\text{out}} = \frac{N}{16}$ , the uncertainty in the population number difference after the measurement  $\delta^2 \hat{J}_z^{\text{out}}$  is [12, 38]:

$$\delta^2 \hat{J}_z^{\text{out}} = \delta^2 \hat{J}_z^{\text{in}} \left( \frac{1}{1 + \tilde{\kappa}^2} \right) \quad (2.29)$$

Note that no decoherence or destruction of the initial state has been taken into account in this derivation. The amount of squeezing is determined by the strength of the interaction  $\tilde{\kappa}^2$  which itself depends on the number of atoms in the state and the photon number used to probe the sample. Without the decoherence effects,

which scale with the probe photon number, the measurement strength starts from weakly projective with little information gain and thus little squeezing to a fully projective measurement where the state is fully known thus perfectly squeezed [29]. Formally, the decohering effects just reduce the effective number of atoms, which reduces the input state variance  $\delta^2 \hat{J}_z^{\text{in}}$  by the decoherence parameter  $\eta$ , compare equations (2.24). To claim squeezing, we therefore have to demand:

$$\delta^2 \hat{J}_z^{\text{out}} = \left( \frac{1}{1 + \tilde{\kappa}^2} \right) \delta^2 \hat{J}_z^{\text{in}} < (1 - \eta)^2 \delta^2 \hat{J}_z^{\text{in}} \quad (2.30)$$

To stay in the language of information and destruction,  $\tilde{\kappa}^2$  parameterizes the gain in information on the state in the measurement while  $\eta$  summarizes the destruction in the state. As we shall see in the next section, decoherence is an unavoidable side product of the interaction,  $\tilde{\kappa}^2 \propto \eta$ . One therefore has to trade information gain against non-destructiveness to achieve optimal squeezing.

After these introductory remarks on atomic states, non-destructive quantum measurements and (pseudo) spin squeezing, let us turn to the atom–light interaction in a more practical way and gather some equations on how to implement a quantum non-demolition measurement in practice.

## 2.3 Light – atom interaction

The purpose of this section is to give a short account on the light – atom interaction focussed on the properties of the light after the interaction. In chapter 5 some of the calculations will be performed in a more thorough way, focussing on the evolution of the atomic states.

When an electromagnetic field interacts with a two level system, the light can be spontaneously scattered, i.e., absorbed and re-emitted into a different field mode. At the same time the phase of the interacting light beam is changed with respect to a reference beam. While the absorption *in general* leads to decoherence or destruction of the quantum state of the atoms, the light phase shift can be used to extract information without necessarily causing decoherence.

In the language of Hamiltonians, the combined interacting system consists of the bare atomic energy  $\hat{H}_{\text{at}}$  (equation (2.4)), the energy of the electromagnetic field  $\hat{H}_{\text{em}} = \hbar\omega\hat{a}^\dagger\hat{a}$  and the interaction Hamiltonian  $\hat{H}_{\text{int}}$ . In the rotating wave approximation one derives [17]:

$$\hat{H}_{\text{int}} = \hbar g \left( |e\rangle\langle g|\hat{a} + |g\rangle\langle e|\hat{a}^\dagger \right) \quad (2.31)$$

$$g = -\sqrt{\frac{\omega}{2\epsilon_0 V \hbar}} \mathbf{e} \cdot \hat{\mathbf{d}}_{eg}, \quad \hat{\mathbf{d}}_{eg} = \langle e|\mathbf{e}\hat{\mathbf{r}}|g\rangle \quad (2.32)$$

$\omega$  is the driving field frequency  $\mathbf{e}$  is its polarization vector, and  $\hat{\mathbf{d}}_{ge}$  the dipole matrix element.  $e$  is the electron charge and  $\hat{\mathbf{r}}$  is the position operator. The interpretation of the Hamiltonian is straight forward: the destruction of a photon

by  $\hat{a}$  transfers the atom from its ground state  $|g\rangle$  into the corresponding excited state  $|e\rangle$ ; the adjoint term accounts for the inverse process. For the two level case one can exploit the spin 1/2 system formalism:

$$|e\rangle \equiv \begin{pmatrix} 1 \\ 0 \end{pmatrix}, |g\rangle \equiv \begin{pmatrix} 0 \\ 1 \end{pmatrix} \quad (2.33)$$

We use the Pauli spin matrices  $\hat{\sigma}_i, i = \{1, 2, 3\}$ ,  $[\hat{\sigma}_1, \hat{\sigma}_2] = 2i\hat{\sigma}_3$ , cyclic and their linear combinations  $\hat{\sigma}_\pm = \frac{1}{2}(\hat{\sigma}_1 \pm i\hat{\sigma}_2)$  which act as rising and lowering operators, i.e., transfer atoms from the ground into the excited state or from the excited state into the ground state. With the spin matrices, the total Hamiltonian reads (choosing the energy zero of the atomic system between the two levels with energy splitting  $\hbar\omega_0$  and neglecting energy offsets):

$$\hat{H} = \frac{1}{2}\hbar\omega_0\hat{\sigma}_3 + \hbar\omega\hat{a}^\dagger\hat{a} + \hbar g (\hat{\sigma}_+\hat{a} + \hat{\sigma}_-\hat{a}^\dagger) \quad (2.34)$$

With the Heisenberg equation of motion (2.15) the time evolution of the operators can be calculated. The effect of spontaneous decay from the excited state into the ground state with decay rate  $\gamma$  is included in a rate equation kind of fashion as known from the Wigner–Weisskopf theory [17, 39]. We will later look at off resonant interactions only, so the excited state's population can be adiabatically eliminated. The final differential equation obtained for the field annihilation operator  $\hat{a}$  can be integrated directly over the interaction time  $\tau$  and we get [1]:

$$\hat{a}'(\tau) = \hat{a}'(0) \exp\left(-g^2 \frac{-i\Delta + \frac{\gamma}{2}}{\Delta^2 + (\frac{\gamma}{2})^2} \hat{\sigma}_z \tau\right) \quad (2.35)$$

In a homogeneous but spatially extended atomic ensemble of  $N$  independent and equally prepared atoms,  $\hat{\sigma}_z \rightarrow \Sigma_z \equiv N\hat{\sigma}_z$  and  $\tau = \frac{l}{c}$  where  $l$  is the length of the ensemble. From equation (2.35) we extract that the outgoing electromagnetic field will be exponentially absorbed with coefficient  $S$ :

$$S = g^2 \frac{\frac{\gamma}{2}}{\Delta^2 + (\frac{\gamma}{2})^2} \hat{\sigma}_z \tau \quad (2.36)$$

and the field has gained an additional phase of:

$$\Delta\phi = g^2 \frac{\Delta}{\Delta^2 + (\frac{\gamma}{2})^2} \hat{\sigma}_z \tau \quad (2.37)$$

An alternative approach to derive the above relations for the phase shift and the absorption is sketched in appendix A.1. The explicit calculation of the coupling strength  $g$ , involving the dipole matrix elements  $\hat{\mathbf{d}}_{eg} = \langle e|e\hat{\mathbf{r}}|g\rangle$  is sketched in appendix A.2 but can be found in many standard texts [18, 40, 41, 42]. For the dipole matrix element one obtains:

$$\begin{aligned} |\langle Fm_F|er_q|F'm'_F\rangle|^2 &= (2F'+1)(2F+1) \begin{pmatrix} F' & 1 & F \\ m'_F & q & -m_F \end{pmatrix}^2 \\ &\times \left\{ \begin{matrix} J & J' & 1 \\ F' & F & I \end{matrix} \right\}^2 \frac{\gamma 3\pi\epsilon_0 \hbar c^3}{\omega^3} (2J'+1) \end{aligned} \quad (2.38)$$

The  $\{\dots\}$  brackets refer to the Wigner 6-j symbol and the  $(\dots)$  brackets denote the Wigner 3-j symbol. Primed values correspond to the quantum numbers of the excited states  $|e\rangle = |J', F', m'_F\rangle$  and  $|g\rangle = |J, F, m_F\rangle$ .  $I = 7/2$  is the spin of the nucleus.  $q \in \{-1, 0, 1\}$  characterizes the polarization of the light relative to the quantization axis of the atoms. For  $\pi$  transitions,  $m_F = m'_F$ ,  $q = 0$ .

### 2.3.1 Specialization to caesium atoms

The discussion can be generalized to the situation where the electromagnetic field couples several different possible transitions at the same time. We then end up with a superposition of different transition paths contributing to the absorption and the phase shift:

$$S = \frac{l}{c} \sum_{F, m_F, F', m'_F} N_{F, m_F} |g_{(F, m_F) \rightarrow (F', m'_F)}|^2 \frac{\gamma/2}{\Delta_{F, F'}^2 + (\gamma/2)^2} \quad (2.39)$$

$$\Delta\phi = \frac{l}{c} \sum_{F, m_F, F', m'_F} N_{F, m_F} |g_{(F, m_F) \rightarrow (F', m'_F)}|^2 \frac{\Delta_{F, F'}}{\Delta_{F, F'}^2 + (\gamma/2)^2} \quad (2.40)$$

Since  $\hat{\sigma}_z$  in equations (2.36) and (2.37) is the population operator, and we have eliminated the excited state population, it can be expressed as the number of atoms  $N_{F, m_F}$  in the corresponding states. The detuning from the transition  $\Delta \rightarrow \Delta_{F, F'}$  depends on the transition involved and the corresponding dipole matrix element  $g$  goes over into  $g_{(F, m_F) \rightarrow (F', m'_F)}$ . We finally obtain the population dependent, off resonant phase shift and the electric field amplitude absorption coefficient:

$$S = \phi_0 \sum_{F, m_F, F', m'_F} N_{F, m_F} S(F, m_F, F', m'_F) \frac{(\gamma/2)^2}{\Delta_{F, F'}^2 + (\gamma/2)^2} \quad (2.41)$$

$$\Delta\phi = \phi_0 \sum_{F, m_F, F', m'_F} N_{F, m_F} S(F, m_F, F', m'_F) \frac{(\gamma/2)\Delta_{F, F'}}{\Delta_{F, F'}^2 + (\gamma/2)^2} \quad (2.42)$$

$$\phi_0 = \frac{3l\lambda^2}{4\pi V} (2J' + 1)$$

$$S(F, m_F, F', m'_F) = (2F' + 1)(2F + 1) \begin{pmatrix} F' & 1 & F \\ m'_F & q & -m_F \end{pmatrix}^2 \left\{ \begin{matrix} J & J' & 1 \\ F' & F & I \end{matrix} \right\}^2$$

From the formulas one can see that while the absorption and thus the spontaneous photon scattering reduces with  $1/\Delta^2$ , the phase shift only drops off with  $1/\Delta$ . By detuning far enough from resonance, it is therefore possible to suppress spontaneous photon scattering while still being able to get an appreciable light phase shift. In principle, spontaneous photon scattering can be suppressed to an arbitrarily low level. However, as we shall see later, a certain coupling strength between the atomic system and the light, which can be formulated in terms of spontaneous photon scattering probability, is necessary to obtain optimal squeezing. A moderate detuning of  $\Delta \sim 100 - 200$  MHz is sufficient to the balance these effects.

In the experiment we will mainly use atoms prepared in the  $F = 3, m_F = 0$  and  $F = 4, m_F = 0$  states. In addition, the probe light used will be rather close,  $\Delta_{3,2} \approx -150$  MHz,  $\Delta_{4,5} \approx 150$  MHz, to either the  $F = 3 \rightarrow F' = 2$  or the  $F = 4 \rightarrow F' = 5$  transition. For those two cases, the phase shift of  $F = 3 \rightarrow F' = 2$  light is dominated by atomic population in  $F = 3$  and the phase shift for light close to the  $F = 4 \rightarrow F' = 5$  is mainly due to population in  $F = 4$ . The phase shift formula can therefore be reduced to:

$$\Delta\phi_3 = \frac{3}{28}\phi_0 N_3 \frac{(\gamma/2)\Delta_{3,2}}{\Delta_{3,2}^2 + (\gamma/2)^2} \quad (2.43)$$

$$\Delta\phi_4 = \frac{5}{36}\phi_0 N_4 \frac{(\gamma/2)\Delta_{4,5}}{\Delta_{4,5}^2 + (\gamma/2)^2} \quad (2.44)$$

$\phi_0 = 3l\lambda^2/\pi V$ . Figure 2.3 shows the light phase shift normalized to  $\phi_0$  and  $N_3, N_4$ ,  $N_3 = N_4$  as a function of the laser frequency detuning  $\Delta_{4,5}$  from the  $F = 4 \rightarrow F' = 5$  transition. The graph also “justifies” the simplification of the phase shift

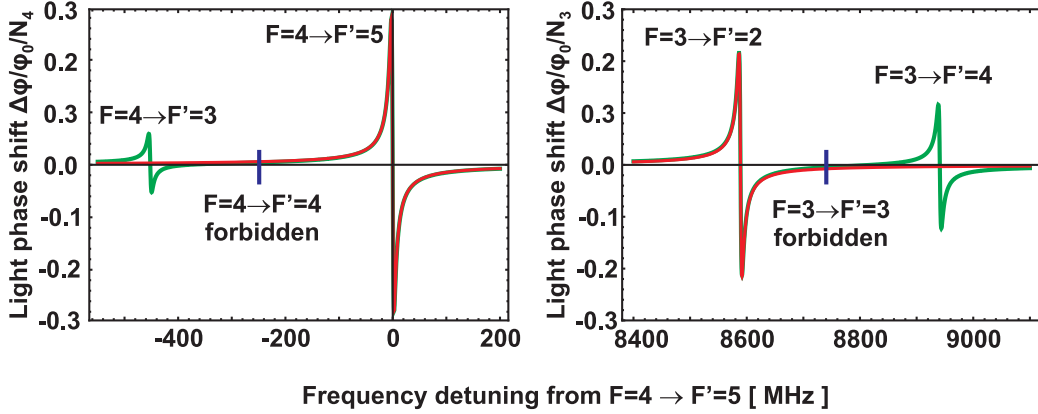


**FIGURE 2.3:** Normalized light phase shift as function of the laser light detuning from the  $F = 4 \rightarrow F = 5$  transition in caesium-133. We assume that only the  $m_F = 0$  substates of  $F = 3$  and  $F = 4$  are (equally) populated, leading to forbidden  $\Delta F = 0, \Delta m_F = 0$  transitions. The grey, dashed lines include all possible transitions while solid lines indicate the reduced phase shift formulas only taking the  $F = 3 \rightarrow F' = 2$  and  $F = 4 \rightarrow F' = 5$  into account. The forbidden  $F = 3 \rightarrow F' = 3$  and  $F = 4 \rightarrow F' = 4$  transitions for  $m_F = 0$  are due to the selection rules and manifest themselves in a general symmetry property of the Clebsch–Gordan coefficients.

formulas to (2.43) and (2.44) for detunings close to the two strongest transitions. For detunings  $\Delta_{4,5} \sim +150$  MHz and  $\Delta_{3,2} \sim -150$  MHz the phase shifts cannot be distinguished within the resolution of the plot.

## 2.4 Mach Zehnder interferometer

In the above discussion we have seen that the main point about non-destructive probing of an atomic ensemble boils down to measuring the phase shift of off-resonant probe light. A very straight forward way of measuring a light phase shift is using an interferometer as shown in figure 2.4. The probe beam, which also

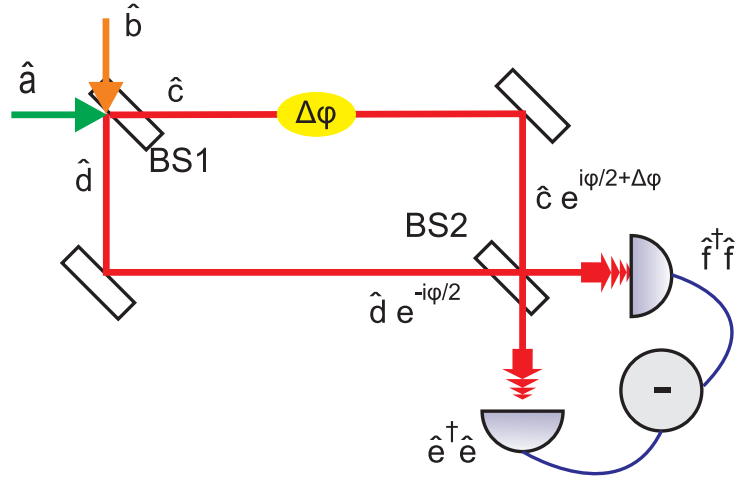


**FIGURE 2.4:** Schematic drawing of a Mach Zehnder interferometer. Two input modes  $\hat{a}, \hat{b}$  enter on the input beam splitter BS1. The modes inside the interferometer gain a differential phase  $\phi$  and are overlapped on BS2. At the output the photon numbers  $\langle \hat{e}^\dagger \hat{e} \rangle - \langle \hat{f}^\dagger \hat{f} \rangle$  of both modes are detected and subtracted.

interacts with the atomic ensemble, interferes with a reference beam on a beam splitter (BS2). The output signal of the interferometer depends on the differential phase shift of the beams in the two interferometer arms. When both arms have exactly the same length, all the light entering on port  $\hat{a}$  will exit again on port  $\hat{f}$ . The atomic ensemble acts as a refractive medium in the probe arm and changes the optical path length difference according to the population in its energy levels. From the interference signal the induced light phase shift and thus the atomic state population can be deduced.

### 2.4.1 Single color interferometer

To finish the formal description of the QND measurement, we still lack the spin-like description of the meter variable  $\hat{\mathbf{S}}$ , equation (2.17), page 13. In the present section, we shall only consider an ideal, lossless symmetric interferometer as shown in figure 2.4. Losses and imperfect mode matching of the two interferometer arms have been discussed at length in [1, 2, 14]. The technical realization will be discussed in section 3.2.

Two electromagnetic field modes enter the interferometer on the input beam splitter BS1 and they are characterized by the annihilation operators  $\hat{a}$  and  $\hat{b}$ . For these operators define angular momentum type variables [43]:

$$\hat{S}_x = \frac{1}{2}(\hat{a}^\dagger \hat{b} + \hat{a} \hat{b}^\dagger) \quad (2.45)$$

$$\hat{S}_y = -\frac{i}{2}(\hat{a}^\dagger \hat{b} - \hat{a} \hat{b}^\dagger) \quad (2.46)$$

$$\hat{S}_z = \frac{1}{2}(\hat{a}^\dagger \hat{a} - \hat{b}^\dagger \hat{b}) \quad (2.47)$$

At the output of the interferometer we measure the photon number difference

between the two output ports  $\hat{e}, \hat{f}$ , which corresponds to measuring  $\langle \hat{S}_z \rangle_{\text{out}} = \langle \hat{e}^\dagger \hat{e} - \hat{f}^\dagger \hat{f} \rangle$ .

The transformation for the field operators by a symmetric 50/50 beam splitter is well known [17]:

$$\begin{pmatrix} \hat{c} \\ \hat{d} \end{pmatrix} = \begin{pmatrix} \frac{1}{\sqrt{2}} & \frac{i}{\sqrt{2}} \\ \frac{i}{\sqrt{2}} & \frac{1}{\sqrt{2}} \end{pmatrix} \begin{pmatrix} \hat{a} \\ \hat{b} \end{pmatrix} \quad (2.48)$$

A differential phase shift  $\phi$ , e.g., due to an optical path length difference  $\Delta l = \frac{\lambda}{2\pi}\phi$ , transforms the field operators according to:

$$\begin{pmatrix} \hat{c}' \\ \hat{d}' \end{pmatrix} = \begin{pmatrix} e^{i\phi/2} & 0 \\ 0 & e^{-i\phi/2} \end{pmatrix} \begin{pmatrix} \hat{c} \\ \hat{d} \end{pmatrix} \quad (2.49)$$

From these transformation matrices for the field operators one can derive the transformation matrices for the angular momentum type operators  $\hat{S}_i$ . For the operation of a 50/50 beam splitter one finds [43]:

$$\begin{pmatrix} \hat{S}_x \\ \hat{S}_y \\ \hat{S}_z \end{pmatrix}_{\text{out}} = \begin{pmatrix} 1 & 0 & 0 \\ 0 & 0 & 1 \\ 0 & -1 & 0 \end{pmatrix} \begin{pmatrix} \hat{S}_x \\ \hat{S}_y \\ \hat{S}_z \end{pmatrix}_{\text{in}} \quad (2.50)$$

and for a differential phase shift  $\phi$  one gets:

$$\begin{pmatrix} \hat{S}_x \\ \hat{S}_y \\ \hat{S}_z \end{pmatrix}_{\text{out}} = \begin{pmatrix} \cos \phi & +\sin \phi & 0 \\ -\sin \phi & \cos \phi & 0 \\ 0 & 0 & 1 \end{pmatrix} \begin{pmatrix} \hat{S}_x \\ \hat{S}_y \\ \hat{S}_z \end{pmatrix}_{\text{in}} \quad (2.51)$$

We arrange the length of the interferometer arms such that the differential phase shift is  $\phi = \pi/2$ .

Since we have achieved a vector like description of the interferometer, the action of its components on the input field state can be visualized on a sphere as shown in figure 2.5. To start out, we operate the interferometer with a single coherent input mode  $|\alpha\rangle$  in mode  $\hat{a}$  and a vacuum state  $|0\rangle$  in mode  $\hat{b}$ :

$$|\Xi\rangle_{\text{in}} = |\alpha\rangle_a |0\rangle_b \Rightarrow \langle \hat{S}_x \rangle = \langle \hat{S}_y \rangle = 0, \langle \hat{S}_z \rangle = \frac{|\alpha|^2}{2} = \frac{\bar{n}}{2} \quad (2.52)$$

corresponding to a vector pointing along the positive  $z$ -axis with length  $\bar{n}/2$ , half the mean photon number in the coherent input state. The first beam splitter rotates the vector around the  $x$ -axis and transfers the state into the equatorial plane, figure 2.5(a). The  $\phi = \pi/2$  phase shift between the arms rotates the state vector around the  $z$ -axis until it is parallel to the  $x$ -axis, figure 2.5(b). A second rotation in the same direction around the  $x$ -axis by  $\frac{\pi}{2}$  as induced by the second beam splitter does not change the state and a measurement of  $\hat{S}_z$  returns zero mean value. Since we are dealing with non-commuting quantum variables again, the uncertainties in equations (2.25) – (2.27) hold. As for the atomic system, losses (decoherence) in the interferometer change the length of the spin like vector.

With atoms present in the probe arm, the accumulated phase shift in the interferometer is  $\phi = \pi/2 + \Delta\phi_{\text{at}}$ . The last beam splitter changes the orientation of

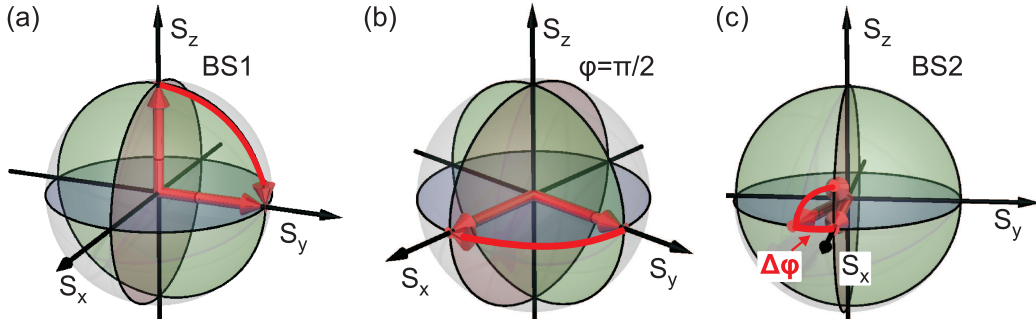


**FIGURE 2.5:** (a) The first beam splitter rotates the interferometer state vector  $\hat{S}$  into the equatorial plane. (b) Arranging the phase shift between the two arms of the interferometer to  $\pi/2$  rotates the vector around the  $z$ -axis until it is parallel to the  $x$ -axis. (c) With no additional phase shift, the second beam splitter does not rotate the vector further (it rotates it by  $\pi/2$  around its own axis) and the mean output measured  $\langle \hat{S}_z \rangle$  is zero. An additional phase shift  $\Delta\phi$  prior to the last rotation maps the additional phase onto a non-zero differential signal in  $\langle \hat{S}_z \rangle$ .

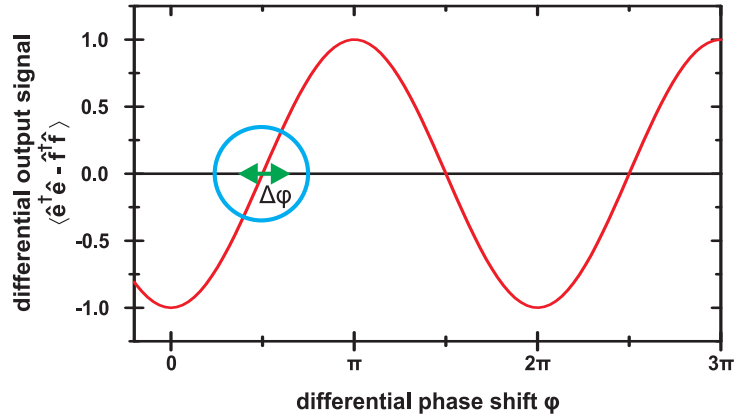


**FIGURE 2.6:** Output of the interferometer  $\langle \hat{S}_z \rangle$  as function of the phase shift between the arms  $\phi$  and the additional phase shift  $\Delta\phi$  around the  $\phi = \pi/2$  point.

the vector depending on the additional phase shift  $\Delta\phi_{\text{at}}$ , see figure 2.5(c). Measuring the  $z$ -projection of the spin like vector,  $\hat{S}_{z,\text{out}}$  thus allows one to extract the atom induced phase shift. The signal  $\langle \hat{S}_z \rangle_{\text{out}}$  can be extracted by multiplying the transformation matrices together and one gets the much more familiar interference fringes:

$$\langle \hat{S}_z \rangle_{\text{out}} = -\frac{1}{2}\bar{n} \cos(\Delta\phi_{\text{at}} + \pi/2) = \frac{1}{2}\bar{n} \sin \Delta\phi_{\text{at}} \quad (2.53)$$

The  $z$ -projection as function of the phase shift between the arms  $\phi$  and the additional phase shift  $\Delta\phi$  around the  $\phi = \pi/2$  point is illustrated in figure 2.6.

### 2.4.2 Interaction Hamiltonian in QND form

We have now described the measurement apparatus for the off-resonant phase shift of light in terms of a spin-1/2 system to get it on equal footings with the atomic

system. With these descriptions at hand we can write the interaction Hamiltonian  $\hat{H}_{\text{int}}$  given in equation (2.31) in a QND form as equation (2.17) proposes.

In the spirit of the discussion at the end of section 2.3.1, we restrict the interaction to the case where the probe mode only couples to atoms in the  $F = 4$  state via the  $F = 4 \rightarrow F' = 5$  transition. However, we add a second, spatially overlapped, but different frequency mode in the same input port of the interferometer which couples to the atoms in  $F = 3$  via the  $F = 3 \rightarrow F' = 2$  transition.

To illustrate this two color input mode setup, consider figure 2.7. We basically run

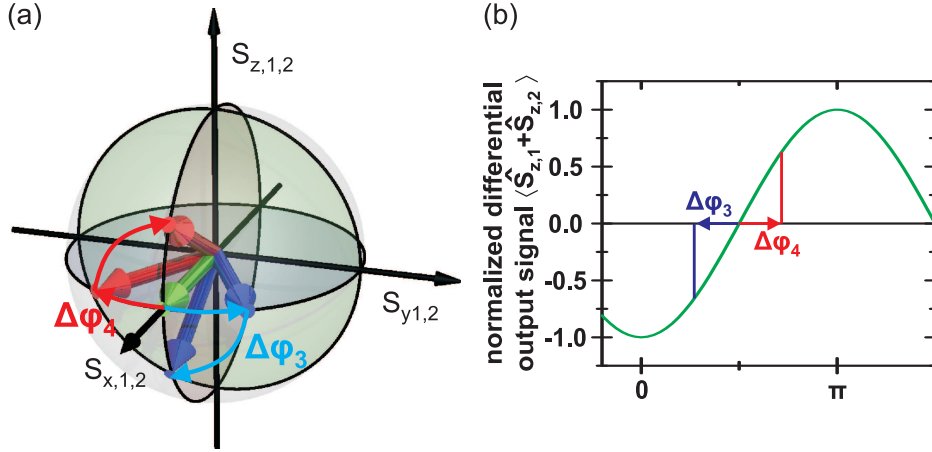


**FIGURE 2.7:** (a) Vector representation of the two color interferometer for an equal atomic superposition state  $\Delta\phi_3 = -\Delta\phi_4$  input. The green vector represents the empty interferometer for both colors, the red vector represents the  $F = 4 \rightarrow F' = 5$  light interferometer and the blue vector represents the  $F = 3 \rightarrow F' = 2$  light. Due to the arrangement of the light detunings, the equal populations in  $F = 3$  and  $F = 4$  lead to opposite phase shifts and are rotated by the last beam splitter to give opposite output signals. Since the photo detector does not distinguish between the different probe colors, the combined output signal is zero. (b)  $\langle \hat{S}_{z,3} + \hat{S}_{z,4} \rangle$  projection of the interferometer vector as measured by the photo detector at the output of the interferometer.

two interferometers in parallel, the two modes can *in principle* be distinguished also at the output. We arrange the couplings to the  $F = 3 \rightarrow F' = 2$  and  $F = 4 \rightarrow F' = 5$  transition such that the atomic phase shifts for population in  $F = 3$  and  $F = 4$  have opposite sign by choosing  $\text{sign}(\Delta_{3,2}) = -\text{sign}(\Delta_{4,5})$ . The two independent interferometers return opposite output signals for atomic population in  $F = 3$  and  $F = 4$  – and each color couples only to atoms in either  $F = 3$  or  $F = 4$ . The signals (differential photo charges) are merely summed up at the photo detector. An atomic input state  $|\Psi\rangle = |3\rangle^{\otimes N}$  yields a negative signal  $\langle \hat{S}_z \rangle^{\text{out}} \propto \langle \hat{J}_z \rangle \propto \Delta\phi_3 = -\Delta\phi_{\text{max}}$  and  $|\Psi\rangle = |4\rangle^{\otimes N}$  a positive signal  $\langle \hat{S}_z \rangle^{\text{out}} \propto \langle \hat{J}_z \rangle \propto \Delta\phi_4 = \Delta\phi_{\text{max}}$ . An equal superposition state  $|\Psi\rangle = \frac{|3\rangle + e^{i\phi}|4\rangle}{\sqrt{2}}^{\otimes N}$  will consequently return a zero mean output signal  $\langle \hat{S}_z \rangle^{\text{out}} = 0$  with an uncertainty  $\delta^2 \hat{S}_z^{\text{out}}$  caused by the shot noise of light and the projection noise of atoms.

In the adiabatic and off resonant limit (no population in the excited states), the interaction Hamiltonians  $\hat{H}_{\text{int},\{3,4\}}$  of the two ground levels with each their inter-

ferometer probing the population, can be written as [12]:

$$\hat{H}_{\text{int},3} = -2\hbar|g_{32}|^2 \frac{\Delta_{32}}{\Delta_{32}^2 + (\frac{\gamma}{2})^2} \hat{\Sigma}_{33} \hat{c}_3^\dagger \hat{c}_3 \equiv g_3 \hat{\Sigma}_{33} \hat{c}_3^\dagger \hat{c}_3 \quad (2.54)$$

$$\hat{H}_{\text{int},4} = -2\hbar|g_{45}|^2 \frac{\Delta_{45}}{\Delta_{45}^2 + (\frac{\gamma}{2})^2} \hat{\Sigma}_{44} \hat{c}_4^\dagger \hat{c}_4 \equiv g_4 \hat{\Sigma}_{44} \hat{c}_4^\dagger \hat{c}_4 \quad (2.55)$$

We arrange the couplings as discussed above, i.e., the detunings  $\Delta_{32}$  and  $\Delta_{45}$  such that  $g = g_4 = -g_3$ . Using equations (2.7, p.9) and (2.47, p.21) noting that  $\hat{\Sigma}_{33} + \hat{\Sigma}_{44} = \hat{N}$ ,  $\hat{c}_i^\dagger \hat{c}_i + \hat{d}_i^\dagger \hat{d}_i = \hat{n}_i, i = 3, 4$ , we can rewrite the total effective interaction Hamiltonian as:

$$\begin{aligned} \hat{H}_{\text{int}} &= g \left[ \left( \hat{J}_z + \frac{\hat{N}}{2} \right) \left( \hat{S}_{z,4} + \frac{\hat{n}_4}{2} \right) + \left( \hat{J}_z - \frac{\hat{N}}{2} \right) \left( \hat{S}_{z,3} + \frac{\hat{n}_3}{2} \right) \right] \\ &= g \left[ \hat{J}_z \left( \hat{S}_{z,4} + \hat{S}_{z,3} \right) + \hat{J}_z \frac{\hat{n}_4 + \hat{n}_3}{2} + \frac{\hat{N}}{2} \left( \hat{S}_{z,4} - \hat{S}_{z,3} \right) + \frac{\hat{N}}{2} \frac{\hat{n}_4 - \hat{n}_3}{2} \right] \end{aligned} \quad (2.56)$$

This is a Hamiltonian whose first term is of QND form. It couples the the  $z$ -components of two spins  $\mathbf{J}$  and  $\mathbf{S} = \mathbf{S}_4 + \mathbf{S}_3$ .  $\hat{J}_z$  represents the atomic system and accounts for the atomic projection noise.  $\hat{S}_{z,4} + \hat{S}_{z,3}$  are the two independent interferometers; the mean value  $\langle \hat{S}_{z,4} + \hat{S}_{z,3} \rangle = 0$  is zero due to the equal coupling configuration and its variance corresponds to the light shot noise of the two probe modes. The second term in the effective Hamiltonian can be associated with the ac Stark shift of the atomic levels caused by the probe light and its implications will be discussed thoroughly chapter 5. The induced effects can be revoked by using spin echo techniques but it can also be canceled by arranging the two probe colors in two spatially different input ports. This setting will be discussed in section 3.2.3 and chapter 6. The third term arises from the fact that we have two independent probe modes each interacting with “half” the population. Its mean value is zero, but its variance scales with the number of atoms squared. It is negligible with respect to the QND term as long as the photon number in each probe mode is large compared to the atom number. The mean value of the last term is canceled by demanding  $\bar{n}_3 = \bar{n}_4$ . Its variance is only sensitive to anticorrelated noise sources. By reducing uncorrelated noise sources, e.g., independent laser amplitude fluctuations this term can also be suppressed with respect to the atomic projection noise term. With the right choice of parameters, the QND part of the Hamiltonian is dominant and the interaction assumes QND form.

Note that the  $\hat{S}_z$  coupling in the Hamiltonian does not correspond to the  $\langle \hat{S}_z \rangle^{\text{out}}$  measured at the output of the interferometer. Comparing with the Hamiltonian in equation (2.17) and the input – output relation (2.20) it is clear that  $\hat{S}_z$  is a constant of motion and does consequently not change. It corresponds to  $\hat{S}_z = \frac{1}{2} \left( \hat{c}^\dagger \hat{c} - \hat{d}^\dagger \hat{d} \right)$  inside the interferometer. With figure 2.5 it becomes clear that the phase shift  $\Delta\phi$  of the atoms to first order only changes  $\hat{S}_y$  inside the interferometer and this change is mapped onto  $\langle \hat{S}_z \rangle^{\text{out}}$  by the second beam splitter.

## 2.5 Experimental proposal

In the previous sections we have gathered the basic equations and principles of the experiment which will be described in the next sections: The population number difference of an atomic ensemble of caesium atoms, initialized into a coherent superposition state  $|\Psi\rangle = \left(\frac{|3\rangle+|4\rangle}{\sqrt{2}}\right)^{\otimes N}$  shall be measured non-destructively. We have seen that a non-destructive measurement character can be obtained by measuring the off-resonant phase shift an atomic ensemble imposes onto a probe light field. Detuning the probe light far enough from the atomic transitions assures that photon absorption is kept (arbitrarily) low. A Mach-Zehnder interferometer will serve as measurement apparatus for the light phase shift. In the setup, we desire to resolve atomic quantum projection noise. Ideally, the stability of the interferometer has to be such that it can resolve the shot noise of the applied probe light. The phase stability of the interferometer has to be better than the quantum mechanical uncertainty in the phase measurement caused by the finite probe photon number. Correlations between two consecutive measurements on the same ensemble will then allow us to study the predicted reduction of the measurement uncertainty to below the standard quantum limit by using the information obtained in the first of the two measurements.

To reduce the influence of atomic motion and at the same time obtain a high coupling strength  $\tilde{\kappa}^2$  (which boils down to having a large optical depth,  $\tilde{\kappa}^2 \propto OD$ , [44]), we use a cold, dipole trapped atomic ensemble. The following chapter is dedicated to the experimental techniques of producing a cold atomic sample, the measurement apparatus and a short characterization of the system. It is clear that in order to study the noise properties of the system and to approach the standard quantum limit, we need to have a very good understanding of the sample properties, the measurement process and the decoherence effects caused by the probe light. The main part of chapter 5 is therefore devoted to these issues. Especially microwave spectroscopy sequences will be used to study the decohering and destructive components of the interaction. Finally, we will look at the noise properties of the system in chapter 6, discuss the implementation of different balanced measurement sequences and show the obtained projection noise and quantum noise squeezing results.

---

# Experimental techniques

In the introductory chapter we have discussed the basic plan behind the experiments conducted: To apply a non-demolition measurement to the quantum state of a cold atomic ensemble. The atoms are confined to a well defined spatial region by using an optical dipole trap. Readout of the atomic population distribution between the two ground state levels is performed with a Mach-Zehnder interferometer.

The chapter starts out with a short review of the experimental techniques we apply to generate a cold trapped ensemble of caesium-133 atoms. We then continue by discussing the probing scheme and focus on two slightly different interferometer arrangements: In the two color – single port version, two probe beams of different frequency enter through the same port of the input beam splitter while in the two color – two port setup, the two probe beams enter on different beam splitter ports. After discussing some specifics of the experimental sequence and experiment control, the chapter concludes with a demonstration of how the non-destructive character of the measurement setup can be used to extract parameters of the dipole trapped sample.

## 3.1 Generation of cold Cs atoms

Our setup for cooling and trapping a cloud of caesium has not changed dramatically with respect to the presentation in [2]. We shall therefore gather the most relevant numbers for completeness, only. It is implicitly assumed that the basic principles of laser cooling [45, 46] are familiar to the reader.

### 3.1.1 Layout of setup

To mechanically decouple the interferometer from the rest of the setup the experiment is distributed onto three optical tables. One is reserved for the diode lasers, the preparation of the cooling and trapping light and the interferometer probe and lock lasers. All the light beams are coupled into optical fibers and transported onto the interferometer table where the vacuum setup is mounted and the actual

experiment takes place. A third table accommodates the dipole trap laser. The experiment itself happens inside a glass vacuum cell and a schematic drawing of the vacuum setup is depicted in figure 3.1.

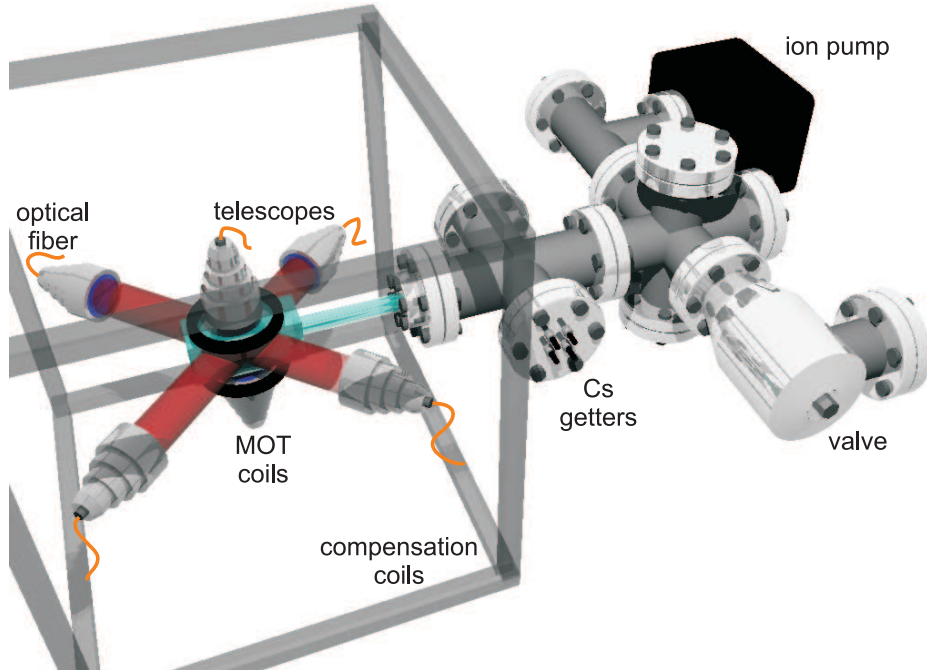


**FIGURE 3.1:** *Experimental setup. The vacuum in the chamber maintained by a single ion pump. Four getter sources are used to produce the necessary Cs background vapor. Six fiber coupled telescopes deliver the cooling and trapping light to the vacuum cell; a pair of anti-Helmholtz coils produces the magnetic field gradient for the MOT. Three orthogonal pairs of Helmholtz coils are used to compensate static magnetic background fields.*

The vacuum chamber is pumped by a single 201/s Varian Star Cell ion pump. When the setup was originally devised no vacuum gauge or secondary pump (e.g. a titanium sublimation pump) has been included. Over time, contamination of the ion pump has caused an increase of the pump current to 2 mA which makes pressure determination from the pump current impossible. With a temporary externally attached turbo pump and vacuum gage (not shown in the figure), the pressure in the chamber was determined to be slightly below  $10^{-9}$  mbar, which is on the edge of what we are willing to tolerate. The necessary Cs vapor is created with 4 SAES getter sources in series, running at  $\lesssim 4$  A. After creating a sufficient pressure in  $\sim 15$  min continuous mode operation, the Cs background is maintained by operating the getters at  $\sim 3$  A. The actual experiment takes place in a glass cell from Starna, external dimensions  $120 \times 48 \times 48$  mm<sup>3</sup>. The walls of the cell are anti reflection coated from the outside.

### 3.1.2 Magneto-Optical Trap

The atoms are trapped and cooled in a standard 6-beam magneto optical trap (MOT) [45, 46]. The light is delivered to the setup with six optical fibers directly

entering custom made beam expanders. We use about 5 mW of cooling light per  $\sim \varnothing 30$  mm beam and have  $\sim 1$  mW of repump light coupled through the same optical fibers.

The magnetic field gradient for the MOT operation is created by two anti-Helmholtz coils with 50 mm radius, 38 windings per coils, separated by 50 mm and running at a current of about 5 A. To compensate external static magnetic fields at the position of the MOT, three pairs of rectangular Helmholtz coils with outer dimensions of  $55 \times 55$  cm<sup>2</sup> are mounted around the setup. Coarse field compensation is done by optimizing the trapping and cooling in the MOT. Fine tuning of the field by using the magnetic splitting of the hyperfine states is discussed in section 5.3.2.

### MOT laser light generation

To generate the laser light for the magneto optical trap, we use two external grating stabilized diode lasers as masters. The basic design is an adapted version of the Littrow external cavity setup [47, 48]. It is a constantly revised and improved version of the design used throughout the QUANTOP labs [2, 49]. We use ridge waveguide laser diodes from Eagleyard Photonics with anti-reflection coated output facets of type numbers EYP-RWE-0870 and EYP-RWE-0850 for generating the  $\lambda = 852$  nm light. The gain profile of the EYP-RWE-0850 versions drops considerably around  $\lambda = 850$  nm (figure 3.2(a)). As a result, it can be rather cumbersome to pull the diode to lase single mode in this wavelength range. In addition, due to the operation at the edge of the gain profile, the externally stabilized laser diode still emits significant incoherent background radiation in the gain profile. Figure 3.2(b) shows the output spectrum of a RWE-850 diode when pulled to  $\lambda = 852$  nm and when lasing at a more favorable wavelength inside the gain profile. The incoherent background when the diode is operated at the edge of its gain profile is clearly visible. For the operation of the magneto optical trap, the incoherent background is not problematic, especially because the light is amplified with slave diodes which do not amplify the background. Since we put much higher requirements to the probe lasers, section 3.2.1, either laser line filters or different diodes with more favorable gain profile (RWE-0870) are used to suppress the incoherent background.

We illustrate the path of the master lasers' output beams in figure 3.3. Only the basic principle is shown, for more details refer to [2]. The frequencies of the master lasers are stabilized to atomic transitions using saturated absorption spectroscopy and a Pound-Drever-Hall like error signal generation. The necessary sidebands are created by direct laser diode current modulation via the current supply. We use modulation frequencies of 20 MHz ("cooler", stabilized to  $F = 4 \rightarrow F' = 3 \times 4$  crossover) and 4 MHz ("repumper", stabilized the  $F = 3 \rightarrow F' = 2 \times 3$  crossover). Demodulation with a local oscillator is done directly at the photodiode monitoring the saturated absorption signal, and its response is peaked to the corresponding frequency values. The linewidth of the stabilized lasers on a few seconds timescale is determined to be  $\sim 500$  kHz by observing the beat note between the two masters.

The frequency stabilized output beam of both lasers is frequency shifted with acousto optical modulators (AOMs) and injected into high power ( $\sim 100$  mW) slave diodes. The output of these diodes is further frequency shifted to the desired

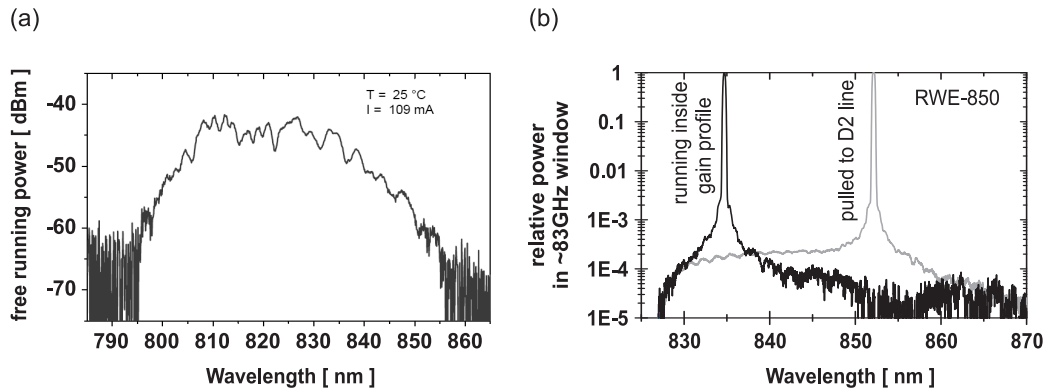


**FIGURE 3.2:** (a) Gain profile of a free running RWE-850 diode, adapted from Eagleyard datasheet for serial number 030912. (b) When pulling a RWE-850 diode to the edge of its gain profile, a strong incoherent background is visible in the spectrum. The spectrum is measured with a 1200 lines/mm diffraction grating. In the center of the gain profile, the incoherent background is strongly suppressed.

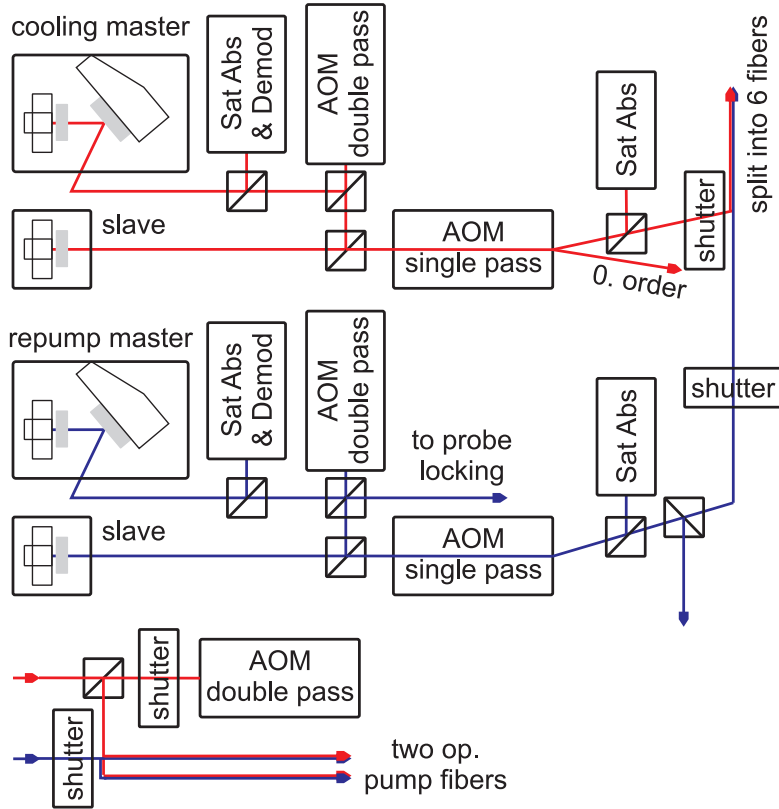
frequencies for the MOT operation and power modulated with single pass AOMs. The diffracted orders of these AOMs are mode matched, split into six beams and coupled into optical fibers which transport the light to the vacuum setup, figure 3.1. To assure perfect extinction, mechanical shutters are placed into each beam. The output of the slave lasers is monitored on additional saturated absorption setups to verify their single mode performance and frequency following when the injection frequency is changed with the two double pass AOMs. We also tap of light from the zeroth order of the second cooler AOM and from the main repump beam for the atomic state preparation discussed in 5.3.2. Part of the light from the repump master laser is also used for beat note locking of the probe lasers, compare section 3.2.1.

### Control of the MOT parameters

A LabView programme, accessing the outputs of three National Instruments data bus cards, allows us to control the slow timing (1 ms time slot resolution) of the experimental setup. We have implemented an access to

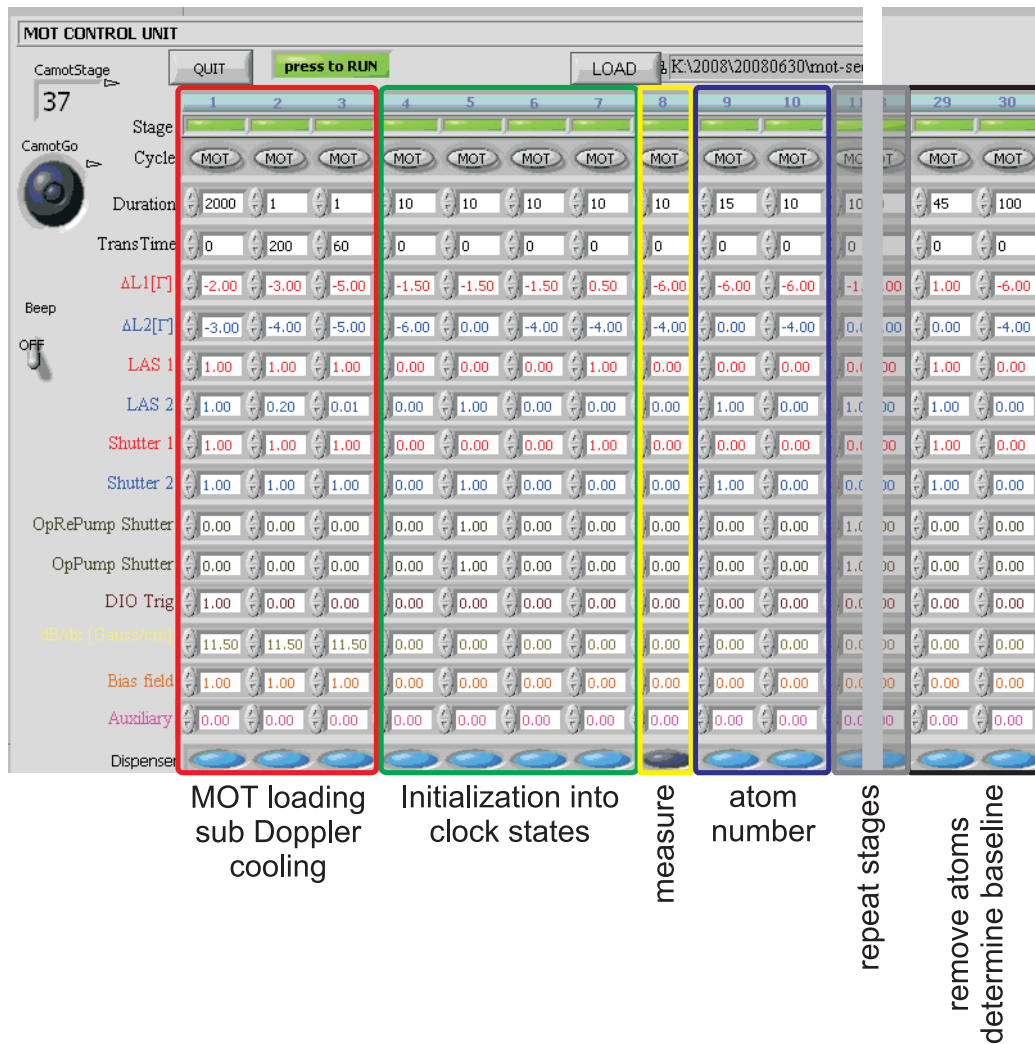
- the frequency detuning of both lasers ( $\sim \pm 6$  linewidths from the  $F = 3 \rightarrow F = 4$  and  $F = 4 \rightarrow F = 5$  MOT transitions), power and mechanical shutters
- magnetic quadrupole field on/off
- dispenser on/off
- external magnetic guiding field on/off (see section 5.3.2)
- mechanical shutters for optical pumping and repumping beams (see section 5.3.2)

Figure 3.4 shows a view of part of the front panel and the controls implemented. We will come back to the single experimental stages displayed again later. Right



**FIGURE 3.3:** Schematic drawing of the laser setup for the magneto optical trap and the optical pumping. The output from external grating stabilized diode lasers are frequency stabilized to atomic transition lines using the signal from saturated absorption spectroscopy setups. The stabilized frequency is shifted in a double pass AOM and amplified with slave diodes. A second AOM is mainly used for power modulation. For optical pumping, light is tapped off from the slaves; the optical pump light has to be frequency shifted first, while the repump light can be directly used for the clock state preparation. Shutters help to physically block the light beams. The combined light from the two lasers is coupled into six optical fibers delivering about 5 mW per beam of cooling light and about 1 mW repump light to the vacuum setup. The saturated absorption setups for the slave diodes monitor their single mode performance and frequency following.

now, we are only interested in the first three stages. These stages illustrate typical values for loading and cooling atoms in the MOT. To load atoms, we switch on the magnetic gradient field, and start with typically 2 s of both cooling and repumping light at full power,  $\Delta_{32} = -2\gamma$ ,  $\Delta_{45} = -3\gamma$ ,  $\gamma = 5.2$  MHz is the natural linewidth of the D2 transitions. We then apply two step rudimentary sub-Doppler cooling by reducing the power of the repump laser to 20% and increasing both detunings  $\Delta_{32} \rightarrow -3\gamma$ ,  $\Delta_{45} \rightarrow -4\gamma$  in 200 ms and in a second step, further reducing the repump laser power to 1% of its initial value and increasing the detunings further to  $\Delta_{32} \rightarrow -5\gamma$ ,  $\Delta_{45} \rightarrow -5\gamma$  in another 60 ms. The values reported here are long time averages, they are slightly adjusted on a day to day basis, taking, e.g., power changes due to fiber coupling efficiencies or the Cs vapor pressure into account.



**FIGURE 3.4:** Front panel view of the LabView programme controlling the slow timing of the experiment. The red controls ( $\Delta L1[\Gamma]$ , LAS1, Shutter 1) correspond to the cooler laser (detuning from  $F = 4 \rightarrow F = 5$  transition, power, binary shutter value), the blue controls ( $\Delta L2[\Gamma]$ , LAS2, Shutter 2) to the repump laser. DIO Trig is used for synchronization with another computer card used for fast timing (50 ns time slot resolution). The other controls should be self explaining.

### 3.1.3 Optical dipole trap

After the cooling stages, a sample of cold Cs atoms has been prepared in a rather well defined spatial region. Since the hyperfine state population of the atoms is constantly reshuffled while the MOT light is on, the atoms have to be transferred into a different trap which does not change the atomic state population. Without the application of a further trapping potential, the atoms would move towards the walls of the vacuum system and be lost for experiments within few tens of milliseconds. Furthermore, although the positions of the atoms are rather well defined, we would like to confine them to a much smaller region and thereby increase their density. To this end we apply the techniques of optical dipole trapping [50]. In section 2.3 we have been discussing the light–atom interaction, focussed on the

effect the presence of atoms has on the electromagnetic field. Now we shall look at the implications of the interaction on the energy of the atomic states.

### Light shift and trapping potential

The Hamiltonian for the atom – light system of equation (2.34) can be written in the interaction picture as (for convenience, we shift the energy zero to the ground level this time)[17]:

$$\hat{H} = \hbar\omega_0|e\rangle\langle e| + \hbar\omega_0\hat{a}^\dagger\hat{a} + \frac{\hbar\Omega}{2} \left( |e\rangle\langle g|\hat{a}e^{i\Delta t} + |g\rangle\langle e|\hat{a}^\dagger e^{-i\Delta t} \right) \quad (3.1)$$

where we have introduced the Rabi frequency by  $\hbar\Omega = -eE_0(\mathbf{r})|\langle e|\mathbf{e}\cdot\mathbf{r}|g\rangle|$  and the detuning  $\Delta$  of the light with respect to the transition.

In matrix form we obtain:

$$\hat{H} = \hbar \begin{pmatrix} |e\rangle & |g\rangle \end{pmatrix} \begin{pmatrix} \omega_0 + \omega(n-1) & \frac{\Omega}{2}\sqrt{n}e^{i\Delta t} \\ \frac{\Omega}{2}\sqrt{n}e^{-i\Delta t} & \omega n \end{pmatrix} \begin{pmatrix} \langle e| \\ \langle g| \end{pmatrix} \quad (3.2)$$

where  $n = \langle \hat{a}^\dagger\hat{a} \rangle$  is the excitation number of the electromagnetic field. When diagonalizing the Hamiltonian, we get the new energy eigenvalues of the combined system as:

$$E_\pm(n) = \hbar \left( -\frac{\Delta}{2} + \omega n \pm \frac{1}{2}\sqrt{\Delta^2 + \Omega^2 n} \right) \quad (3.3)$$

In the limit of  $\Delta \gg \Omega$  the square root can be expanded and we get an energy difference between states differing by one excitation number of:

$$\Delta E = E_\pm(n+1) - E_\pm(n) = \pm \frac{\hbar\Omega^2}{4\Delta} + \hbar\omega \quad (3.4)$$

The ground state of the atom is therefore shifted in energy by:

$$\Delta E_g = \frac{\hbar\Omega^2}{4\Delta} \quad (3.5)$$

For  $\Delta < 0$  an atom can reduce its energy by moving into a region inside the electromagnetic field where the Rabi frequency, i.e., the electric field strength is increased with respect to its current position.

Introducing the intensity  $I(\mathbf{r}) = \frac{1}{2}c\epsilon_0 E(\mathbf{r})^2$  of the electromagnetic field [46] and inserting the dipole matrix element (appendix A.2) one obtains the dipole potential as:

$$U(\mathbf{r}) = \frac{3\pi c^2}{2\omega_0^3} \frac{\gamma}{\Delta} I(\mathbf{r}) \quad (3.6)$$

For detunings of the order or larger than the finestructure splitting, i.e., the difference between the D1 and D2 transition line, all relevant transitions have to be taken into account. For linearly polarized trap light the final expression reads [50]:

$$U(\mathbf{r}) = \frac{\pi c^2}{2} \left( \frac{2\gamma_{D2}}{\omega_{0,D2}^3 \Delta_{D2}} + \frac{\gamma_{D1}}{\omega_{0,D1}^3 \Delta_{D1}} \right) I(\mathbf{r}) \quad (3.7)$$

where  $\gamma_{D1} = 2\pi \times 4.56$  MHz and  $\gamma_{D2} = 2\pi \times 5.22$  MHz are the linewidths of the D1 and D2 transitions, [18], and  $\Delta_{D1}$  and  $\Delta_{D2}$  are the detunings from the transitions which themselves have transition frequencies of  $\omega_{D1} = 2\pi \frac{c}{895 \text{ nm}}$  and  $\omega_{D2} = 2\pi \frac{c}{852 \text{ nm}}$ .

The spatial form of the dipole trap potential is given by the intensity distribution  $I(\mathbf{r})$  of the field. We use a Gaussian laser beam which has an intensity distribution  $I(\mathbf{r})$  according to:

$$I(\mathbf{r}) = \frac{2}{\pi} P \frac{1}{w(z)^2} \exp\left(-\frac{2r^2}{w(z)^2}\right) \quad (3.8)$$

where  $P = \frac{1}{2}\pi I_0 w_0^2$  is the beam power and  $w(z)$  is the position dependent spot size:

$$w(z) = w_0 \sqrt{1 + \left(\frac{z}{z_R}\right)^2}, \quad z_R = \frac{\pi w_0^2}{\lambda} \quad (3.9)$$

with  $z$  as the propagation direction,  $\lambda$  the wavelength of the beam and  $w_0$  the beam waist. With these parameterizations we obtain the optical dipole potential as:

$$U(\mathbf{r}) = U_0 \frac{w_0^2}{w(z)^2} \exp\left(-\frac{2r^2}{w(z)^2}\right) \quad (3.10)$$

$$U_0 = \frac{c^2 P}{w_0^2} \left( \frac{\gamma_{D1}}{\omega_{0,D1}^3 \Delta_{D1}} + \frac{2\gamma_{D2}}{\omega_{0,D2}^3 \Delta_{D2}} \right) \quad (3.11)$$

For a waist of  $w_0 = 50 \mu\text{m}$  and a power of  $P = 4$  W in a laser beam with wavelength  $\lambda = 1032$  nm, we get a trap depth in the center of  $U_0/k = 280 \mu\text{K}$ .

To characterize an atom trap one usually quotes the quasi harmonic eigenfrequencies of the trap. These can be obtained by comparing the potential for the trap in an expansion to second order with a classical harmonic potential. The eigenfrequencies are then given as:

$$\omega_{\perp} = \sqrt{\frac{4U_0}{m_{\text{at}} w_0^2}}, \quad \omega_{\parallel} = \sqrt{\frac{2U_0}{m_{\text{at}} z_R^2}} \quad (3.12)$$

For the above values we would expect a radial trap frequency around  $\omega_{\perp} \sim 2\pi \times 840$  Hz and an axial frequency of  $\omega_{\parallel} \sim 2\pi \times 4$  Hz.

### Technical realization

The experimental realization of a dipole trap is almost as straight forward as the last section suggests. We take up to 4 W of the light from an ELS VersaDisk, 1032 nm diode pumped Yb:YAG disc laser. An AOM in the beam path is used to control and stabilize the power of the trap light. The laser is mounted on its own optical table to avoid acoustic noise coupling from the water cooling of the laser head to the interferometer. A free-space link transports the light onto the interferometer table where it is focussed down to a waist of  $w_0 \sim 50 \mu\text{m}$  with  $f=100$  mm achromatic doublets at the position of the cold cloud. We keep the dipole trap light on during the whole experimental cycle. After the sub-Doppler cooling stage in the MOT, atoms with low enough kinetic energies remain trapped in the dipole beam. The

operation parameters for the MOT as discussed in section 3.1.2 are determined by maximizing the number of atoms transferred into the optical trap and their lifetime in the trap. To this end also the position of the MOT is optimized by changing the relative light power in opposing cooling beams and the location of the trap inside the cold sample.

The single frequency mode performance of the trap laser is constantly monitored on an external Fabry Perot cavity. The laser has very short servicing intervals and needs frequent cleaning of the intra cavity components to assure an acceptable performance. Excessive dual and multi mode behavior has been observed and clear correlations between the number of atoms in the trap and the single mode performance of the laser have been observed. In addition, the laser power entering the actual experimental setup has to be actively stabilized to compensate for long term power fluctuations of up to 30% during 24 h operation. We place a photo detector into the leakage through a mirror which steers the light to a beam dump and feed its signal back onto the rf power of the AOM.

The orientation of the dipole trap beam with respect to the rest of the setup is shown in figure 3.5. Two dichroic mirrors, high reflectors under  $45^\circ$  at 1032 nm and anti reflection coated for 852 nm, overlap the beam with the cloud. A symmetric telescope with two  $f=100$  mm achromatic doublets focusses and re-collimates the beam which is then dumped on a beam block. The third dichroic mirror which is not in the direct beam path of the trap beam directs back scattered light from the cell surface which leaks through the first dichroic mirror out of the direction of the interferometer beams.

## 3.2 Interferometer setup

The heart of the non-destructive quantum state measurement setup for the cold Cs cloud is a free space Mach Zehnder interferometer. The basic operation principle has been introduced in section 2.4. We start out by discussing a single input port interferometer as it has been used for most of the experiments presented in section 5. The components are shown in figure 3.5. Due to reasons which will become more obvious in section 5.5 and after, the interferometer has been changed to a two-input port setup which will be discussed together with the setup of the probe and interferometer locking lasers.

### Optical setup of the interferometer

Let us first consider the setup sketched in figure 3.5. The light for the interferometer is guided onto the interferometer table with a polarization maintaining single mode fiber (Thorlabs PM 780-HP); the output coupler is a standard Thorlabs F220FC-B lens system with about 2 mm output beam waist. A polarizing beam splitter (PBS1) on a rotation mount is matched to the fiber axis to clean the polarization and assure maximum power stability. A vertically polarized beam then enters the interferometer itself which is composed of two non-polarizing beam splitters (BS1,BS2), two folding mirrors whereof one is mounted on a piezo electric

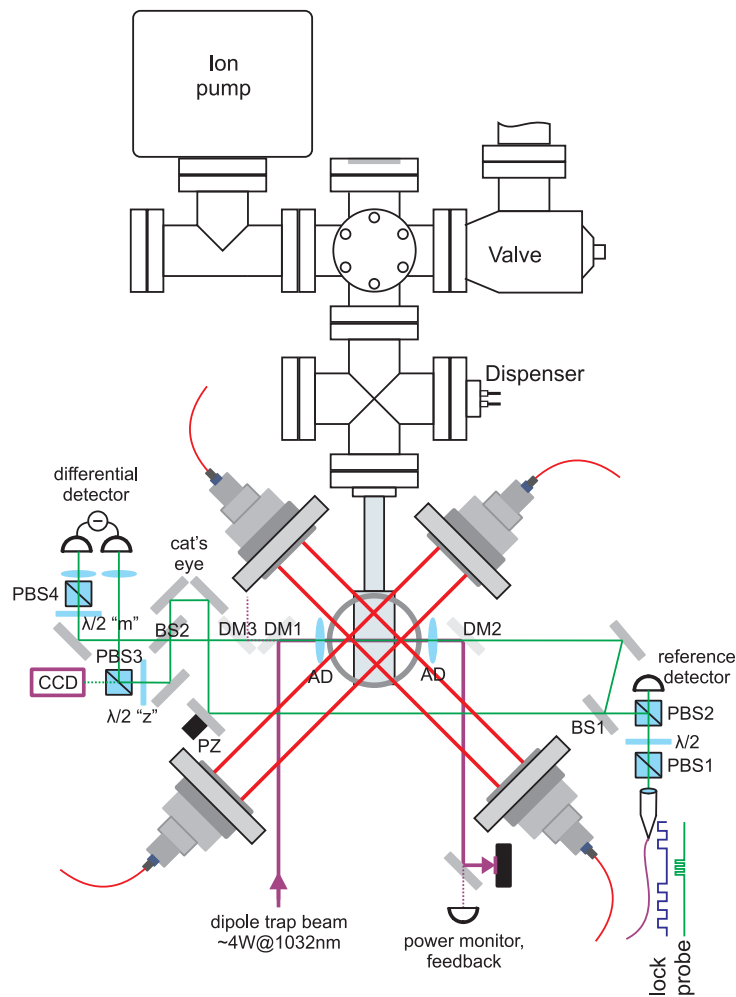


**FIGURE 3.5:** *Experimental setup.* The dipole trap beam is steered into the vacuum cell with a dichroic mirror (DM1), focussed and re-collimated with two achromatic doublets (AD) and reflected off a second dichroic mirror (DM2). Leak light is collected on a power detector at a mirror before the beam dump to stabilize the trap power. The main components of the Mach-Zehnder interferometer are the two non-polarizing beam splitters BS1 and BS2, two folding mirrors whereof one is mounted on a piezo electric transducer (PZ) and a cat's eye to adjust the differential path length of the two interferometer arms. The light polarization is controlled by various polarizing beam splitters (PBS1-4) and zero ("z") or multi ("m") order waveplates. The interference signal at the interferometer output can be monitored on a CCD camera for alignment purposes, but in general all light is directed onto a differential photo detector.

actuator (PZ) and a cat's eye to adjust the path length difference between the two interferometer arms. To obtain maximum overlap of the interaction region of the atomic sample and the interferometer light, the beams are focussed and re-collimated with the same pair of achromatic doublets (AD) also used for the dipole trap. To optimize the overlap, the trap beam pointing is changed until a maximum in the atomic signal is reached. The interference signal between the two beams at both output ports of the second non-polarizing beam splitter (BS2) are polarization cleaned (PBS3, PBS4) and detected on a directly subtracting photo-amplifier. To optimize the mode overlap of the two beams in the interferometer arms we also

have implemented the possibility to direct part of the beam onto a CCD camera. We obtain an interference fringe visibility of up to 98%.

### 3.2.1 Probe laser setup

The probe light is generated with two external cavity diode lasers as discussed in section 3.1.2. The optical setup is sketched in figure 3.6. Let us first consider the

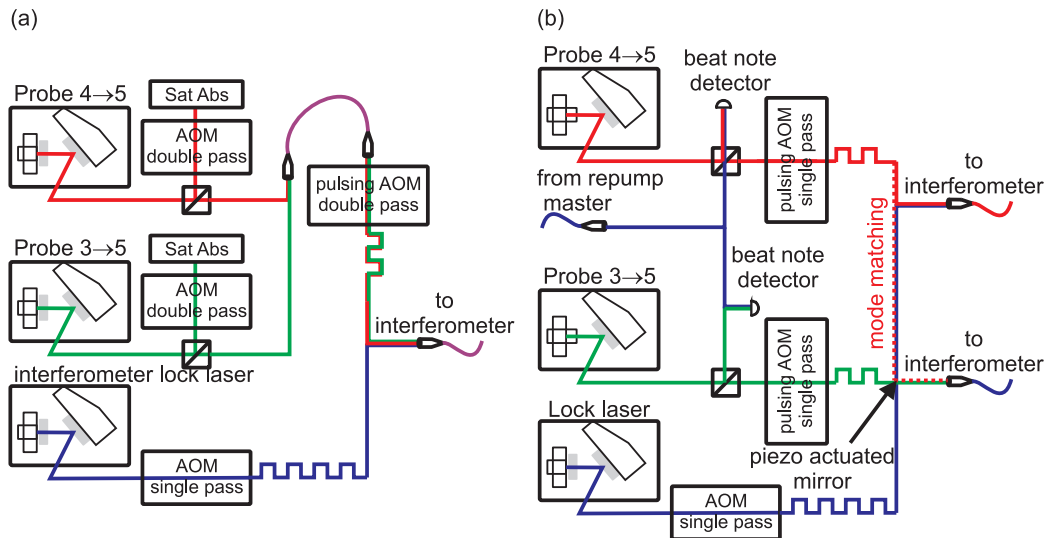


**FIGURE 3.6:** Probe and interferometer lock laser setup. (a) Setup as used for most of the data presented in chapter 5. The lasers are frequency stabilized by frequency modulating the rf driving frequency of a dedicated AOM in the lock light path; the signal from the saturated absorption setup is then demodulated and used for feedback. Both probe lasers are mode matched into a fiber and bi-chromatic pulses are generated on the “pulsing AOM”. An additional laser is separately power modulated and injected into the fiber transporting the three laser beams to the interferometer setup. This laser is used for actively stabilizing the interferometer path length difference. (b) In a more recent development, the probe lasers are frequency stabilized by referencing them to the MOT repump laser with beat note locks. The probe pulses are then generated separately for each laser and coupled into separate fibers. The setup allows us to mimic the previous setup since the  $F = 4 \rightarrow F' = 5$  light is coupled into the fiber together with the  $F = 3 \rightarrow F' = 2$  light inserting a suitable mirror.

setup in figure 3.6(a) which was used in the experiments presented in section 5. The setup in figure 3.6(b) was used for the projection noise data presented in section 6.3 and is designed for the two input port interferometer which will be discussed in 3.2.3.

We put higher requirements to the frequency purity of the probe lasers than for the ones generating the MOT light. When probing an atomic quantum state, we cannot tolerate the strong incoherent background as mentioned in section 3.1.2. Any kind of near resonant light in the probe region will inevitably change or destroy the quantum state prepared in the atomic ensemble. Apart from the detrimental effect on the atoms, the interference fringe visibility in the interferometer is also corrupted by a broad incoherent background because the optical components we use only perform optimally in a very narrow wavelength band. We therefore either

insert laser line filters of below 10 nm bandwidth into the beams or we use the RWE-0870 laser diodes.<sup>1</sup> Furthermore, the sidebands on the laser light used in the Pound–Drever–Hall setup to generate the error signal for frequency stabilization are disturbing when doing noise measurements, compare section 6.2.2. Additionally, we would like to not stabilize the actual laser output frequency onto an atomic transition or crossover line, since leaking zero order light from the pulsing AOM can also reduce the coherence of the atomic ensemble quantum state considerably. Both requirements can be met by inserting an AOM into part of the beam used for locking, modulating its rf driving frequency and demodulating the output signal of the saturated absorption signal.

We build two almost identical laser setups for the two colors and stabilize them to an appropriate transition in the  $F = 3 \rightarrow F' = 2, 3, 4$  and  $F = 4 \rightarrow F' = 3, 4, 5$  manifold. The stabilized light from both probe lasers is matched into a single mode fiber for convenience and mode cleaning and send them through an AOM for frequency shifting and light pulse generation. The pulsed light beams are finally overlapped with the pulses used for locking and all three laser beams are matched into the fiber transporting the light to the interferometer.

### Probe laser setup for two input port interferometer

The probe laser setup has been changed to the one depicted in figure 3.6(b) in early 2008. The main reason was the desire to be able to detune the light from resonance by almost arbitrary values without changing the optical setup (e.g., replacing or realigning AOMs). In addition, the need to inject the second probe beam from the second input port of the input beam splitter became apparent, consider figure 3.9 for the corresponding interferometer setup. In the new version of the probe laser setup, the lasers are stabilized to the MOT repump master laser (using the tapped off beam in figure 3.3) with a beat note lock. We achieve a relative frequency stability of the two probe lasers of  $\sim 10$  kHz.

The stabilized laser light is shaped into pulses individually for the two lasers and coupled into two fibers. For alignment purposes, the  $F = 4 \rightarrow F' = 5$  laser is coupled into both fibers where one coupling mirror is piezo-actuated such that the phase shift between the two input modes on the interferometer beam splitter can be modulated. This way, the mode matching of the two fiber outputs on the input beam splitter of the interferometer can be determined. This is necessary to assure that the two probe colors *in fact* interact with the same spatial region of the atomic cloud.

### 3.2.2 White light alignment and interferometer locking

To assure the best possible laser phase noise suppression in the interferometer, it is beneficial to align it close to the so-called “white light” position [1]. In this configuration both interferometer arms have the same length and the output signal is independent of the laser frequency. Note that the interferometer will be aligned to

---

<sup>1</sup>Unfortunately, we acquired these diodes only rather late compared to the time frame presented here; better customer service from Eagleyard who had suggested the RWE-0850 for our applications could have saved us a lot of pain.

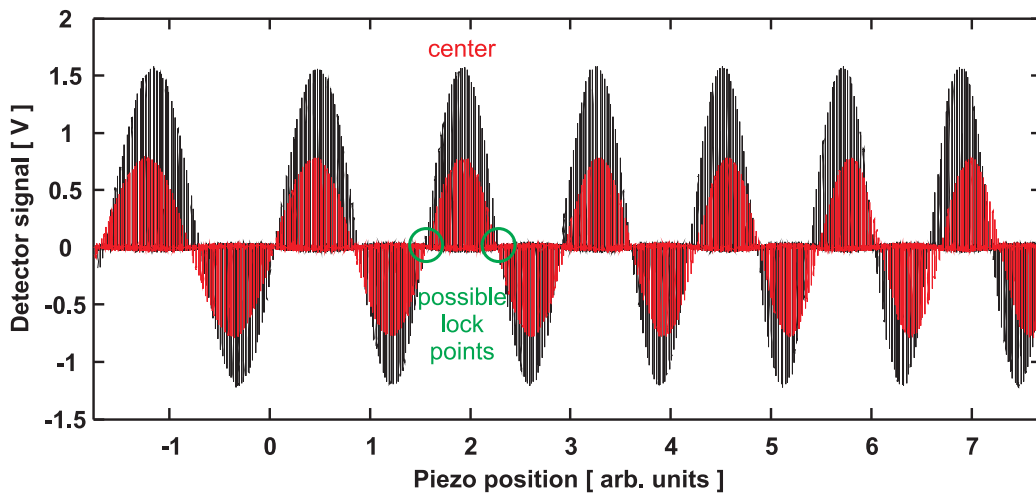


**FIGURE 3.7:** Interference fringes for the lock laser (black) and for the  $4 \rightarrow 5$  probe laser (red). One can clearly see a shift of the two fringes with respect to each other. At the white light position, the two maxima (or minima) overlap exactly. The zero crossing of the lock laser fringe to either side of the exact white light position can be used as stabilization point. Probe and lock laser pulses with  $2 \mu\text{s}$  duration and  $200 \mu\text{s}$  repetition period have been applied alternately. The asymmetry of the lock laser fringes is due to the not optimal splitting ratio of the interferometer output beam splitter for  $840 \text{ nm}$  light.

a differential path length of  $\Delta l = \lambda \Delta \phi / 2\pi = \lambda/4$  as discussed in section 2.4.<sup>2</sup> The interferometer will therefore always be at least  $\lambda/4$  away from white light position. The white light position is initially found by coupling a broad band light source (fiber coupled light emitting diode with  $\sim 20 \text{ nm}$  bandwidth) into the interferometer and looking for interference fringes on a CCD camera. When interference fringes are observed, we start scanning the path length difference with the piezo actuated folding mirror of the interferometer and send both probe and lock laser pulses ( $2 \mu\text{s}$  duration,  $100 \mu\text{s}$  repetition period) alternately through the interferometer. We obtain the interference fringes as depicted in figure 3.7. Because the two lasers have considerably different wavelengths, the fringes gain a visible phase difference very quickly. *In principle*, the zero crossing of the lock laser fringe to either side of the center fringe can be used as stabilization points. However, due to technical imperfections they are not exactly equal, so we usually pick the side where the probe signal is closest to being balanced in the locked configuration. The clear asymmetry in the fringes from the lock laser are due to the not optimal splitting ratio of the output beam splitter for  $840 \text{ nm}$  light since the splitting ratio depends on the applied light wavelength.

Due to its mere size, it is obvious that the interferometer has to be actively stabilized against thermal drifts and acoustic noise. To stabilize the interferometer to half fringe position,  $\Delta \phi = \pi/2$ , we use another one of our external cavity diode lasers, with output wavelength around  $840 \text{ nm}$ . The setup is illustrated in figure 3.6. This laser is not frequency stabilized, its single mode operation is monitored

<sup>2</sup>It is obvious that the phase sensitivity of the interferometer is largest at  $\Delta \phi = \pi/2$  phase difference between the two arms. At the maximum of a fringe, the output signal is to first order independent of the differential phaseshift.

on a Fabry–Perot cavity. The actual wavelength of the lock laser is of minor importance as long as the light does not interact considerably with the atoms in the sample. One just has to be aware of the fact that many optical components (and not only the wavelength specific polarization control elements) are wavelength sensitive. This holds especially for the interferometer beam splitters. To compensate for different splitting ratios on the beam splitters, one of the output ports sports a multi order  $\lambda/2$  plate and polarizing beam splitter combination (PBS4 in figure 3.5). The multi order nature of the waveplate allows us to introduce frequency dependent losses on the following beam splitter.

The error signal for the stabilization loop is obtained in a lock-in type technique. To that end, the lock beam is power modulated (actually the modulation depth is 100%, so it is basically pulsed on and off) with a  $\sim 100$  kHz square wave. The interferometer output detected on the differential detector is then demodulated with a local oscillator and the obtained error signal is used for feedback onto the piezo actuated folding mirror. The feedback bandwidth of the stabilization loop is below 1 kHz. Acoustic resonances in the setup hinder us from pushing the bandwidth higher. On short timescales we therefore have to rely on the passive stability of the interferometer; this will become important when we determine the noise performance of the interferometer in chapter 6. To avoid contamination of the actual measurement signal, i.e., when probe pulses are sent through the interferometer, we gate the modulation of the lock laser light such that it is off for a well defined period around the probe pulses as indicated in figure 3.5. Switching the feedback loop off for several hundred microseconds does not disturb the interferometer balancing since the feedback loop is too slow anyway. Since the detector is basically used in a balanced configuration during interferometer locking, only short transient times need to be taken into account to assure that the differential detector performs optimally (see chapter 4).

### 3.2.3 Noise properties of the interferometer

In the introductory chapter and several times on the way, we have stated the final goal of our efforts: quantum noise limited measurement precision. In the context of atoms in the interferometer this boils down to a light shot noise limited measurement of the light phase shift. In the preceding sections, an attempt has been made to omit the discussion of noise properties of the system, since this is the main contents of chapter 6. To motivate the change to a different interferometer setup, we do, however, have to indulge into a short discussion on the classical noise cancelation features of a balanced measurement in the context of interferometers.

When classical (large) signals are measured, the classical amplitude fluctuations are often so large that they mask the tiny intrinsic quantum mechanical fluctuations. It is therefore beneficial to devise a measurement scheme which intrinsically cancels the classical amplitude fluctuations. Measuring the difference of the output ports in a balanced interferometer configuration is such a classical amplitude noise suppressing setup – if the power in one of the interferometer arms were increased significantly with respect to the other, the connection to a homodyne measurement setup is obvious. Arranging the interferometer in white light position in addition

makes the phase shift insensitive to the light frequency and therefore helps to cancel classical laser phase noise.

### Classical noise suppression

To formalize the classical noise suppression property, let us look at the signals of our Mach Zehnder interferometer output ports individually. Both show a signal  $S_{D1,D2}$  with amplitude  $S \propto P$ , where  $P$  is the power of the input beam. We can separate the amplitude fluctuations  $\delta S_{1,2} = \sqrt{\delta^2 S_{1,2}}$  from the mean beam signal  $S_0$ :

$$S_{D1} = \frac{1}{2}(S_0 + \delta S_1)(1 + \cos \phi) \quad (3.13)$$

$$S_{D2} = \frac{1}{2}(S_0 + \delta S_2)(1 - \cos \phi) \quad (3.14)$$

The amplitude fluctuations can be further divided into correlated and uncorrelated parts:  $\delta S_1 = \delta S_{\text{corr}} + \delta S_{1,\text{uncorr}}$  and  $\delta S_2 = \delta S_{\text{corr}} + \delta S_{2,\text{uncorr}}$ . Subtracting the two outputs at the detector yields a signal:

$$\begin{aligned} S_- &= S_{D1} - S_{D2} = (S_{\text{max}} + \delta S_{\text{corr}}) \cos \phi \\ &\quad + \frac{1}{2}(\delta S_{1,\text{uncorr}} - \delta S_{2,\text{uncorr}} + (\delta S_{1,\text{uncorr}} + \delta S_{2,\text{uncorr}}) \cos \phi) \end{aligned}$$

At  $\phi = \pi/2 + \Delta\phi$  the equation can be linearized around  $\Delta\phi \approx 0$ . The mean value of the signal is zero:  $\langle S_- \rangle = 0$ , and the variance  $\delta^2 S_-$  evaluates to:

$$\delta^2 S_{-, \phi=\pi/2} = \delta^2 S_{\text{uncorr}} \quad (3.15)$$

We have assumed that  $\delta^2(\Delta\phi) = 0$ , i.e., the interferometer is stable in itself and no atoms are present whose projection noise would lead to  $\delta^2(\Delta\phi) \propto N$ . Furthermore, both interferometer arms are assumed to have the same uncorrelated noise contribution  $\sqrt{\delta^2 S_{1,\text{uncorr}}} = \sqrt{\delta^2 S_{2,\text{uncorr}}} \equiv \sqrt{\delta^2 S_{\text{uncorr}}}$ . In the ideal case, the uncorrelated fluctuations are only of quantum mechanical nature – the light shot noise of the output modes.

At balanced position,  $\phi = \pi/2$ , the classical, correlated noise contributions are maximally suppressed and we are only left with the quantum mechanical uncertainties. If, on the other hand, a signal produced by considerable phase offset  $\phi = \pi/2 + \Delta\phi$ ,  $\Delta\phi \approx \pi/2$  is considered, the amplitude fluctuations  $\delta^2 S_{\text{class.}}$  are not suppressed:

$$\delta^2 S_{-, \phi=0} = \delta^2 S_{\text{quant.}} + \delta^2 S_{\text{class.}} \quad (3.16)$$

and the signal is usually dominated by the classical amplitude noise.

### Two port interferometer setup

Ideally, we would like to achieve a situation where amplitude fluctuations are canceled during the measurement. When no atoms are present in the system, this is assured by stabilizing the interferometer to  $\phi = \pi/2$ . The two color – single port interferometer produces an output signal with zero mean value when atoms

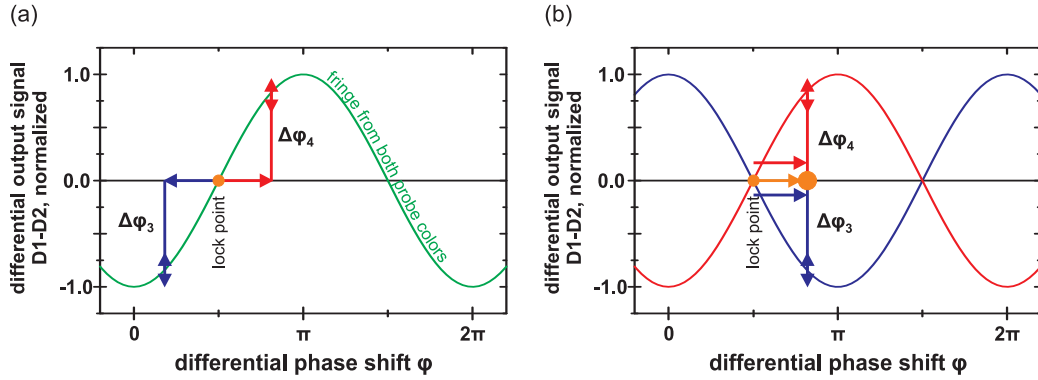


**FIGURE 3.8:** Comparison between the different two color setups. (a) Two color – single port interferometer. For equal power, both probe colors show the same interference fringe. When locked to half fringe position,  $\phi = \pi/2$ , a zero output signal (which is ideal for noise measurements) for atoms in the equal superposition state is obtained when the colors are shifted in opposite direction,  $\Delta\phi_3 = -\Delta\phi_4$ . The two, each on their own imbalanced, signals are added at the detector and a zero signal is observed. Amplitude fluctuations from the two lasers add up. (b) Two color – two port setup. The two interferometers are  $180^\circ$  out of phase and the output signal for an empty interferometer is independent of the path length difference – equal amplitudes provided. When both probe lasers obtain a phase shift  $\Delta\phi_3, \Delta\phi_4$  in the same direction by atoms in  $F = 3$  and  $F = 4$ , the signal for an equal superposition state is again zero. The lock point can then be shifted to compensate for the phase offset and amplitude noise suppression for both colors individually can be achieved.

in the equal superposition state are present as depicted in figure 3.8(a). However, by introducing the atoms, each single probe laser color is in itself not balanced. Classical amplitude fluctuations are therefore not suppressed in the presence of atoms and may easily compromise the signal.

This issue can be amended by introducing the second probe color through the second port of the input beam splitter as shown in figure 3.9. We refer to this type of setup as two color – two port arrangement<sup>3</sup>. Obviously, the interference fringes of the two input modes are exactly out of phase, as depicted in figure 3.8(b). By arranging the probe frequencies and powers in the right way, we again achieve a situation where the mean value of the interferometer output signal is zero. In principle, again each color is unbalanced on its own and the setup is prone to classical amplitude fluctuations. However, since the atomic signals now arise from interferometer phase shifts on the same side of the stabilization point, the lock point of the interferometer can be moved to the position indicated in figure 3.8(b), where both probe colors are individually balanced. At this position, the classical amplitude fluctuations of each individual laser cancel and we obtain an ideal configuration for noise measurements!<sup>4</sup>

The setup has two more clear advantages:

<sup>3</sup>It is clear that every interferometer has two input modes, but often one of them is assumed to be an electromagnetic vacuum field state. When we refer to the “two port setup”, we want to stress that the second mode is populated in a non-trivial way.

<sup>4</sup>This would also be possible for the single color – single port interferometer setup. However, in the two color – two port case the signal is independent of the number of atoms so changing the lock point only suppresses the amplitude noise. In the single color – single port setup, the signal also depends on the atom number and is thus prone to shot-to-shot atom number fluctuations.

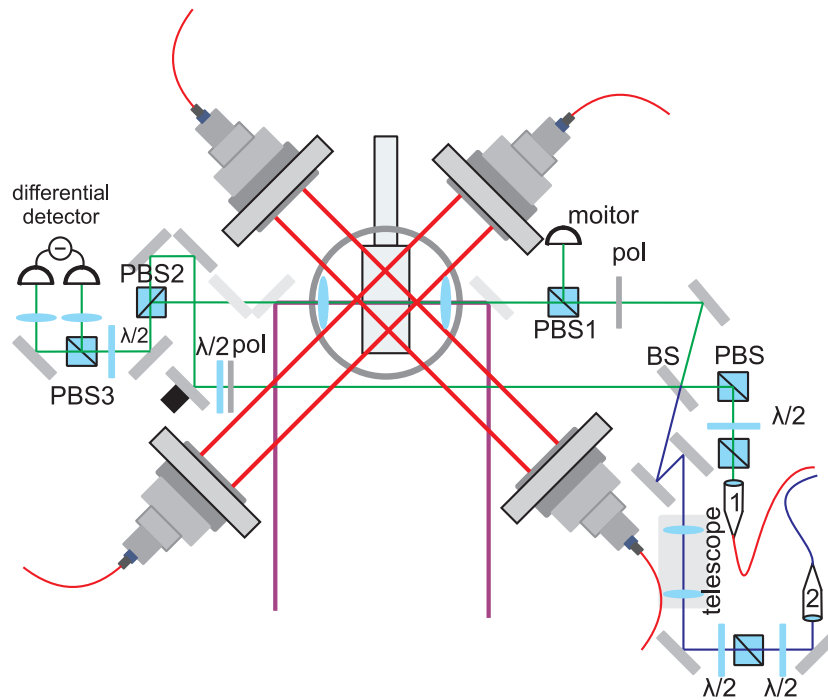


**FIGURE 3.9:** *Two port interferometer setup. The optical setup for the second input (2) resembles the original input's setup (1). The telescope is needed to compensate for slightly different beam waists due to the different fiber core sizes; we generally achieve a mode matching of the two input ports on the input beam splitter (BS) above 97%. Polarization components in the interferometer (polymer polarizers (pol) and polarizing beam splitters (PBS1)) allow us to change the power ratio between the probe and reference arm. The interferometer beams are matched on PBS2, their polarization rotated by 45° and interfered on PBS3. The two output ports are again detected on a differential photo amplifier. The other components are described in the caption of figure 3.5*

- Acoustic noise suppression: when the two probe beams have equal fringe amplitude, the combined output signal is independent of the geometric path length difference. Vibrations will thus not change the signal; the interferometer is only sensitive to an atomic population difference
- Light shift cancelation. The problem of differential light shift between the clock levels during the application of probe pulses will be discussed in section 5.5. To obtain a signal which is in fact proportional to the population difference in the atomic sample in the two port – two color setup, the probe lasers both have to be detuned to the same side of the closest transition – both probe lasers need to gain a light phase shift in the same direction (compare figures 2.3 and 3.8). In this configuration also the light shifts of the ground states (equation (3.5)) have the same sign and can be adjusted to be equal.

### Optical setup of two color – two port interferometer setup

The optical setup of the interferometer with two active input ports is shown in figure 3.9. Apart from adding light in the second input port of the interferometer

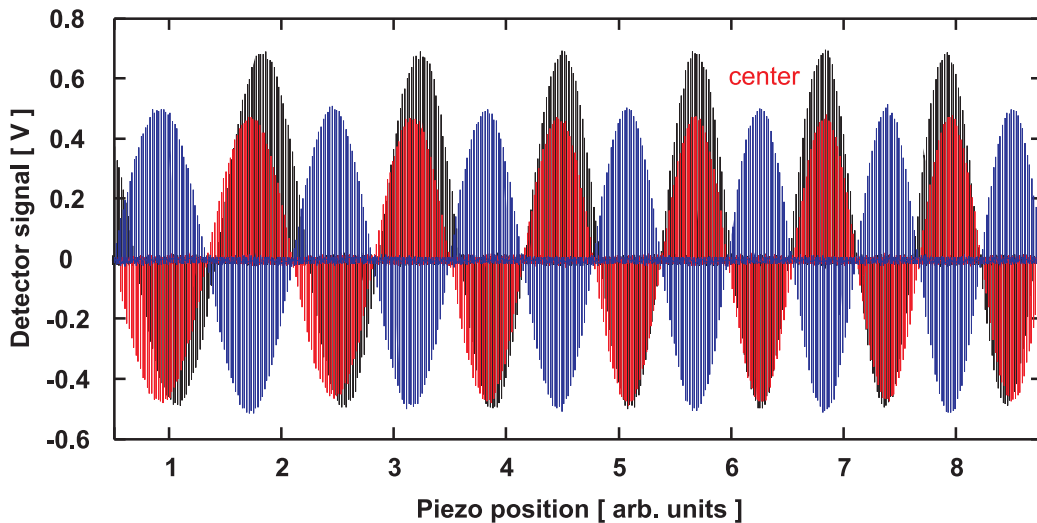


**FIGURE 3.10:** *Interference fringes of the lock laser (black), the  $F = 4 \rightarrow F' = 5$  probe laser (red) entering through the same port as the lock laser and of the  $F = 3 \rightarrow F' = 2$  probe laser (blue) entering through the second input port. The asymmetry in the fringes from the lock laser is due to the polarization dependence of the interfering beam splitter.*

through a second fiber, we also introduce losses in the probe arm of the interferometer by using polarization optics. This way, the relative power between the probe and the reference arm can be adjusted and the reference arm can be changed to take the role of a strong local oscillator. The interferometer then acts as a homodyning setup for one of the probe light quadratures. In addition, the single component, non-polarizing output beam splitter has been changed to a combination of two polarizing beam splitters (PBS2 and PBS3), where the actual interference happens on PBS3 (caused by the polarization mixing induced by the preceding  $\lambda/2$  plate). This became necessary because the splitting ratio of the previously used non-polarizing output coupler was not exactly 50/50, leading to a signal imbalance too large for the detector to cope with.

In figure 3.10 we show the actual interference fringes of the two probe and the interferometer lock lasers in pulsed mode. The white light position can be identified in the same way as for the single input port interferometer. As predicted, the fringes from the two input ports are shifted by  $\pi$  with respect to each other.

We have now introduced and discussed the two main interferometer setups used for the data shown in the later chapters. The light shot noise limited performance of both setups will be discussed in chapter 6 together with the projection noise measurements. Until then, we do not concern ourselves with the noise properties of the system.

### 3.3 Experiment control

Part of the experiment control has already been discussed in section 3.1.2. As mentioned, the input/output cards used for the timing of the MOT sequence have a time resolution of 1 ms. To probe the atomic ensemble we want to use light

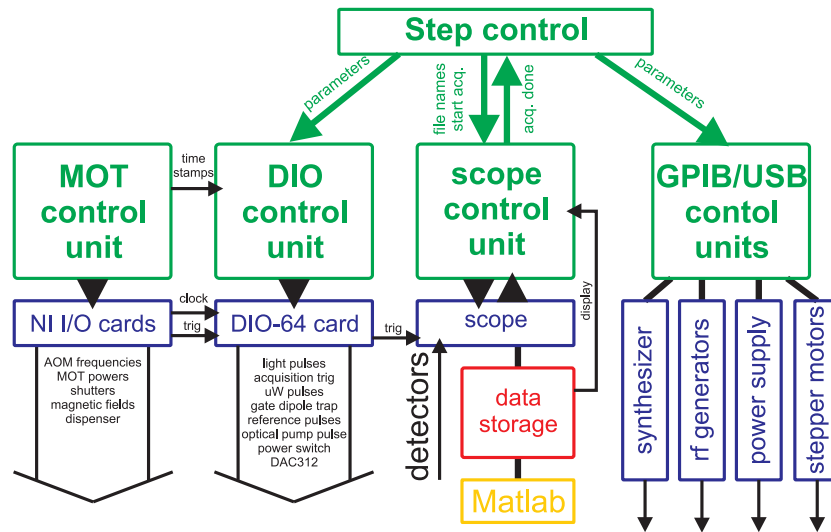


**FIGURE 3.11:** Programme and system component hierarchies. One programme controls the three National Instruments cards, used for timing with 1 ms resolution, mainly MOT parameter control (section 3.1.2, figure 3.4). A second programme controls the fast timing through the Viewpoint Systems DIO-64 FPGA board (section 3.3.1, figure 3.12). A further programme (running on another computer) takes care of the data acquisition with the DSO and the storage (section 3.3.2). Further equipment is controlled by several stand alone Labview applications, controlling one or more devices via USB or GPIB interfaces (section 3.3.2). When necessary, the small stepping routine manages a continuous parameter change and the timing between the programmes. The extremely modular programme architecture is due to historical reasons. Most of the Labview programmes have a meaningful life without all the rest. This makes the structure very versatile and flexible but sometimes hard to follow for new members of the work group.

pulses of few microseconds duration; in addition, arbitrary pulse sequences with sub microsecond resolution are required to create ensemble superposition states and for the microwave spectroscopy to study the coherent evolution of the two level system. We have therefore added a Viewpoint Systems DIO-64 digital input/output card to the setup. Further, we have implemented remote computer control to various components in the setup, mainly for convenience and to speed up the data taking process.

The different programmes used to control the various parts will be discussed in the next sections and are summarized in figure 3.11 together with the equipment they control and their mutual dependencies.

### 3.3.1 Fast pulse sequence generation

From a historical and least-invasive point of view, the implementation of an arbitrary pulse form generator as stand alone Labview application seemed the quickest and most straight forward approach to the needs of the experiment in terms of flexible probe and microwave pulse train generation. The choice fell on a Viewpoint Systems PCI-DIO64 FPGA input/output card. The card has four 16-bit input or output busses. We configure all ports as outputs. One of the big advantages in the programming of the card is that the buffer only requires time stamps when

the output state is supposed to change. The time sequence generating Labview programme therefore only has to supply a time stamp with the corresponding bit values of the output ports when actually something is supposed to happen – two time stamps for one pulse. This reduces the buffer which needs to be transferred to the card significantly with respect to the conventional way of programming, where a buffer value at each clock cycle has to be supplied. Running output operations for 3 seconds with 50 ns time slot resolution would else require 480 MB of buffer size!

The on board buffer of the card can only hold 512 time stamps and corresponding output port bit values. For extended pulse trains we therefore use one output bit of the card to stop the cards own output operation and thereby re-arm the card for a new output sequence. In this mode the buffer can be almost arbitrarily large. The disadvantage of this mode is that the card can run a single buffer only once (it can only loop over its internal buffer), one therefore has to constantly feed the allocated memory space with buffer blocks to not cause the card to starve from lack of time stamps. The card is synchronized to the MOT cycle with a hardware trigger (see figure 3.4) and it uses the same clock as the other timing cards to assure synchronous operation. Figure 3.12 shows one of the Labview programme front panels corresponding to one arbitrary pulse train generation unit with typical values. The entries are described in the figure caption. The values will serve as example for data shown in chapter 5. A number of such pulse generation units

Stage	delay	number of pulses	pulse duration	repetition period	Pulses finished after
7	16497.00	2	10.00	23.00	16530
8	5850.00	10	2.00	10.00	5942
10	5000.00	10	2.00	10.00	5092
12	5000.00	10	2.00	10.00	0
10	5045.00	10	2.00	10.00	0
22	5000.00	5	4.00	16.00	0
26	5045.00	5	4.00	16.00	0
28	5000.00	5	4.00	16.00	0
30	5045.00	10	2.00	10.00	5137
31	5045.00	5	4.00	16.00	0

**FIGURE 3.12:** Part of the front panel of one pulse generation units. The boolean control determines whether the corresponding row is supposed to be executed. The stage numbers refer to the stages in the MOT programme. Delays are defined relative to the start of the relevant stage unless two rows with the same stage number are supposed to be executed. In the latter case, the delay refers to the end point of the last pulse of the previous train in the same stage. Times are given in microseconds. For example, the second entry line will produce 10 pulses with  $2\mu\text{s}$  duration and  $10\mu\text{s}$  repetition period, the first pulse starting after  $5850\mu\text{s}$  when stage 8 of the MOT programme has started.

comprise the DIO control programme. Some of the controls implemented are: Gating the probe light (of each laser), triggering the acquisition of the oscilloscope, gating the lock laser modulation, sending additional lock pulses as reference pulses,

creating microwave pulses, triggering sweeps on the microwave synthesizer, gating the dipole trap laser, gating the optical pump pulses, switching probe power levels. Additionally, we use twelve bits of one port to drive a parallel 12-bit high speed, fast settling digital to analog converter which we can, e.g, use to change the dipole trap power between pulses.

### 3.3.2 Data readout and postprocessing

Extensive noise measurements have shown that the readout of the detector signal by direct analog integration and digitization with a National Instruments computer card as presented in [1, 2] is (also in terms of flexibility) inferior to the direct digitization on an oscilloscope. We therefore use an Agilent Infiniium 54832D digital storage oscilloscope (DSO) to acquire the data from the detectors. We employ the DSO in segmented mode, where a predefined number of time segments is recorded. Each of these segments is individually triggered by a DIO output pulse; the segments can in principle be arbitrarily far spaced in time. When the acquisition of all data segments is finished, the data is transferred to another computer and stored for post processing. The obvious advantage of this triggering mode is the reduction of used disk space and the possibility to operate the DSO at the maximum time resolution. As we shall see, a single experimental run usually contains several probe segments, where each segment is only few tens of microseconds long, but the segments are distributed over several hundred milliseconds.

To illustrate the procedure on a realistic time and pulse sequence consider figure 3.4 and figure 3.12 again. We do not know what exactly, yet, but let us assume that we want to measure in stages 8, 10 and 30 of the main timing sequence, figure 3.4. The DIO cards generates pulses in stage 8, 10 and 30 according to the sequence shown in 3.12. The three DSO segments would therefore be triggered at  $t = 5850, 5000, 5045 \mu\text{s}$  in these stages. To acquire the ten pulses, only a  $100 \mu\text{s}$  time window per segment is required; between the triggers which are separated by several tens of milliseconds, the DSO just idles and waits. When the acquisition is finished, the data is transferred to the auxiliary computer.

The control of the DSO, e.g., change scales, number of channels displayed and stored, setting up the DSO mode and number of segments is taken care of by a further stand alone Labview programme. The programme manages the DSO, the storage and the displaying of the data on the control computer. The data recorded with the DSO is stored in internal binary format and is post processed using Matlab. Usually, we are only interested in the area of the pulse, so after reading the binary data, the Matlab script prepares a processed data file containing the duration normalized integrals of the individual pulses. Since the whole trace is available, more involved integrating function as used for baseline subtraction (compare section 4.3) are easily implemented.

#### Further control parameters

Apart from the analog and digital signal generation discussed up to now, some system parameters are controlled by additional Labview programmes. Some of

the rf frequency generators, e.g., the function generators providing the reference frequency for the beat note locks (section 3.2.1) have GPIB interfaces which are used to remotely set the frequencies. Also the microwave synthesizer parameters (section 5.2) are controlled with its GPIB interface and the settings of a general purpose power supply. Two USB interfaced, motorized rotation mounts equipped with  $\lambda/2$  plates, which are used to control and stabilize the power of the probe lasers, are also Labview controlled.

### Stepping routines

In many of the experiments performed and discussed in chapter 5, parameter values, like pulse durations or separations, light powers or frequencies have to be changed from one data point to the next. To make this walk in parameter space time efficient and less prone to mistakes from the experimentalists side, we have implemented stepping routines. In a small programme routine, we define the parameter interval. This programme then changes the entry in the specific Labview applications, gates the DSO acquisition programme and manages the data file names (compare figure 3.11). In this way, the experiment can run basically on its own taking, e.g., ten datasets at the same parameter set and then move on to the next set. This stepping programme has saved many hours of tedious by-hand parameter changing, file renaming etc. and almost made the experiment into a data production facility [51].

We have now gathered the main principles and experimental techniques used in our setup. To conclude this chapter, we apply the described techniques in the next section to extract some properties of a dipole trapped sample. The example is mainly given to illustrate the basic measurement procedure and to set the stage for the main experimental body, chapters 5 and 6.

## 3.4 Non-destructive probing of dipole trapped sample

In section 3.1.2 and 3.1.3 we have discussed the generation of a cold ensemble of caesium atoms, trapped in a single beam far off resonance dipole trap. The atoms captured in the MOT and then loaded into the dipole trap can be observed by using fluorescence imaging techniques [2]. One triggers the acquisition of a CCD camera while flashing the sample with resonant  $F = 4 \rightarrow F' = 5$  pump and  $F = 3 \rightarrow F' = 4$  repump light. This way of observing the ensemble is fully destructive; the spontaneous photon scattering, which is used to detect the atoms, heats the sample up and within few tens of microseconds, the atoms are lost from the trapping region. To determine the relevant parameters of the dipole trapped sample like atom number, temperature, lifetime of the atoms in the trap and trap frequency, we use the interferometer. As a reference for the later chapters, we shall now introduce the general measurement procedure when probing the sample non-destructively on a practical example: the determination of the trap lifetime and the longitudinal trap frequency.

### 3.4.1 General measurement procedure

For most of the experiments presented here and in chapter 5 we use a single color – single port interferometer setup. The probe light is (unless otherwise specified) blue detuned by  $\Delta_{45} = +160$  MHz from the  $F = 4 \rightarrow F' = 5$  transition. We *generally* use probe pulses of  $2 \mu\text{s}$  duration; for specific applications, the duration may be adapted. The duration of  $2 \mu\text{s}$  is chosen to fit to the best operation point of the differential photo detector we use to measure the interferometer phase shift (chapter 4). In addition, a  $2 \mu\text{s}$  pulse duration is advantageous when one is interested in the sample dynamics: Effects of atomic motion can be neglected during that time, so a single pulse corresponds to an instantaneous parameter readout. The photon numbers in a single pulse are adapted such that the spontaneous photon scattering induced by a series of pulses is negligible. As typical value we use  $\sim 10^6$  photons per probe pulse, corresponding to a dc beam power of  $\sim 125$  nW during  $2 \mu\text{s}$ .

#### Interferometer baseline

The phase shift caused by the atomic ensemble can usually not be directly inferred from the measurement signal. Due to technical imperfections, the zero crossing of the lock laser interference fringe and the probe laser interference fringe do not exactly coincide (compare figure 3.7), even close to white light position. The differential detector signal  $S \equiv S_- = S_{D1} - S_{D2} = S_{\max} \sin \Delta\phi_{\text{baseline}}$  is therefore not zero when no atoms are present. We casually refer to this case as “the empty interferometer signal”. When we refer to the interferometer (output) signal  $S$ , we always mean the differential output signal of the two output ports; the single photo diode currents are not accessible in the detector we use. Since the actual size of the signal in terms of phase shift units is usually not of interest, we do in general not normalize the signal to the actual fringe amplitude. The interferometer lock offset (interferometer baseline) has to be subtracted from atom measurement signals to get the real atomic phase shift. We try to keep this offset as low as possible. The combined offset plus atomic signal is usually below 40% of the total interference fringe amplitude, such that the output signal is still almost linear in the phase shift:  $S_- = S_{\max} \sin(\Delta\phi_{\text{atomic}} + \Delta\phi_{\text{baseline}}) \approx S_{\max}(\Delta\phi_{\text{atomic}} + \Delta\phi_{\text{baseline}})$ . The error in this approximation is 2.6% at 40% fringe amplitude, which is acceptable.

#### Measuring atoms in the trap

The experimental cycle to measure on a dipole trapped atomic ensemble is summarized in figure 3.13. As described in section 3.1, we trap and cool atoms with a magneto optical trap and transfer them into an optical dipole trap during a sub-Doppler cooling stage. After the cooling stage, the atoms are about equally distributed between the two ground state manifolds  $F = 3$  and  $F = 4$ . To read out the total atomic population, we therefore first repump the atoms into  $F = 4$  using the MOT repump laser. After this initialization, we are ready to apply whichever manipulation and probing scheme we desire. At the end of the sequence, we heat the atoms out of the trapping region by applying the MOT light (both pump and repump light) detuned to the blue side of the transitions. By detuning the lasers

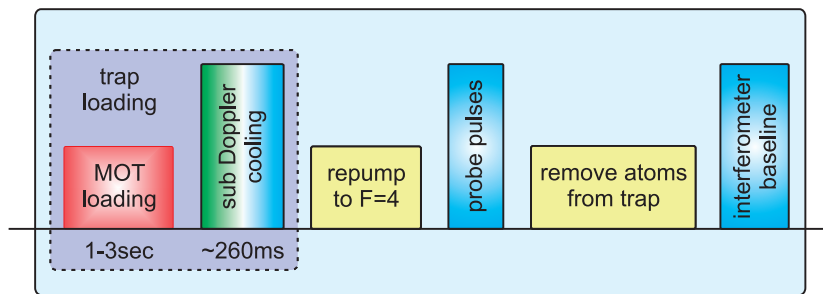


**FIGURE 3.13:** *Simple measurement sequence.* We load atoms into the dipole trap by running the magneto optical trap and performing rudimentary sub-Doppler cooling. The atoms confined in the trap are then initialized into the  $F = 4$  hyperfine ground state and ready for whichever measurement we desire to do. After the measurement, we remove the atoms from the probing region by heating them out of the trap with blue detuned MOT light and determine the interferometer lock offset for signal calibration. The whole cycle takes a few seconds and is repeated until enough statistics for a single parameter configuration is obtained.

to the blue side of the transitions we avoid optical molasses effects which would freeze the atoms. When all atoms have been removed, we measure the empty interferometer phase shift signal and use it for baseline subtraction.

The graphs presented in figure 3.14 illustrate the path from raw data recorded on the oscilloscope to the single pulse integrals used in the data processing for an atomic sample prepared in the just described way. The data in 3.14(a) shows a recording of the trap dynamics just after the loading is finished. To record the data, we send 2000 probe pulses with  $2\ \mu\text{s}$  duration and  $250\ \mu\text{s}$  repetition period in the beginning of stage 5 of the experimental cycle (compare figure 3.4). After about 450 ms of probing, the sample is heated out of the trap by applying both blue detuned  $F = 4 \rightarrow F' = 5$  and  $F = 3 \rightarrow F' = 4$  light and the interferometer baseline is determined. Figure 3.14(b) shows a zoom into that part of the data and 3.14(c) zooms into a single probe pulse. The full raw data is stored and the pulses are then integrated numerically in the limits shown. We are then left with the single pulse values (actually we normalize the integrals to the pulse duration to get only the pulse amplitude), ready for post processing. In general, all the data shown in the following is interferometer baseline subtracted, in the sense that the mean value of several empty interferometer measurements is subtracted from the data.

### 3.4.2 Lifetime of atoms in the trap

From the data shown in figure 3.14 we extract the baseline subtracted pulse values as discussed above. We then end up with data as shown in figure 3.15 from which we calculate the trap decay time. An exponential fit returns a  $1/e$  lifetime of  $\tau = 250\ \text{ms}$  which corresponds to the average trap decay time we observe. It is considerably shorter than the values reported in [2] for a comparable setup in our lab. This is most likely due to increased background pressure in the vacuum system as discussed in section 3.1.1. The single exponential decay is only an approximation

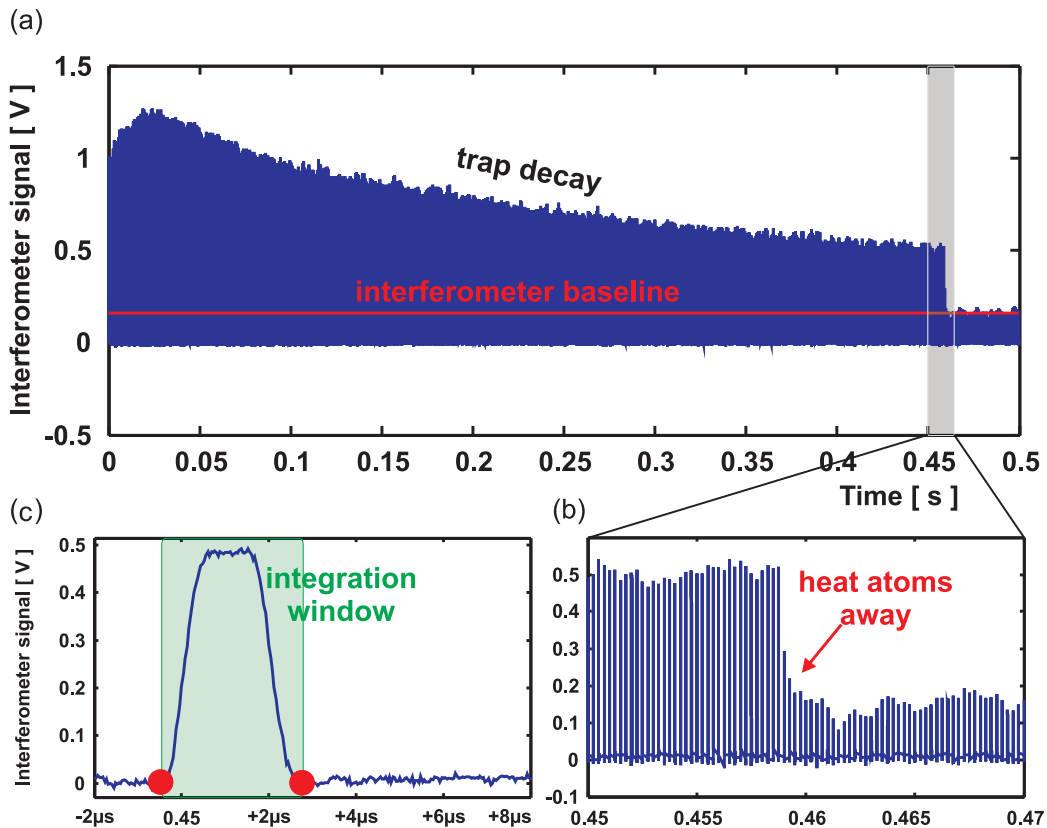


**FIGURE 3.14:** Raw data from non-destructive trap decay observation. (a) 2000 probe pulses with  $2\ \mu\text{s}$  duration and  $250\ \mu\text{s}$  repetition period are applied to an atomic sample loaded into the dipole trap. After about  $450\ \text{ms}$  quasi continuous probing, the atoms are heated out of the trap and an “empty interferometer baseline” is established. (b) Zoom into the transition region where the atoms are expelled from the trap, resolving the single pulses. (c) Single probe pulse. The directly digitized and stored raw data is numerically integrated and normalized to the pulse duration. This compressed information is then used for postprocessing.

and discards effects caused by density dependent losses. The exact loading and decay dynamics has been studied in detail in [2, 15].

A single data trace as shown in the figure can be used to optimize the trap loading very efficiently. A single shot measurement is used to extract the trap decay and the number of atoms in the interaction region. Changing parameters during the MOT and sub-Doppler cooling stages, moving the position of the MOT cloud or the position of the dipole trap beam between two experimental runs have immediate consequences and can be followed basically online.

### 3.4.3 The problem with the atom number

At first sight it seems straight forward to extract the total number of atoms in the interaction region from the interferometer phase shift as given in equations (2.43) and (2.44) on page 20. The maximum number of atoms we can load into the trap produces an interferometer phase shift of  $\Delta\phi_4 \sim 0.4\ \text{rad}$  at a detuning

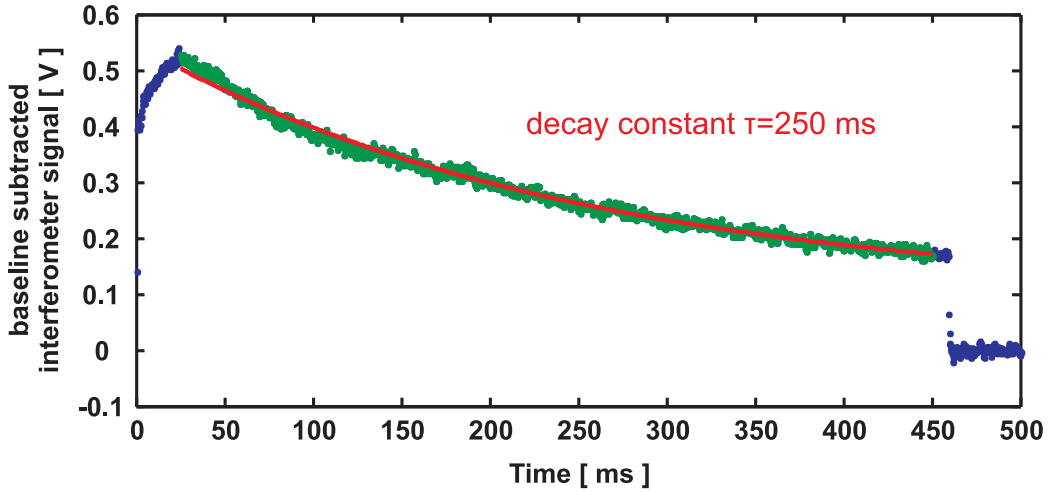


**FIGURE 3.15:** Baseline corrected data for trap lifetime determination and trap loading optimization. An exponential fit through the data returns a decay time constant of 250 ms. The exact shape of the trap decay is not single exponential. Details on the trap loading and the decay can be found in [2].

$\Delta_{4,5} = +150$  MHz. Assuming a homogeneous probe area  $A = V/l = \pi w_0^2$  with a probe waist of  $w_0 = 20 \mu\text{m}$ , one finds the number of atoms in the interaction region to be  $N_4 \sim 3 \times 10^5$  and a corresponding on resonance optical depth  $\alpha_0 = 2S_0 \sim 30$ . This simple approach assumes a homogeneous atom number distribution across a homogeneous interaction region. Due to the intensity distribution of the dipole trap beam  $I(r) = I_0 e^{-2r^2/w_0^2}$  and assuming that the atoms in the trap are in thermal equilibrium, the spatial profile of the atomic ensemble can be approximated by a Gaussian column density distribution:

$$n(r) = n_0 \exp\left(-\frac{2r^2}{r_0^2}\right) \quad (3.17)$$

Here we introduce a sample waist  $r_0$  similar to the Gaussian light beam waist  $w_0$  which does not correspond to the usual definition of the sample width<sup>5</sup>. The total number of atoms in the trap becomes:  $N = \frac{\pi}{2} r_0^2 n_0$ . The main complication now arises from the fact that we couple a Gaussian probe beam with smaller waist  $w_0 < r_0$  to the ensemble. So in addition to the Gaussian density distribution we get a spatially inhomogeneous coupling to the atoms. When we denote the light phase shift per atom with  $k$  and write  $\Delta\phi_4 = kn(r)$ , the interferometer signal  $S_-$  reads:

$$S_- = \int kn(r)I(r)2\pi r dr \quad (3.18)$$

which can be evaluated to:

$$S_- = 2\pi k I_0 n_0 \frac{w^2 \varrho^2}{4 + 4\varrho^2} \quad (3.19)$$

which depends on the ratio  $\varrho = r_0/w_0$  of the sample waist to the probe beam waist. The definition of an effective atom number is now considerably more complicated.

<sup>5</sup>Usually the sample size is defined via the thermal RMS radius of the Gaussian density distribution  $n(r) = n_0 \exp\left(-\frac{r^2}{2\sigma^2}\right)$ ,  $\sigma = \frac{t}{2\pi} \sqrt{kT/m}$  where  $t$  is the trap period.

However, if  $\varrho$  is known, the maximum values of the column density can be extracted from the effectively measured phase shift:

$$\Delta\phi_{\text{eff}} = \frac{\int kn(r)I(r)2\pi r dr}{\int I(r)2\pi r dr} = kn_0 \frac{\varrho^2}{1 + \varrho^2} \quad (3.20)$$

which can be used to determine the total number of atoms  $N = \frac{\pi}{2}r_0^2 n_0$  in the trap.

An effective atom number  $N_{\text{eff}}$  can be introduced by demanding that the noise scaling for a coherent atomic state  $\delta^2 N_{\text{eff}} = N_{\text{eff}}$  is fulfilled. For the signal scaling we get:

$$\frac{S_-^2}{\delta^2 S_-} = \pi w_0^2 n_0 \frac{\varrho^2(1 + 2\varrho^2)}{2(1 + \varrho^2)^2} \quad (3.21)$$

where we have used that  $\delta^2 n = n$  and therefore the signal noise can be expressed as  $\delta^2 S_- = \int k^2 I^2(r)n(r)2\pi r dr$ . To fulfill  $\delta^2 N_{\text{eff}} = N_{\text{eff}}$  we need to define the effective atom number as:

$$N_{\text{eff}} = \pi w_0^2 n_0 \frac{\varrho^2(1 + 2\varrho^2)}{2(1 + \varrho^2)^2} = \frac{(1 + 2\varrho^2)}{2(1 + \varrho^2)} \frac{\pi w_0^2}{k} \Delta\phi_{\text{eff}} \quad (3.22)$$

The ratio  $\varrho = r_0/w_0$  has been determined in several independent experiments to be between  $\varrho \in [1.3 \dots 3.0]$  depending on the number of atoms loaded into the trap and the MOT cooling performance during the loading. The spatial inhomogeneity of the probe beam together with the inhomogeneous atom number distribution will play an important role in the discussion of the non-destructive characterization of coherent state evolution in sections 5.5 and 5.7.4.

### 3.4.4 Longitudinal oscillations

When the overlap of the trap with the probe region is suboptimal, longitudinal trap oscillations can be observed. We on purpose misalign of the dipole trap beam with the MOT position and the probe region. The movement of the atoms in the trap is then visible as signal oscillations due to varying atom numbers in the probe volume. The corresponding data is shown in figure 3.16. The sample has been probed in a similar fashion as described in section 3.4.1 but using 500 pulses of  $2 \mu\text{s}$  duration and 1 ms repetition period. Clear oscillations of the signal are visible and by subtracting the exponential trap decay from the data, the oscillation frequency can be determined as shown in the inset of figure 3.16. The oscillations have a period of 147 ms corresponding to 6.8 Hz. These density oscillations correspond to a longitudinal trap frequency of  $\omega_{\parallel} = 2\pi \times 3.4 \text{ Hz}$ . This is in good agreement with the values estimated in section 3.1.3. More thorough studies of the trap dynamics using non-destructive probing can be found in [2]. In 5.10.1 we use microwave spectroscopy to extract the radial trap frequency.

### 3.4.5 Direct observation of trap induced light shift on probe transition

To conclude this chapter on the experimental techniques, we use non-destructive sample measurements to determine the differential light shift on the  $F = 4 \rightarrow$

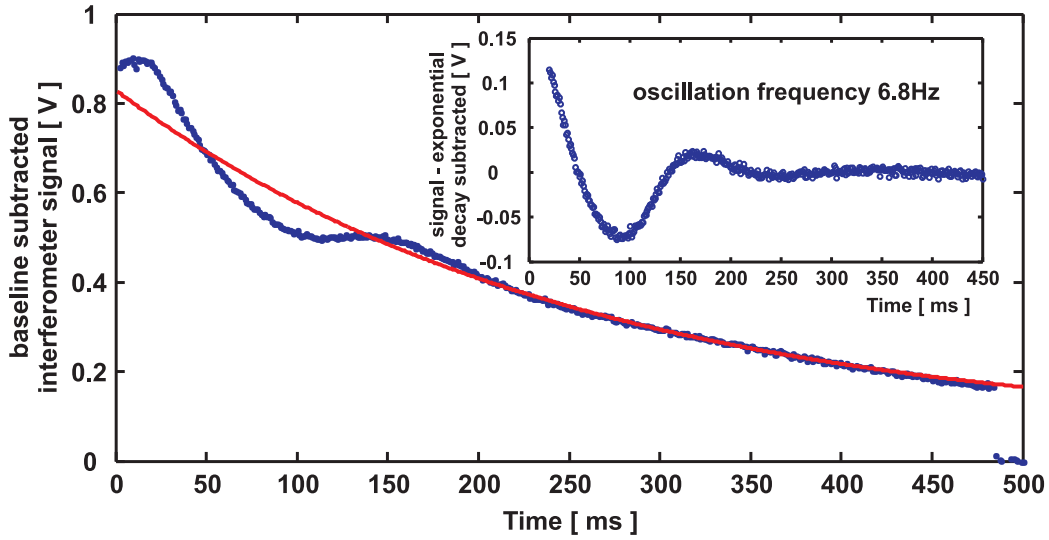


**FIGURE 3.16:** *Observation of longitudinal trap oscillations. When the trap center and trap axis are misaligned with respect to the probe beam, the motion of the atoms becomes visible. When the exponential trap decay is subtracted from the data, the oscillation frequency can be easily extracted as shown in the inset. We obtain a sloshing frequency of 6.8 Hz, corresponding to a longitudinal trap frequency of  $\omega_{\parallel} = 2\pi \times 3.4 \text{ Hz}$ . The faster damping of the oscillations compared to the trap decay time is most likely due to trap anharmonicity.*

$F' = 5$  transition due to the dipole trap beam. To that end, we load atoms into the trap, probe the sample continuously and scan the probe laser frequency across the Doppler profile while probing. We record the error signal used for laser locking (corresponding to the dispersion signal from the atoms in the vapor cell of the saturated absorption setup) together with the phase shift signal observed in the interferometer. The frequency shift between the two dispersion profiles is due to the differential light shift between the two atomic states  $F = 4$  and  $F' = 5$ . Corresponding data is shown in figure 3.17(a).

In a largely simplified discussion, we only consider the two levels coupled by the probe light. The energy shift  $\Delta E_g < 0$  of the ground level  $F = 4$  due to the dipole trap is given by equation (3.5); at the same time, the excited level  $F' = 5$  is shifted upwards in energy by the same amount  $\Delta E_e = -\Delta E_g$ . The transition frequency  $\Delta\omega_{F=4 \rightarrow F'=5}$  is therefore increased by  $\hbar\Delta\omega_{\text{lightshift}} = \Delta E = 2\Delta E_g$ . Since the energy splitting depends on the dipole trap depth, we expect the dispersion profiles to shift proportionally to the dipole trap laser power. Figure 3.17(b) shows the change in the transition frequency as function of dipole trap power, which confirms this linear power scaling. With a maximum power of  $\sim 4 \text{ W}$ , we get a frequency shift of  $\Delta\omega_{\text{lightshift}} = 2\pi \times 2 \text{ MHz/W}$ .

Since the caesium atom is (unfortunately) not a two level system, the situation is much more complicated as just described. Since the dipole trap laser couples to several excited states at the same time, the ground state energy is shifted by the other transitions as well. The energy shifts are therefore not equally distributed between the ground and the excited state. From the trap depth,  $U_0/k = 280 \mu\text{K} \hat{=} 2\pi \times 5.8 \text{ MHz}$  we know that the lower state is shifted by  $\Delta E_g = -5.8 \text{ MHz}$ ;

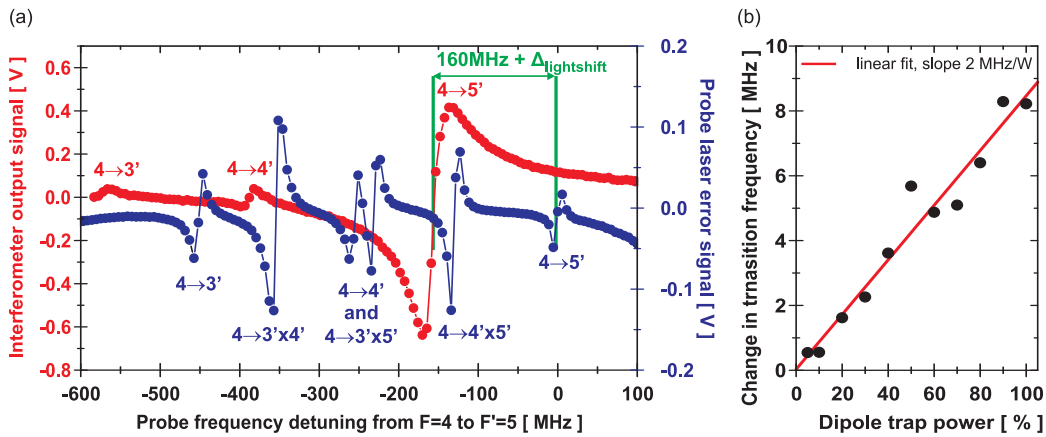


**FIGURE 3.17:** Observation of differential light shift on the probe transition caused by the dipole trap potential. (a) The dispersion profiles are shifted with respect to each other due to the light shift creating the trapping potential. In the data shown, the profiles are shifted by additional 160 MHz because of the 80 MHz pulsing AOM used in double pass. (b) By subtracting the shift from the pulsing AOM, we extract the differential light shift on the  $F = 4 \rightarrow F' = 5$  transition. As expected, the shift increases linearly with the trap power.

consequently we would claim a shift of the excited level by  $\Delta E_e = 2.2$  MHz. The shift extracted from the data, however, is an average light shift value, which also takes the spatial inhomogeneity of both the probe and the sample into account, while the trap depth only gives the maximum shift. To complicate the situation even more, we note that the probe laser itself causes a differential light shift – this will be discussed and investigated thoroughly in section 5.5 and 5.7.4. In any case, the discussion shows that there are many interesting effects to investigate in our system!

With these first sets of experimental data we conclude the chapter on basic experimental principles and take a closer look at the differential detector used in the setup. The following section is only partly necessary to follow the later experimental chapters. We return to the actual interferometer setup in chapter 5.



---

# Differential, integrating photo detector

In the previous chapter we have discussed the basic principle of our measurement setup and applied it to extract properties for the dipole trapped sample. It is obvious that for the light–atom interaction to be as non–destructive as possible for a given probe detuning, the photon number per pulse has to be reduced as far as possible. When reducing the number of photons, a natural lower limit is set by the intrinsic electronic noise of the detector. The electronics noise level of the detector used in [15], made the usage of pulses with photon numbers below  $n = 10^6$  infeasible. Since also the progress in the neighboring BEC lab [49] made low electronics noise detectors necessary, this was taken as a welcome motivation to develop a new generation of ultra low noise, differential, integrating ac photo detectors. This chapter is a summary of the work, which was mainly done together with Jörg Helge Müller. The circuit layout follows in part the basic principle as the previous version [1, 2] which was adapted from the design of [52]. We have constructed several detectors, based on two different sets of electronic components, referred to as the Amptek and the Cremat versions. With these detectors we obtain an equivalent noise charge (ENC) of  $ENC \sim 300$ , which reduces the shot noise limited photon number level to  $n_{3dB} \sim 10^5$ . The main purpose of the chapter is to summarize the development process and make the results and considerations accessible for future reference. Parts of the chapter are also summarized in [6]. Due to the nature of the subject, some sections are rather technical but the importance of the results justify a discussion.

The chapter starts out by describing the working principle of integrating detectors and the technical realization of the two different approaches. The noise analysis for continuous light beams and pulses of light is discussed and the results compared for consistency. To compensate for technical imperfections, optimization procedures in the analysis are presented and finally the different technical realizations are compared.

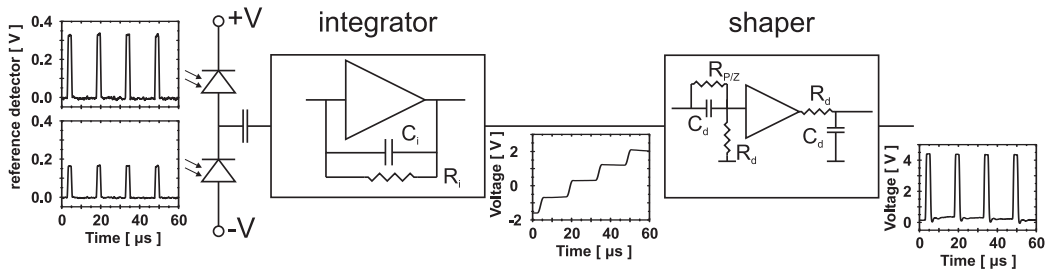


**FIGURE 4.1:** Schematic block diagram of the detector circuit. The difference signal of two reversely biased photodiodes is ac coupled into a charge sensitive amplifier (integrator) with time constant  $\tau = R_i C_i$ . From the integrated signal, Gaussian pulses are formed at the output by passing the integrated signal through a high pass filter followed by a low pass. A pole-zero cancellation resistor  $R_{P/Z}$  helps to return zero output signal during the decay time of the integrator.

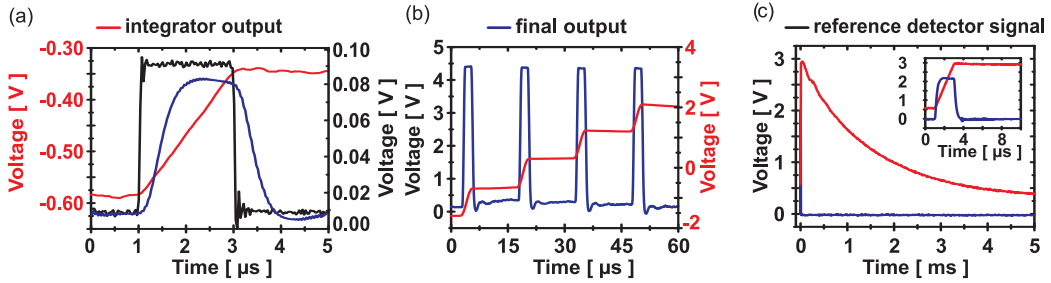


**FIGURE 4.2:** Detector response to an imbalanced input signal. (a) The integrated signal rises linearly during the pulse. The shaping stage transfers the linear slope into a gaussian pulse whose integral is proportional to the signal imbalance. (b) Several pulses are applied to the detector on a timescale short to the decay time of the integrator. Each integration step is transferred into a Gaussian pulse and the baseline after each pulse returns to zero due to the properly adjusted pole zero cancelation. (c) After a single, strong imbalanced pulse, the integrator output decays to its initial value with a time constant of  $\tau = 1.46$  ms. The output of the detector is zero during that time.

## 4.1 Principle of operation

Before the circuits of the two detector types are discussed more specifically, let us consider the reduced block diagram shown in figure 4.1 to grasp the operation principle. The difference signal from two photodiodes is obtained by connecting them in series and sensing the differential photo charge between the diodes. To reduce the capacitance of the diodes and thereby decrease their response time, they are reversely biased. The differential charge is ac coupled into an integrator stage with time constant  $\tau = R_i C_i$ , where  $R_i$  is the feedback discharge resistor and  $C_i$  is the feedback capacitor of the operational amplifier used as integrator. Since the integrator basically converts an input charge into a voltage, this type of setup is often also referred to as charge sensitive amplifier. For an input signal change faster than  $\tau$ , the capacitance of  $C_i$  determines the charge to voltage conversion factor, thus the gain of the first stage. The response of the integrator to an imbalanced signal is shown as insets in figure 4.1; for better reference, the signals at different stages in the detector are shown in figure 4.2 on various timescales and for different input

pulse configurations. After a response time of  $\sim 5$  ns, the signal at the integrator output rises linearly with a slope of  $\frac{dQ}{C_i dt}$  as long as the pulse duration is much smaller than  $\tau$ , figure 4.2(a). After such a pulse, the signal decays exponentially with time constant  $\tau$  to its initial value (compare figure 4.2(c)). The integrated signal is fed into an high pass filter (C–R combination) with rise time  $\tau_2 = R_d C_d$ , followed by a low pass filter (R–C combination) with same time constant. The combination can also be viewed as an active differentiator with a low pass filter at the output. For a duration of the initial pulse much smaller than  $\tau_2$  and  $\tau_2 \ll \tau$ , the integrator output can be approximated by a step function  $V(t) = V_0 \Theta(t)$ . Here  $\Theta$  is the Heaviside theta function  $\Theta(x) = \begin{cases} 1 & \text{for } x > 0 \\ 0 & \text{for } x \leq 0 \end{cases}$  and  $V_0$  the voltage level after the pulse. Let us look at the transfer function of the composite system to see what the different stages do. The transfer function is defined as the Laplace transform of the output voltage  $V(t)$ :

$$H(s) = \int_0^{\infty} V(t) e^{st}, \quad s \text{ complex} \quad (4.1)$$

If we for a moment neglect the influence of the discharge resistor  $R_i$  in the integrator stage, the transfer function of the integrator is  $H_{\text{step}} = V_0/s$ . For the high pass one finds:

$$H(s)_{\text{highpass}} = \frac{\tau_2 s}{1 + s\tau_2} \quad (4.2)$$

and for the low pass:

$$H(s)_{\text{lowpass}} = \frac{1}{1 + s\tau_2} \quad (4.3)$$

After the inverse Laplace transform of the product of the three systems:

$$H_{\text{combined}}(s) = \frac{V_0}{s} \frac{\tau_2 s}{1 + s\tau_2} \frac{1}{1 + s\tau_2} \quad (4.4)$$

we arrive at:

$$V_{\text{out}} = V_0 \frac{t e^{-t/\tau_2}}{\tau_2} \quad (4.5)$$

The theoretical response of the single systems and the combined filter is shown in figure 4.3(a). For a step function like input (a delta pulse at the integrator's input) the filter combination thus produces a pulse which can crudely be approximated by a Gaussian with a "standard deviation" of  $\tau_2$ . The FWHM of such a pulse is then  $2\sqrt{2 \ln 2} \tau_2 = 2.4 \tau_2$ , where  $\tau_2$  is then also referred to as the shaping time. Filter combinations of that kind are often called Gaussian shaping amplifiers. The type presented here is one of the most simple circuits.

As mentioned, after a pulse the output of the integrator decays to its initial value with time constant  $\tau$ . Taking this into account, the transfer function of the integrator stage reads:

$$H_{\text{int}}(s) = V_0 \frac{s\tau}{1 + s\tau} \quad (4.6)$$

Now, the output of the shaper does not return to zero but undershoots on a timescale of  $\tau$  (compare figure 4.3(b)). This is due to the pole of the transfer function created by the  $R_i C_i$  combination at  $\tau s = -1 \Leftrightarrow |s| = 1/R_i C_i$ . By adding

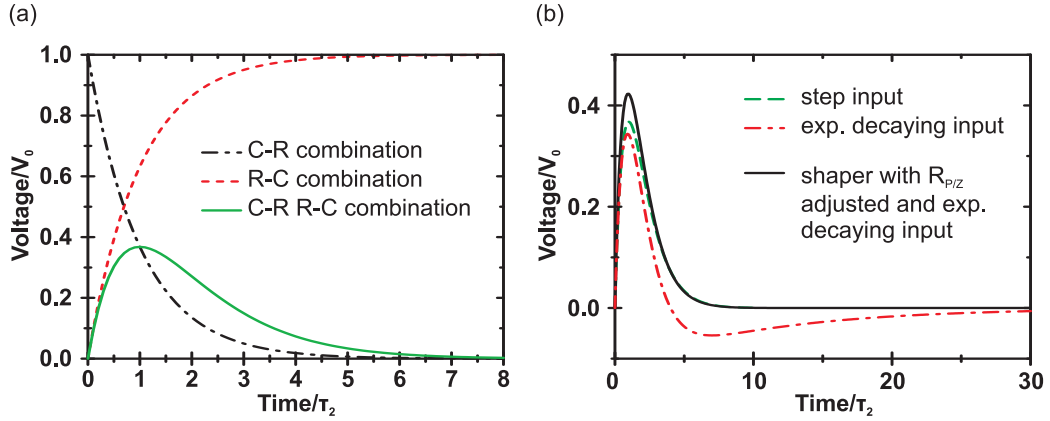


**FIGURE 4.3:** (a) Temporal shape of output response of an high pass filter (C–R combination), a low pass (R–C combination) and the composite system to a step like input. Both filters have the same time constant  $\tau_2$ . The output resembles a pulse with Gaussian shape and a duration of  $2.4\tau_2$ . (b) Taking the exponential decay of the integrator output into account, the shaped pulse undershoots compared to the pulse created from a step like input. With appropriate choice of an pole–zero cancellation resistor, the undershooting can be compensated. For the plot  $\tau = 10\tau_2$  has been chosen.

a zero in the transfer function of the high pass, this pole of the integrator can be compensated. With a resistor  $R_{P/Z}$  added in parallel to the differentiator’s input capacitor  $C_d$ , the transfer function of the high pass reads:

$$H_{\text{combined}}(s) = V_0 \frac{\tau_2(R_{P/Z}C_d s + 1)}{\tau_2 + R_{P/Z}C_d + R_{P/Z}C_d \tau_2 s}. \quad (4.7)$$

Adjusting  $R_{P/Z}$  such that  $R_{P/Z}C_d = \tau = R_i C_i$  the transfer function of the whole circuit reduces to:

$$H_{P/Z}(s) = V_0 \frac{\tau'}{1 + s\tau'} \frac{1}{1 + s\tau_2}, \quad \tau' = \frac{\tau\tau_2}{\tau + \tau_2} \quad (4.8)$$

thus the pole is canceled and we arrive at a transfer function similar to the one given in equation 4.4 with slightly different durations. Since  $\tau_2$  is also the time constant for the low pass, by changing the time constant of the low pass to  $\tau'$  a symmetric configuration can be obtained. With correctly adjusted pole–zero cancellation resistor, the differentiator (ideally) returns zero signal during the discharge time of the integrator, i.e., the detector output for a imbalanced signal is a pulse with Gaussian shape and with the same baseline regardless of the previous history of the input signal (compare figure 4.3(b)). Imperfect pole–zero cancellation will result in pulling (or pushing) of the output signal baseline as indicated in the figure.

The basic principle of first integrating and then deriving the difference signal is chosen to obtain a very low electronics noise output level. A direct amplification of the difference signal with constant gain over the total bandwidth of the detector would require an operational amplifier with unrealistically high gain–bandwidth product to achieve the necessary gain in a single stage. Cascading amplifiers of lower gain introduces the so–called Johnson noise of the 1st stage feedback resistor which soon becomes larger than the signal of interest.

Based on the basic principle discussed, we now consider the circuit layouts of the two detector types which have been built, one based on Amptek [53] amplifiers and one based on Cremat [54] modules. The two approaches are compared in table 4.1.

	AMPTEK	Cremat
integrator	A250, external FET and feedback, time constants user defined	CR 110, hybrid, time constant fixed
decay constant	$\tau=1.5$ ms	$\tau=140$ $\mu$ s
buffering	gains of shaper adjusted for optimal dynamical range	buffer between amplifier and shaper to optimize dynamical range
shaper	$2 \times$ A275, 3 pole, $\tau_2=330$ ns user defined shaping times and external feedback networks	CR-200, hybrid, $\tau_2 = 250$ ns, commercial package, modules with different predefined time constants available
$n_{\text{photon,3dB}}$	$0.8 \cdot 10^5$	$1.2 \cdot 10^5$
ENC	280 $e^-$ in 1 $\mu$ s	340 $e^-$ in 1 $\mu$ s

TABLE 4.1: Comparison of the two detector versions.

#### 4.1.1 Detector layout based on Amptek amplifiers

The circuit layout of the detector based on an Amptek A250 charge sensitive amplifier and Amptek A275 shaping modules, following closely the general designs used in [1, 2, 52] can be found in appendix C.2. Some differences compared to the basic principle discussed above are worth mentioning:

The Amptek A250 amplifier, which is basically an operational amplifier optimized for being used as a charge sensitive amplifier, requires an external field-effect-transistor (FET) to complete its input stage. This has the advantage that it can be chosen to meet the capacitance of the photodiodes. On the other hand, the main external noise source is actually the (very high) impedance input stage, therefore close attention has to be paid to the circuit board layout at that stage. To achieve a high transimpedance gain, the feedback network of the integrator requires rather inconvenient values. We chose a capacitance of  $C_i = 0.3$  pF which is very close to the stray capacitance of two standard SMD soldering pads and the resistance of  $R_i = 5$  G $\Omega$  to achieve decay constants in the milliseconds range can easily be corrupted, e.g., by the flux used while soldering. With the values given here, the theoretical decay constant of the integrator is 1.5 ms. The signals at different detector stages shown in figure 4.2 were actually recorded for this detector version. The data presented in figure 4.2(c) returns a decay time constant of  $\tau = 1.46$  ms confirming the theoretically expected value. An influence of stray capacitances or creep currents reducing the resistor size is thus not observable. A second detector with lower transimpedance gain using an equivalent layout but with  $R_i = 300$  M $\Omega$  and  $C_i = 1$  pF has been built as well. With lower gain at the input stage, the

detector can cope with stronger single pulse imbalances since the integrator does only saturate for a larger integrated charge.

Another difference compared to the layout suggested by the general principle is a third stage of the detector which makes the simple two pole Gaussian shaper stage with pole–zero cancelation into a three pole shaping amplifier with pole–zero cancelation. The third pole arises from the complex resistance of an inductor placed in series with the input resistor of the low pass. The third stage is mainly used to add additional gain at the output which helps to use a larger span of the dynamical range of the amplifiers for the input signals expected. The additional pole of the shaper is placed such as to make the step response of the filter more symmetric, i.e. Gaussian, it therefore also changes the peaking time of the detector. For the three pole filter, the shaping time is set to 330 ns, leading to a FWHM of the output pulse of 790 ns.

#### 4.1.2 Detector based on CREMAT modules

Cremat offers a self contained charge sensitive preamplifier unit CR-110 which contains both the input FET and the feedback network. Further, shaping modules CR-200 with predefined shaping times are available which only require an external resistor network for pole–zero cancelation. We have only used the 250 ns shaping time modules, but the designed circuit also works with the other modules available. In general, the Cremat modules are easier to handle than the Amptek amplifiers although at the expense of flexibility, e.g., the user has no access to the gain of the charge sensitive preamplifier. The circuit layout for this version, also shown in appendix C.2, is thus much simpler than for the Amptek design. To open the possibility to add additional gain in the detector, an ac coupled buffer stage has been added between the preamplifier and the shaper. Adding gain at this stage of the detector helps to use the full dynamic range of the shaper when knowing the range of input signals expected. This is not equivalent to being able to change the gain of the integrator. The size of  $C_i$  determines the total charge the integrator can take before it saturates. In the Cremat CR-110, this is fixed to  $2.6 \times 10^7$  electrons; a single pulse photocharge imbalance of more than this amount can thus not be detected properly. Since it takes the integrator output of the CR-110  $\tau = 140 \mu\text{s}$  to decay, this also limits the total amount of photon imbalance on this time scale. Another drawback of the Cremat modules is that the output stage of the shaping amplifier only delivers up to 10 mA and is therefore not able to drive its full output swing on a  $50 \Omega$  terminated cable. This has to be taken into account when using these modules.

#### 4.1.3 Detector test setup

To test the performance of the detectors we use the setup shown in figure 4.4. A light beam derived from an external grating stabilized, frequency locked diode laser, pulsed with a standard acousto–optical modulator, is coupled into an optical fiber. At the output of the fiber the polarization is stabilized with a polarizing beam splitter. To monitor the power of the pulses, a large fraction of the beam is

directed onto a fast photo detector. The rest of the beam is split into two parts on a polarizing beam splitter and each beam is focussed onto one photo diode of the differential detector. To calibrate the powers and to automate the data taking procedure, the power of the input beam is controlled with the computer interface which also controls the storage oscilloscope. The oscilloscope is usually

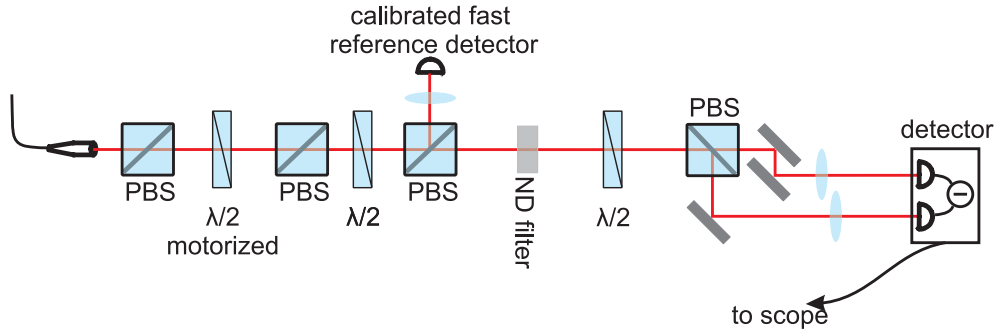


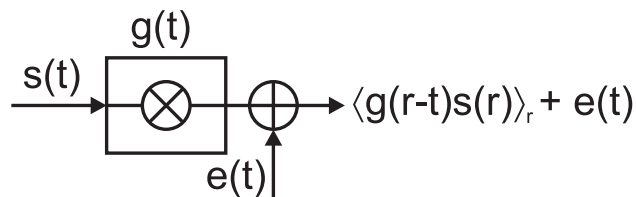
**FIGURE 4.4:** *Test setup. The light beam derived from a grating stabilized diode laser arrives at the output of an optical fiber. A large fraction of the power is diverted into a fast, calibrated reference detector and the rest of the beam is further attenuated, split into two parts and focussed onto the two photodiodes. The output is directly digitized on a storage oscilloscope and saved to a hard drive for postprocessing.*

run in segmented mode, where several trigger events with time separations much larger than the on screen display duration are combined into one file. This helps to reduce the disk space required when separating single pulses by much more than their duration.

## 4.2 DC operation and noise measurements

Although the detector is specifically designed for pulsed input light operation, information about the expected noise performance can be obtained with continuous light beams and observing the detector output on a spectrum analyzer. A spectrum analyzer can be used to display the spectral noise power density  $\Omega(\omega)$ , which is defined as the Fourier transform of the autocorrelation function  $\Omega(r) = \langle o(t)o(t+r) \rangle_t$  of a time dependent signal  $o(t)$  [55].

Let us consider the detector as a black box with gain function  $g(t)$  with an additional noise process  $e(t)$  at the output, and an independent noise process at the input – the signal noise  $s(t)$ .



The whole noise of the blank detector circuit with no input is merged into  $e(t)$ . Different from the usual practice in electronics, the amplifier noise is here the

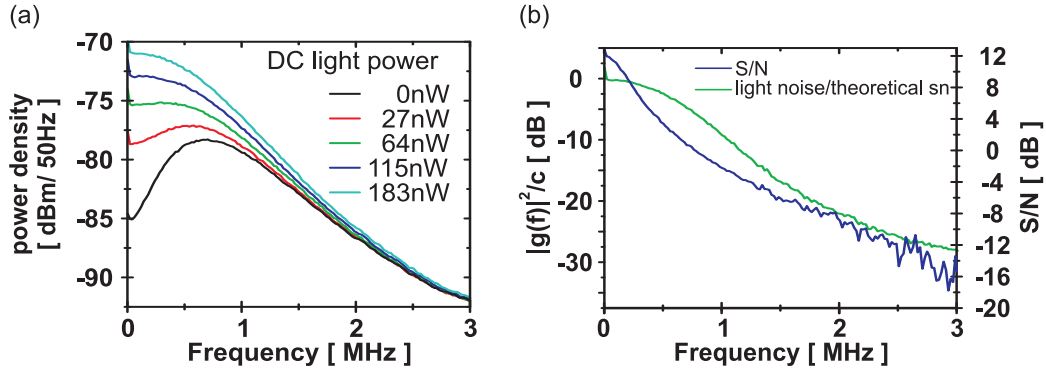


**FIGURE 4.5:** (a) Spectral noise power density of the Amptek detector for different input light levels. (b) Gain function and signal-to-noise ratio, where the signal is the input light noise. To obtain the gain, the electronics noise level is subtracted from the noise power densities and normalized to the (theoretical) shot noise of light. The latter is calculated by assuming that the input light is in a coherent state and therefore its noise power density is independent of the frequency. For a known input light level, the white shot noise can be divided out. For the data the DC spectrum of 115 nW has been used.

output reference noise, which is directly accessible to measurement and the relevant quantity in a practical assessment of the detector performance. The gain function only acts on the signal input and the result is a convolution of the gain function with the signal. Therefore, the output signal  $o(t)$  can then be written as:

$$o(t) = \langle g(r-t)s(r) \rangle_r + e(t). \quad (4.9)$$

If  $s(t)$  and  $e(t)$  are described as wide-sense stationary noise processes (instead of known functions in time) the Wiener-Khinchin-theorem (see appendix C.1), relates the spectral noise power density  $\Omega(\omega)$  to the square of the Fourier components  $o(\omega)$  of the original signal  $o(t)$ :

$$\Omega(\omega) = \frac{1}{2\pi} \int_{-\infty}^{\infty} \langle o(t)o(t+s) \rangle e^{-i\omega s} ds \quad (4.10)$$

$$= \left\langle \left| \frac{1}{2\pi} \int_{-\infty}^{\infty} o(t)e^{-i\omega t} dt \right|^2 \right\rangle \quad (4.11)$$

$$= \langle |o(\omega)|^2 \rangle \quad (4.12)$$

Since the two noise processes  $s(t)$  and  $e(t)$  are independent, the spectral noise power density of the output signal becomes

$$\Omega(\omega) = |g(\omega)|^2 |s(\omega)|^2 + |e(\omega)|^2 \quad (4.13)$$

where  $g(\omega)$  is the spectral response of the detector. Here we have invoked Parseval's theorem to write the Fourier transform of the convolution of the gain function with the input random variable as a product of the Fourier components.

The noise power density for the Amptek detector is shown in figure 4.5(a) for different dc input light levels. When we assume that the input light is a coherent state and the detector is fully balanced (thus classical input light level fluctuations

cancel out), the input noise is only shot noise of light. The spectrum of shot noise is white, the noise power density of the input signal  $|s(\omega)|^2$  is thus a constant  $s_0^2$  and proportional to the photon number in the inverse bandwidth of the detection. The intrinsic noise level of the detector – the electronics noise level – can be determined by recording the noise power density at the output with no input signal. By subtracting this level from the spectrum and normalizing the spectrum to the constant input noise level, we can extract the gain function:

$$|g(\omega)|^2 = \frac{\Omega(\omega) - |e(\omega)|^2}{s_0^2} \quad (4.14)$$

From the corresponding graph in figure 4.5(b), we extract that the gain drops by 3 dB within  $\sim 600$  kHz. This corresponds well to the total inverse pulse duration we shall encounter further down. By normalizing the spectral noise power density for a given input power to the electronics noise level, the signal-to-noise (S/N) ratio can be extracted as a function of frequency, where the signal is actually the light noise.

The transformation from the frequency domain into the pulsed regime would in principle require to compute the convolution of an input pulse  $p(t)$  with the total signal  $o(t)$ . This becomes straight forward in the frequency domain of the signals where total noise becomes an integral over the power spectra of the product of the pulse  $|p(\omega)|^2$  and the signal  $\Omega(\omega)$ :

$$\begin{aligned} \text{noise} &= \text{light noise} + \text{electronics noise} \\ &= \int_0^\infty \Omega(\omega) |p(\omega)|^2 d\omega \\ &= \int_0^\infty |g(\omega)|^2 |s(\omega)|^2 |p(\omega)|^2 d\omega + \int_0^\infty |e(\omega)|^2 |p(\omega)|^2 d\omega. \end{aligned} \quad (4.15)$$

This basically corresponds to frequency band filtering of the signal with the power spectrum of the pulse. For a single square (boxcar) pulse  $p_{\text{bc},\sigma}(t)$  with duration  $\sigma$ :

$$p_{\text{bc},\sigma}(t) = \frac{\Theta(t + \sigma/2) - \Theta(t - \sigma/2)}{\sigma}, \quad (4.16)$$

where  $\Theta(t)$  is again the Heaviside theta function, the power spectrum is:

$$|p_{\text{bc},\sigma}(\omega)|^2 = \left( \frac{\sin(\omega\sigma/2)}{\omega\sigma/2} \right)^2 \quad (4.17)$$

Both the temporal shape and the spectrum of the pulse are illustrated in figure 4.6. From measurements with the spectrum analyzer we can thus predict the noise scaling expected when using real pulses. In figure 4.7 the noise scaling with input light power is shown for different durations  $\sigma$  of the virtual pulse  $p_{\text{bc},\sigma}(t)$ , i.e., equation (4.15) has been evaluated for the power spectra in equation (4.17) for various  $\sigma$  parameters. At zero input power the electronics noise level can be extracted. The linear scaling with light power confirms the light shot noise nature of the observed extra signal noise. As we shall discuss in more detail further down, the performance of the detector is characterized by the light power level, where the light noise is equal to the bare electronics noise level – the 3 dB level.

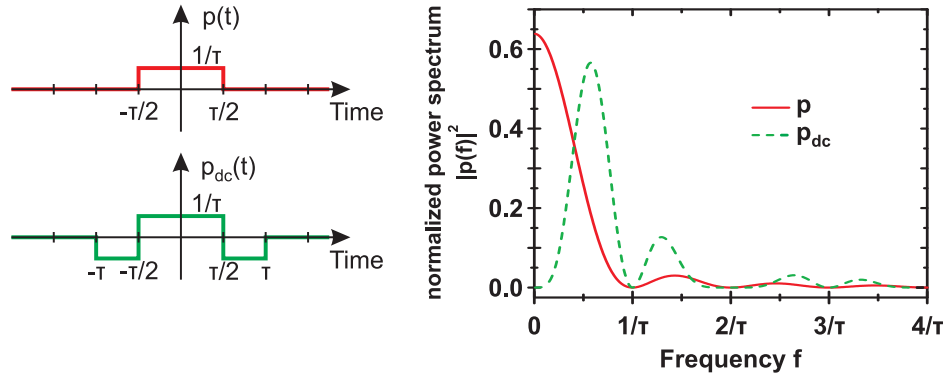


**FIGURE 4.6:** Integration pulse shapes  $p_{bc,\sigma}(t)$  and  $p_{dcs,\sigma}(t)$  and their power spectra  $|p_{bc,\sigma}(\omega/2\pi)|^2$  and  $|p_{dcs,\sigma}(\omega/2\pi)|^2$ . The integrated power spectra have been normalized to unity on the interval  $[0, \infty]$ .

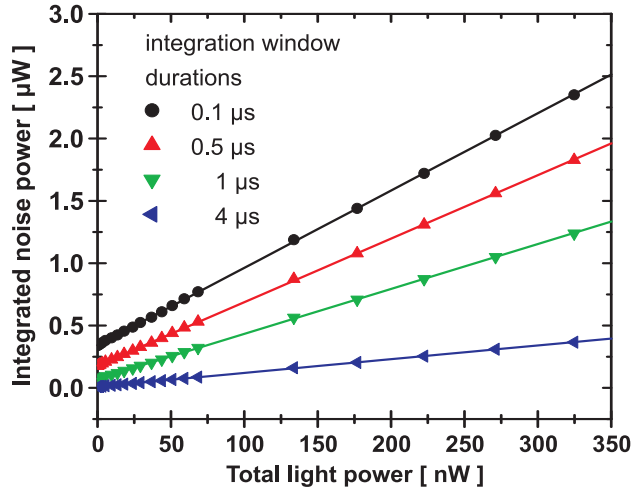


**FIGURE 4.7:** Integrated noise powers for different integration window durations (power spectra). The noise power densities similar to the ones shown in figure 4.5(a) have multiplied with the pulse spectrum  $p(\omega)$  shown in figure 4.6(b) for different durations  $\tau$  and integrated over. For zero input light powers we get the electronics noise levels. The linear scaling of the curves confirms the shot noise character of the signal noise.

From the spectrum of the square pulse (4.17) it is clear that especially low frequency components in the signal, as created e.g., by imperfect pole-zero cancelation which causes correlations in the signal over long timescales  $\sim \tau$ , contribute significantly to the noise. To circumvent this problem, we can change form the single square pulse  $p_{bc,\sigma}(t)$  to a window function:

$$p_{dcs,\sigma}(t) = \frac{\Theta(t + \sigma/2) - \Theta(t - \sigma/2)}{\sigma/2} - \frac{\Theta(t + \sigma) - \Theta(t - \sigma)}{\sigma} \quad (4.18)$$

The resulting power spectrum:

$$|p_{dcs,\sigma}(\omega)|^2 = 4 \left( \frac{\sin(\omega\sigma/2)}{\omega\sigma/2} - \frac{\sin(\omega\sigma)}{\omega\sigma} \right)^2 \quad (4.19)$$

has no contribution at  $\omega = 0$ . The pulse shape  $p_{dcs,\sigma}(t)$  and its power spectra is also illustrated in figure 4.6. Using the integration function  $p_{dcs,\sigma}(t)$  thus reduces the

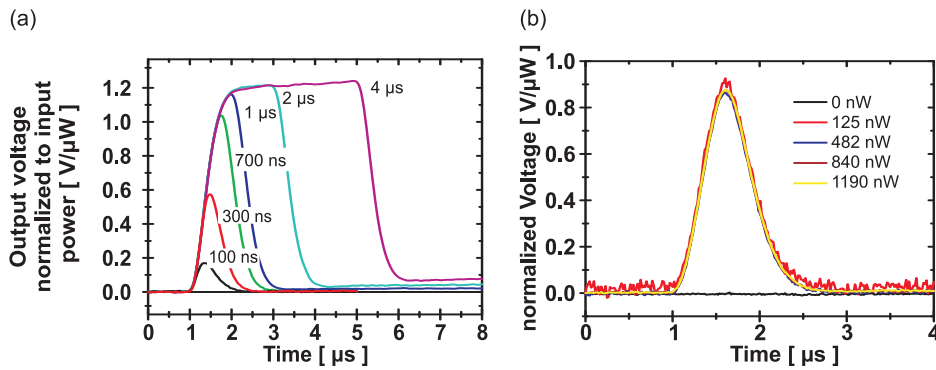


**FIGURE 4.8:** (a) Electronic response of the detector to input pulses of different durations. For input light pulse durations comparable or longer than the shaping time, the output pulse duration the input pulse duration, extended by the shaping time. (b) Normalizing the output signals for a fixed input pulse duration of 500 ns to the corresponding input signal strength, the linearity of the detector response is verified.

influence of low frequency noise contributions and allows one to cancel the effect of baseline pulling. Generally, the integration with a certain gating function  $p(t)$  can be understood as frequency (band) pass filtering of the signal with the power spectrum of the gating function  $|p(\omega)|^2$ . Using the integration function  $p_{\text{dcs},\sigma}$  is very similar to the double-correlated sampling technique sometimes applied in CCD readout units to reduce correlated noise sources.

With these techniques at hand, we shall now go over to pulsed operation of the detector and discuss the analysis in that case. We will come back to the dc spectra discussed above and compare the results of the two analysis methods.

### 4.3 Pulsed detector operation and noise analysis

We now apply pulsed light signals to the the setup discussed in section 4.1.3. The typical durations are between 100 ns and 4  $\mu\text{s}$ . We slightly imbalance the signal by splitting the input beam asymmetrically. Figure 4.8(a) shows the detector output signal for different configurations. For input pulses shorter than the defined shaping time of the Gaussian filters, we get the pulse forms as expected from the theoretical treatment of the circuit in section 4.1. When the input pulse duration approaches the shaping time, the pulse tops start to flatten out and a constant level is reached. The resulting electronic output pulse is longer than the light input pulse by approximately the delta shaping time. In any case, the full area of the pulse is proportional to the total differential photon number of the input pulse. Linearity of the amplifiers can be confirmed by normalizing the output pulses to the input power<sup>1</sup> as shown in figure 4.8(b). Fitting a Gaussian to the output pulse we extract a FWHM of the pulse of 760 ns, which corresponds very well with the theoretical

<sup>1</sup>In general, in pulsed operation where the mean photon number per pulse is the only meaningful characterizing unit, the power is to be understood as the corresponding dc power level.

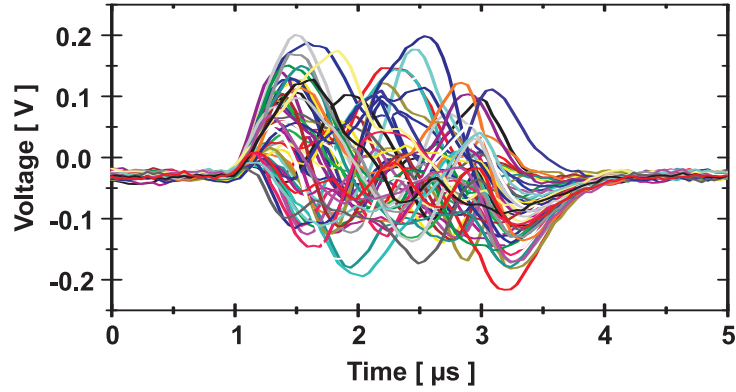


**FIGURE 4.9:** *Electronic output signal of the detector for balanced input light pulses of  $2\ \mu\text{s}$  duration. Also during the pulse, the mean value of the signal is zero but the noise is clearly increased.*

value of 790 ns. Here and in the following the data presented has been obtained with the Amptek detector version discussed in section 4.1.1 – unless otherwise noted.

### 4.3.1 Shot noise limited performance and optimization

To determine the light noise of pulses similar to a real experiment with the Mach Zehnder interferometer (see chapter 6), we use  $k$  light pulses  $p_i$  of duration  $\tau$  and repetition period  $r$ , where  $r$  is typically of the order of some  $10\ \mu\text{s}$ . As mentioned in section 2.1.1 we associate the variance of the photon numbers with the term noise. A typical detector output signal for several balanced pulses with  $2\ \mu\text{s}$  duration, plotted on top of each other, is shown in figure 4.9. One can clearly see an increase in the variance of the signal for the duration of the pulse. The electronic signal  $S(t)$  shown in the figure is read from the oscilloscope and thereafter integrated with the gating function  $p_{\text{bc},\sigma}(t)$  or  $p_{\text{dcs},\sigma}(t)$  to give the area of the pulse normalized to its duration. To take timing issues, e.g., from the response time from the pulsing device into account, we allow for a time translation  $t \rightarrow t - t_0$ . In general, both the duration of the integration window  $\sigma$  and its position in time  $t_0$  have to be optimized for each detector/experimental setup. After the integration, we are left with the pulses  $p_i$ :

$$p_i = \int_{-\infty}^{+\infty} p_{\text{bc},\sigma}(t) S(t) dt = \frac{1}{\sigma} \int_{t_0+(i-1)r}^{t_0+(i-1)r+\sigma} S(t) dt \quad (4.20)$$

of which we calculate the variance:

$$\delta^2 p \equiv \frac{1}{k} \sum_{i=1}^k \left( p_i^2 - \left( \frac{1}{k} \sum_{i=1}^k p_i \right)^2 \right) \quad (4.21)$$

to evaluate the noise of the signal. For pulses of  $1\ \mu\text{s}$  duration and 20 kHz repetition rate, the (optimized) result is shown in figure 4.10. An integration gating window  $p_{\text{bc},\sigma}(t)$  with  $\sigma = 1.5\ \mu\text{s}$  was used to obtain this result. The electronics noise level

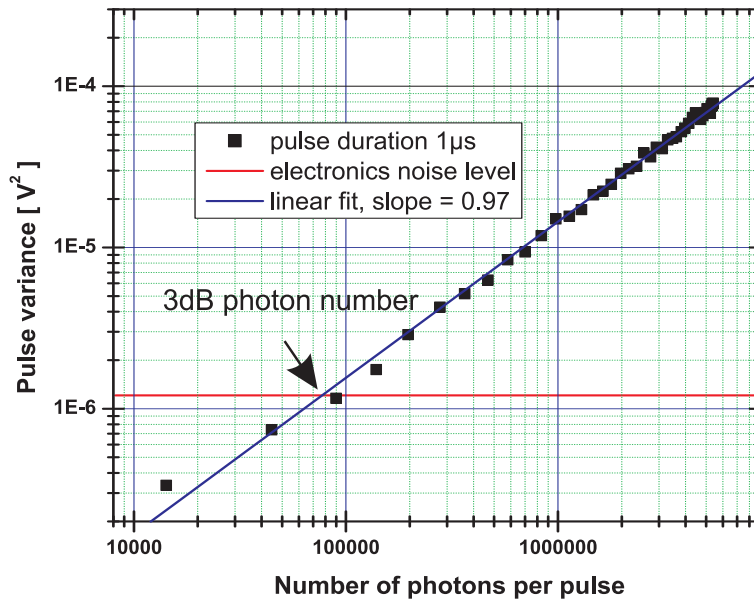


**FIGURE 4.10:** *Scaling of the output pulse variance for  $1\ \mu\text{s}$  light pulses as function of the total mean photon number per input pulse. The slope of the data in the log–log plot is 1, confirming the quantum nature of the noise. The 3 dB photon number of  $n_{3\text{dB}} = 8 \times 10^4$  photons per pulse is equivalent to a light power level of  $20\ \text{nW}$  for  $1\ \mu\text{s}$  duration of the light pulse.*

has been subtracted from the data. As mentioned above, the performance of the detectors is quantified through the electronics noise equivalent light power level (3 dB level) or noise equivalent photon number (3 dB photon number  $n_{3\text{dB}}$ ). From the data we read a photon number of  $n_{3\text{dB}} = 8 \times 10^4$ . Instead of using the variance, one often also uses the standard deviation or root-mean-square (RMS) values for characterization. The electronics noise level, which is equivalent to the 3 dB photon number then corresponds to an equivalent noise charge (ENC) of  $n_e \sim 280$ . Since the 3 dB levels set the scale from where on the detector output noise is dominated by the input light noise and no longer by the intrinsic electronics noise, we call the detector shot noise limited above this photon number or equivalent power level. Above this level, the photon number in a single pulse can be measured with an accuracy of better than  $n_e \sim 280$  photons, such that the intrinsic photon number fluctuations in a light pulse, the shot noise, becomes accessible or dominant in the signal.

The analysis of the pulses can be optimized in several ways by changing the integration gating function. It is obvious that for a given input light pulse duration, a too short integration window will lead to an increased 3 dB level since the noise power integrated over will be smaller than the one expected from the assigned photon number. For a too long integration window, the 3 dB level will also be artificially increased since the integration only picks up electronics noise power after the pulse has passed. The performance of the detector can therefore be optimized in the analysis by finding an appropriate duration  $\sigma$  of the integration window. Figure 4.11(a) shows the 3 dB levels for different integration windows, applied to a series of initial light pulse durations. For the data shown, the integration function  $p_{\text{bc},\sigma}(t)$

was used. For durations smaller than the shaping time, the expected scaling of the 3 dB level with pulse duration, i.e., the independence of the 3 dB photon number from the pulse duration can be observed. From these measurements we extract

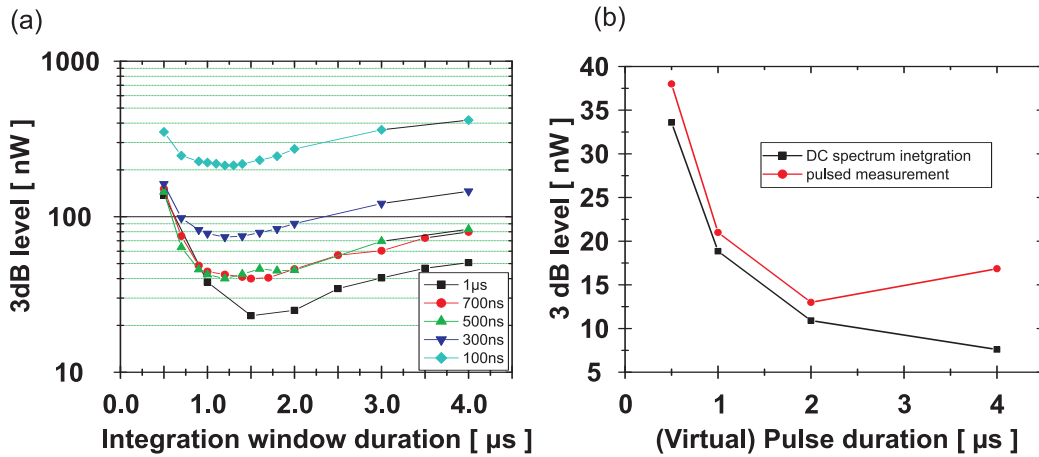


**FIGURE 4.11:** (a) Optimization of the integration window for different input light pulse durations. (b) Comparison of the 3 dB power levels for pulsed and continuous detector operation.

that for light pulses below 500 ns, an integration window of  $1.2 \mu\text{s}$  is appropriate; for longer pulses, the integration window has to be 500 ns longer than the input pulse. These 500 ns basically correspond to the shaping time of the amplifiers.

The performance when using pulse light can be compared to the analysis of the dc power spectra as demonstrated in figure 4.7. The extracted 3 dB levels for the dc and the pulsed operation mode are compared in figure 4.11(b) and a good agreement can be observed. This confirms that the spectrum analyzer measurements are reliable in determining the noise performance of our integrating detectors. This is especially important for troubleshooting during the development process, since these measurements require much less time and effort.

### 4.3.2 Baseline pulling and offset subtraction

Close examination of the pulses for durations larger than 700 ns in figure 4.8 shows that the detector baseline does not fully recover to zero just after the pulse. This is mainly due to imperfections in the pole-zero cancellation discussed in section 4.1. Especially when high photon numbers need to be detected, adjusting the cancellation resistor can be quite challenging. This is especially true for the case of the Amptek design, because the compensation resistor necessary is of similar magnitude as the input impedance of the A275 amplifier. It is generally not desirable or possible to extend the repetition period of the pulses so far that the baseline has completely reset. In this case, a later pulse will “ride” on the baseline which is pulled or pushed by the earlier pulses and its integral will obviously be correlated with the previous pulse(s). Such classical correlations result in classical noise scaling and ruin the light shot noise limited performance of the detectors. To circumvent this problem, we have already in section 4.2 introduced the double-correlated sampling

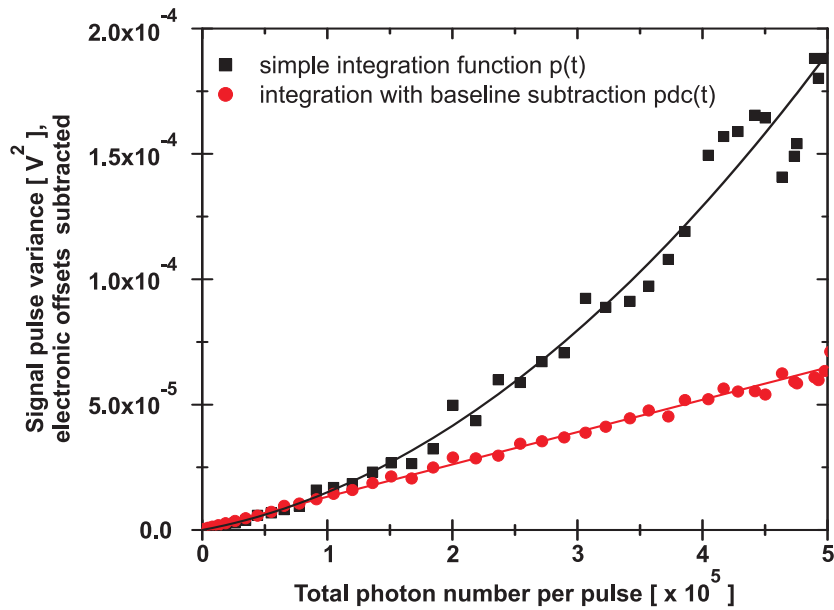


**FIGURE 4.12:** (a) Due to technical imperfections in the pole/zero cancelation of the Gaussian filter, the detector baseline piles up when the incident light pulses are not fully balanced. (b) When analyzing the signal from an imbalanced input, the variance of pulses integrated with with the simple integration gating function  $p_{bc}$  shows a clear contribution of classical – correlated noise. Using the baseline subtracting window function  $p_{dcs}$ , the linear scaling characteristic for shot noise is regained. In both data sets, the electronics noise level has been subtracted. The black curve corresponds to a  $f(x) = a \cdot x + b \cdot x^2$  fit; the linear part of the fit (grey), giving the shot noise contribution to the noise, cannot be distinguished from a fit to the data obtained with the  $p_{dcs,\sigma}(t)$  integration gating function.

integration window  $p_{dcs,\sigma}$ . As discussed, such an integration window removes the low frequency contributions of the noise spectrum and therefore reduces the effect of baseline pulling. The timescale for baseline recovery is  $\tau = R_i C_i = 1.5$  ms in the Amptek design; the effect from a previous pulse can therefore be regarded as a dc baseline level shift over the duration of a typical light pulse of  $\tau \sim \mu s$ .

Baseline subtraction is mainly necessary when not entirely balanced signals are considered or when their balancing changes over time. In figure 4.12 we compare the noise scaling with about 10% input signal imbalance for the two integration gating functions  $p(t)$  and  $p(t)_{dc}$  discussed above. When using the simple integration window  $p_{bc,\sigma}(t)$ , a clear classical noise contribution is visible. Since the classical and the quantum noise are independent, the shot noise contribution can be extracted as the linear part of a quadratic fit:  $f(x) = e + a \cdot x + b \cdot x^2$ .  $e$  is the electronics noise level which has been subtracted from the data in the figure. The shot noise part of the fit is indistinguishable from a fit through the data, when analyzed with the baseline subtracting gating function  $p_{dcs,\sigma}(t)$  – also electronics noise subtracted. Using the double correlated sampling window function thus allows one to circumvent the technical imperfection of the detectors.

Note that in general the baseline subtraction adds electronics noise through the

analysis. The integration function can be split up into:

$$\begin{aligned}
p'_i &= \int_{-\infty}^{+\infty} p_{\text{dcs},\sigma}(t)S(t)dt & (4.22) \\
&= \frac{1}{\sigma} \left( \int_{t_0+(i-1)r}^{t_0+(i-1)r+\sigma} S(t)dt \right) \\
&\quad - \frac{1}{\sigma} \left( \int_{t_0+(i-1)r-\sigma/2}^{t_0+(i-1)r} S(t)dt + \int_{t_0+(i-1)r+\sigma}^{t_0+(i-1)r+3/2\sigma} S(t)dt \right) \\
&\equiv p_i - b_i
\end{aligned}$$

Splitting the (combined) baseline pulse  $b_i$  and the light  $p_i$  up into the – below the bandwidth of the detector – uncorrelated and correlated parts:

$$p_i = p_{i,\text{uncorr.}} + p_{i,\text{corr.}} \quad (4.23)$$

$$b_i = b_{i,\text{uncorr.}} + b_{i,\text{corr.}} \quad (4.24)$$

$$\Rightarrow p'_i = p_{i,\text{uncorr.}} - b_{i,\text{uncorr.}} + p_{i,\text{corr.}} - b_{i,\text{corr.}} \quad (4.25)$$

we ideally have  $p_{i,\text{corr.}} = b_{i,\text{corr.}}$  and are left with  $p'_i = p_{i,\text{uncorr.}} - b_{i,\text{uncorr.}}$ . The variance of the baseline subtracted pulses  $p'_i$  thus contains an additional electronics noise contribution from  $b_{i,\text{uncorr.}}$ . Since baseline pulling is in general only important when high photon numbers are involved, this contribution is generally small. It should be noted that the symmetry of the integration window  $p_{\text{dcs},\sigma}$  is not a requirement, the only condition for low frequency noise suppression is a vanishing integral. The duration of the negative contribution to the integral can be changed – even to an asymmetric contribution from before and after the pulse. Under these optimized analysis conditions, the performance of the detector stays constant for all degrees of imbalance (of course only as long as the detector does not saturate). This is confirmed by the data shown in figure 4.13 where the slope of noise curves is plotted versus the degree of detector photodiode imbalance. When changing the balancing of the diodes, the slope of the noise data in a linear plot stays constant and the slope in a log–log plot is consistent with 1, indicating no classical noise contributions. Note that this shot noise limited performance for imbalanced input signals puts a limit onto the amplitude instability of the lasers used in these measurements, since in an imbalanced operation classical amplitude fluctuations do not cancel.

## 4.4 Comparison of performances

In total four different detectors have been built. Two based on the Amptek design, with the main difference being  $R_i$  and  $C_i$ . For the high gain version,  $R_i = 5 \text{ G}\Omega$  and  $C_i = 0.3 \text{ pF}$  was used and for the lower gain version  $R_i = 300 \text{ M}\Omega$  and  $C_i = 1 \text{ pF}$ . The two Cremat versions are, disregarding some small layout changes, basically equal.

The performance data of the Amptek detector has been used as an example in the previous sections already. To summarize, the 3 dB level is found at  $n_{3\text{dB}} = 8 \times 10^4$  photons per  $1 \mu\text{s}$ , which corresponds to an equivalent noise charge of  $\text{ENC} \sim 280$

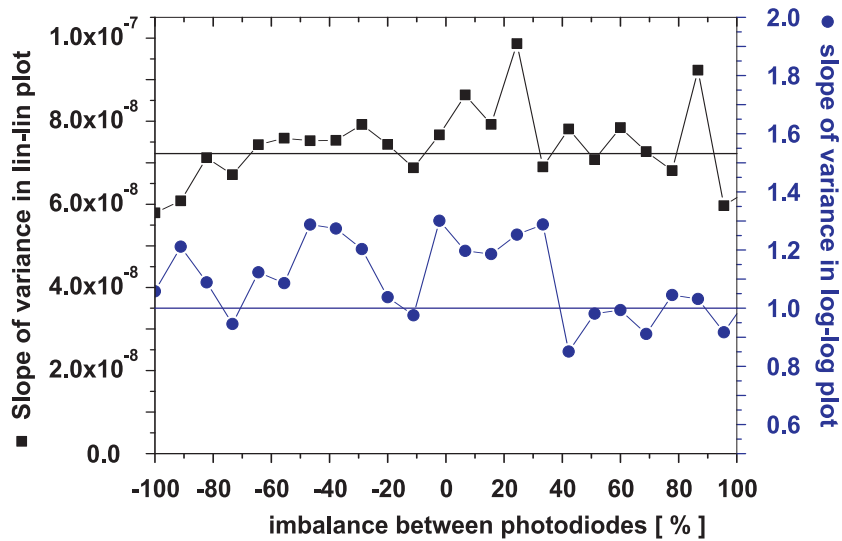


**FIGURE 4.13:** Slopes of noise curves for different detector imbalancing.  $\pm 100\%$  imbalance corresponds to all light into one diode. The slopes stay constant in the lin–lin plot and are compatible with 1 in the log–log plot, confirming that for all degrees of input pulse imbalance, the observed noise is due to shot noise of light.

electrons in a single detection event. This figure holds as long as the input pulse duration is shorter than the shaping time time of  $0.8 \mu\text{s}$ . For longer pulses the 3 dB level rises linearly. Using the double correlated sampling integration window, the 3 dB level rises by a factor of two. This performance is significantly better than the one reported in [1, 2], where a 3 dB level of  $4 \times 10^6$  photons per  $1 \mu\text{s}$  was measured, corresponding to  $\text{ENC}=2000$  electrons RMS and still better by more than a factor of two with respect to the numbers of  $\text{ENC}=780$  RMS electrons reported in [52].

For the two Cremat detector versions, we consistently measure a 3 dB photon number of  $n_{3\text{dB}} = 1.2 \times 10^5$  photons, corresponding to an RMS electronic noise of  $\text{ENC}=340$  electrons [56]. This can be compared with the numbers obtained from the theoretical formula given in the data sheet of the CR-110 [54]. According to the formula the RMS electron number or equivalent noise charge is:

$$\text{ENC} = \sqrt{\frac{43(C_{\text{detector}} + 15)^2}{\sigma_2} + 8\sigma_2(I_{\text{detector}}) + 50000} = 360 \quad (4.26)$$

where  $C_{\text{detector}}$  is the capacitance of the photodiodes in pF,  $\tau_2$  the shaping time in  $\mu\text{s}$  and  $I_{\text{detector}}$  the leak current of the detector in pA. For the Hamamatsu S3883 [57] photodiodes used,  $C_{\text{detector}} = 12$  pF (two diodes, each 6 pF), and  $I_{\text{detector}} \approx 100$  pA;  $\tau_2 = 250$  ns for the shaper used in the setup. The actual detector thus performs at the factory limit of the modules. Note that from the formula one observes that the dark current of the diodes actually plays little role in the choice of the photodiodes, very much to the contrary of what has been claimed in [1, 2]. The choice in favor of the Hamamatsu S3883 is rather motivated by the high quantum efficiency  $\eta_{850\text{nm}} \approx 0.9$  and the conveniently low capacitance for the size of the active area.

As mentioned, the above work was (actually mainly) motivated by the detector

requirements for the BEC lab. The best detector, the first Amptek version was therefore implemented in the BEC experiment [49]. In the experiments presented in the following, one of the Cremat detectors was used. The second Cremat detector was given to a friendly group at the Institut de Ciències Fotòniques in Barcelona. With this detector we can reduce the photon number to  $n_{3\text{dB}} = 1.2 \times 10^5$  without being limited by intrinsic detector noise. This is an enormous improvement compared to the previous detector used and made many of the observations and experiments presented in the next chapter possible.

---

## Microwave spectroscopy

At the end of chapter 3 we have discussed measurements on the dipole trapped ensemble of cold atoms with our interferometric setup. In that case, the atomic population was distributed incoherently across all  $F = 4, m_F \in [-4 \dots 4]$  magnetic substates. The initialization into those levels was achieved by pumping all atoms out of the  $F = 3, m_F \in [-3 \dots 3]$  states. We shall now reduce the number of occupied atomic states to two levels, the so-called clock states.

The magnetic dipole transition between the  $6S_{1/2}(F = 3, m_F = 0) \leftrightarrow 6S_{1/2}(F = 4, m_F = 0)$  magnetic hyperfine states of the caesium-133 isotope is the so called clock transition. Its frequency has been defined to be  $\omega_0 = 2\pi \cdot 9,192,631,770$  Hz and microwave spectroscopy of the transition is used as the prime standard of time. The line width of the transition is so small that the lifetime of the states in an experimental setup is rather limited by technical imperfections than by the natural lifetime. To address the transition and change the probability distribution for the atoms to be in the two clock states, electro-magnetic radiation with angular frequency  $\omega \approx \omega_0$  can be used. Towards the ultimate goal of demonstrating squeezing of the clock state population number uncertainty, we have to be able to:

- create a pure ensemble of atoms, initialized in one of the clock levels
- coherently control the populations in the clock states
- perform non-destructive measurements on the quantum state of the ensemble
- characterize and understand the effects of the probe pulses on the quantum state

Before discussing the experimental techniques to prepare a dipole trapped ensemble of Cs atoms in the clock states and coherently manipulate the ensemble state with microwave radiation, the basic theoretical framework of microwave spectroscopy is presented. With these techniques at hand, we will use the Mach-Zehnder interferometer to non-destructively read out the populations of the clock states when they are subjected to external microwave fields. Using Rabi, Ramsey and spin-echo spectroscopy tools, the non-destructive light-matter interface will be characterized

with special focus on the effect of probe induced clock level perturbations (light shifts) and spontaneous scattering of probe light. Finally, the induced level perturbations are used to obtain information about the atomic motion inside the trapping potential. Parts of this chapter have been published as [4, 5, 7].

## 5.1 Light–atom coupling applied to the clock transition

In sections 2.3 and 3.1.3 we have discussed the interaction between atoms and an electromagnetic radiation field. While in the first case, the effect on the electromagnetic field was in the focus of the discussion, and in the second case the change of the energy level structure of the atoms, we shall now consider the effect on the probability distribution among the states involved. Here we will explicitly not adiabatically eliminate the excited state population. Since the two states are basically stable, a decay rate does not have to be included in the description. Among the first to study the two–level problem in this setting were Rabi [58] and Bloch [59]. We will encounter both names frequently in the next sections.

### 5.1.1 Theoretical background

Since many standard text books describe the problem in a more coherent and complete way than possible here, only the most important corner stones of the derivation are presented. The treatment is inspired by Allen and Eberly [60]. A very comprehensive treatment can also be found in [61].

From the start we reduce the treatment of the Cs atom to a two level system, the two energy eigenstates  $6S_{1/2}(F = 3, m_F = 0) \equiv |3\rangle$  and  $6S_{1/2}(F = 4, m_F = 0) \equiv |4\rangle$  of the Cs atom with an energy difference of  $\hbar\omega_0$ . When choosing the energy zero to be in the center between the two levels, the Hamiltonian  $\hat{H}_A$  of the free atomic system reads:

$$\hat{H}_A = \begin{pmatrix} \frac{\hbar\omega_0}{2} & 0 \\ 0 & -\frac{\hbar\omega_0}{2} \end{pmatrix} = \frac{\hbar\omega_0}{2} \hat{\sigma}_3 \quad (5.1)$$

where  $\hat{\sigma}_3$  is the third of the Pauli spin matrices. The interaction Hamiltonian  $\hat{H}_{\text{int}}$  of the atoms with magnetic moment  $\hat{\boldsymbol{\mu}}$  with a magnetic field  $\hat{\mathbf{B}}$  is

$$\hat{H}_{\text{int}} = -\hat{\boldsymbol{\mu}} \cdot \hat{\mathbf{B}} \quad (5.2)$$

The coupling parameter is the (complex) magnetic moment:

$$\hat{\boldsymbol{\mu}} = \begin{pmatrix} 0 & \boldsymbol{\mu}_r + i\boldsymbol{\mu}_i \\ \boldsymbol{\mu}_r - i\boldsymbol{\mu}_i & 0 \end{pmatrix} = \boldsymbol{\mu}_r \hat{\sigma}_1 - \boldsymbol{\mu}_i \hat{\sigma}_2 \quad (5.3)$$

For  $\Delta m_F = 0$  transitions, the complex contribution  $\boldsymbol{\mu}_i$  vanishes. The Hamiltonian of the full system then reads, omitting the energy of the electro magnetic field  $\hat{H}_{\text{em}} = \hbar\omega(\hat{a}^\dagger \hat{a} + \frac{1}{2})$ :

$$\hat{H} = \hat{H}_A + \hat{H}_{\text{int}} = \frac{\hbar\omega_0}{2} \hat{\sigma}_3 - \boldsymbol{\mu}_r \hat{\sigma}_1 \hat{\mathbf{B}} \quad (5.4)$$

The Pauli spin matrix operators become time dependent in the Heisenberg picture and govern the evolution of the two level pseudo spin state. Their temporal evolution is given by the Heisenberg equation of motion:

$$\dot{\hat{\sigma}}_k = \frac{-i}{\hbar} [\hat{\sigma}_k, \hat{H}], \quad k = 1, 2, 3 \quad (5.5)$$

Inserting equation (5.4) into equation (5.5) we end up with a set of differential equations:

$$\dot{\hat{\sigma}}_1(t) = -\omega_0 \hat{\sigma}_2(t) \quad (5.6)$$

$$\dot{\hat{\sigma}}_2(t) = \omega_0 \hat{\sigma}_1(t) + \frac{2}{\hbar} (\boldsymbol{\mu}_r \cdot \hat{\mathbf{B}}(t)) \sigma_3(t) \quad (5.7)$$

$$\dot{\hat{\sigma}}_3(t) = -\frac{2}{\hbar} (\boldsymbol{\mu}_r \cdot \hat{\mathbf{B}}(t)) \hat{\sigma}_2(t) \quad (5.8)$$

### Semiclassical approximation

With the solution of equations (5.6) – (5.8), the time evolution of an input atomic state  $|\psi\rangle_{\text{in}}$  and input light field state  $|\alpha\rangle_{\text{in}}$  can be calculated as:

$$|\psi\rangle_{\text{out}} |\alpha\rangle_{\text{out}} = \hat{\boldsymbol{\sigma}}(t) |\psi\rangle_{\text{in}} |\alpha\rangle_{\text{in}} \quad (5.9)$$

For high enough microwave power, the magnetic field can be regarded as a classical field and the field operator  $\hat{\mathbf{B}}$  is replaced by its classical mean value  $\hat{\mathbf{B}}(t) \rightarrow \langle \hat{\mathbf{B}} \rangle = \mathbf{B}_0 \cos(\omega t)$ , where  $\omega$  is the angular frequency of the driving field and  $\mathbf{B}_0$  is the field amplitude. We have already restricted the treatment to  $\Delta m_F = 0$  transitions which requires the magnetic field orientation to be parallel to the quantization axis of the atomic state. We will define the quantization axis by applying a homogeneous external magnetic field. The vector character of the field can therefore be omitted,  $\mathbf{B}_0 = B_0$ . The mean value of the operator product  $\langle \hat{\mathbf{B}}(t) \hat{\sigma}_x(t) \rangle$  factorizes, i.e., quantum mechanical atom–field correlations are neglected; for convenience we introduce:

$$\langle \hat{\sigma}_k(t) \rangle \equiv s_k(t), \quad k = 1, 2, 3 \quad (5.10)$$

### Rotating wave approximation

A short glimpse at equations (5.6) and (5.7) suggests that besides the radiation field, also the state vector will have some oscillatory term. To separate off one of the oscillations one transforms into a reference frame which rotates with the microwave frequency  $\omega$  by using:

$$\begin{pmatrix} u \\ v \\ w \end{pmatrix} = \begin{pmatrix} \cos \omega t & \sin \omega t & 0 \\ -\sin \omega t & \cos \omega t & 0 \\ 0 & 0 & 1 \end{pmatrix} \begin{pmatrix} s_1 \\ s_2 \\ s_3 \end{pmatrix} \quad (5.11)$$

Transforming equations (5.6) – (5.8) into the rotating frame we obtain:

$$\dot{u} = \Delta v + \Omega_R \sin 2\omega t w \quad (5.12)$$

$$\dot{v} = -\Delta u + \Omega_R(1 + \cos 2\omega t) w \quad (5.13)$$

$$\dot{w} = -\Omega_R \sin 2\omega t u - \Omega_R(1 + \cos 2\omega t) v \quad (5.14)$$

introducing the abbreviations  $\Delta = \omega - \omega_0$ , the detuning of the microwave field relative to the transition, and the Rabi frequency  $\Omega_R = 2\mu_r B_0/\hbar$ . In the rotating wave approximation the terms varying with frequency  $2\omega$  are assumed to average out and we are left with the Bloch equations:

$$\dot{u} = \Delta v \quad (5.15)$$

$$\dot{v} = -\Delta u + \Omega_R w \quad (5.16)$$

$$\dot{w} = -\Omega_R v \quad (5.17)$$

which can be written as:

$$\dot{\mathbf{u}} = -\mathbf{\Omega} \times \mathbf{u} \quad (5.18)$$

with  $\mathbf{\Omega} \equiv (\Omega_R, 0, \Delta)$  and the Bloch vector  $\mathbf{u} \equiv (u, v, w)$ . These equations are well known from the mathematical description of a vector  $\mathbf{u}$  rotating around a torque vector  $\mathbf{\Omega}$  with angular frequency  $\Omega = |\mathbf{\Omega}| = \sqrt{\Omega_R^2 + \Delta^2}$  [62].

For a period of time  $t$  during which the system parameters do not change, the general solution of this set of differential equations is found to be a rotation matrix  $R(t, \Delta, \Omega_R)$ :

$$u(t) = R(t, \Delta, \Omega_R) \cdot u(t=0) \quad (5.19)$$

$$R(t, \Delta, \Omega_R) = \begin{pmatrix} \frac{\Omega_R^2 + \Delta^2 \cos \Omega t}{\Omega^2} & \frac{-\Delta}{\Omega} \sin \Omega t & \frac{\Delta \Omega_R}{\Omega^2} (1 - \cos \Omega t) \\ \frac{\Delta}{\Omega} \sin \Omega t & \cos \Omega t & \frac{-\Omega_R}{\Omega} \sin \Omega t \\ \frac{\Delta \Omega_R}{\Omega^2} (1 - \cos \Omega t) & \frac{\Omega_R}{\Omega} \sin \Omega t & \frac{\Delta^2 + \Omega_R^2 \cos \Omega t}{\Omega^2} \end{pmatrix} \quad (5.20)$$

The direction of rotation depends on the initial choice of the microwave field phase with respect to the atomic system. In the rotating frame, this boils down to the rotation direction of the rotating frame. In general, the direction is of minor importance but we try to be consistent.

### Application to atomic state vector

The connection between the Bloch vector components and the probability amplitudes of an atomic state  $|\psi\rangle = a|4\rangle + b|3\rangle$  can be easily obtained, with  $\hat{\sigma}_i$  in the rotating frame:

$$u = \langle \psi | \hat{\sigma}_1 | \psi \rangle = a^* b + a b^* \quad (5.21)$$

$$v = \langle \psi | \hat{\sigma}_2 | \psi \rangle = -i(a^* b - a b^*) \quad (5.22)$$

$$w = \langle \psi | \hat{\sigma}_3 | \psi \rangle = |a|^2 - |b|^2 \quad (5.23)$$

The  $w$ -component of the Bloch vector is thus the difference of the probabilities for the atom being in  $|4\rangle$  and  $|3\rangle$ <sup>1</sup>. The  $u$ - and  $v$ -components on the other hand

<sup>1</sup>We have often and will often use the term ‘‘atomic population’’ in different states. This is a colloquial way of expressing that we will be dealing with an ensemble and get the mean values of the probability distribution in a single measurement.

represent the phase relation between the atomic state and the frame rotating with the microwave frequency. Note that the Bloch vector components correspond to the mean values of the angular momentum operator components  $\hat{\mathbf{j}} = (\hat{j}_x, \hat{j}_y, \hat{j}_z)$  introduced in section 2.1.1 up to a factor of 2 in the normalization.

Since the state vector is normalized  $\langle \psi | \psi \rangle = 1$  it is obvious that it can also be mapped onto a unit sphere at polar angle  $\theta$  and azimuthal angle  $\phi$ . This becomes more obvious when writing the state vector as:

$$|\psi\rangle = \cos \frac{\theta}{2} |4\rangle + \sin \frac{\theta}{2} e^{i\phi} |3\rangle \quad (5.24)$$

for which the Bloch vector components assume the form:

$$u = \sin \theta \cos \phi \quad (5.25)$$

$$v = \sin \theta \sin \phi \quad (5.26)$$

$$w = \cos \theta \quad (5.27)$$

We have above derived the action of an external field onto the Bloch vector and shown the connection between the atomic state vector and the Bloch picture. It is also possible to directly derive the rotation matrix for the state vector  $|\psi\rangle$  when an external field is applied.

### 5.1.2 Loss of coherence in ensembles of atoms

So far the Bloch vector  $\mathbf{u}$  has been introduced for a single atom. If an ensemble of  $N$  uncorrelated atoms is considered, we can describe the ensemble state  $|\Psi\rangle = \prod_{i=1}^N (a_i |4\rangle_i + e^{i\phi_i} b_i |3\rangle_i)$  by a normalized total Bloch vector  $\mathbf{U} = \frac{1}{N} \sum_i \mathbf{u}_i$ . When all the atoms are in the same state  $a \equiv a_i, b \equiv b_i, \phi \equiv \phi_i$ , the length of the total Bloch vector is one. If a phase distribution  $\phi_i \neq \text{const.}$  is present in the ensemble (while the probability amplitudes are still the same for all atoms,  $a \equiv a_i, b \equiv b_i$ ), i.e., the atomic ensemble is not in a coherent state, the length of the mean Bloch vector is reduced. The length of  $\mathbf{U}$  thus gives information about the coherence of the ensemble state. The mean Bloch vector is similar to the collective angular momentum operator  $\hat{\mathbf{J}}$  introduced in section 2.1.1 with the main difference being the normalization. Note that the Bloch vector is an explicit rotating frame description while the the angular momentum operator has been introduced in a more general setting. The interpretation of the length of the vector as measure for the coherence of the ensemble remains, compare section 2.1.1.

Later we shall encounter three forms of decoherence. The length of the Bloch vector changes when a distribution of phases  $\phi_i$  in the ensemble exists. If the phase distribution is induced in a deterministic way, such that it is known which atom  $j$  obtained which phase shift  $\phi_j$ , the dephasing is reversible by the spin echo techniques we will discuss in section 5.8. If the dephasing, on the other hand is induced in a random way, it is irreversible. A third way of reducing the length of the mean Bloch vector length is induced by the projective character of spontaneous light scattering of the probe light field. Right after a probe pulse, atoms that have undergone a real transition will have been projected into one of the energy

eigenstates. If the atom(s) were not in such a state prior to the measurement, the probability amplitudes for the projected atoms will be different to the rest of the atoms and thus  $a_j \neq a, b_j \neq b$  for those atoms. Spontaneous light scattering will therefore introduce a distribution of the probability amplitudes in the ensemble state  $|\Psi\rangle$  and change both the orientation and length of  $\mathbf{U}$ .

The introduction of the mean Bloch vector  $\mathbf{U}$  is equivalent to performing an ensemble average. Since quantum mechanics is a probabilistic theory, the same results would be obtained by taking  $N$  single atoms, measuring them independently and averaging over the measurement outcomes afterwards.

Although a measurement on an ensemble returns the components of  $\mathbf{U}$ , it can be more instructive to look at the ensemble as a collection of independent Bloch spheres and plot them on top of each other. This way, the actual distribution of the phases  $\phi_i$  can be visualized. We shall use both pictures later on.

### 5.1.3 Rabi oscillations and state rotations

In our system, the  $U$ - and  $V$ - components of the mean Bloch vector cannot be measured directly. The  $W$ -component on the other hand is obtained by measuring the population of the two energy eigenstates and subtracting these values. After applying a certain sequence of microwave pulse operations, we are therefore mainly interested in the  $W$  component of the Bloch vector. For an ensemble prepared in the  $|3\rangle$  state<sup>2</sup>, the Bloch vector is  $\mathbf{U}_0 = (0, 0, -1)$ . The evolution of the state for a constant driving field is then given by equation (5.19) and for the  $W$ - component we get:

$$W(t, \Delta, \Omega_R) = -\frac{\Delta^2 + \Omega_R^2 \cos \sqrt{\Omega_R^2 + \Delta^2} t}{\Omega_R^2 + \Delta^2} \quad (5.28)$$

which we can use to obtain the population (probability amplitude)  $|a|^2$  of the  $|4\rangle$  state as:

$$P_4 = |a|^2 = \frac{W + 1}{2} = \frac{\Omega_R^2}{\Omega_R^2 + \Delta^2} \sin^2 \left( \frac{1}{2} \sqrt{\Omega_R^2 + \Delta^2} t \right) \quad (5.29)$$

Since the Bloch vector  $\mathbf{U}$  is normalized to the number of atoms,  $P_4$  is independent of the number of atoms,  $|a| = \frac{1}{N}|a|N$ . The population oscillates between the two states with an angular frequency of  $\Omega = \sqrt{\Omega_R^2 + \Delta^2}$ . These are the famous Rabi oscillations. For  $\Delta = 0$  the rotation of the Bloch vector is illustrated in figure 5.1(a).

### Resonant driving

On resonance,  $\Delta = 0$ , the oscillations correspond to a rotation of the Bloch vector around the  $U$ -axis with the Rabi frequency  $\Omega_R$ . In this case, the rotation matrix

<sup>2</sup>This again is colloquial language which will be encountered frequently. Of course, each single atom  $i$  is prepared in its ground state  $|\psi\rangle_i = |3\rangle_i$  and the collective state is  $|\Psi\rangle = |3\rangle^{\otimes N}$ .

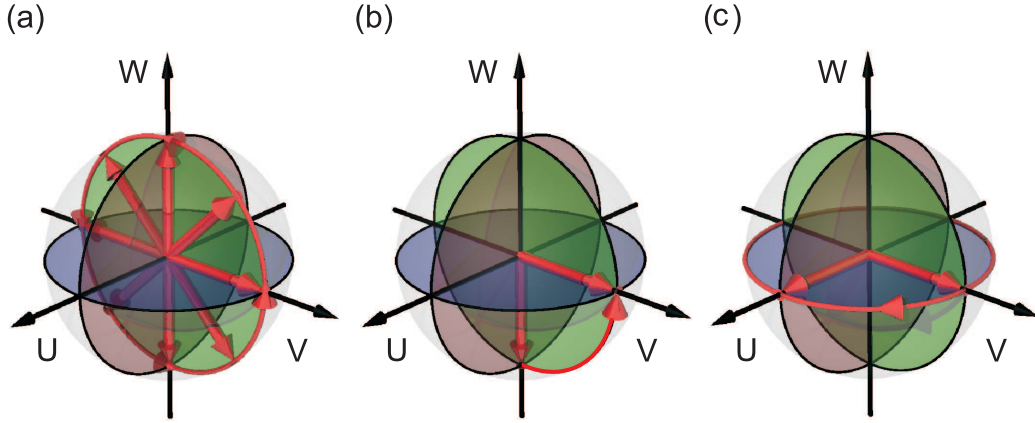


**FIGURE 5.1:** *Rotation of Bloch vector. (a) Resonant driving of the transition such that the Bloch vector rotates around the  $U$ -axis. (b) When the driving takes the vector into the  $U$ - $V$ -plane through a  $\pi/2$ -pulse, the ensemble is prepared in a superposition state with equal probability amplitudes. (c) The Bloch vector precesses freely around the  $W$ -axis with angular frequency  $\Delta$  when the driving field is off but detuned by  $\Delta < 0$  from the resonance. The direction of rotation depends on the initial choice of the phase of the microwave field with respect to the atomic system.*

in equation (5.20) reduces to:

$$R(t, 0, \Omega_R) = \begin{pmatrix} 1 & 0 & 0 \\ 0 & \cos \Omega_R t & -\sin \Omega_R t \\ 0 & \sin \Omega_R t & \cos \Omega_R t \end{pmatrix} \quad (5.30)$$

The rotation angle is given by  $\theta = \Omega_R t$ . When a single pulse is applied such that  $\theta = \pi$ , the pulse is called a  $\pi$ -pulse. For an initial ensemble state  $|\Psi\rangle = |3\rangle^{\otimes N}$ , the population is fully transferred into the  $|4\rangle$  level, resulting in  $|\Psi\rangle_{R(\pi)} = |4\rangle^{\otimes N}$ .

The other most prominent pulse we shall encounter rotates the Bloch vector by  $\theta = \pi/2$  around the  $U$ -axis and is for obvious reasons called a  $\pi/2$ -pulse. In the language of the atomic state  $|\Psi\rangle$ , starting with a coherent state  $|\Psi\rangle = |3\rangle^{\otimes N}$ , this produces a coherent superposition state with equal probability amplitudes:  $|\Psi\rangle_{R(\pi/2)} = \left(\frac{|3\rangle + i|4\rangle}{\sqrt{2}}\right)^{\otimes N}$ . The action of a  $\pi/2$ -pulse on the Bloch sphere is illustrated in figure 5.1(b).

### Change of phase relation between atomic state and rotating frame

Since we have transformed into a rotating frame, the Bloch vector can also change its position when the driving field is off,  $\Omega_R = 0$ . In this case the rotation matrix reduces to:

$$R_{\text{free}}(t, \Delta, 0) = \begin{pmatrix} \cos t\Delta & -\sin t\Delta & 0 \\ \sin t\Delta & \cos t\Delta & 0 \\ 0 & 0 & 1 \end{pmatrix} \quad (5.31)$$

which describes a rotation around the  $W$ -axis by an angle  $\phi(t) = t\Delta$ . If the detuning  $\Delta$  is time dependent,  $\phi(t) = \int_0^t \Delta(t') dt'$ . The graphical interpretation of

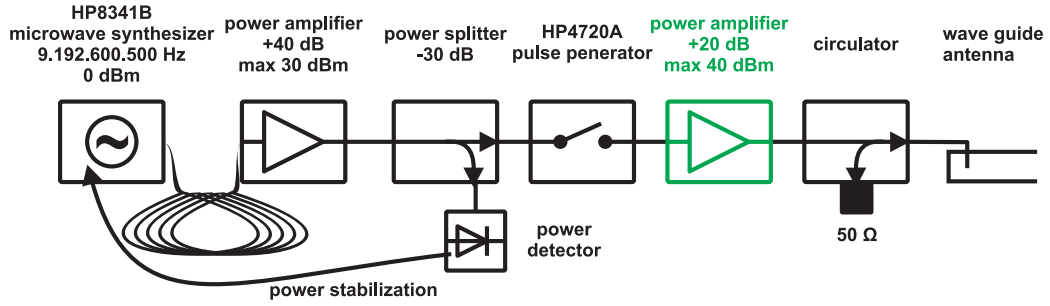


**FIGURE 5.2:** *Microwave equipment.* A 10 m long coaxial cable transports the output of the synthesizer to the setup. At the output of the cable, the signal is amplified up to 1 W and actively stabilized. After creating the pulses with a microwave switch, a low loss cable connects the switch and the coaxial-to-waveguide adapter. A cut-to-length square waveguide acts as antenna. The amplifier is protected by a circulator which dumps reflected power due to improper impedance matching of the coaxial cable and the waveguide. To obtain higher power a 10 W power amplifier is added after the pulse generator.

the rotation applied to an equal superposition state is given in figure 5.1(c). This free precession of the vector can be understood as a change in the phase relation between the rotating frame of the driving field and the atomic ensemble. For the atomic state  $|\Psi\rangle$ , the phase change results in the transformation:

$$|3\rangle \rightarrow e^{-i\phi/2}|3\rangle \quad (5.32)$$

$$|4\rangle \rightarrow e^{i\phi/2}|4\rangle \quad (5.33)$$

## 5.2 Generation of microwave pulses

To apply the Bloch vector rotation techniques discussed above to the ensemble of dipole trapped Cs atoms in the experimental setup, we need to couple the magnetic field component of electromagnetic radiation with  $\omega \approx \omega_0$  to the atoms. To produce the 9.192 GHz microwave radiation we use a HP8341B precision synthesizer. Most of the controls of the synthesizer have been implemented into a Labview programme which communicates with the other Labview programmes controlling the rest of the experiment as discussed in section 3.3.2; this way we can use stepping routines to dynamically change the power or frequency of the synthesizer during one set of measurements. Since the interferometer (and the users in the lab) are rather sensitive to acoustic noise, especially from the cooling fans of the synthesizer, it is located in a separate compartment next to the lab. Therefore, the output power of the synthesizer has to be stabilized actively after the 10 m long coaxial cable which transports the microwaves to the setup. A schematic diagram of the microwave setup is shown in figure 5.2. We stabilize the synthesizer output power after the long coaxial cable and a 1 W amplification stage. The amplifier comes from Narda West model DBS-0411N630. For the stabilization we use an Agilent 33330B Schottky diode power detector and feed its signal back onto the dedicated synthesizer input port. The bandwidth of this external feedback loop is 80 kHz. The remaining microwave signal enters a pulse modulator (HP 4720A)

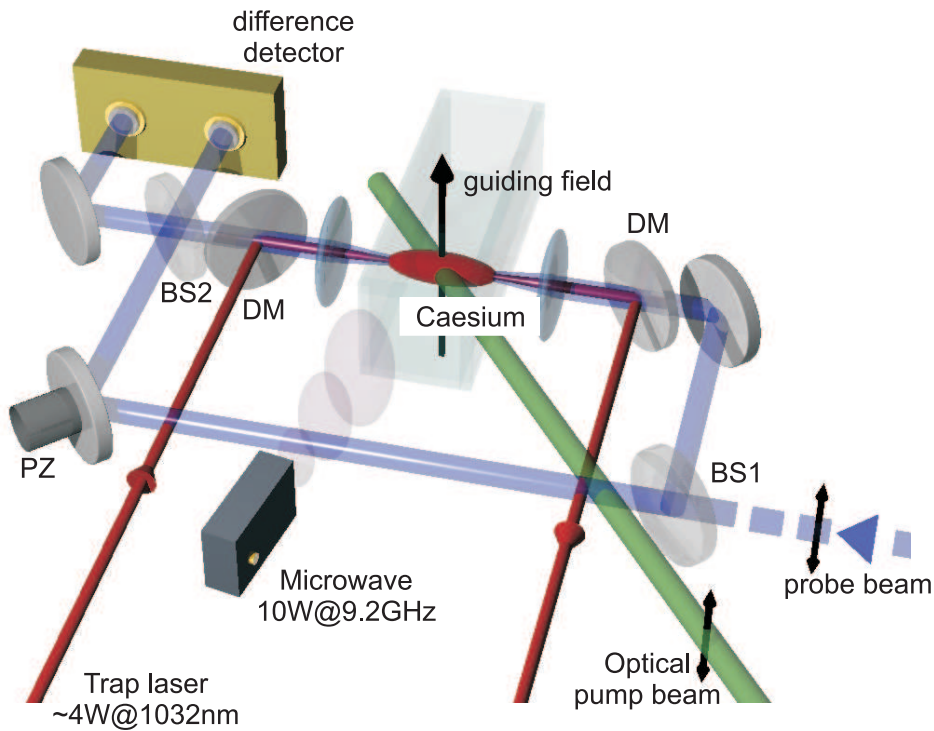


**FIGURE 5.3:** Schematics of the interferometer including the microwave antenna, the orientation of the magnetic guiding field and the positioning of the two counter propagating optical pumping beams. The interferometer itself and the surrounding setup has been discussed in section 3.2.

which is gated with the signals for the Viewpoint Systems DIO-64 output card. A high quality microwave cable transports the pulses to a rectangular waveguide whose length has been adjusted for minimum standing wave reflection power. The coaxial-to-waveguide adapter is oriented such that the magnetic field vector of the microwave field is parallel to the magnetic guiding field of the atoms (discussed in section 5.3.2). A circulator protects the amplifier from reflected signals.

Most of the data presented in the next sections has been taken with this setup. We later acquired a 10 W power amplifier from Kuhne electronic. The additional amplifier is placed as second amplification stage after the microwave switch. The only (apparent) reason for using this higher microwave power setup is that the Rabi frequency increases with the driving field power  $P$  as:  $\Omega_R \propto B_0 \propto \sqrt{P}$ . This way, the duration of the  $\pi$ -pulses can be reduced by a factor of 3 which will become especially important when we apply spin-echo spectroscopy techniques to gain information in the oscillation dynamics of the ensemble in the trap, section 5.10.

A schematic drawing of the whole interferometer setup including the microwave antenna, and the guiding field and optical pumping beams introduced below is shown in figure 5.3. The other components are discussed in section 3.2.

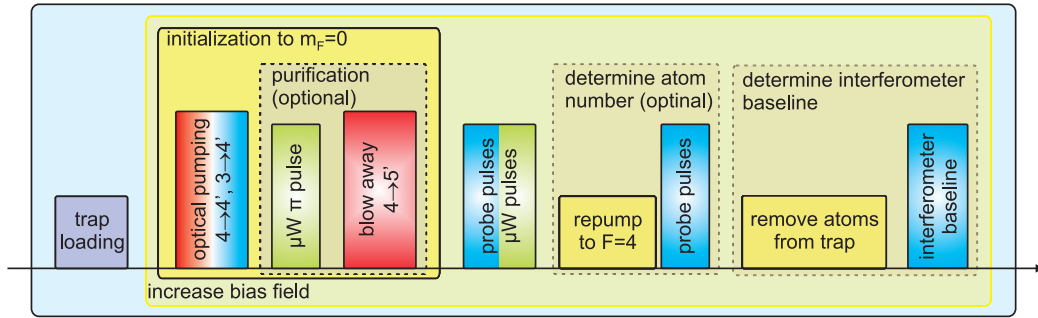


**FIGURE 5.4:** Time sequence of single experimental run. After atoms have been loaded into the trap, we initialize them into one of the clock states by optical pumping techniques and optionally purify the ensemble further. In the next step, the desired microwave and probe operations are applied. The number of the remaining atoms can be determined by repumping the sample after the microwave/probe sequence for normalization purposes. At the end of each run, we remove the atoms from the trap and determine the interferometer baseline.

## 5.3 Quantum state preparation

### 5.3.1 General measurement procedure

In chapter 3 the generation of a cold dipole trapped ensemble of atoms inside one arm of the Mach–Zehnder interferometer as depicted in figure 5.3 has been discussed. We use the interferometer as a means of state selectively detecting the number of atoms in the probe region. To this end we send a number of probe light pulses through the interferometer and detect the phase shift signal at the output as presented in section 3.4.1. Unless otherwise stated we only use the  $F = 4 \rightarrow F' = 5$  probe light with a detuning of  $\Delta_{45} = +160$  MHz, i.e., we read out the population in the  $F = 4$  state.

The time sequence of a typical single run of the experiment is shown in figure 5.4. After loading the atoms into the trap, they are initialized to the clock states by using optical pumping techniques as discussed in the next section. Subsequently the desired microwave and probe light pulses are applied. Since the probing does not remove the atoms from the dipole trap, it is possible to re-initialize the atoms into the  $F = 4$  state again after the application of the microwaves by applying repump light on the  $F = 3 \rightarrow F' = 4$  transition. The trap lifetime is known, it is therefore possible to determine the number of atoms in the probe region during the microwave pulse and probe sequence by using a later measurement result for normalization. After we have expelled all the atoms from the dipole trap, the lock point of the interferometer can be determined and used as baseline for the two atom measurements, compare section 3.4.1. This is necessary because the lock and probe laser interference fringes do not cross the zero phase shift line at the same point.

To make the link with the actual experimental setup, the control programme shown in figure 3.4, page 32, and the pulse generation unit shown in figure 3.12, page 46, show realistic values for this measurement configuration. Probing of the initialized ensemble happens in stage 8. In stage 9 the repump laser is switched on and after

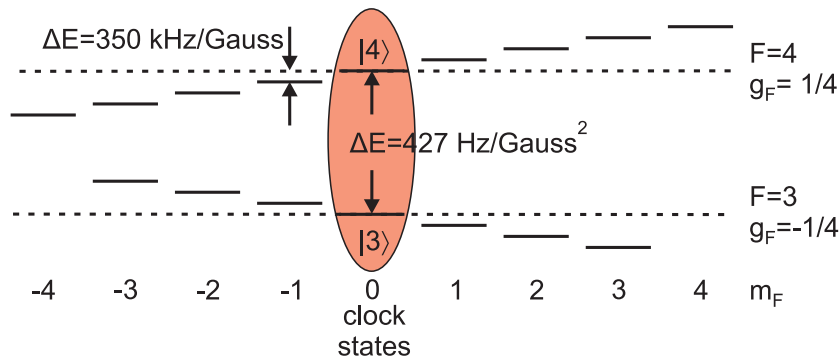


**FIGURE 5.5:** Level splitting of the caesium hyperfine ground states due to an external magnetic field.

the shutter is closed again, the atom number is determined in stage 10. Stage 29 expels the atoms from the trap and in stage 30 we determine the empty interferometer baseline. Each measurement stage, saved into one scope segment (compare section 3.3.2), contains ten pulses, whose areas (amplitudes) are usually averaged over during postprocessing.

In the following, the subtraction of the interferometer baseline is implicitly assumed unless noted otherwise! Several measurement results of these single runs of the experiment with the same experimental conditions can be combined to reduce technical fluctuations. Usually averaging over three runs is sufficient. So, *in general*, we average over three runs each containing three segments where we average over the ten pulses in each segment.

### 5.3.2 Sample initialization to the clock states

In figure 5.5 the hyperfine ground states of Cs are shown. After the sub-Doppler cooling stage which loads the atoms into the dipole trap, the atoms are distributed over all  $m_F$  sublevels. To accumulate the atoms in one of the clock states we have to

- define a quantization axis to make the levels with different  $m_F$  quantum numbers non-degenerate and  $m_F$  a good quantum number
- optically pump the atoms into the  $m_F = 0$  state.

#### Defining a quantization axis

To lift the degeneracy of the magnetic sublevels of the ground states and to define a quantization axis for the atomic system, we use an external magnetic field. Around the experimental setup, three pairs of coils in Helmholtz configuration with  $50 \times 50 \text{ cm}^2$  outer dimensions are installed to compensate static magnetic fields at the position of the atomic sample as shown in figure 3.1. By increasing the current in one set of coils – we use the horizontal pair and call it the  $z$ -direction – a homogeneous guiding field is produced and defines the quantization axis for the atoms.

To make the quantization axis as well defined as possible by the externally applied field, we minimize the magnetic background field without the bias field applied first. Well compensated external fields are also beneficial for the MOT and su-Doppler cooling stage performance. The optimal field compensation can be obtained by using microwave spectroscopy. As shown in figure 5.5 on page 85, an external magnetic field lifts the degeneracy of the magnetic sublevels according to the Zeeman shift. The first order Zeeman energy shift of a magnetic sublevel  $m_F$  when a magnetic field  $B = |\mathbf{B}|$  is applied, is given by:

$$\Delta E = \mu_B g_F m_F B = \pm 350 \text{ kHz} \cdot m_F \cdot B [\text{Gauss}] \quad (5.34)$$

where  $\mu_B$  is the Bohr magnetic moment and  $g_F$  is the Landé factor, which has opposite signs for  $F = 3$  and  $F = 4$ . The clock levels  $m_F = 0$  are not affected to first order. Second order perturbation theory gives a clock level shift  $\Delta\omega_{\text{clock}}$  of [18]:

$$\Delta\omega_{\text{clock}} = \frac{(g_J - g_I)^2 \mu_B^2}{2\hbar \Delta E_{\text{hfs}}} B^2 = 2\pi \cdot 427.45 \text{ Hz} B^2 [\text{Gauss}]^2 \quad (5.35)$$

$\Delta E_{\text{hfs}}/\hbar = 2\pi \cdot 9.192 \text{ GHz}$  is the unperturbed hyperfine splitting  $g_J$  and  $g_I$  are the finestructure and nuclear Landé factors. When we apply a microwave driving field whose frequency is swept across the different transitions, the population of an ensemble initially prepared in one of the hyperfine manifolds will be stepwise transferred into the other state. The mechanism behind the transfer is a rapid-adiabatic-passage [46]. Since the ensemble is not polarized, the lowest frequency transition accessible is the  $F = 4, m_F = -4 \rightarrow F = 3, m_F = -3$  transition. Towards higher frequencies, all the possible  $\sigma$  and  $\pi$  transitions come into play until the highest frequency transition, the  $F = 4, m_F = 4 \rightarrow F = 3, m_F = 3$  transition is reached. The width of the transfer region is proportional to the magnetic background field according the Zeeman formula (5.34). A change in the compensation (or bias) coils will therefore also change the frequency width of the transfer region. Figure 5.6(a) shows the transfer of a population initially prepared in  $F = 4$  over to the  $F = 3$  levels when the applied microwave field is scanned in frequency from 9,192.1 MHz to 9,193.1 MHz for different  $z$ -axis bias coil currents.<sup>3</sup> The sweep is performed in 10 ms and the population in  $F = 4$  is determined by using 100 pulses of 2  $\mu\text{s}$  duration and 100  $\mu\text{s}$  repetition period. We trigger the sweep together with the first pulse and the application of the microwave field. The width of the transfer region can be easily extracted by, e.g., fitting an error function to the data. In figure 5.6(b) the frequency width of the transfer region is shown as a function of the  $y$ -axis coil currents. The frequency width can be converted into magnetic field by noting that the total Zeeman-splitting is  $\Delta f_{\text{alllevels}} = 14 \cdot 350 \text{ kHz} \cdot B$  [Gauss]. After optimizing the settings of all three directions the remaining uncompensated field is calculated to be  $B_{\text{uncomp.}} \approx 34 \text{ mGauss}$ .

<sup>3</sup>Here and throughout the chapter, the frequency values given refer to the value set on the synthesizer. Since the synthesizer time base has aged for several years, the true output frequency is different! From comparison with a newly calibrated spectrum analyzer we know that the output frequency is wrong by 30.841 kHz. On a daily basis we use a synthesizer set frequency of  $\omega \sim 9.192.600.750 \text{ Hz}$  which is only 179 Hz off from the defined transition frequency when taking the offset into account. The remaining offset is due to differential light shifts and the second order Zeeman shift.

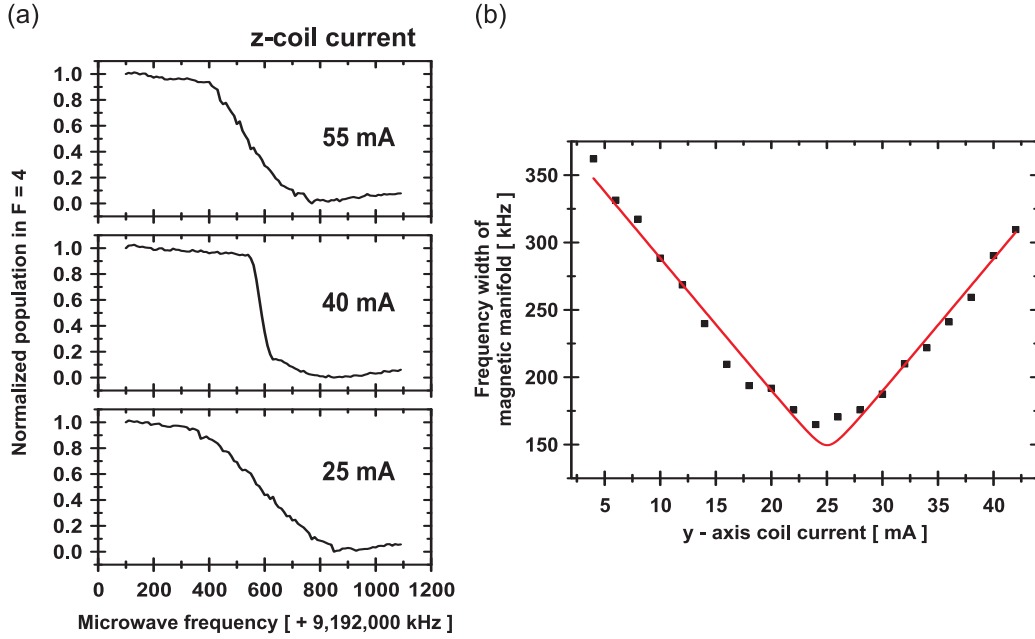


**FIGURE 5.6:** (a) Population transfer when the microwave driving frequency is swept across the hyperfine manifold transitions. The width of the transfer region is proportional to the splitting of the magnetic sublevels, thus to the magnetic background field. (b) Widths of the transfer region extracted from data similar to (a) as a function of the  $y$ -axis bias coil current. From the minimum width, the remaining bias field can be extracted. After an optimization in all three directions, we end up with an uncompensated field of  $B_{\text{uncomp.}} \approx 34 \text{ mGauss}$ .

After the magnetic field is nulled in all three dimensions, we define the quantization axis for the ensemble by switching the  $z$ -axis bias coil to a current of  $I_z \sim 250 \text{ mA}$  (the coil current used for field nulling is  $I_z = 43 \text{ mA}$  in this coil). A similar frequency sweep with increased bias coil current allows us to extract the magnitude of the bias field. The corresponding data is shown in figure 5.7. A clear stepwise increase in the population of the  $F = 4$  states can be observed. The frequency of the clock transition is known from other measurements (further down), so the nature of the observed transitions can be inferred. From the frequency spacing between the transitions the magnitude of the quantization field is evaluated to  $B_{\text{bias}} = 1.6 \text{ Gauss}$ .

### Optical pumping and sample cleaning

To initialize the atomic sample in the  $(F = 4, m_F = 0) \equiv |4\rangle$  clock state, we can use the fact that the optical D2 (or D1) line transition  $(F = 4, m_F = 0) \rightarrow (F' = 4, m_F = 0)$  is electric dipole forbidden. When  $\pi$ -polarized light, i.e., light whose linear polarization is parallel to the quantization axis of the atoms, is applied to the atomic ensemble on the  $6S_{1/2}(F = 4) \rightarrow 6P_{3/2}(F' = 4)$  transition, due to the selection rules only atoms in  $F = 4, m_F \neq 0$  are addressed by the laser and excited to their  $F' = 4$  counterparts. From these excited levels, the atoms can decay via all channels ( $\sigma^\pm, \pi$  transitions) into the corresponding  $m_F$  sublevels of the  $F = 3$  and  $F = 4$  states. With an additional laser coupling the  $F = 3 \rightarrow F' = 4$  states,

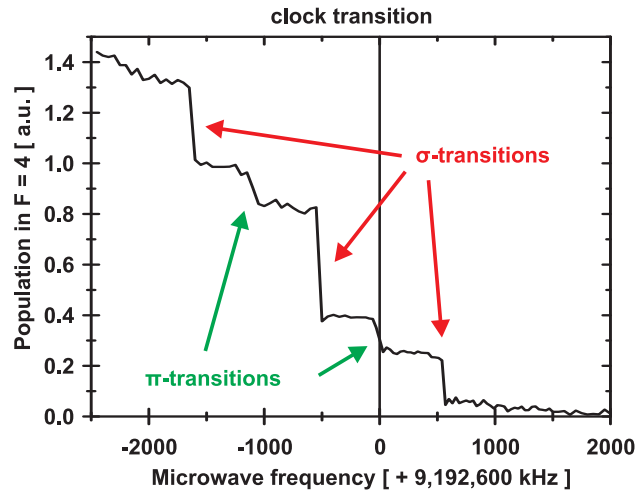


**FIGURE 5.7:** Frequency sweep across the inner  $m_F$  manifold for considerably increased  $z$ -compensation coil current. The steps in the  $F = 4$  level population correspond to different transitions. Since two  $\sigma$  transitions exist with the same transition frequency, these are more pronounced than the  $\pi$  transitions. From the splitting of the transitions the bias or guiding field is evaluated to  $B_{\text{bias}} = 1.6$  Gauss.

atoms will thus be pumped among their ground states until they are either heated out of the trap or have decayed into the  $F = 4, m_F = 0$  state [63, 64]. In the experimental sequence of figure 5.4, the pumping step corresponds to stage 5 in the programme panel shown in figure 3.4. The parameters of the optical pumping process to optimize are:

- light polarization relative to quantization axis
- duration (or power) of the optical pumping light pulse
- frequency of the pump light

Both the  $F = 4 \rightarrow F' = 4$  and  $F = 3 \rightarrow F' = 4$  optical pumping light is coupled into one optical fiber and the fiber output is polarization cleaned with a Glan-Thompson prism. The light itself is derived from the high power slave laser diodes, compare figure 3.3. We use two counter propagating beams as shown in figure 5.3 to balance the momentum transfer from the pump light onto the atoms which would otherwise induce trap oscillations. The repump light is kept on for several milliseconds while the  $F = 4 \rightarrow F' = 4$  light involving the dark state is pulsed on for  $50 - 300 \mu\text{s}$  only. In both beams we have a dc light power of about 1 mW available.

After the Rabi frequency has been determined,<sup>4</sup> the different pumping parameters are optimized by considering the efficiency of a microwave  $\pi$ -pulse, resonant only to the clock transition. Since the clock transition is very narrow and the other

<sup>4</sup>The optimization of the pumping, finding the Rabi frequency and determining the clock transition frequency are iterative processes. The pumping can also be optimized with a slightly off resonant microwave pulse of wrong duration, however, the transfer efficiency will not reflect the polarization of the sample.

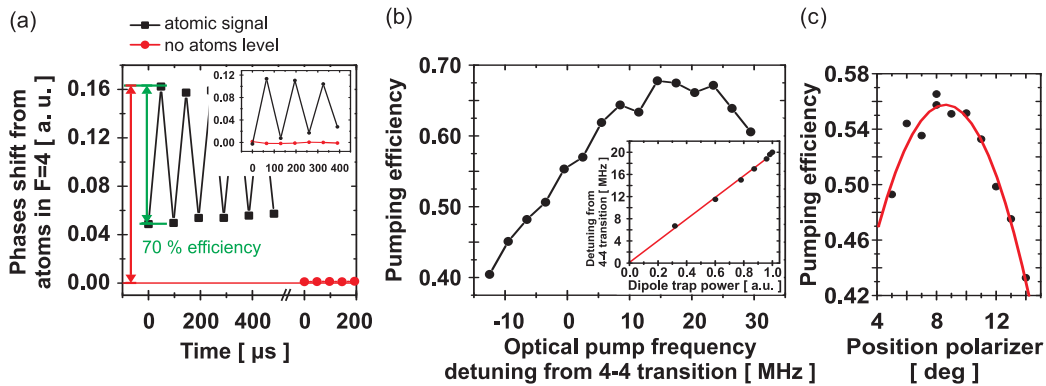


**FIGURE 5.8:** (a) Extraction of optical pumping efficiency. The contrast from a microwave  $\pi$  pulse is determined by normalizing the transfer from the  $F = 4 \rightarrow F = 3$  state to the total number of atoms. The inset shows the effect of state purification. Removing atoms which have not been pumped into the clock state yields a microwave transfer efficiency close to 100%. (b) Optical pumping efficiency into the clock state for the highest dipole trap power as function of the pump light detuning from the (bare)  $F = 4 \rightarrow F' = 4$  transition. The optimal value for the detuning depends on the power of the dipole trap laser due to the differential light shift from the trap laser onto the pump transition. The inset shows the optimal frequency detuning as function of the trap laser power. (c) Optimization of the pump beam polarization. When the axis of the Glan-Thompson polarizer is not optimal, the  $F = 4, m_F = 0$  state is no longer a dark state and pumping is less efficient.

possible  $\pi$ -transitions are shifted out of resonance by several hundreds of kilohertz by the Zeeman shift due to the magnetic guiding field, a microwave field resonant to the clock transition only affects atoms in  $m_F = 0$ . We send single probe light pulses of  $2\mu\text{s}$  duration before and after the microwave pulse; after heating the atoms out of the trap we then determine the lock point of the interferometer with further pulses. After the optical pumping process, the atoms populate only  $m_F$  substates of the  $F = 4$  manifold. The reduction of the phaseshift signal when using  $F = 4 \rightarrow F' = 5$  probe light tells us how many atoms can be transferred into the  $(F = 3, m_F = 0) \equiv |3\rangle$  state. From the corresponding data in figure 5.8(a), we extract a transfer efficiency of 70%.

Optimizing the optical pump parameters carefully, we obtain a state polarization of up to 75%. The optimization for two parameters, the pumping frequency and the polarization of the pump light is illustrated in figures 5.8(b) and (c). Figure 5.8(b) confirms that the optimal pumping frequency depends on the trap power due to the differential light shift the trap causes on the pump transition (compare with section 3.4.5). Generally, this effect can be reduced by increasing the pump power or the pump pulse duration. The optimization of the matching of the pump light polarization to the quantization axis of the atoms is shown in figure 5.8(c). When the polarization is not matched properly, the  $\sigma^\pm$  components in the pump light compromise the accumulation of population in  $F = 4, m_F = 0$ , and the pumping efficiency is reduced.

The overall pumping efficiency is most likely limited by  $\Delta F = 1, \Delta m_F = 0$  coherences induced by the narrow linewidth of the two pumping lasers [65]. Basically, two photon Raman processes take place and undermine the necessary real excitations

of the atoms and subsequent decay into the clock level. These coherences can be reduced moving one of the lasers to the D1 line. A laser  $\pi$ -polarized relative to the quantization axis of the atoms and applied to the  $6S_{1/2}(F=4) \rightarrow 6P_{1/2}(F'=4)$  transition again cannot address the  $F=4, m_F=0$  atoms and the population will accumulate in  $|4\rangle$ . The two photon resonance of the pump laser and the repump light (which is kept on the  $6S_{1/2}(F=3) \rightarrow 6P_{3/2}(F'=4)$ ) transition does not exist. In addition, the off resonant excitation channels  $F=4 \rightarrow F'_{D2}=3, 5$  which are only  $\Delta_{F'_{D2}=3, F'_{D2}=4} = 201$  MHz and  $\Delta_{F'_{D2}=4, F'_{D2}=5} = 251$  MHz detuned from the pump transition are reduced to a single channel  $F=4 \rightarrow F'_{D1}=3$  which is significantly further detuned ( $\Delta_{F'_{D1}=3, F'_{D1}=4} = 1.2$  GHz) from the desired pump transition involving the dark state. The laser setup for this “D1 line pumping configuration” is discussed in appendix B. This way, we can improve the optical pumping efficiency by about 10%. All of the data presented has, however, been acquired with optical pumping on the D2 line, since the gain in the efficiency was judged too small compared to the effort of keeping an additional laser stabilized.

The purity of the ensemble partly initialized to the  $|4\rangle$  clock state can be further enhanced. Here we exploit the fact that the microwave transition is very narrow compared to the splitting of the magnetic substates due to the magnetic bias field. The field shifts the magnetic field sensitive transitions so far out of resonance that their population will not respond to a driving field at the clock frequency, compare figure 5.7. A microwave  $\pi$ -pulse resonant with the clock transition therefore only transfers the  $|4\rangle$  atoms into  $|3\rangle$ , while atoms in  $F=4, m_F \neq 0$  are not affected. With the clock level atoms stored in the  $|3\rangle$  state, blue detuned laser light on the cycling  $F=4 \rightarrow F'=5$  transition from the MOT beams only affects the unwanted atoms and after few hundred microseconds of pumping pushes these atoms out of the dipole trap. The effect of this state purification is illustrated in the inset of figure 5.8(a). It can also very nicely be observed by comparing figure 5.9 where no cleaning has been applied and the transfer efficiency of the microwave is limited to figure 5.10 where the microwave can transfer basically all atoms in the sample. This purification stage is also indicated in figure 5.4. Comparing again with the programme stages in figure 3.4, the  $\pi$  pulse is applied at the end of stage 6 (stage 6 as such is only a waiting stage to make sure that the shutters are closed) and the actual cleaning takes place in stage 7 by opening the shutter of the cooling laser (blue detuned, so it is, *in fact*, a heating laser) and switching its AOM on. With this state cleaning mechanism, we produce samples of  $\gtrsim 99\%$  purity.

## 5.4 Non-destructive observation of Rabi oscillations

Both in section 3.4 and in the previous sections, the non-destructive character of the interferometric probing has been demonstrated for atoms prepared in their energy eigenstate. It is, however, a far larger challenge to actually measure a “real” quantum mechanical state non-destructively, i.e., a superposition state  $|\psi\rangle = a|4\rangle + b|3\rangle$  with arbitrary probability amplitudes. Furthermore, we want to observe the evolution of the clock state population under resonant driving – follow Rabi oscillations in real time. Before we discuss the corresponding experimental data, let us shortly discuss which additional complications to expect due to probe photon

absorption by the single atoms.

### 5.4.1 Spontaneous photon scattering

For probe light blue detuned ( $\Delta_{45} = +160$  MHz) from the transition, the treatment of the light-atom coupling can to lowest order be restricted to the  $F = 4 \rightarrow F' = 5$  transition. When a probe photon is spontaneously scattered by an atom, i.e., the atom is excited to a  $F' = 5$  level and subsequently emits a photon, two cases have to be distinguished. In the case of elastic Rayleigh photon scattering, the excited atom (since we assume a polarized sample, the  $\pi$ -polarized probe light can only excite it into the  $F' = 5, m_{F'} = 0$  level) decays back into the  $F = 4, m_F = 0$  level. If the atom originally was in the  $|4\rangle$  state, the scattering event also takes the atoms back into its original internal state. The coherence of the ensemble remains unchanged. If, on the other hand, the ensemble was in a superposition state  $|\Psi\rangle = (a|4\rangle + b|3\rangle)^{\otimes N}$  the single atom  $i$  undergoing a transition will be projected into  $|4\rangle$ . The probability for this to happen is proportional to the scattering probability and the probability  $|a|^2$  for the atom to actually be in state  $|4\rangle$ . This changes the length of the mean Bloch vector (unless  $|a|^2 = 1$  or  $|a|^2 = 0$ ) and therefore the coherence of the sample. The situation would be different if the probe light were detuned exactly between the  $F = 4 \rightarrow F' = 5$  and  $F = 3 \rightarrow F' = 2$  transitions, such that the scattered photon does not carry any information on the state of the atoms and therefore superposition states are still allowed after the interaction [66]. When the atom, on the other hand, decays through a  $\sigma^\pm$  transition into one of the neighboring  $F = 4, m_F = \pm 1$  magnetic substates, the atom is inevitably removed from the clock states and coherence is lost regardless of the previous state of the atom. The branching ratio for these inelastic Raman scattering events relative to the elastic Rayleigh events is  $\sqrt{\frac{8}{5}}$ . Since the dipole trap has a depth of  $\sim 3000$  photon recoil units, single scattering events do only change the coherence of the atomic ensemble but do not expel the atoms from the trap. To measure the quantum state of the atomic ensemble in a non-destructive way, the light level of the probe beam therefore has to be reduced to a level where these scattering events become negligible. In this sense, non-destructive probing of a superposition state is much more challenging than probing trap properties as demonstrated in section 3.4 and [2]. The necessary reduction of probe photon number was one of the main motivations to develop and implement the ultra low noise photo detector discussed in chapter 4.

### 5.4.2 Experimental observation of Rabi oscillations

To observe Rabi oscillations on the clock transition, we first make sure that the synthesizer output frequency is close to the clock transition frequency. The most accurate way is Ramsey spectroscopy which will be discussed in section 5.7. The transition frequency can also be determined by minimizing the effective Rabi frequency of the oscillations  $\Omega = \sqrt{\Omega_R^2 + \Delta^2}$  one observes [51]. Of course, Rabi oscillations can also be observed with off-resonant driving, only the Rabi frequency cannot be directly extracted.

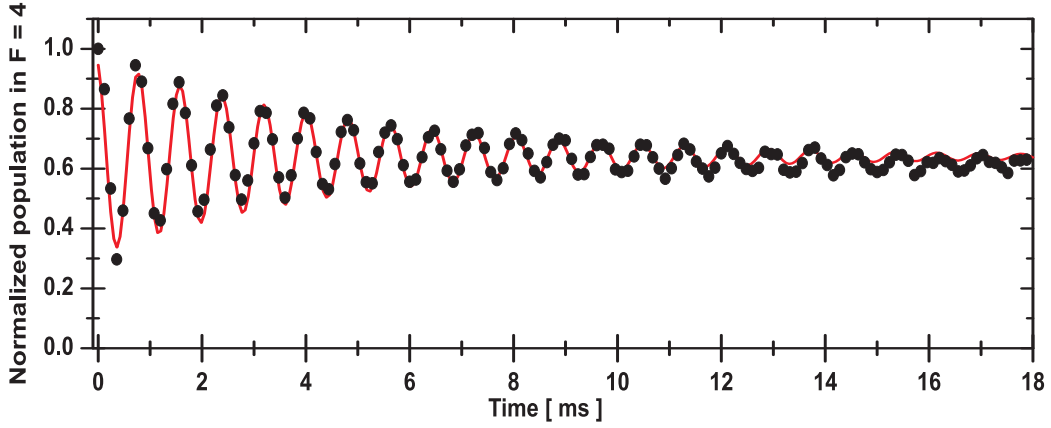


**FIGURE 5.9:** *Non-destructive observation of Rabi oscillations. The sample has not been purified prior to inducing the oscillations. The optical pumping efficiency is not optimized fully, therefore we only have about 70% of the atoms oscillating between the states. The sample is probed every 120  $\mu\text{s}$  with 2  $\mu\text{s}$  probe pulse duration. We observe a Rabi frequency of  $\Omega_R = 1.25 \text{ kHz}$  induced by about  $P = 20 \text{ mW}$  microwave power.*

A first example of non-destructive probing of coherent state evolution is shown in figure 5.9. Here, the sample has not been purified after optical pumping, so the oscillations rest on a baseline which is not the empty interferometer level. After optical pumping, we induce oscillations by applying a dc microwave field of  $\sim 20 \text{ mW}$  power. We probe the sample every 120  $\mu\text{s}$  with 2  $\mu\text{s}$  long pulses and extract a Rabi frequency of  $\Omega = 1.25 \text{ kHz}$ . The synthesizer frequency was set to 9.192.600.700 Hz which corresponds to an actual output frequency of  $\omega_0 = 9.192.631.541 \text{ Hz}$  when determined on a newly calibrated spectrum analyzer. From the data, an optical pumping efficiency of 70% is estimated.

When we increase the microwave power to 1 W and use a purified sample, we obtain signals as shown in figure 5.10. In the data presented, the ensemble quantum state has been probed with 0.2  $\mu\text{s}$  long light pulses at a repetition period of 2.3  $\mu\text{s}$  and the microwave field has been kept on during the whole observation. Each probe pulse contains  $\lesssim 10^5$  probe photons and with the repetition rate given, the oscillations are probed almost 50 times per Rabi cycle! In the not-averaged raw data shown in figure 5.10(a), the oscillations are clearly visible albeit with some noise. The signal to noise ratio can easily be improved by averaging over several experimental realizations as shown in figure 5.10(b) and (c). Applying a running average filter after 8 ms of continuous driving, the oscillations are still clearly visible – after having been probed  $\sim 3500$  times up to then. Altogether, this demonstrates the capability of the setup to measure the quantum state, i.e., also arbitrary superposition states  $|\Psi\rangle = (a|4\rangle + b|3\rangle)^{\otimes N}$  and its coherent evolution non-destructively and in real time.

The decay of the oscillation envelope is due to the movement of the atoms in the trap – differential light shift of the ground states in the dipole trap and the inhomogeneity of the microwave field across the sample. The spontaneous probe photon scattering probability per light pulse is negligible. We have confirmed this interpretation by starting the probe pulses after the microwave field had already

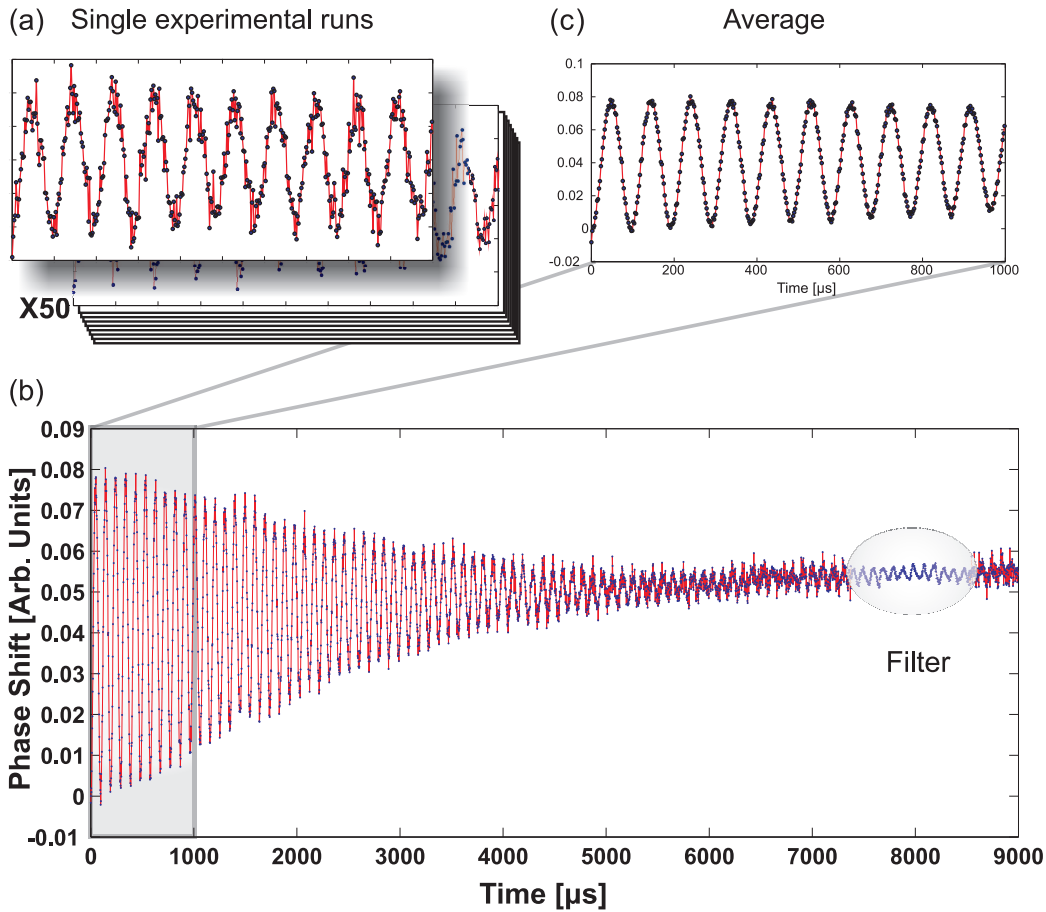


**FIGURE 5.10:** *Non-destructive observation of Rabi oscillations on the clock transition. (a) Single experimental realization of quantum state probing. The population in  $F = 4$  is determined by light pulses with  $0.2 \mu\text{s}$  duration at  $2.3 \mu\text{s}$  repetition period. (b) The oscillations are clearly visible through a 8-point running average filter, even after  $8 \text{ ms}$ , where the sample had been probed for  $\sim 3500$  times. (c) A zoom into the first millisecond of the data reveals the quality of the data. The signal to noise ratio is impressive.*

been applied for  $t = 500 \mu\text{s} - 3 \text{ ms}$ . The oscillation amplitude observed at that later time  $t$  is equal to the remaining amplitude observed in figure 5.10 at that delay time  $t$ . The effects of probing on the Rabi oscillations will be studied in detail in section 5.5. The shorter coherence time of the data in figure 5.10 compared to the data in figure 5.9 is due to the inhomogeneity of the microwave field across the sample and the differential light shift. By augmenting the microwave power between the two data sets from  $P \sim 20 \text{ mW}$  to  $P \sim 1 \text{ W}$ , we increase the Rabi frequency to  $\Omega = 10.1 \text{ kHz}$ . Rearranging the microwave setup depicted in figure 5.2 to minimize power loss in various components allows us to increase the Rabi frequency to up to  $\Omega = 16 \text{ kHz}$ .

### Multiple observation of oscillations

From section 3.4.1 we know that the lifetime of the trapped ensemble is much longer than the coherence time observed above. We can therefore repeat the preparation

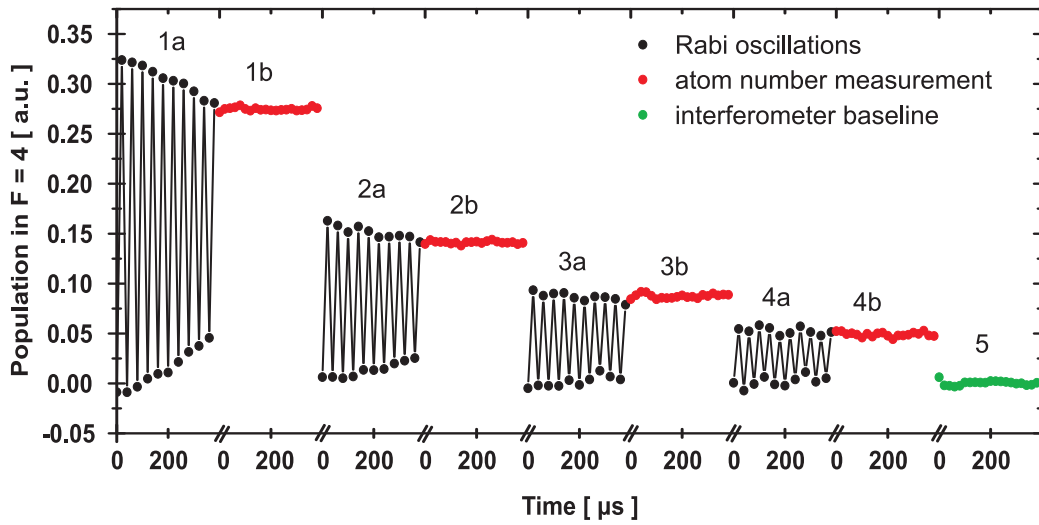


**FIGURE 5.11:** Multiple preparations of the ensemble, observation of Rabi oscillations (1a, 2a, 3a, 4a) and determination of the respective atom numbers (1b, 2b, 3b, 4b) after repumping the ensemble. Where the time axis is discontinuous, the preparation, repumping or removing stages take place; these last several 10 ms. The graph clearly demonstrates the advantages of segmented data storage as discussed in section 3.3.2.

and probe stages several times after loading the trap once. The data presented in figure 5.11 shows four observations of oscillations and corresponding atom number measurements in one trap cycle. The sequence also serves as an illustration of the atom number estimation and normalization procedures, and interferometer baseline determination mentioned in section 5.3.1. After a sample has been initialized to the  $|\Psi\rangle = |3\rangle^{\otimes N}$  state, i.e., optically pumped and cleaned, Rabi oscillations are induced and observed (time section 1a). The sample is then repumped to the  $F = 4$  level and the remaining number of atoms is measured (1b). This procedure (initialization to  $|3\rangle$ , observation of Rabi oscillations, repumping and determination of remaining atom number) is repeated four times. Thereafter the atoms are heated out of the trap and the lock point of the interferometer during the cycle is measured. Subtracting the baseline from the other data removes the influence of interferometer drifts, and knowing the trap decay time allows one to normalize the oscillations to the number of atoms present in the respective stages.

### “Top–bottom” probing

During optimization of the microwave parameters, for example when finding the  $\pi$ -pulse duration, it is beneficial not to be limited by the technical noise present in a single measurement cycle as shown in figure 5.10(a). The most obvious way to get a better signal to noise ratio is increasing the probe photon number. This, however, will have direct effects on the spontaneous photon scattering probability and the dephasing caused by the differential light shift to be discussed in section 5.5. The influence of both effects can be reduced by probing the sample when all atoms are in an energy eigenstate, i.e., on the poles of the Bloch sphere. The only directly destructive effects are then caused by inelastic scattering events. To obtain this

situation, we split the extended microwave pulse into  $\pi$  pulses and probe in between these pulses. We then get signals as shown in figures 5.8(a) and figure 5.11. The oscillations are then only sampled two times per oscillation period which reduces the number of photons interacting with the atoms compared to the oscillation over sampling shown, e.g., in figure 5.10. This allows one to increase the photon number per pulse while keeping the spontaneous photon scattering probability constant, which increases the single-shot signal to noise ratio. Additionally, the differential light shift effects discussed in section 5.5 are suppressed.

### 5.4.3 Two color probing of Rabi oscillations

In the data presented until now only probe pulses sensitive to the  $F = 4$  state have been used. As discussed in section 2.4.2 and 3.2 using a second probe laser beam close to resonance to the  $F = 3 \rightarrow F' = 2$  transition allows to determine the population in the  $F = 3$  states. We chose the additional probe color to be  $\Delta_{32} = -135$  MHz red detuned from the  $6S_{1/2}(F = 3) \rightarrow 6S_{3/2}(F' = 2)$  transition. The detuning has been chosen such that the phase shift of the second probe color  $\Delta\phi_3$  is the same as  $-\Delta\phi_4$  for equal populations in each level as discussed in connection with figure 3.8(a). Using the same probe power in both colors, the interferometer fringes have the same amplitude and consequently the signals  $S_{\max,3}$  for  $|\Psi\rangle = |3\rangle^{\otimes N}$  and  $S_{\max,4}$  for  $|\Psi\rangle = |4\rangle^{\otimes N}$  are related as  $S_{\max,4} = -S_{\max,3}$ . In figure 5.12(a) the individual signals of the two probe colors. The sample has not been purified, so the  $F = 4$  signal rests on a baseline while the oscillations of the  $F = 3$  state populations start out at zero. When we send bi-chromatic probe pulses through the interferometer, the phase shift signal gives directly the difference between the clock level populations. Figure 5.12(b) shows the observation of Rabi oscillations with both probe pulse colors at the same time for a purified sample and with the probe coupling strengths optimized to satisfy  $S_{\max,4} = -S_{\max,3}$ . Normalizing the data to the atom number would directly give the  $W$ -component of the ensemble Bloch vector  $\mathbf{U}$ . The association of the length of the Bloch vector with the coherence in the sample is very nicely illustrated. When coherence is lost, i.e., the sample dephases or is partly projected into a mixed state, the amplitude of the Rabi oscillations decreases. On the timescales in question here, the lifetime of the atoms in the trap can be regarded as a minor issue.

## 5.5 Inhomogeneous light shift effects on Rabi oscillations

In section 5.4.1 we have discussed the influence of spontaneous photon scattering on the quantum state of the ensemble. In the data shown in the previous section, the probing is non-destructive in the sense that the spontaneous photon scattering per probe pulse is kept very low. However, even for negligible spontaneous scattering, the atomic quantum state will be affected: The dispersive light-atom interaction will introduce a phase shift between the atomic states  $|3\rangle$  and  $|4\rangle$  due to the differential light shift on the clock transition caused by the probe itself [67]. In this section, which follows very closely the discussions in [5], we consider the effect

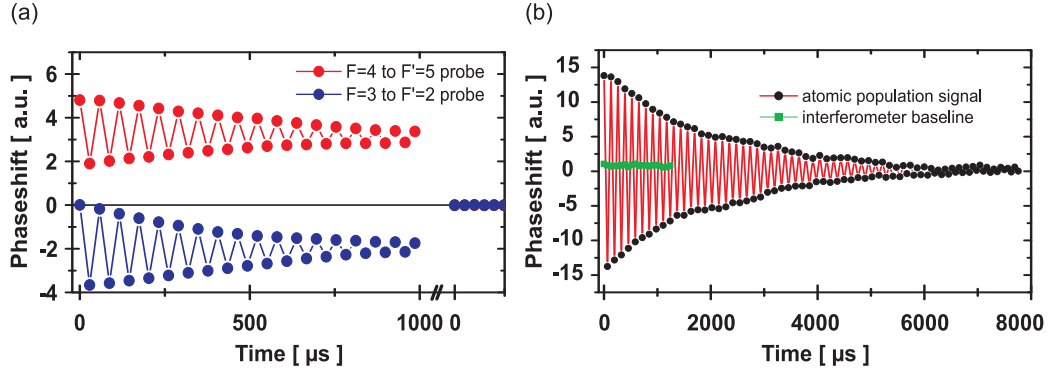


**FIGURE 5.12:** *Two color observation of Rabi oscillations. (a) The individual probe colors gain opposite phase shifts from the atoms they couple to. The sample has not been cleaned so the  $F = 4$  signal rests on a baseline from atoms not being addressed by the microwaves. (b) Oscillations from a cleaned sample. The phase shift signals have opposite sign for atoms in  $|3\rangle$  and  $|4\rangle$ , the oscillations are therefore centered around the empty interferometer baseline. For an equal superposition state  $|\Psi\rangle_{R(\pi/2)} = \frac{|3\rangle + |4\rangle}{\sqrt{2}}$  the interferometer signal is zero. Using bi-chromatic probing, the connection of the signal to the Bloch vector component  $W$  is very obvious.*

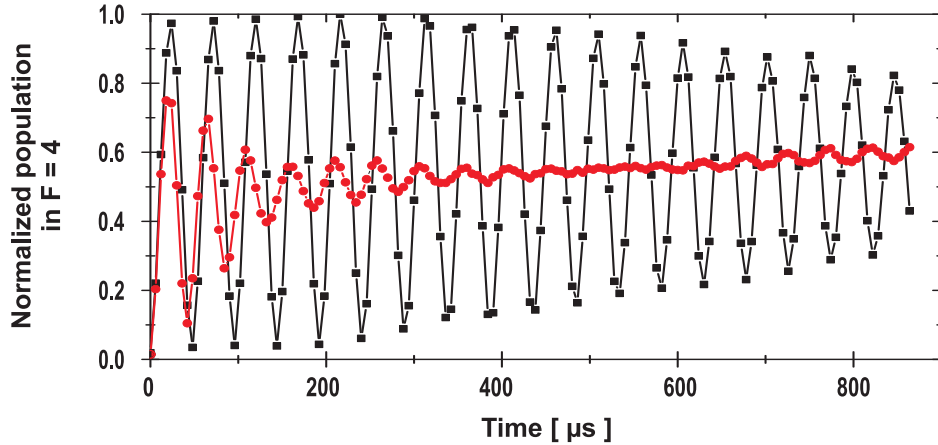


**FIGURE 5.13:** *Rabi oscillations for different probe powers. Changing the probe strength from  $1.5 \times 10^5$  photons per pulse (data indicated with ■) by a moderate factor of 4, a drastic change in the Rabi oscillation's envelope occurs (data indicated by ●). The solid lines are to guide the eye, only.*

of probing on the quantum state more closely with focus on the implications for the non-destructive probing of Rabi oscillations. We will continue the discussion in section 5.7 to gain further insight.

When probing Rabi oscillations non-destructively as demonstrated in figure 5.10, we observe a very distinct change in the envelope when changing the probe power rather moderately. Figure 5.13 shows two traces of Rabi oscillations recorded with the same probe pulse duration of  $1.0 \mu\text{s}$  and  $7 \mu\text{s}$  repetition period but with different probe photon numbers. With  $1.5 \times 10^5$  photons per pulse we obtain a decay constant of  $\tau = 1.5 \text{ ms}$ , which reduces to  $\tau = 80 \mu\text{s}$  when the photon number per pulse is increased to  $6.3 \times 10^5$ . This much faster decay cannot be explained just

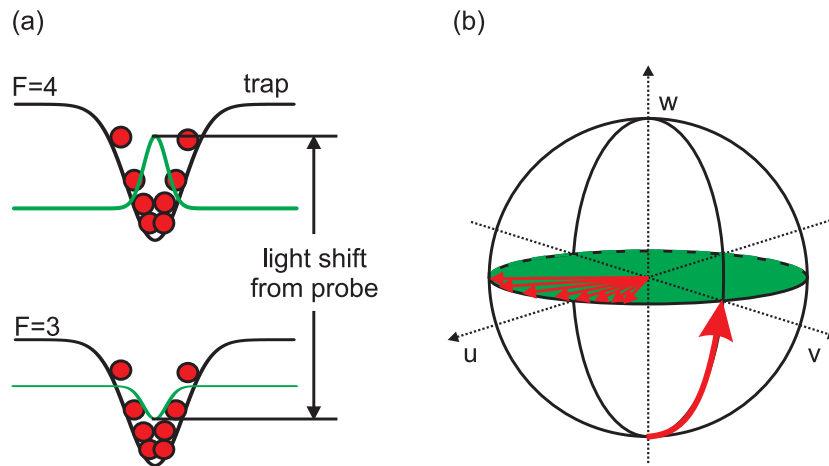


**FIGURE 5.14:** (a) The probe light shifts the energy levels of the atoms according to their position in the probe beam. While being blue detuned from one transition, thereby augmenting its energy, the probe beam is at the same time red detuned from the other transition and reduces its energy. (b) The position dependence of the differential light shift induces a position dependent phase shift in the atomic ensemble. This dephasing of the single atoms, indicated by the phase distribution of the single atom Bloch vectors leads to a reduction of the mean Bloch vector length.

by the four times higher spontaneous excitation probability. Additionally, the trace corresponding to the higher probe power shows a clear revival of the oscillations at around  $t = 800 \mu\text{s}$ , and an increase in the Rabi oscillation frequency is observable. In the following sections, we systematically analyze these effects and demonstrate that they can be well understood when taking the spatial inhomogeneity of the probe beam into account which causes a spatial distribution of the differential light shift between the clock states.

### 5.5.1 Theoretical model

#### Light shift revisited

In section 3.1.3 we have discussed the working principle of an optical dipole trap: the off resonant coupling of an electro magnetic radiation field shifts the energy levels of the atoms. The energy shift  $\Delta E_g$  of the ground state is given in equation (3.5). Applying off-resonant probe light shifts the energy levels as well. While the blue detuned  $F = 4 \rightarrow F' = 5$  light increases the energy of the  $F = 4$  state, it also interacts as  $\Delta \sim -9.2 \text{ GHz}$  red detuned light with the  $F = 3 \rightarrow F' = 2$  transition, shifting the energy of the  $F = 3$  ground state downwards. The result is a differential light shift between of the clock levels which changes the transition frequency as illustrated in figure 5.14(a). The trapping potential (equation (3.7) on page 33), and thus the energy shift can also be written as [46]:

$$\delta E_g(\mathbf{r}) = \hbar \Delta \omega = \frac{\hbar \gamma^2}{8} \frac{I(\mathbf{r})}{I_s} \frac{1}{\Delta} \quad (5.36)$$

where we have introduced the saturation intensity  $I_s = 1.1 \text{ mW/cm}^2$ . We therefore expect a transition frequency shift of:

$$\chi(\mathbf{r}) \equiv \Delta\omega(\mathbf{r}) = \frac{\gamma^2 I(\mathbf{r})}{8 I_s} \left( \frac{1}{\Delta_{45}} - \frac{1}{\Delta_{45} - 9.192 \text{ GHz}} \right) \quad (5.37)$$

for the time a probe laser is applied with detuning  $\Delta_{45}$  from the  $F = 4 \rightarrow F' = 5$  resonance. Assuming a homogeneous power distribution of a 100 nW beam across an area corresponding to a beam waist of  $w_0 = 20 \mu\text{m}$  we get a differential light shift of  $\chi = 2\pi \cdot 0.25 \text{ MHz}$ . Since the differential light shift is position dependent, following the intensity distribution of the Gaussian probe beam, the atomic levels will be shifted according to the atoms position in the probe beam. This leads to an inhomogeneous light shift distribution:

$$\chi(\mathbf{r}) = \chi_0 \exp\left(-\frac{2r^2}{w(z)^2}\right) \quad (5.38)$$

where  $\chi_0 = \chi(r = 0, z = 0)$  corresponds to the maximum light shift at the center of the Gaussian beam. This dephasing is indicated in figure 5.14(b) for an ensemble in a equal superposition state.

### Inhomogeneous light shift distribution across the atomic ensemble

To model the inhomogeneous coupling of a probe beam with Gaussian intensity distribution to an atomic ensemble confined by a dipole trap beam with Gaussian intensity, we introduce the column density of the atomic sample in polar coordinates  $(r, \phi)$  by  $n(r) = n_0 \exp(-2r^2/r_0^2)$ . The slightly unconventional definition of the column density is motivated by the comparison with the light intensity distribution; this way, the final result only depends on the ratio between the probe beam waist  $w_0$  and the sample ‘‘waist’’  $r_0$  without additional factors of 2.  $n_0$  is the peak column density and  $r_0$  characterizes the sample radius. The atomic sample interacts with a Gaussian laser beam propagating along the  $z$ -axis and focussed at the sample’s location. In the case when the axial size of the atomic sample is short compared to the Rayleigh range of the laser beam we can approximate the light intensity distribution within the interaction volume by  $I(r) = I_0 \exp(-2r^2/w_0^2)$ , where  $I_0$  is the peak intensity and  $w_0$  is the Gaussian beam waist, the  $z$  dependence of  $\chi(\mathbf{r}) = \chi(r, z)$  is thus integrated over.

As discussed in section 5.1.1 the evolution of an initial Bloch vector  $\mathbf{U}_0$  can be propagated by multiplying the corresponding matrices, e.g., (5.30) and (5.31) in succession to get an overall transfer matrix  $T(\chi, t)$ . Due to symmetry, it is obvious that a differential light shift  $\hbar\chi = \Delta E$  of the clock levels for a certain duration  $t$  has the same effect as detuning the microwave field from resonance by the same amount  $\Delta = \Delta E$  for the same time  $t$ .

From the Gaussian intensity profile of the laser beam, we get a position dependent light shift and  $\chi$  will vary radially as  $\propto I(r)$  as given in equation (5.38). Moreover, in the detection of the  $W$ -projection of  $\mathbf{U}$ , the Gaussian intensity dependence of the probe laser beam in conjunction with the Gaussian column density of the atomic

sample gives rise to a signal:

$$\begin{aligned}
S_\phi(t) &\propto \int_0^\infty [T(\chi(r), t)\mathbf{U}]_W n(r) I(r) r dr \\
&\propto \int_0^\infty [T(\chi(r), t)\mathbf{U}]_W n_0 I_0 e^{-2\left(\frac{r}{r_0}\right)^2} e^{-2\left(\frac{r}{w_0}\right)^2} r dr \\
&\propto \int_0^{\chi_0} [T(\chi, t)\mathbf{U}]_W \chi \left(\frac{w_0}{r_0}\right)^2 d\chi
\end{aligned} \tag{5.39}$$

Hence, for a given ratio between  $r_0$  and  $w_0$  the net measured Bloch vector results from infinitesimal contributions from atoms with light shifts  $\chi = [0 \dots \chi_0]$  carrying a weight  $\chi \left(\frac{w_0}{r_0}\right)^2$ . In figure 5.15(c) we plot the weighting factor for a few values of the ratio  $k = w_0/r_0$ . As would be expected, the atoms contributing to the net Bloch vector have undergone practically the same light shift close to the maximum  $\chi_0$  if the laser beam waist is much larger than the atomic sample radius  $w_0 \gg r_0$ . At the other extreme  $w_0 \ll r_0$ , our detected signal will have a uniform contribution from light shifts in the interval  $[0 \dots \chi_0]$ .

### 5.5.2 Application to Rabi oscillations

To separate the rotations on the Bloch sphere caused by the driving field and the light shift, let us consider the theoretical model for the case of alternating microwave and probe pulses. If we neglect the inhomogeneity of the induced light shift, each single probe pulse will cause the tip of the Bloch vector to rotate around the  $W$ -axis according to the transformation matrix (5.31) by an angle  $\phi = \chi t$ , proportional to the number of photons of the probe pulse. Alternating microwave pulses, rotating around the  $U$ -axis according to matrix (5.30), and probe pulses, we expect a step-like evolution as shown in figure 5.15(a). In figure 5.15(b), we show the expected measurement result for each probe pulse when changing the photon number or the rotation angle  $\chi t$  induced per probe pulse. As can be seen, the discretely induced transition frequency change  $\Delta E = \hbar\chi$ , resulting from the differential light shift between the clock states, leads to a higher effective Rabi frequency  $\Omega' = \sqrt{\Omega^2 + \overline{\Delta E}^2}$ .

We can simplify the dynamics according to the above model of equation (5.39) to a quasi continuous case when the light pulses probe the sample quasi continuously. The signal can then be written as:

$$S(t) = \int_0^{\chi_0} \frac{\Omega_R^2}{\Omega_R^2 + \chi^2} \sin^2 \left( \frac{1}{2} \sqrt{\Omega_R^2 + \chi^2} t \right) \chi^{(w_0/r_0)^2} d\chi \tag{5.40}$$

The signal is basically an integral over single atom Rabi oscillations with different Rabi frequencies due to the differential light shift. In this case, the time averaged frequency change  $\overline{\Delta E} = \frac{1}{2\pi} \int \Delta E(t) dt$  can be introduced. The effect now is very similar to the Rabi frequency change one observes when the transition frequency is permanently shifted relative to the driving field by  $\Delta E$ , e.g., due to off-resonant driving or a homogeneous light shift across the sample [68]. Introducing a light-shift at discrete intervals changes the observed Rabi frequency stepwise during

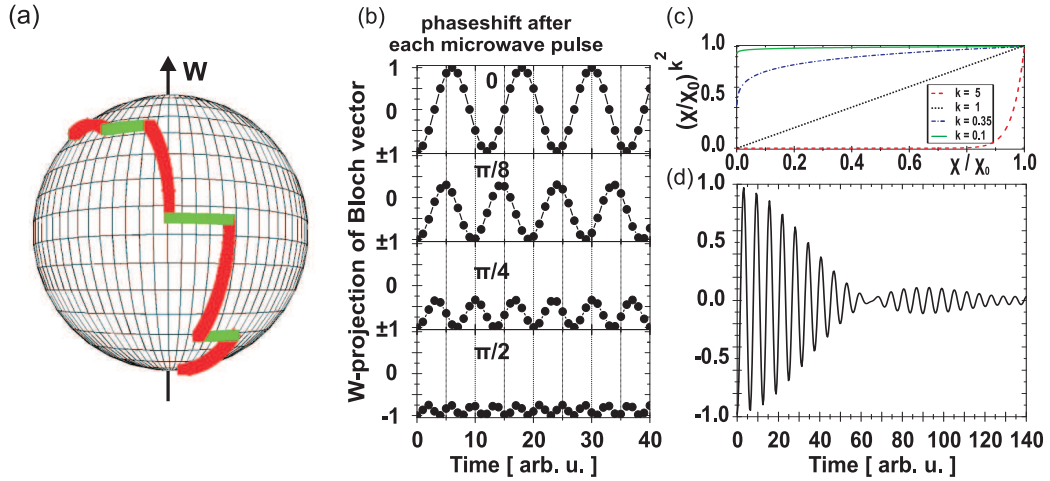


**FIGURE 5.15:** (a) State evolution on the Bloch sphere with alternating microwave pulses, each pulse shifting by  $\pi/4$  around the  $U$ -axis, and probe pulses, each causing a homogeneous shift of  $\pi/9$  around the  $W$ -axis. (b)  $W$ -projection of the Bloch vector for different homogeneous light shifts, applied discretely in between separated  $\pi/6$  microwave pulses. (c) Weighting factor of the oscillations with different frequency due to the inhomogeneity of the probe beam and the sample. The factor is plotted for different ratios  $k$  of the probe beam waist  $\omega_0$  to the sample size  $r_0$ , and normalized to its maximum value. For large ratios  $k \gg 1$ , an almost homogeneous shift is induced, for small ratios  $k \ll 1$  the distribution is flat. (d) Rabi-oscillations resulting from inhomogeneous light shift distribution across the probe area.

the single period, however, after each period  $T = \frac{2\pi}{\Omega}$  the effect is the same as if the transition frequency had been changed by a mean value  $\overline{\Delta E}$  during the whole period. In the experiment, a continuous distribution of light shifts  $\chi = [0 \dots \chi_0]$  is present and thus oscillations of different frequencies, weighted in amplitude with the density distribution of the sample across the probe beam, interfere. The resulting oscillations are shown in figure 5.15(d) for a probe size to sample ratio  $k = 0.35$  and a maximum shift of  $\chi_0 = 0.3$  rad per pulse. In the quasi continuous probing regime, the change in the Rabi frequency which happens discretely at the times of the probe pulses, is replaced with an average change.

When the light pulses are distributed more sparsely during the Rabi period, a time discrete analysis has to be applied. The effect of probing (as phase shift on the Bloch sphere as rotation around the  $W$  axis) and the driving through the microwave field (as rotation around the  $U$  axis) then have to be considered separately as indicated in figure 5.15(a) with different phase shifts according to the atomic and the probe light intensity distribution, leading to inhomogeneous dephasing as indicated in figure 5.18(a). The limiting case where the probe pulses are only applied when the Bloch vector points in the direction of the poles, has already been discussed as “top-bottom” probing of Rabi oscillations in section 5.4.2. A second case, where the probe pulses are only applied when the vector is pointing into the equatorial plane, is studied thoroughly in section 5.7 since the situation then corresponds to Ramsey and spin-echo measurements.

## Experimental results

To study the perturbing effects of the inhomogeneous atom-probe interaction systematically for the quasi continuous case, we alternate microwave and probe pulses and record data sets for different probe powers. In figure 5.16(a) we show a collection of data together with fits of the theoretical model from equation (5.40). In the fitting model, we have allowed for a small number of spontaneous scattering events, pumping atoms into the  $F = 4, m_F \neq 0$  states and homogeneous dephasing mechanisms like magnetic background fluctuations, microwave driving field inhomogeneities or cloud temperature effects [69]. The data is remarkably

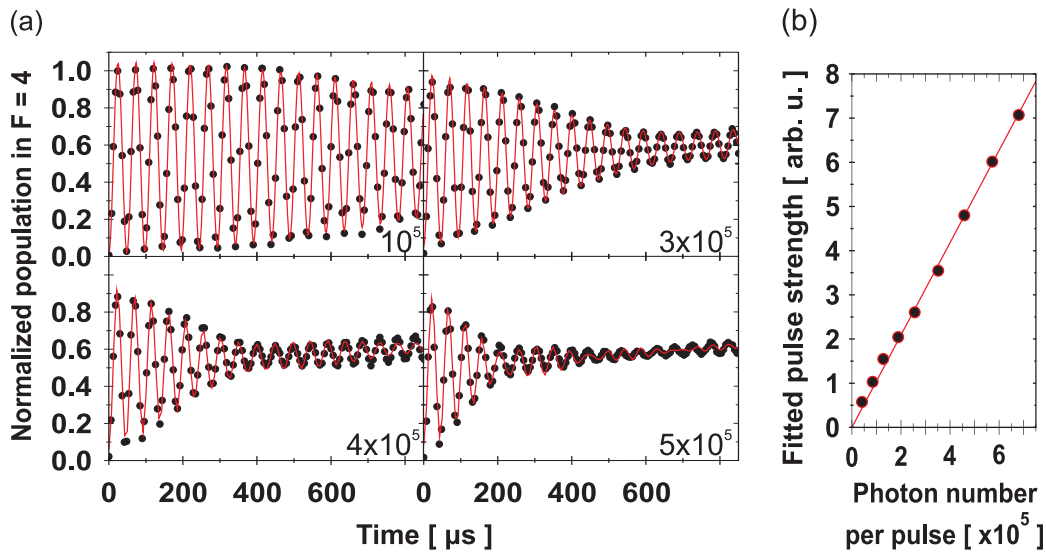


**FIGURE 5.16:** (a) *Non-destructively probed Rabi oscillations.* The photon number per probe pulse is given in the lower right corner of each graph. The solid line represents a fit to the data with the model discussed in the text. (b) *Comparison of the photon number per pulse as measured in the experiment to the pulse strength returned from the fitting routine.* The scaling is well described by a linear function through the origin.

well described by the simple model. In particular, the envelope together with the revival of the oscillations is very well reproduced. To fit the data we have used the programme Mathematica. The non-linear regression fit function can directly take arguments which are defined as integrals. The theoretical model in equation (5.40) can therefore be directly used as fitting function. The fitting routine returns a parameter  $\propto \chi_0$ , the maximum phase shift caused by the light shift, which is expected to be directly proportional to the photon number in the light-shifting pulses. The value is shown in figure 5.16(b) as function of the applied photon number, confirming the validity of our model within the given parameter range.

## 5.6 Rabi spectroscopy - transition line shape

To conclude this section on Rabi spectroscopy we use the Rabi formula (5.29) directly to determine the transition frequency. To this end, we fix a microwave pulse duration  $t = \pi/\Omega_R$  such that the pulse it resembles a  $\pi$  pulse. In this case,

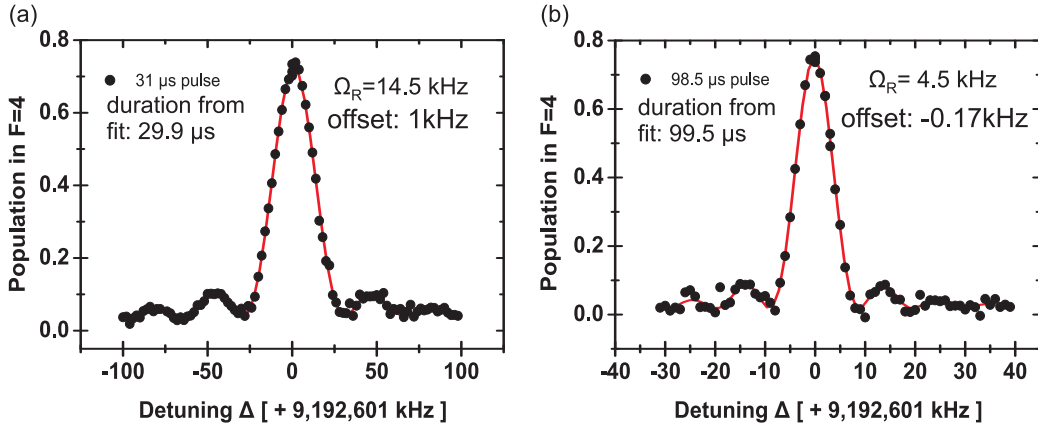


**FIGURE 5.17:** Rabi spectroscopy with two different microwave powers and corresponding Rabi frequencies. The microwave pulse duration has been arranged such that it is close to a  $\pi$  pulse on resonance. A fit to the data returns Rabi frequencies of  $\Omega = 14.5$  kHz and  $\Omega = 4.5$  kHz for the two powers, respectively, which fits to the microwave pulse durations actually used. The frequency resolution in (a) is rather poor. The value of the transition frequency extracted from (b) fits very well with the defined value, taking the offset of the synthesizer of  $30.841$  Hz into account.

the population in  $F = 4$  can be written as:

$$P_4 = \frac{\Omega_R^2}{\Omega_R^2 + \Delta^2} \sin^2 \left( \frac{\pi}{2\Omega_R} \sqrt{\Omega_R^2 + \Delta^2} \right) \quad (5.41)$$

which has its maximum at  $\Delta = 0$ . If the microwave pulse duration is slightly wrong, the maximum will remain at  $\Delta = 0$ . The maximum stays at  $\Delta = 0$  as long as the pulse is longer than a  $\pi/2$  pulse, which can be shown by deriving equation (5.29). This way, the transition frequency can be determined. In figure 5.17 two corresponding measurements are shown. The frequency resolution depends strongly on the pulse duration but the principle can be well recognized. Using equation (5.41) to fit the data allows us to extract the values of the Rabi frequency, the pulse duration and the frequency offset. From the data in figure 5.17(b) a transition frequency of  $9.192.631.751$  Hz is extracted, which is only 19 Hz off from the defined value. The main contributions to this offset are due to the second order Zeeman shift, equation (5.35), which is estimated to  $\Delta\omega_{\text{clock}} = 2\pi \cdot 427 \cdot (1.6)^2$  Hz =  $2\pi \cdot 1093$  Hz and the differential light shift from the dipole trap whose maximum value is  $\Delta\omega_l = 2\pi \cdot (-1.1)$  kHz as we shall discuss later. Minor contributions come from density shifts.

In the data shown, we also observe a maximum  $\pi$  pulse transfer efficiency of 75%, which confirms the claimed maximum optical pumping efficiency we obtain.

## 5.7 Ramsey spectroscopy

Coherence and decoherence has already been mentioned in the previous sections. Especially in the context of quantum information science, where information is stored in the coherence of atomic levels, the coherence time is equivalent to the

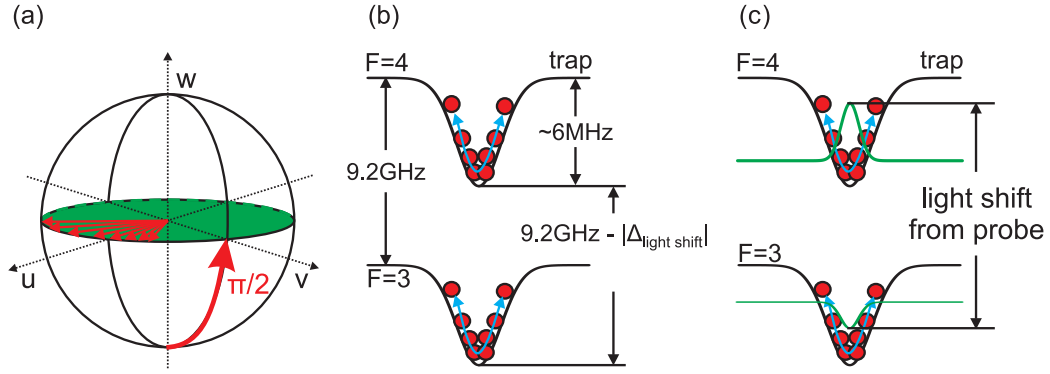


**FIGURE 5.18:** (a) Illustration of sample dephasing when initialized to an equal superposition state with a microwave  $\pi/2$  pulse. The Bloch vectors  $\mathbf{u}_i = (u, v, w)_i$  of individual atoms  $i$  obtain different phases  $\phi_i = \int_0^t \Delta_i(t') dt'$  during free precession for time  $t$ . The mean Bloch vector  $\mathbf{U} = \sum \mathbf{u}_i$  is therefore shortened and parameterizes the phase coherence of the sample. (b) The trap potential is slightly different for the two ground states  $F = 3$  and  $F = 4$  due to the hyperfine splitting  $\Delta_{\text{hfs}}$  which leads to a differential level shift of  $\Delta_{\text{light shift}} < 0$ . When atoms move back and forth in the trap as indicated by the arrows, their states gain a relative phase shift with respect to each other. (c) The coupling of a single color probe beam close to the  $F = 4 \rightarrow F' = 5$  transition increases the level splitting by different amounts, depending on the position of the atoms in the beam. The probe beam blue detuned to  $F = 4 \rightarrow F' = 5$  increases the energy of the  $F = 4$  ground state while it at the same time is red detuned from the  $F = 3 \rightarrow F' = 2$  transition and thereby decreases the energy of the  $F = 3$  ground state. When atoms move while the light pulses are applied, the differential phase shift obtained can vary in time.

maximum storage time of the medium. The most common way to determine the coherence time of a system is Ramsey and spin echo spectroscopy and these techniques are in the focus of this section. As we shall see, Ramsey spectroscopy basically determines the phase accumulation between the two states during a free precession time relative to the rotating frame of the microwave field. Ramsey spectroscopy itself can be cast into the language of an interferometer again, the sequence can then be regarded as an interferometric determination of the phase difference, very much like the Mach Zehnder interferometer. It therefore presents an ideal toolbox to study external perturbation of these levels, as caused, e.g., by the differential light shift of applied probe light pulses or the dipole trap potential. When studying the reversibility of the induced perturbations with echo spectroscopy, information on the nature of the perturbations and on the trap dynamics can be extracted.

In a dipole trapped sample, dephasing is the main decoherence mechanism. When a coherent superposition state  $|\Psi\rangle = \left(\frac{|3\rangle + |4\rangle}{\sqrt{2}}\right)^{\otimes N}$  is prepared, perturbations of the transition, leading to a time dependent detuning  $\Delta_i(t)$  of the microwave field from the transition, change the phase  $\phi_i = \int \Delta_i(t') dt'$  between the two clock states according to equation (5.31):  $|\Psi\rangle \rightarrow \frac{1}{\sqrt{2}^N} \prod_i (|3\rangle + e^{i\phi_i} |4\rangle)$ . Since the detuning can be different for each atom  $i$  in the sample, the phase accumulated differs from atom to atom and leads to the effective reduction of the Bloch vector as discussed in section 5.1.2. The process is illustrated in figure 5.18(a). We will discuss two different dephasing mechanisms. The first one is induced by the differential light shift between the clock levels caused by the dipole trapping potential. Further, we con-

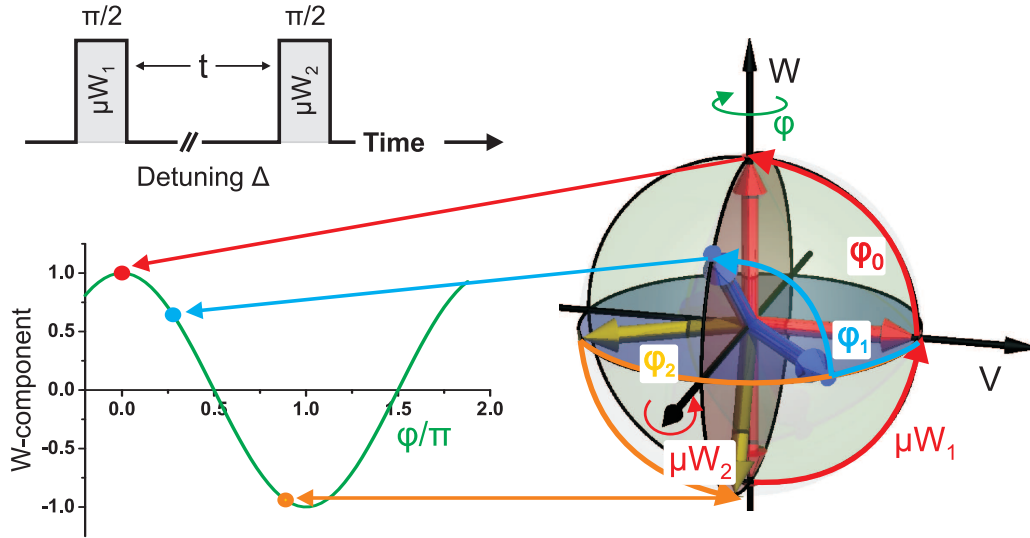


**FIGURE 5.19:** Principle of Ramsey spectroscopy. Two microwave  $\pi/2$ -pulses are applied to the sample with temporal separation  $t$  and microwave field detuning  $\Delta < 0$ . During the free precession time  $t$  in the superposition state created by the first  $\pi/2$  pulse, the atomic states accumulate a relative phase  $\phi = t\Delta$  with respect to the rotating frame of the microwaves. This shifts the orientation of the Bloch vector by the angle  $\phi$ . The second  $\pi/2$  pulse projects this phase onto the  $W$ -axis of the Bloch sphere and thereby becomes measurable as population difference. The rotations and measurement results are illustrated for  $\phi_0 = 0^\circ$ ,  $\phi_1 = 50^\circ$  and  $\phi_3 = 150^\circ$ .

tinue the discussion of the influence of the spatial inhomogeneity and consequently the inhomogeneous differential light shift induced by probe light, as discussed in section 5.5.1.

### 5.7.1 Principle of Ramsey spectroscopy

#### Illustration in the Bloch vector picture

The basic microwave pulse sequence for Ramsey spectroscopy is illustrated in figure 5.19 together with the induced rotations of the Bloch vector. Briefly, the principle is as follows: Beginning from an initial state, where all atoms reside in  $|3\rangle$ ,  $\mathbf{U}_0 = (0, 0, -1)$ , a  $\pi/2$ -pulse brings the ensemble into a superposition state  $|\Psi\rangle = \left(\frac{|3\rangle + i|4\rangle}{\sqrt{2}}\right)^{\otimes N}$ .<sup>5</sup> The quantum state then evolves freely for a fixed time  $t$ . The population measured in  $|4\rangle$  after a second  $\pi/2$ -pulse depends on the relative phase  $\phi$  between the two atomic states  $|3\rangle$  and  $|4\rangle$ ,  $|\Psi\rangle_{\text{in}} \mapsto |\Psi\rangle_{\text{evol}} = \frac{1}{\sqrt{2}^N}(|3\rangle + e^{i\phi}|4\rangle)^{\otimes N}$  acquired during the free evolution. For  $\phi \bmod 2\pi = 0$  we end up at  $|\Psi\rangle_{\text{out}} = |4\rangle^{\otimes N}$ ,

<sup>5</sup>We have not been entirely consistent in the transformations between the Bloch vector  $\mathbf{U}$  and the atomic state vector  $|\Psi\rangle$ . According to the definitions in section 2.3, the state corresponding to  $\mathbf{U}_{\pi/2} = (0, 1, 0)$  is  $|\Psi\rangle = \left(\frac{|3\rangle + i|4\rangle}{\sqrt{2}}\right)^{\otimes N}$ . We have, however, often referred to the superposition state after a single  $\pi/2$  pulse as  $|\Psi\rangle = \left(\frac{|3\rangle + |4\rangle}{\sqrt{2}}\right)^{\otimes N}$ . In the end, the effect is a trivial rotation of the coordinate system and can be formally accounted for by putting the phase of the microwave field to  $\pi/2$  before transforming into the rotating frame.

$\phi \bmod 2\pi = \pi$  yields  $|\Psi\rangle_{\text{out}} = |3\rangle^{\otimes N}$  and  $\phi \bmod 2\pi = (\pi/2, 3\pi/2)$  yields  $|\Psi\rangle_{\text{out}} = \left(\frac{|3\rangle \pm |4\rangle}{\sqrt{2}}\right)^{\otimes N}$ . It is clear that the output signal of such a measurement depends on the phase  $\phi(t) = \int_0^t \Delta(t') dt'$  accumulated during the free evolution time, where  $\Delta(t)$  is the detuning of the microwave field relative to the transition. This detuning can be time and position dependent and different for each single atom in the ensemble as discussed above. The  $W$ -projection of the Bloch vector after the microwave sequence can easily be calculated from the rotation matrixes (5.30) and (5.31):

$$\begin{aligned} \mathbf{U}_{\text{out}} &= \underbrace{\begin{pmatrix} 1 & 0 & 0 \\ 0 & 0 & -1 \\ 0 & 1 & 0 \end{pmatrix}}_{\text{second } \pi/2 \text{ pulse}} \times \underbrace{\begin{pmatrix} \cos t\Delta & \sin t\Delta & 0 \\ -\sin t\Delta & \cos t\Delta & 0 \\ 0 & 0 & 1 \end{pmatrix}}_{\text{free precession for time } t} \\ &\times \underbrace{\begin{pmatrix} 1 & 0 & 0 \\ 0 & 0 & -1 \\ 0 & 1 & 0 \end{pmatrix}}_{\text{first } \pi/2 \text{ pulse}} \times \underbrace{\begin{pmatrix} 0 \\ 0 \\ -1 \end{pmatrix}}_{\text{initial state}} \end{aligned} \quad (5.42)$$

$$= \begin{pmatrix} \sin \Delta t \\ 0 \\ \cos \Delta t \end{pmatrix} \mapsto \begin{pmatrix} -\sin \phi(t) \\ 0 \\ \cos \phi(t) \end{pmatrix} \quad (5.43)$$

Without decoherence, the output signal of a Ramsey measurement, only sensitive to the atoms in  $F = 4$ , has an oscillatory behavior and is called Ramsey fringes:

$$P_4 = \frac{1 + \cos \phi(t)}{2} \quad (5.44)$$

### 5.7.2 Inhomogeneous dephasing due to differential light shift of the dipole trap

First, we shall consider the effect of spatial inhomogeneity caused by the dipole trapping beam. We expect the trap depth to be slightly different for the two ground states  $F = 3$  and  $F = 4$  because one of them is detuned by 9.2 GHz more from the trap laser than the other. The difference in the light shift of the two levels is equivalent to the difference discussed in section 5.5.1 for the probe beam coupling off resonantly to the two ground levels.

In section 3.1.3 we have discussed the dipole trap potential, equation (3.11):

$$U_0 = \frac{c^2 P}{w_0^2} \left( \frac{\gamma_{D1}}{\omega_{D1}^3 \Delta_{D1}} + \frac{2\gamma_{D2}}{\omega_{D2}^3 \Delta_{D2}} \right) \quad (5.45)$$

where  $P$  is the power of the trapping beam and  $w_0$  is its waist.  $\Delta_{D1}$  and  $\Delta_{D2}$  are the detunings of the trap laser from the D1 and D2 line with transition frequencies  $\omega_{D1}$  and  $\omega_{D2}$ , whose natural linewidths are  $\gamma_{D1}$  and  $\gamma_{D2}$ , respectively. This equation can be simplified by neglecting the difference in the transition frequencies  $\omega_0 \equiv$

$\omega_{D1} \approx \omega_{D2}$  and in the linewidths  $\gamma \equiv \gamma_{D1} \approx \gamma_{D2}$ , and by introducing the effective detuning [50]:

$$\frac{1}{\Delta_{\text{eff}}} = \frac{1}{3} \left( \frac{1}{\Delta_{D1}} + \frac{2}{\Delta_{D2}} \right) \quad (5.46)$$

For caesium and the dipole trap laser at 1032 nm,  $\Delta_{\text{eff}} \approx 1.1 \cdot 10^7 \gamma$ . Using the effective detuning, the trap depth can be written as:

$$U_0 = \frac{3c^2 P}{w_0^2} \frac{\gamma}{\Delta_{\text{eff}}} \quad (5.47)$$

Since the detuning of the dipole trap laser is different for the two hyperfine ground states  $F = 3$  and  $F = 4$  by the hyperfine splitting  $\Delta_{\text{hfs}} = 9.192$  GHz, the trap depth or light shift is different for the two levels. This results in a differential energy shift of:

$$\begin{aligned} \hbar \Delta \omega_{\text{trap}} &= \frac{3c^2 P}{w_0^2} \gamma \left( \frac{1}{\Delta_{\text{eff}}} - \frac{1}{\Delta_{\text{eff}} + \Delta_{\text{hfs}}} \right) \\ &= U_0 \frac{\Delta_{\text{hfs}}}{\Delta_{\text{eff}} + \Delta_{\text{hfs}}} \end{aligned} \quad (5.48)$$

For red detuning, the frequency shift is negative. For a trap depth of  $U_0/k = 300 \mu\text{K}$ , we get a maximum differential light shift of  $\Delta \omega_{\text{trap}} = 2\pi \cdot (-1.1) \text{kHz}$ .

The atoms in the dipole trap are not stationary. The differential light shift has the same spatial dependence as the trap beam intensity. An atom sampling different spatial regions in the trap will therefore also sample different differential light shift regions, as illustrated in figure 5.18(b). Depending on the motional state of the atoms, it accumulates different amounts of phase shift. The envelope of the Ramsey signal in equation 5.44 will therefore be altered and depend on the temperature of the sample.

Assuming that the atoms in the trap are in thermal equilibrium, i.e., the kinetic energy is Maxwell–Boltzmann distributed, the theoretical shape of the expected Ramsey signal in the time domain, that is at fixed synthesizer detuning from the resonance  $\Delta$  but varying free precession time  $t$  can be shown to be [69]:

$$W(t) = \alpha(t) \cos[(\Delta - \delta)t + \kappa(t)] \quad (5.49)$$

with the amplitude  $\alpha(t)$  and phase  $\kappa(t)$  function

$$\alpha(t) = \left( 1 + \frac{t^2}{K^2} \right)^{-3/4} \quad \text{and} \quad \kappa(t) = -\frac{3}{2} \arctan \left( \frac{t}{K} \right), \quad K(T) = \frac{2\hbar}{kT} \frac{\Delta_{\text{eff}}}{\Delta_{\text{hfs}}} \quad (5.50)$$

The “ $e^{-1}$ -time” is now obtained to be:

$$T_2 = 1.67 \frac{2\hbar}{kT} \frac{\Delta_{\text{eff}}}{\Delta_{\text{hfs}}} \quad (5.51)$$

From the dephasing time of the Ramsey signal we can thus extract the temperature of the sample.

### Experimental data

In figure 5.20 a dataset for Ramsey spectroscopy in the time domain is shown together with a fit of the model discussed. The driving field has been detuned by  $\Delta = 280\text{ Hz}$  from the transition frequency. From the extracted decay time  $T_2 = 5.4\text{ ms}$  we extract a temperature of the sample  $T = 28\text{ }\mu\text{K}$ . The time delay between the two  $\pi/2$  pulses as shown in figure 5.19 is varied between 0 and 10 ms and the population of the ensemble in  $F = 4$  is determined after the microwave pulse sequence and normalized to the total number of atoms as discussed in section 5.3.1. The temperature determined in this way fits well together with the estimates given in [2] for our setup. There the temperature has been determined by release and recapture techniques. It should be mentioned that the above measurement corresponds to a typical value for medium size samples; especially when considering large samples, the cooling in the MOT and subsequent sub-Doppler stage is less optimal and the decay time of the Ramsey fringes suggests temperatures around  $T \approx 100\text{ }\mu\text{K}$ .

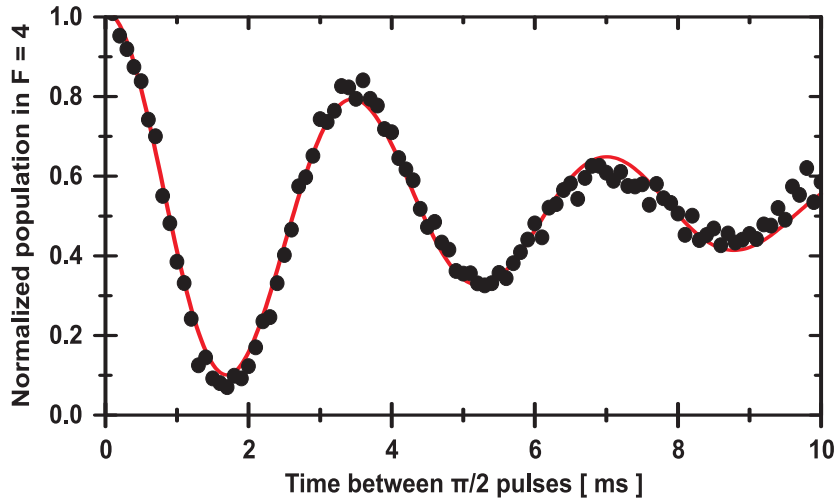


**FIGURE 5.20:** Ramsey spectroscopy in the time domain. The synthesizer is detuned from the clock transition by about 300 Hz and the free precession time between the two  $\pi/2$ -pulses is stepped between 0 and 10 ms in steps of 100  $\mu\text{s}$ . Each data point represents an average of 5 measurements. The fitted curve returns a decay time  $T_2 = 5.4\text{ ms}$ .

### 5.7.3 Running a Cs atomic clock

We have discussed Rabi spectroscopy as a procedure to determine the clock state transition frequency in section 5.6. For a given Rabi frequency, a much more precise value can be obtained with Ramsey spectroscopy in the frequency domain. The general principle is the same as in the time domain discussed above, but instead of changing the free precession time  $t$  between the  $\pi/2$  pulses, we detune the microwave driving field by variable amounts  $\Delta$ . Since we fix the free precession time to one value, the decoherence reduces the overall fringe amplitude of equation (5.44). The frequency of the Ramsey fringes [equation (5.44)  $P_4 = \frac{1}{2}(1 + \cos \phi(t)) = \frac{1}{2}(1 + \cos t\Delta)$ ] is determined by the waiting time  $t$ ; the clock transition can therefore

be found by determining the central fringe maximum which does not move in frequency space when the waiting time is changed. The longer the waiting time  $t$  is, the more precise the transition frequency can be determined. In figure 5.21 the experimental data for different waiting times is compared. The central fringe can be clearly identified and a frequency zoom into the data allows to extract the clock transition frequency down to a few Hertz accuracy. Figure 5.22(a) shows a Ramsey

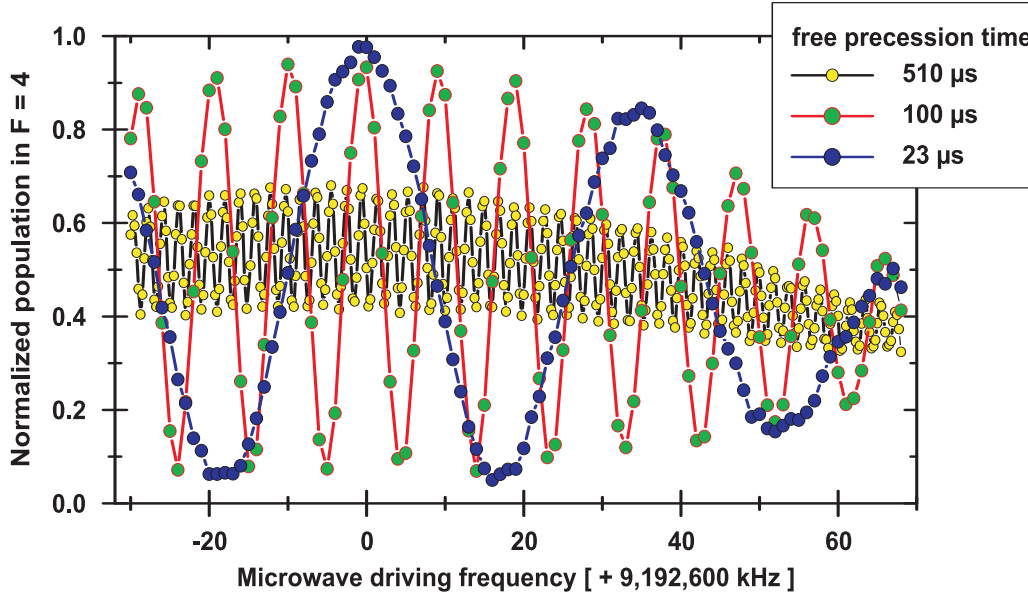


**FIGURE 5.21:** Atomic clock operation. Ramsey fringes for different free precession times  $t$ . The frequency of the fringes are determined by the waiting times. The central fringe can be clearly identified and the clock transition frequency extracted. The overall envelope of the signal is due to the fact that the two microwave pulses are also performed off-resonantly and the rotation on the Bloch sphere is no longer a simple as suggested by (5.44). It can be calculated straightforwardly from the general rotation matrix, equation (5.20).

fringe obtained with 2.2 ms free precession time between the two  $\pi/2$  pulses. The fit to the data has an uncertainty of 2 Hz, which corresponds to the precision of our Cs clock. The (long term) stability on the other hand is much worse! This is mainly due to changing external conditions – drifts in the bias magnetic field, different dipole trap power or different temperature of the sample. On a daily basis, the frequency is determined to the 250 Hz accuracy level. Relative to a Rabi frequency of  $\Omega_R \approx 10$  kHz, an uncertainty of  $\delta\omega = 250$  Hz is negligible. The effective Rabi frequency  $\Omega = \Omega_R \sqrt{1 + \frac{\Delta^2}{\Omega_R^2}} \approx \Omega_R(1 + 3 \cdot 10^{-4})$  only changes on the  $10^{-4}$  level.

Using the described techniques, the influences of external fields on the transition frequency can *in principle* be studied. At the time when the data presented here was taken, no absolute frequency reference was available. An accurate determination of transition frequency and comparing it with a commercial frequency standard would help to determine the different sources for the transition frequency shifts; only then the precision and accuracy of the actual setup can be determined.

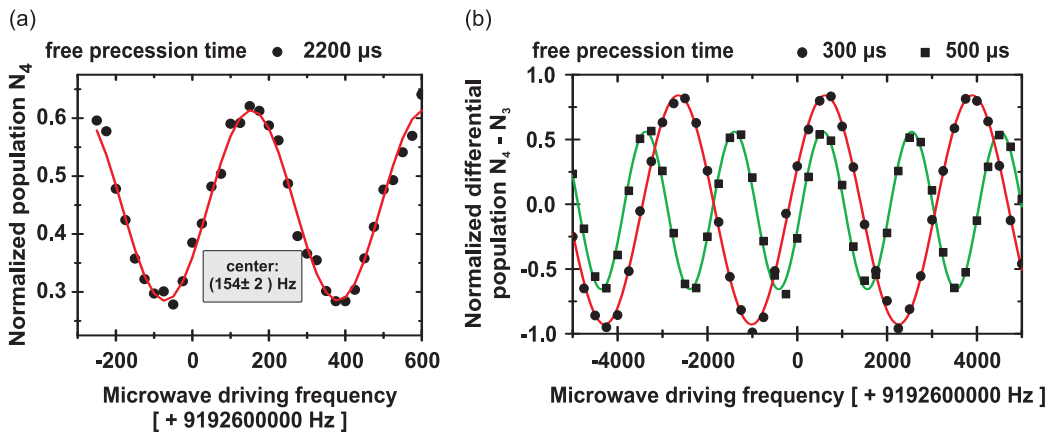


**FIGURE 5.22:** (a) Precise determination of the transition frequency. With a free precession time of  $t = 2.2$  ms, the transition frequency can be determined with an uncertainty of a few Hertz. (b) Two color recording of Ramsey fringes. The signal axis corresponds to the  $W$ -component of the Bloch sphere. The reduction in the fringe from  $300 \mu\text{s}$  to  $500 \mu\text{s}$  free precession time is due to the decoherence discussed in connection with figure 5.20. The solid lines are cosine fits to the data.

### Two color Ramsey spectroscopy

For completeness, figure 5.22(b) shows a recording of the Ramsey fringes with two color probing as discussed in section 5.12. When using two probe colors, the interferometer phase shift is proportional to the differential number of atoms  $N_4 - N_3$ . The normalized signal is equivalent to the  $W$ -component of the Bloch vector and positive and negative values can be observed.

#### 5.7.4 Inhomogeneous light shift of probe pulses

As discussed in section 5.1.3 and at the beginning of section 5.7, the accumulated phase shift  $\phi(t) = t\Delta$  measured in the Ramsey sequence can also be induced by shifting the transition out of resonance, e.g., by applying a probe pulse instead of detuning the driving field from resonance. The situation is schematically illustrated in figure 5.18(c). When we apply light shifting pulses while the atomic state evolves freely, the differential light shift adds a phase shift distribution proportional to the number of photons interacting with the atoms at their position. The process has been discussed in section 5.5 and is illustrated in figure 5.15 and 5.18. The readout of the population averages over the atomic sample according to the spatial overlap of the probe beam and the sample density distribution, compare equation (5.39). The additional phase shift induced by the probe pulses will shift the position of the Ramsey fringes in frequency space, accordingly.

The graphs (a1)–(a4) of figure 5.23(a) show four examples of Ramsey fringes where a probe pulse of different power (photon number) has been applied between the two  $\pi/2$  pulses of the microwave sequence together with a reference trace, where no light-shifting pulse has been applied. By normalizing the frequency shift  $\delta\nu$  to the period of the Ramsey fringes defined by the free precession time  $t$ , we can directly extract the mean phase shift angle of the Bloch vector caused by the probe

pulse. In a homogeneous system, as studied by Featonby *et al.* [67], where a constant differential light shift is applied across the whole sample, the Ramsey fringe position shifts proportionally to the photon number of the probe pulse. In the inhomogeneous situation we are considering, the spatial profile of the light pulse will create a phase shift distribution along the equator as discussed in section 5.5. We can therefore no longer expect the shift to be exactly proportional to the probe pulse strength, since states gaining the same phase angle  $\phi = (\chi t \bmod 2\pi)$  are equivalent in a Ramsey experiment. The phase distribution of the ensemble also acts to wash out the Ramsey fringe visibility, since the externally introduced distribution is basically a standard dephasing mechanism as discussed in connection with figure 5.18.

In figure 5.23(b) the normalized phase shift and amplitude of the fringes extracted from the Ramsey spectroscopy measurements are shown. One can see a clear deviation from a linear scaling when the accumulated phase shift exceeds  $2\pi$ . The Ramsey fringe amplitude also shows the expected revival when the phase distribution starts to overlap above  $2\pi$  and Bloch vector components with the same phase modulo  $2\pi$  add up. The graph also contains the theoretical predictions from the model given above and a good correspondence is observed.

The free parameters in the theoretical model are the ratio of sample size  $r_0$  to probe beam waist  $w_0$  and the maximum differential light shift  $\chi_0$  induced by the probe. We start out with an ensemble state  $|\Psi\rangle = \prod_i \frac{1}{\sqrt{2}} (|3\rangle_i + e^{i\phi}|4\rangle_i)$ . The interaction introduces a distribution of the phases  $\phi \rightarrow \{\chi_i\}$  which is projected onto a distribution of probability amplitudes  $\{a_i\}$  by the second  $\pi/2$  pulse of the Ramsey sequence. The probability distribution is then sampled with a weighting according to the Gaussian intensity distribution of the probe beam. The probe beam first induces an inhomogeneous phase distribution and then also couples with the same inhomogeneity to this distribution. As shown in equation (5.39) this process corresponds to multiplying the phase distribution  $e^{i\chi}$  with  $\chi \in [0 \dots \chi_0]$  with the weighting factor  $\chi^{(w_0/r_0)^2}$ . In a two dimensional projection of the Bloch vector (this is either the equatorial  $U$ - $V$ - plane in the Bloch sphere before the second  $\pi/2$  pulse or the  $U$ - $W$ -plane after the second rotation) we can use complex polar coordinates to simplify the calculations. Figure 5.24 represents an attempt to illustrate the projection of the Bloch vector into the equatorial plane together with the phase distribution and the inhomogeneous sampling. When we write the two relevant components of the ensemble state in complex coordinates, we get:

$$\mathbf{U}_{\text{plane}} = \int_0^{\chi_0} e^{i\chi} \frac{1}{c} \chi^{(w_0/r_0)^2} d\chi, \quad c = \int_0^{\chi_0} \chi^{(w_0/r_0)^2} d\chi \quad (5.52)$$

The length of the vector:

$$|\mathbf{U}_{\text{plane}}| = \left| \int_0^{\chi_0} e^{i\chi} \frac{1}{c} \chi^{(w_0/r_0)^2} d\chi \right| \quad (5.53)$$

is proportional to the amplitude of the Ramsey signal. The mean phase shift  $\bar{\phi}$ , which corresponds to the orientation of the Bloch vector in the complex plane, is given by:

$$\bar{\phi} = \arctan \frac{\text{Im}(\mathbf{U}_{\text{plane}})}{\text{Re}(\mathbf{U}_{\text{plane}})} \quad (5.54)$$

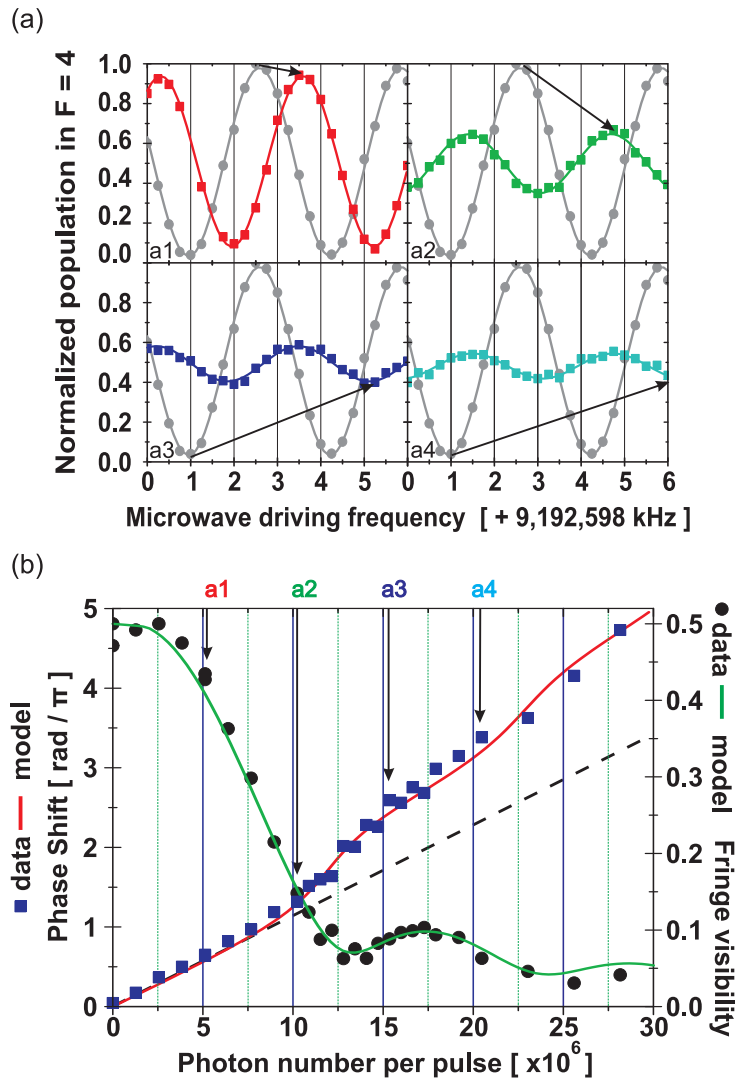


**FIGURE 5.23:** (a) Ramsey fringes, discrete points represent experimental data, the solid lines are cosine fits to the data. The data indicated with  $\bullet$  represents the reference trace where no light shifting pulse has been applied to the superposition state during the Ramsey sequence. From (a1)–(a4), the probe pulse photon number has been increased by  $5.12 \times 10^6$  in each step, starting with  $5.12 \times 10^6$ . (b) Normalized phase shift and fringe amplitude of Ramsey fringes, extracted from data similar to (a1)–(a4). The solid lines represent the theory curves and follow the experimental data remarkably well. The dashed line in the phase shift data corresponds to the linear dependence expected for a system with homogeneous light shift distribution.

By adapting the values for  $\chi_0$  and  $w_0/r_0$  to the data, the theory curves in figure 5.23(b) have been obtained. Considering the simplicity of this approach, the observed agreement with the experimental data is marvelous! The observation and interpretation of the observed effects have increased the level of understanding our experimental system dramatically and provoked most of the detailed studies of the inhomogeneous interaction presented in the next sections. Last but not least, the above findings have triggered the reconsideration of the single port interferometer setup and a change towards the two port setup in which intrinsically offers the

possibility of differential light shift cancelation.

## 5.8 Sample rephasing – Spin echo techniques

Naturally the question arises whether the dephasing of the ensemble can be reversed and how the destruction of the sample and the loss of coherence, e.g., due to spontaneous photon scattering can be studied. We shall make use of the spin echo techniques first invented by Hahn [70], and later applied to dipole trapped atoms in [71] and [69]. The main idea behind the techniques is an inversion of the sign of the accumulated phase  $\phi_1 = \int_0^\tau \phi(t)dt$  at a given instance  $\tau$  and the application of the same level perturbation, i.e., the accumulation of the same phase  $\phi_2 = \int_\tau^{2\tau} \phi(t)dt \stackrel{!}{=} \phi_1$  once more. Due to the opposite sign, the phases cancel and the ensemble is rephased at time  $2\tau$  after the inversion. An illustration of the pulse sequence and the effect on single atom Bloch vectors is shown in figure 5.25.

The sign-inversion can be achieved by applying a resonant microwave  $\pi$ -pulse to the atoms in the superposition state. By multiplying the corresponding matrices one immediately obtains

$$U(2\tau)_{\pi/2-\pi-\pi/2} = U_{\pi/2} \times U_{\text{free prec}}(\tau) \times U_\pi \times U_{\text{free prec}}(\tau) \times U_{\pi/2} \times U_0 = U_0 \text{ for all } U_{\text{free prec}}.$$

### 5.8.1 Rephasing the dipole trap shift effects

In section 5.7.2 we have studied the dephasing induced by the differential light shift of the dipole trapping potential. More specifically, we have used the decay of the Ramsey signal with free precession time  $t$  to determine the temperature of the

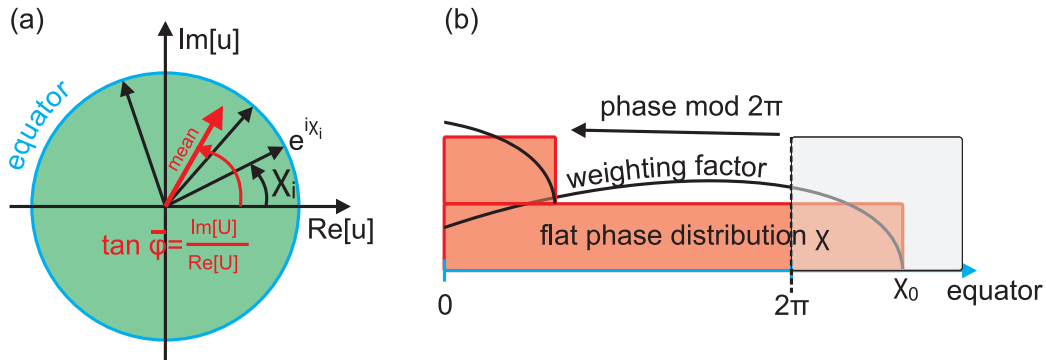


**FIGURE 5.24:** (a) In a projection into the equatorial plane, we represent the Bloch vector of a single particle as a complex number  $u_{\text{plane},i} = e^{ix_i}$ . We then sum the independent particles up according to their weighting due to the inhomogeneous probe beam coupling. The resulting signal is represented with the mean Bloch vector  $\mathbf{U}_{\text{plane}}$  whose orientation  $\bar{\phi}$  and length  $|\mathbf{U}_{\text{plane}}|$  can easily be calculated. A phase distribution obviously causes a reduced mean Bloch vector length. (b) In the simulation we start out with a flat phase distribution  $\chi = [0 \dots \chi_0]$  and we weight the different phases according to the factor  $\chi^{(w_0/r_0)^2}$ . When the phase exceeds  $\chi_0 > 2\pi$  we project it onto its  $\chi \rightarrow (\chi \bmod 2\pi)$  value.

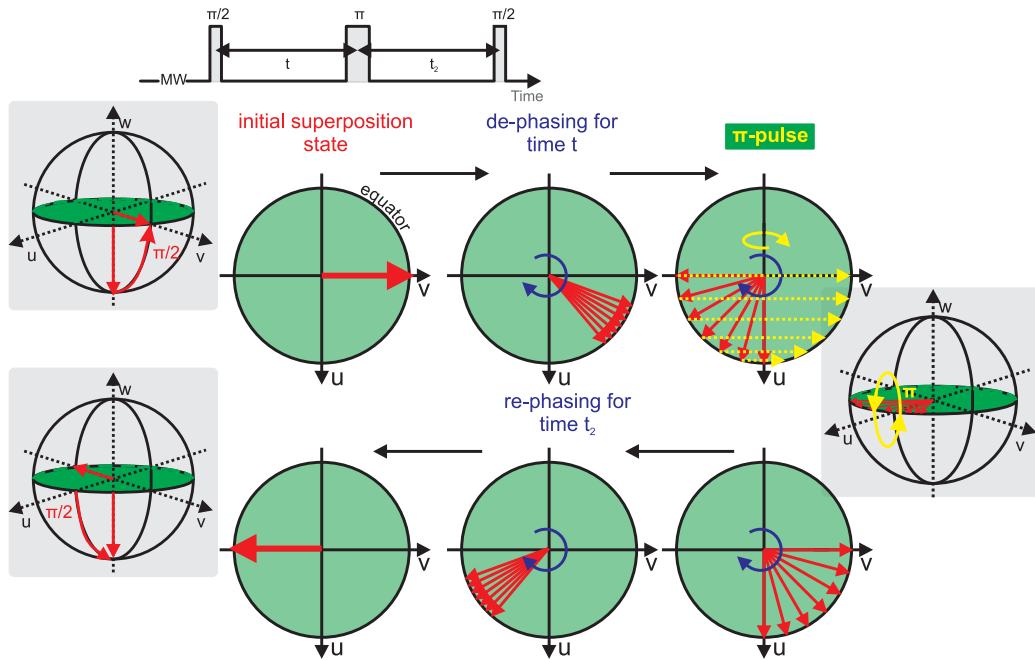


**FIGURE 5.25:** Illustration of spin echo sequence. After the sample is initialized into a coherent superposition state with a  $\pi/2$  pulse, perturbations of the clock levels transition frequency cause dephasing of the ensemble. After a time  $t$  the application of a microwave  $\pi$ -pulse inverts the sign of the phase and after the same free evolution time  $t$  (actually the same level perturbation) the state is rephased and the combined microwave sequence transfers the atoms back into the initial state.

ensemble. The spin echo sequence can be used to reverse the evolution in time and undo part of the dephasing induced by the dipole trap [69, 71].

In a classical, one dimensional picture, the atoms oscillate back and forth in the (almost) harmonic potential of the trap. Due to the slightly different potential for the two clock states, this causes the transition frequency to be changed periodically. A relative phase between the free evolution of the atoms and the microwave frame accumulates. At time  $t$ , the sign of the accumulated phase is inverted and after  $t_2 = t$ , the same phase is accumulated once more and the net phase change is zero. However, this picture only holds as long as the time  $t$  is a multiple of the oscillation period. If this is not the case, in the worst case, the phase accumulated in half an oscillation period cannot be rephased. Since the trap frequency is about  $\omega_{\perp} = 1$  kHz, this effect plays a minor role on the timescales of several tens of milliseconds. Entirely random perturbations like intensity noise of the trap laser or magnetic background field fluctuations cannot be rephased and cause the echo signal to decay with waiting time  $t + t_2$ . A more complete account on different dephasing mechanisms is given in [69]. As one can see in figure 5.26, the decoherence time is much longer than the timescale on which we intend to demonstrate squeezing, so the details of the dephasing mechanisms are of no immediate concern (yet). To obtain the data, we apply the microwave pulse sequence as discussed in figure 5.25 for different initial dephasing times  $t$  and the corresponding re-phasing times  $t_1 \approx t$ . Here, and for all further spin echo measurements, the microwave driving field is detuned by  $\Delta = 3$  kHz from the transition frequency. In the data set, we

use the two color probing scheme to obtain information on the differential clock state population. The exponentially decaying envelope of the echo signals gives a coherence time of 57 ms.

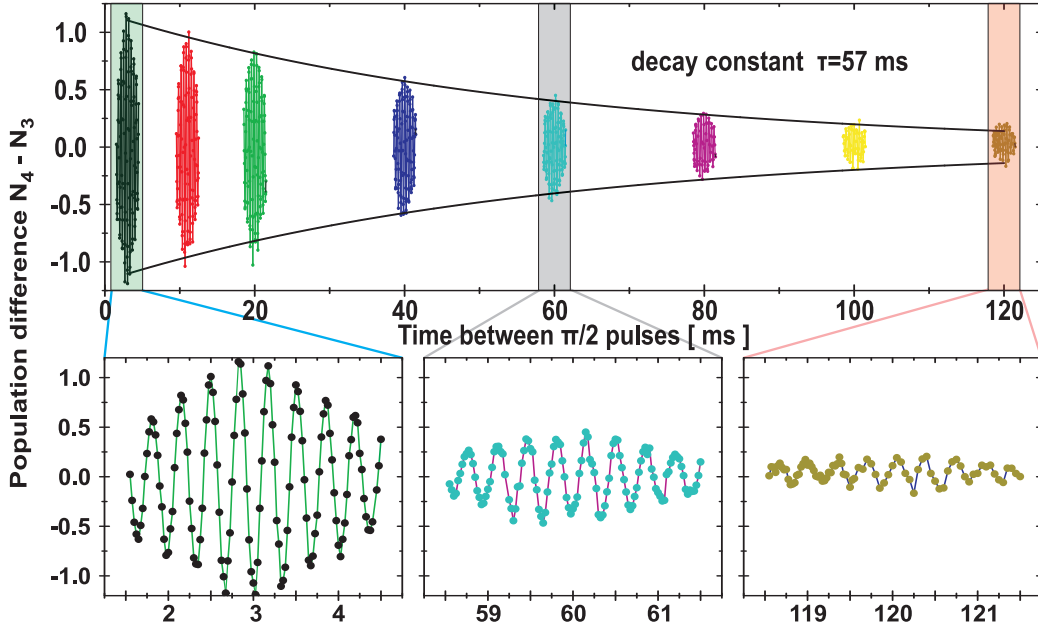


**FIGURE 5.26:** *Spin echos.* Applying a microwave  $\pi$  pulse in the center between the two  $\pi/2$  pulses of the Ramsey sequence allows one to rephase the ensemble. From the time constant of the exponentially decaying envelope we extract a coherence time of  $\tau = 57$  ms. The initial echo amplitude larger than one is caused by the fact that the atom loss from the trap is not taken into account when normalizing the signal to the atom number after the spin echo sequence.

## 5.9 Re-phasing the inhomogeneous light shift from probe pulses

The inhomogeneous phase spread of the ensemble induced by a non-destructive measurement as discussed in section 5.7.4 poses a serious problem for spectroscopy, squeezing, and quantum information applications and challenges the non-destructive nature of the measurement. Obviously, for probe pulses with large photon numbers, the atomic state evolution is dominated by the effect of the probing, as shown for the non-destructive observation of Rabi oscillations in section 5.5. Using a strongly perturbing probe beam, e.g., to predict the quantum state of the ensemble, creates an ensemble state whose phase is distributed around the equator of the Bloch sphere. The spin-echo techniques discussed in the last section can again be applied to reduce or even reverse the effects of inhomogeneous light shifts from the probe light. To study the effect of the differential light shift distribution when probing the sample, light pulses are symmetrically distributed around this refocusing  $\pi$ -pulse. The pulse sequences for these echo measurements are illustrated in figure 5.27(a).

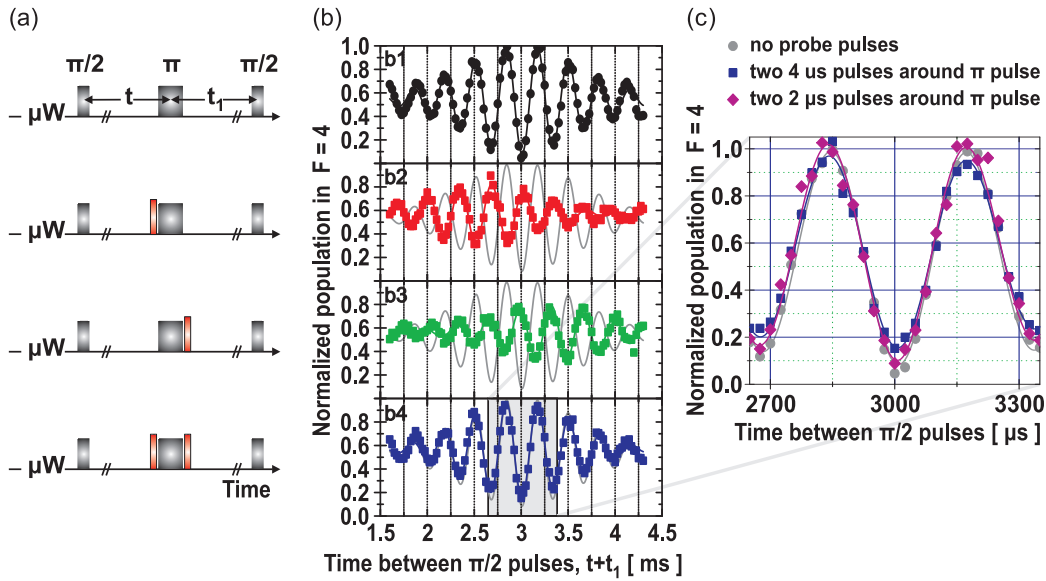


**FIGURE 5.27:** (a) Pulse sequences for spin echo measurements. The black lines correspond to the microwave pulses and the placement of the probe pulses is indicated in red. (b) Spin echo signal observed according to the corresponding pulse sequences to the left. The fit to the plain spin echo trace (b1) is kept for reference in graphs (b2)–(b4). Additional probe pulses, duration  $4\ \mu\text{s}$ , containing  $\sim 10^6$  photons, during the echo sequence shift the echo signal in time space (b2)–(b3), corresponding to the mean phase shift imprinted onto the ensemble. Distributing the probe pulse around the re-phasing microwave pulse, amplitude and phase of the echo signal are regained. The solid lines represent fits to the data. (c) A zoom into the central part of the echo signal shows that the ensemble can be fully re-phased when the probe pulses are distributed symmetrically around the microwave echo pulse. The slight reduction of the fringe contrast when doubling the photon number is due to photon scattering, discussed in section 5.10.2.

The plain spin echo sequence with no perturbing light pulse applied, taking care of dephasing, e.g., caused by the trapping laser, shows a close to perfect refocussing of the sample at the expected time as shown in figure 5.27(b1). When applying a single probe pulse before or after the echo pulse, the echo fringe is shifted in time according to the induced mean phase shift by the probe pulses, figure 5.27(b2)–(b3). As with the Ramsey fringes in figure 5.23(a), the inhomogeneity of the light shift reduces the echo fringe visibility drastically. If we, however, apply light pulses around the spin echo pulse, figure 5.27(b4) shows that we regain the unshifted echo fringe almost perfectly. In graph 5.27(c) we zoom in on the central Ramsey fringe to substantiate this claim. The graph also confirms that the measurements are indeed not limited by spontaneous photon scattering. When the ensemble is in a superposition state, both inelastic Raman and elastic Rayleigh scattering would lead to complete decoherence of the atoms which were excited and reduce the fringe contrast. As can be seen in the graph 5.27(c), the fringe contrast is not reduced appreciably. The influence of photon scattering is slightly visible when comparing the fringe amplitudes of echo signals with different probe pulse photon numbers.

## 5.10 Spontaneous photon scattering probability and trap oscillations

Both for the characterization of the non-destructiveness of the light-matter interface and for the demonstration of spin squeezing, the degree of “real” destruction or irreversible dephasing caused by both the application of probe light and by other effects has to be determined. At first sight it might appear that the reduction of the spin echo fringe as demonstrated in figure 5.27(c) can be ascribed to the spontaneous photon scattering, only.

More thorough considerations, however, reveal that the motion of the atoms inside the trap has to be taken into account. The reversibility of the dephasing relies on the fact that the phase perturbation (e.g., caused by the differential light shift induced by the probe pulses) before and after the sign inversion with the  $\pi$ -pulse in the echo sequence are the same. If the single atom  $i$ , however, moves after the first inhomogeneous light pulse is applied, as indicated in figure 5.18, the atom will generally experience a different light shift of the second pulse and thus the accumulated phases  $\phi_{i,\text{before}} \neq \phi_{i,\text{after}}$  before and after the sign inversion are not identical. Only when choosing the time between the two perturbing light pulses  $\tau_1 + \tau_2$  infinitely short, i.e., that the atoms had no time to move inbetween or such that it is equal to a multiple of half a trap oscillation period, the single atom will experience twice the same light shift and optimal reversibility is possible. In general, the situation is complicated by the fact that the axial and the radial trap frequencies are different. We have determined the longitudinal trap frequency to be of the order of few Hertz in section 3.4.4. The corresponding radial frequencies are of the order of 1 kHz, so the mixing of the two frequencies can be neglected in our case.

### 5.10.1 Effect of trap motion on reversibility of inhomogeneous phase imprints

To study the influence of trap motion on the reversibility of the probe light shift induced phase distribution, we use the pulse sequence as shown in figure 5.28(a) with variable separation  $\tau_1 + \tau_2$  between the light pulses. We then record echo signals with time delay  $t = 1.5$  ms for different separations  $\tau_1 + \tau_2$  between the probe light pulses as indicated in figure 5.28(b). For the data shown, the light pulses have been distributed symmetrically around the  $\pi$  pulse,  $\tau_1 = \tau_2$ . To record the fringes, we detune the microwave by  $\Delta = 3$  kHz from the established transition frequency. A fit to the echo signals returns the fringe amplitude and a typical trace for the echo fringe amplitude as function of  $\tau_1 + \tau_2$  is shown in the inset of figure 5.28(c).<sup>6</sup> One can clearly observe the oscillatory behavior of the signal which we attribute to the movement of the atoms in the dipole trap as discussed above. The oscillation

<sup>6</sup>The data sets shown in 5.28(b) and inset of (c) do not correspond to each other. The echo fringes in (b) have been recorded with two color probe pulses – yielding positive and negative amplitude values while the data for (c) has been recorded with the standard  $F = 4 \rightarrow F' = 5$  probe. Also the probe power has been reduced with respect to the data in (b), therefore the fringe visibility in (c) does not reduce to zero as in (b).

period of the signal corresponds to half the trap period, since the probe beam is assumed to be symmetric. An atom can thus obtain the differential probe light shift on either side from the trap center. The main part of figure 5.28(c) shows the echo signal revival frequency as a function of the dipole trap power. This frequency is expected to be twice the actual trap frequency since the first optimal rephasing time corresponds to half a trap oscillation period. We expect the trap frequency  $\omega_{\perp}$  to scale with the square root of the trap power  $P$ :  $\omega_{\perp} \propto \sqrt{U_0} \propto \sqrt{P}$  [equation (3.12), page 34] which is confirmed by the data. For the range of dipole trap powers used, we get trap frequencies between  $\omega_{\perp} = 375 \dots 1250$  Hz, which corresponds well to values reported in [15] for our setup. Although this is probably one of the most complicated ways of extracting the oscillation frequency of a dipole trapped sample, it still returns a consistent answer. . . Nonetheless, it is worth mentioning that in the approach demonstrated, the trap frequency can be determined without actually exciting a collective motion!

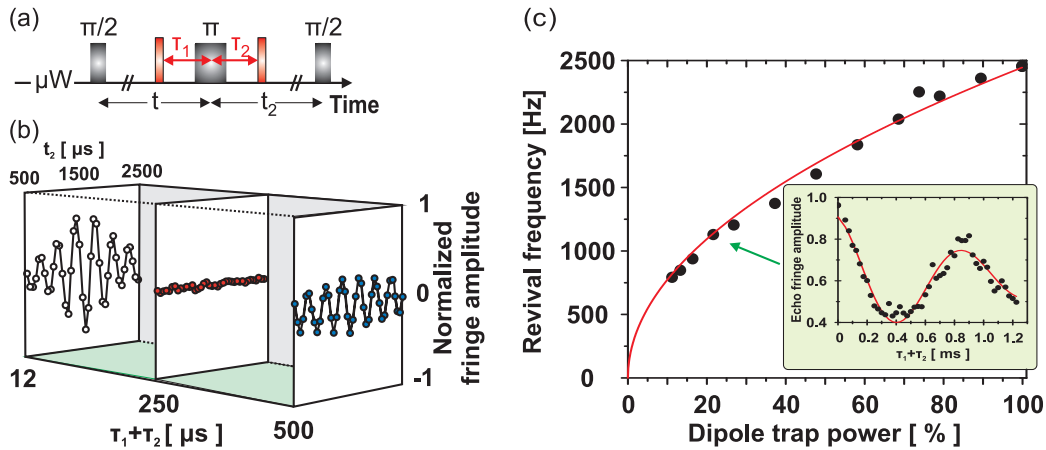


**FIGURE 5.28:** (a) Timing of pulse sequence to study the influence of atomic motion on the phase imprints from light shifting pulses. The time  $t$  is fixed to 1.5 ms and  $t_2$  is varied to obtain the echo signals. Echo fringes are then recorded for different separations  $\tau_1 + \tau_2$ . (b) Spin echo signals for different time separations  $\tau_1 + \tau_2$ ,  $\tau_1 = \tau_2$  between the light pulses. When the atoms have moved between the two light pulses, the atomic level perturbation is different for both pulses, perfect rephasing is not possible and the fringe amplitude drops. The effect is strongest when  $\tau_1 + \tau_2$  corresponds to a quarter of the trap period. The data has been taken using two color probe pulses. (c) The inset shows the echo amplitude as a function of the time separation  $\tau_1 + \tau_2$ , using a single probe color and less probe power than in (b). The main plot shows the echo signal revival frequency as function of the dipole trap power; the scaling of  $\omega \propto \sqrt{P}$  confirms that the echo amplitude oscillations with  $\tau_1 + \tau_2$  are due to the trap motion. From the fit in the data of the inset, we extract a revival time at  $\tau_1 + \tau_2 = 850 \mu\text{s}$  corresponding to a trap frequency of 590 Hz. For higher trap powers we observe trap frequencies of up to  $\omega_{\perp} = 1.25$  kHz.

The effect of probe induced decoherence and the ability to reverse the inhomogeneous light shift by using spin echo techniques as discussed above can be studied further by changing the probe pulse strength and comparing traces of the kind as shown in the inset of figure 5.28(c) for different probe powers. Corresponding raw data is shown in figure 5.29. To reduce the amount of data to be taken, we only record the peak value of the echo fringe, i.e., we fix  $t_2 = t$  and only change the separation  $\tau_1 + \tau_2$  between the light shifting pulses. The stronger the perturba-

tion is, the faster the echo amplitude drops. When applying moderately strong probe pulses, the clear revival of the echo fringe at half the trap oscillation period becomes visible.

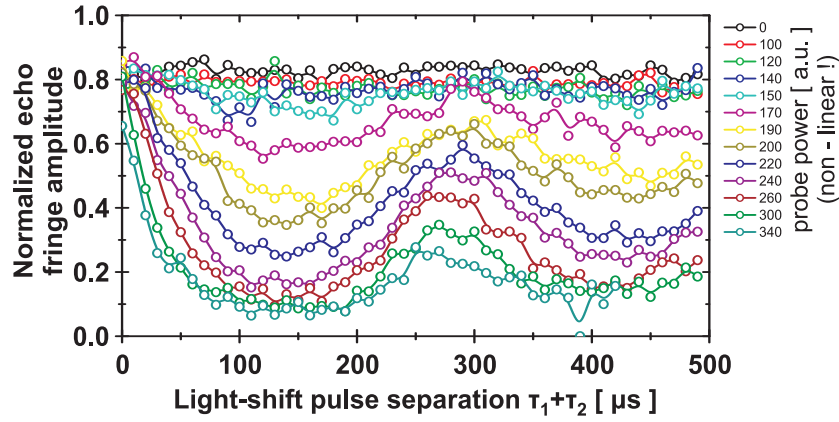


**FIGURE 5.29:** Maximum of echo fringe as function of time separation  $\tau_1 + \tau_2$  for different probe pulse powers. The higher the probe power, the faster the echo fringe amplitude drops and the worse the possibility to rephase the sample. The revival of the echo fringe around half the trap oscillation period is clearly visible. The solid lines interpolate the data and are meant to guide the eye, only.

The dynamics of the atoms in the trap under the influence of probe pulses can be simulated numerically. Details of the simulation can be found in [3, 7]. The result for different probe photon numbers are shown in figure 5.30 together with the experimental data. The data has been obtained in the same fashion as discussed in figure 5.28. The numerical simulation reproduces the experimental values remarkably well.

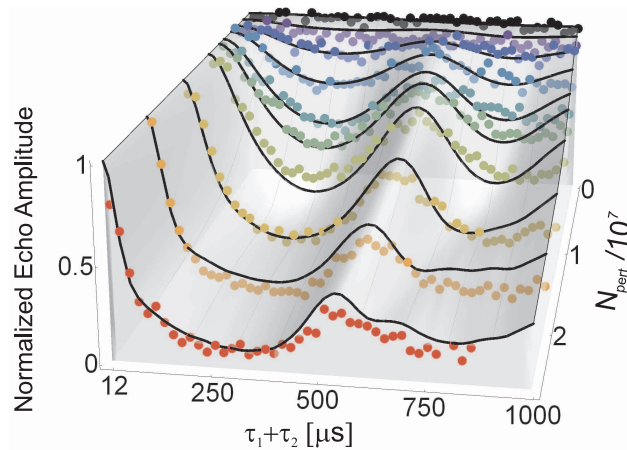


**FIGURE 5.30:** Experimental data for spin echo measurements with additional probe pulses. Along the  $x$ -axis the time between the perturbing light pulses is given and the behavior from figure 5.28 can be observed. When the power of the light pulses is increased as shown along the  $y$ -axis, the oscillations become more and more pronounced due to the stronger phase imprint caused by the probe light and the “stronger need” for active rephasing.

### 5.10.2 Estimation of photon scattering probability

Our main motivation for using spin echo spectroscopy with additional probe pulses applied to the superposition state, is to estimate the irreversible effects of dispersive probing. By determining the reduction of the spin echo fringe when probe light is applied relative to the fringe from an unperturbed system,  $\eta = \frac{\text{amplitude perturbed}}{\text{amplitude reference}}$  obtain the amount of irreversible dephasing.

It is obvious that applying probe pulses to the superposition state corresponds exactly to the squeezing and verification measurement which form the main reason for our undertakings, section 2.5. As has been discussed shortly in section 2.2.3, the amount of squeezing we expect depends on the coupling strength  $\tilde{\kappa}^2$  between the atoms and the probe light. It can be shown in general, that  $\tilde{\kappa}^2$  is proportional to the on resonance optical depth  $\alpha_0 = 2S$  [formula (2.41)] and the spontaneous scattering probability per atom in one measurement  $\eta'$ . In the ideal case, spontaneous photon scattering is the only decoherence mechanism and  $\eta' = \eta$ . The coupling strength depends on  $\eta'$  while the relevant state destruction is given by  $\eta$ . It is the total decoherence induced by the probe pulse which is of relevance in the squeezing criteria given in section 2.2.2.

In the last section we have realized that the estimation of the spontaneous photon scattering probability is complicated by the trap motion. The best estimate is obtained when the two probe pulses have the least possible separation and the microwave  $\pi$  pulse is as short as possible. The duration of the  $\pi$  pulse is set by the Rabi frequency which in return can only be changed by increasing the driving field strength. This was the initial motivation for increasing the microwave power to  $P = 10$  W which allows us to obtain Rabi frequencies up to 60 kHz, i.e.,  $\pi$ -pulse durations of around  $8 \mu\text{s}$  compared to  $\sim 50 \mu\text{s}$  before.<sup>7</sup> With the increased Rabi frequencies, the  $\pi$  pulse durations are short with respect to the trap oscillation period and the influence of trap motion on the reversibility of the inhomogeneous light shift is suppressed. In case the effect of atomic motion is still non-negligible, decreasing the trap depth which decreases the trap frequency can work to our advantage. The bargain is, of course, weaker confinement and generally lower atom numbers in the trap.

In figure 5.31, an example of a calibration measurement for the decoherence is shown. Because it is the reference data for the squeezing measurements discussed in section 6.3, this data has been obtained by using the two color two – port setup, compare section 3.2.3, with different parameters than the data above. Two bi-chromatic probe pulses containing in total  $\bar{n} = 7.1 \cdot 10^6$  photons are sent around a  $\tau_\pi = 9.02 \mu\text{s}$  microwave  $\pi$  pulse. Contrary to the above data, the probes were both red detuned by  $\Delta_{45} = -100$  MHz and  $\Delta_{32} = -79.19$  MHz. The detuning of the microwave field from the transition was  $\Delta = 3.0$  kHz and the transition frequency on that day was measured to be  $\omega = 9.192.631.585$  Hz (synthesizer offset included). The reduction of the echo fringe with respect to a reference measurement without probe light pulses gives a decoherence of  $\eta = 11 \pm 2\%$ .

<sup>7</sup>By putting the second high power amplifier as the last element before the microwave antenna, compare figure 5.2, we could actually achieve an increase in  $\Omega_R$  by more than the expected factor of  $\sqrt{10}$ . This is due to the fact that the microwave pulse generator has a transmission loss of  $\sim 3$  dB.

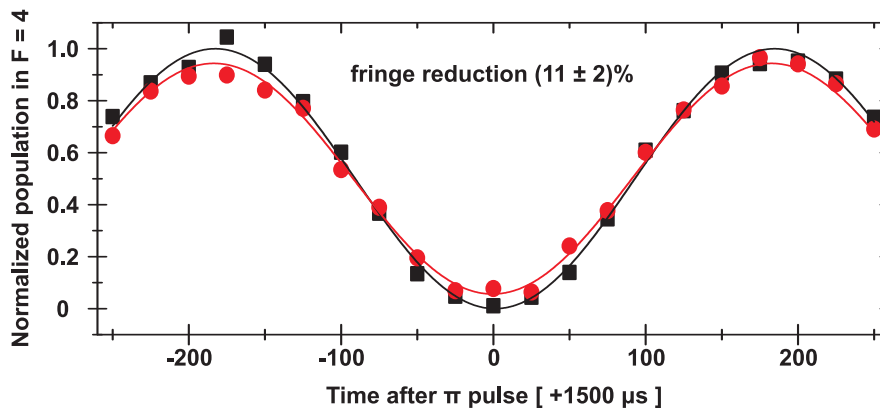


**FIGURE 5.31:** Calibration of probe induced decoherence. The spin echo sequence as discussed in figure 5.27 is used to calibrate the probe induced decoherence. We compare the fringe amplitude with a reference signal (black) and obtain a decoherence of  $\eta = 11 \pm 2\%$  for the two applied bi-chromatic probe pulses of  $10 \mu$ s duration at  $\Delta_{45} = -100$  MHz and  $\Delta_{32} = -79.19$  MHz from the  $F = 4 \rightarrow F' = 5$  and  $F = 3 \rightarrow F' = 2$  transitions. Using a short  $\pi$  pulse of  $9.02 \mu$ s duration reduces the effects of atomic motion.

## 5.11 Two color light shift cancelation

From a general point of view, the ability to rephase an ensemble after a non-destructive measurement is of great importance. For practical applications, however, it would be advantageous if the differential light shift could be canceled by the probing scheme itself. The most straight forward scheme which comes to mind is the usage of a second probe beam with the same spatial intensity distribution. By arranging the detuning of the second laser such that the differential light shift from the second beam is exactly opposite to the first, light shift cancelation can be achieved. Since the sign of the phase shift signal is directly connected to the sign of the detuning from the closest atomic transition, the second probe color has to be introduced in the second mode of the interferometer input beam splitter. We have discussed this two color – two port setup in section 3.2.3. In this configuration both probe lasers have to gain a phase shift with the same sign in order to produce an output interferometer signal which is proportional to the differential number of atoms,  $\Delta N = N_4 - N_3$ . When equal populations in  $F = 3$  and  $F = 4$  produce the same probe light phase shift, also the light shift of the atomic transitions is the same. To this end, the couplings of both lasers to the atoms have to be adapted by optimizing their frequency ratio of relative powers. When we fix the power of the probe beams to be the same, i.e., the empty interferometer fringes have the same amplitude, the phase shift only depends on the detunings  $\Delta_{3,2}$  and  $\Delta_{4,5}$  of the probe lasers.

A very sensitive way to adapt the probe frequencies for light shift cancelation is by using spin echo spectroscopy. The shift in the echo fringe when applying only one probe pulse to either side of the  $\pi$ -pulse as demonstrated in figure 5.27(b) is caused by the differential light shift. Consequently, when no shift of the fringe position is observed, no mean<sup>8</sup> differential light shift is present. In the data presented in

<sup>8</sup>Our readout always averages over the sample, so we only get information on the mean shifts.

figure 5.32 we demonstrate the optimization of the probe detuning of the  $F = 3 \rightarrow F' = 2$  probe frequency for fixed  $F = 4 \rightarrow F' = 5$  detuning using this technique. The power ratio of the two probes is fixed to  $n_3/n_4 \approx 1$ . We record a reference trace, where no light shifting pulses have been applied and traces where one bi-chromatic probe pulse is applied to the sample either before or after the microwave  $\pi$  pulse. When the probe frequencies are not matched the two fringes are shifted with respect to the reference trace as shown in figure 5.32(a). By tuning the  $F = 3 \rightarrow F' = 2$  probe frequency we observe that the position of the fringes moves as expected and we can find a probe frequency where no shift in frequency space relative to the reference data can be observed, as shown in figure 5.32(b). Since the probe frequencies determined depend on the relative power of the two beams the frequency values have to be adapted when the power ratio is changed. For practical reasons we try to keep the empty interferometer fringe amplitudes the same. To that end we use an active power stabilization which will be discussed in section 6.3.1

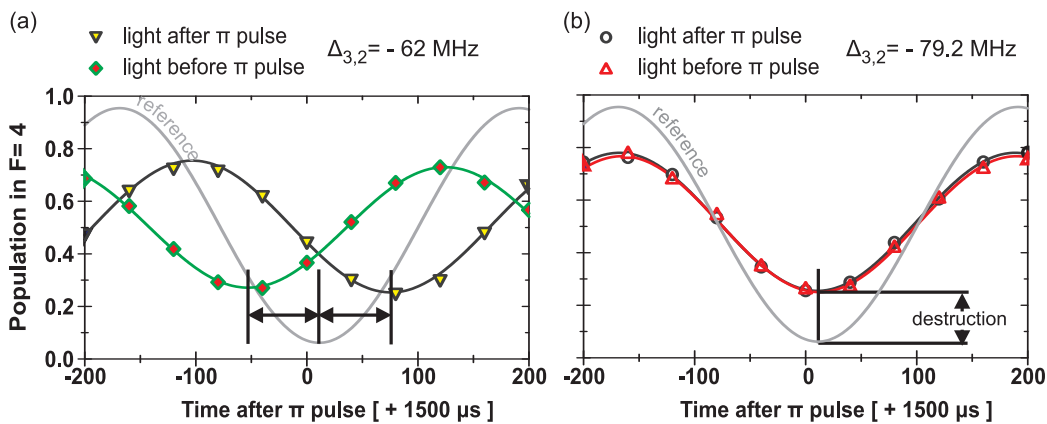


**FIGURE 5.32:** Cancellation of mean light shift in two color probing scheme. One bi-chromatic probe pulse is applied to the ensemble either before or after the microwave  $\pi$  pulse of the echo sequence. (a) When the ratio of the probe frequency detunings is not adjusted properly, the spin echo fringes are shifted in frequency space due to the differential light shift as discussed in section 5.9. (b) With the probe frequencies matched, the echo fringes are not shifted relative to the reference data and the mean light shift from the two probe colors is canceled. The reduction of the fringe is only due to spontaneous photon scattering.

The reduction of the echo fringe with respect to the reference data, as shown in figure 5.32(b) is no longer due to improper rephasing of the sample but can mainly be attributed to spontaneous photon scattering. When physically aligning the two probe beams in the interferometer, care has to be taken that their spatial overlap is optimized. Else, the observed effects in the data will be the same as demonstrated, but a minimum phase distribution due to the differential light shift can no longer be claimed. The part of the sample interacting mainly with one beam will get a phase distribution opposite to the rest of the ensemble; the mean value can still be adjusted to be zero, but the spread can amount to several rad.

## Conclusion

To conclude this chapter, let us shortly look back on what we have achieved. We have demonstrated that we can create an extremely pure ensemble of two level systems, by initializing an ensemble of atoms into one of the clock states of the caesium atom and removing atoms populating other states. Furthermore we have shown the ability to control the two level system coherently by applying a microwave field. Although not mentioned previously and not used in the data presented, we also have a microwave phase shifter available in the lab. Using the additional degree of freedom obtained with this piece of equipment, we can *in principle* generate any desired ensemble state described by a vector in the Bloch sphere picture.

The non-destructive character of the interferometric probing scheme was used to follow Rabi oscillations *in real time* and to extract the corresponding system parameters. The effect of the non-destructive probing has been studied in detail, with especial focus on the inhomogeneous light shift distribution caused by the probe pulses. Here we have made extensive use of Ramsey and spin echo spectroscopy techniques. Overall, a very good and thorough understanding of the dispersive light-atom interaction has been gained. The drawbacks of the single port interferometer in terms of probe induced dephasing due to the spatial inhomogeneity of the differential light shift have been illustrated in various settings and the necessity of active rephasing or light shift cancelation has been highlighted. The observed effects serve as main motivation for changing the probe configuration to a input two port interferometer setup where light shift cancelation can be achieved.

With all the techniques readily available, we can now move to the main goal – demonstration of projection noise limited population readout and projection noise squeezing.

---

# Atomic projection noise measurements and quantum noise squeezing

In the previous chapter we have discussed the techniques to prepare a coherent atomic ensemble superposition state of the two caesium energy eigenstates, the clock levels  $|3\rangle$  and  $|4\rangle$ . Furthermore, we have shown the capability of the experimental setup to perform quantum non-demolition measurements on the quantum state of the atomic ensemble. The probe induced decoherence has been analyzed in detail and the irreversible dephasing and state destruction mechanisms have been studied. With this thorough understanding of the probing scheme we shall now move on to the noise properties of the system. The main driving force behind our experimental efforts is the demonstration of light shot noise and atomic projection noise limited readout of the atomic ensemble population number difference  $\Delta N_{|4\rangle-|3\rangle}$ . At this quantum mechanical limit of the measurement precision, we desire to reduce the measurement uncertainty by squeezing the population number difference below the standard quantum limit. Experimentally, the standard quantum limit is achieved, when the signal variance of the empty interferometer scales linearly with applied photon number and the atomic superposition signal variance scales linearly with atom number.

This chapter starts out with an estimate for the probe parameters to obtain maximal squeezing in the parameter space which is experimentally accessible. These parameters will define the stability requirements on the measurement system and show why measurements at the standard quantum limit with ensembles of atoms are not a trivial task. The discussion backs up a statement ascribed to Jeff Kimble: “Everyone can measure a signal, but it takes a real man to measure noise”<sup>1</sup>. We then turn to the two interferometer setups, the single port and the two port arrangement and discuss both their capability to perform projection noise limited measurements and the obtained projection noise squeezing.

---

<sup>1</sup>We are aware of the political incorrectness of the statement.

## 6.1 Condition for optimal squeezing

In section 2.2.3 we have discussed the reduction of the population number uncertainty of an atomic ensemble initialized in a coherent superposition state by using QND measurements. The final conclusion can be summarized by formula (2.30):

$$\left( \frac{1}{1 + \tilde{\kappa}^2} \right) < (1 - \eta)^2 \quad (6.1)$$

The information gain, which is parameterized by  $\tilde{\kappa}^2$  has to be bargained against the loss of coherence due to the measurement, which we name  $\eta$ . It is clear that  $\tilde{\kappa}^2$  corresponds to the coupling strength between the atomic ensemble and the probe system. It has been shown that  $\tilde{\kappa}^2$  can be written as  $\tilde{\kappa}^2 = \alpha_0 \eta'$  (modulo some prefactor of the order of one) where  $\alpha_0$  is the on resonance optical depth of the atomic ensemble [1, 44].  $\eta'$  is the spontaneous photon scattering probability per applied probe pulse. It is obvious from this correspondence that a high coupling strength is directly connected with decoherence. We can therefore choose to parameterize the coupling strength with the decoherence parameter. In the following, we restrict the treatment to  $\eta' = \eta$ , where all decohering effects are caused by photon scattering, only. If other sources of decoherence are present,  $\eta$  takes them into account.

When we optimize the degree of squeezing:

$$\xi = \frac{\delta^2 \hat{J}_z^{\text{out}}}{(1 - \eta)^2 \delta^2 \hat{J}_z^{\text{in}}} = \frac{1}{(1 + \alpha_0 \eta)(1 - \eta)^2} \quad (6.2)$$

with respect to the decoherence parameter  $\eta$ , we obtain:

$$\eta_{\text{opt}} = \frac{\alpha_0 - 2}{3\alpha_0} \quad (6.3)$$

Correspondingly, the noise reduction one can achieve is:

$$\xi_{\text{max}} = \frac{27\alpha_0^2}{4(1 + \alpha_0)^3} \quad (6.4)$$

To achieve a noise reduction of 50%, i.e.,  $\xi = -3$  dB squeezing, we require an effective optical depth of  $\alpha_0 \approx 10$ . This maximum is assumed at a decoherence parameter of  $\eta_{\text{opt}} = 0.27$ . Since the optimal decoherence parameter depends very little on the optical depth, we expect to achieve more than  $\xi = -3$  dB of squeezing in our setup when adjusting  $\eta \approx 0.3$ . The simple theory presented here and in section 2.2.3 can be extended to include some peculiarities of our two color probe arrangement. Especially off resonant excitations and inelastic Raman scattering alter the derivations slightly; details can be found in [72]. The main conclusion is, however, that a probe induced spontaneous photon scattering probability of 30% per atom and probe pulse is a good starting point.

The decoherence calibration data discussed in section 5.10.2 suggests that a photon number of  $n \approx 2 \times 10^7$  per bi-chromatic probe pulse<sup>2</sup> at frequency detunings

<sup>2</sup>When we talk of the photon number  $n$ , it should be obvious that this is associated with the mean photon number  $\bar{n}$  of the coherent light pulses we are using. At no instance we are dealing with Fock states of light.

$\Delta_{3,2} \sim \Delta_{4,5} \sim 100$  MHz is necessary to inflict the desired amount of damage,  $\eta = 0.27$ .

### Interferometer stability requirements

This estimation of the probe pulse photon number indicates that light shot noise limited performance of the interferometer up to  $\bar{n} \sim 10^8$  photons has to be demanded. In return, this requires a relative phase stability of the interferometer of better than  $\frac{\sqrt{\delta^2 \Delta \phi}}{\Delta \phi} \approx \frac{1}{\sqrt{\bar{n}}} < 10^{-4}$ . At this level of precision, the capability of projection noise readout for  $N_{\text{at}} \sim 10^5$  atoms is assured: The expected phase uncertainty induced by the projection noise of the atoms  $\frac{\sqrt{\delta^2 \Delta \phi_{\text{at}}}}{\Delta \phi_{\text{at}}} \approx \frac{1}{\sqrt{N_{\text{at}}}} \approx 3 \times 10^{-3}$  is larger than the measurement uncertainty due to the finite number of photons. By demanding  $\bar{n} \gg N_{\text{at}}$  we therefore are able to resolve atomic projection noise.

The experimental principle for establishing the shot noise limited performance of an interferometer has been discussed in chapter 4. There we have used an intrinsically stable setup to characterize the performance of the differential detector. As signature of light shot noise, we have used the linear scaling of the signal variance with photon number. Following these principles, we will now first consider the performance of the two color – single port Mach Zehnder interferometer setup. After discussing some technical issues, we consider the projection noise measurements performed with this method. We then turn to the two color – two port interferometer version and discuss the achievements.

## 6.2 Noise measurements with two color – single port interferometer

### 6.2.1 The two-sample variance and the issue of timescales

Our main goal is to measure the distribution of the atomic population between the two clock states with quantum noise limited precision. One prerequisite for the empty interferometer is therefore, that it performs at the shot noise limit when no atoms are present in the interaction region. Subsequently we want to look at the signal of an atomic ensemble prepared in a superposition state and show that the signal variance of a probe pulse  $p$  scales linearly with atom number:  $\delta^2 p \propto N$  since this is the signature of quantum projection noise, see section 2.1.1.

Shot noise limited performance of the interferometer is obtained, when the output signal variance of the empty interferometer scales linearly with the mean photon number in the light pulses, compare section 2.1.2. To characterize the noise performance on different timescales, we use the two point variance  $\delta^2 p(\tau)$ :

$$\delta^2 p(\tau) = \langle (p_i(0) - p_i(\tau))^2 \rangle_i - \langle p_i(0) - p_i(\tau) \rangle_i^2 \quad (6.5)$$

where  $p_i(t)$  is a single pulse at time  $t$ .  $p_i(0)$  and  $p_i(\tau)$  correspond to individual pulses separated by  $\tau$ . This type of variance has been introduced by D. W. Allan

for the very specific case where the measurement points correspond to relative frequency deviations in an atomic clock [73].

The differential path length of the interferometer naturally fluctuates on the timescales which correspond to acoustic frequencies and thermal drifts. The active stabilization loop, discussed in section 3.2.2 has a bandwidth of below 1 kHz, so only noise sources below that frequency are suppressed. The actual spectrum of the acoustic noise depends on many external factors which vary in time. In any case, however, it can be assumed that the noise power spectral density drops off towards high frequencies. On timescales larger than a few microseconds the uncompensated, externally induced interferometer fluctuations mask the quantum mechanical phase measurement uncertainty due to the light shot noise and the measurement precision is limited by the classical fluctuations. On short enough timescales the intrinsic interferometer fluctuations are small compared to the quantum mechanical measurement uncertainty and the measurement can be shot noise limited. In principle, we can tolerate a certain deviation from the ideal shot noise limited performance since the required phase measurement accuracy for the projection is noise lower than for light shot noise with the desired photon numbers. On the other hand, of course, we want the measurement to be as ideal as possible and we would like to be at the standard quantum limit for both the atomic and the light system.

By comparing the noise levels  $\frac{1}{2}\delta^2 p(\tau)$  for different times  $\tau$  with the light shot noise of a single pulse  $\frac{1}{2}\delta^2 p(\tau \rightarrow 0)$ , one can determine from which time separation on the measured signal fluctuations are dominated by interferometer fluctuations and are no longer only due to the intrinsic photon number fluctuations of a coherent light state. From this point on, the interferometer is no longer light shot noise limited. As qualifying signature for light shot noise, we use the expected linear scaling of the signal variance with mean probe pulse photon number.

The two point or two sample variance corresponds to a two point measurement, where one measurement establishes a baseline for the other. One can view the subtraction of two pulses as artificially creating a balanced measurement. The difference between the pulses obviously only considers fluctuations between the two measurement points. This is very similar to the double correlated sampling discussed in section 4.3.2 which was used to cancel baseline pulling effects of the detector due to technical imperfections. By using a two point variance one can remove classical signal correlations on timescales larger than  $\tau$ .

The shot noise limited performance of our setup has been demonstrated for probe pulses containing up to  $n \sim 10^9$  photons on timescales  $\tau$  of few microseconds [1]. While this sounds promising at first, the short timescale on which a baseline needs to be established for the measurement is rather discouraging. The atoms cannot be reliably removed from the trap within few microseconds; an interferometer baseline has to be established in the presence of atoms.<sup>3</sup> Obviously, the probe laser cannot be employed for this purpose.

---

<sup>3</sup> For the measurements discussed in the previous chapters it was sufficient to determine the interferometer baseline within a few hundred milliseconds (compare, e.g., section 3.4.1) because the measurement accuracy required to determine the classical component of the Bloch vector is much smaller.

### Reference pulses

Knowing that the interferometer performs at the shot noise limit within few tens of microseconds, we replace the second pulse in the two point variance with a baseline reference pulse  $b_i$ . To create the baseline measurement pulses, we use high power pulses derived from the interferometer stabilization laser, compare section 3.2.2. Due to the choice of the wavelength of the lock laser  $\lambda \approx 840$  nm, we can assume that it does not interact with the atoms in a destructive way. To create pulses of sufficient photon number, we increase the rf power on the pulsing AOM which is otherwise used to create the interferometer locking pulses. We then send these reference pulses in between the actual atomic sample probe pulses. Since the reference pulses can be almost arbitrarily close in time to the actual probe pulse, we can expect that shot noise limited performance of the interferometer with respect to the probe pulses  $p_i$  is achieved for the combined pulses  $p'_i = p_i - b_i$ .

Part of a typical pulse sequence for measuring the noise performance of the interferometer is shown in figure 6.1. Figure 6.1(a) shows the sequence of light pulses as recorded on a reference detector (compare figure 3.5), where probe  $p_i$  and reference  $b_i$  pulses are alternated. The duration of both pulses is  $4 \mu\text{s}$  and  $p_i$  and  $b_i$  are separated by  $4 \mu\text{s}$ . The separation between  $p_i$  and  $p_{i+1}$  is chosen between several milliseconds and few seconds. The corresponding interferometer output signal is shown in figure 6.1(b). One can clearly observe that the interferometer is not exactly balanced for the probe and the reference pulses at the same time. This is due to the fact that we stabilize the interferometer at  $\pi/2$  away from the white light position and due to the dependence of the beam splitter splitting ratio on the wavelength, compare section 3.2.2

*In general*, we use different powers for the probe and for the reference pulses. Obviously, a high power in the reference pulses allows us to determine the baseline more accurately. We therefore increase the power to the maximum level allowed by the dynamical range of the detector. For equal mean photon numbers in  $p_i$  and  $b_i$ , the reference pulses would add one unit of light shot noise and thereby effectively decrease the measurement accuracy. For high photon numbers, the influence of the photon shot noise of the baseline measurement is reduced since the relative measurement precision scales as  $\frac{\sqrt{\delta^2 \Delta \phi}}{\Delta \phi} \propto \frac{1}{\sqrt{n}}$ . In other words: we want to use the baseline pulses to determine the classical interferometer position and therefore do not want the baseline measurement to be light shot noise limited.

To use the reference pulses  $b_i$  as interferometer baseline for the probe pulses  $p_i$ , one has to rescale the pulse areas to the relative power of the two beams. Since it is difficult to measure the relative power of the pulsed probe and reference beam to an accuracy that the normalization to power does not introduce additional noise, we chose a different approach: We optimize the two point variance with respect to the correlation strength of probe and the reference pulses. From a pulse sequence as discussed above, we calculate the conditional variance:

$$\delta^2 p_{\text{cond}}(\lambda) \equiv \delta^2(p - \lambda b) = \langle (p_i - \lambda b_i)^2 \rangle - \langle p_i - \lambda b_i \rangle^2 \quad (6.6)$$

as a function of the correlation parameter and find the optimal  $\lambda$ . The optimal value can either be found by directly calculating the variance for different values

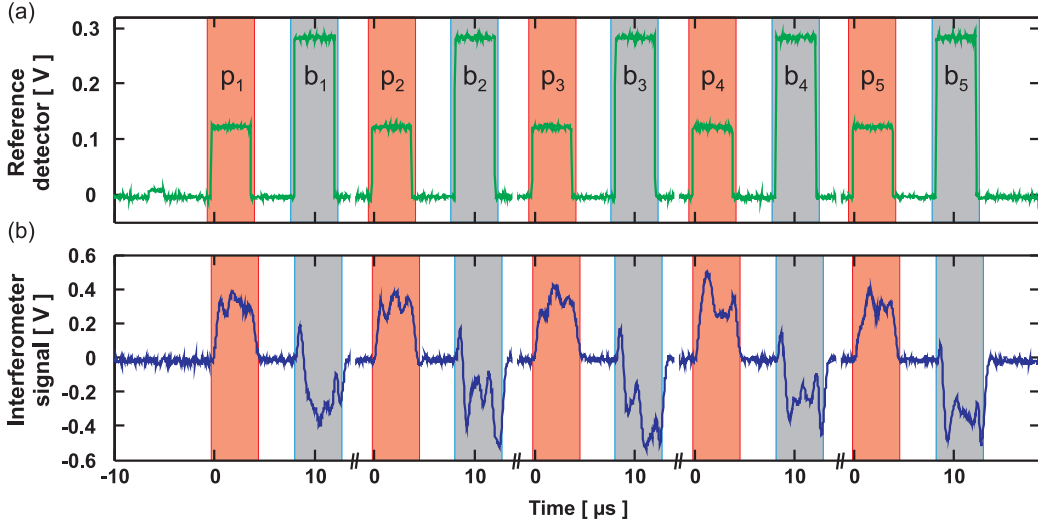


**FIGURE 6.1:** Pulse sequence to establish the noise performance of the interferometer. (a) Probe pulses  $p_i$  from one of the probe lasers and reference pulses  $b_i$  derived from the lock laser are alternated. To establish the interferometer baseline with the reference pulses to high accuracy, their power is increased to the maximum value allowed by the differential detector. (b) Corresponding interferometer signal. The individual pulses are integrated with optimized integration windows and used to calculate a conditional two point variance  $\delta^2(p - \lambda b)$ .

of  $\lambda$  or by invoking the covariance:

$$\frac{d}{d\lambda} \delta^2(p - \lambda b) = \frac{d}{d\lambda} (\delta^2 p + \lambda^2 \delta^2 b - 2\lambda \text{cov}(p, b)) \stackrel{!}{=} 0 \quad (6.7)$$

$$\Leftrightarrow \lambda = \frac{\text{cov}(p, b)}{\delta^2 p} \quad (6.8)$$

where  $\text{cov}(p, b) = \langle p \cdot b \rangle - \langle p \rangle \langle b \rangle$ . Calculating the covariance can be more straight forward than finding the optimal value in an optimization procedure.

First, we establish a reference shot noise level in the setup by confirming the linear scaling of the two point variance with photon number on short timescales using only probe laser pulses. In figure 6.2(a) the two point variance  $\frac{1}{2} \delta^2 p(16 \mu\text{s})$  of two consecutive probe pulses  $p$  with a time separation of  $16 \mu\text{s}$  is shown. A small quadratic, i.e., classical noise contribution is visible but the variance is clearly dominated by the linear noise scaling characteristic for light shot noise. When we switch to using the reference pulse as second pulse in the two point variance, we obtain the optimized data as shown in figure 6.2(b). Corresponding raw data is shown in figure 6.1(b); we use 200 combined  $p_i - b_i$  pulse sets to calculate the variance. Since the photon number of the baseline pulses is not changed in the measurement they contribute with a constant amount of shot noise which has been subtracted in the plot. We compare the single probe pulse shot noise obtained from the two point measurement with two probe pulses  $\frac{1}{2} \delta^2 p(16 \mu\text{s})$  with the single probe pulse shot noise  $\delta^2(p - \lambda_{\text{opt}} b)$  (baseline shot noise). We observe that the scaling of the variance is clearly dominated by the linear shot noise part. At  $n = 3 \times 10^8$  photons we observe an additional classical noise component of 23%. Below  $n = 1 \times 10^8$  photons the classical noise contribution is negligible; since we

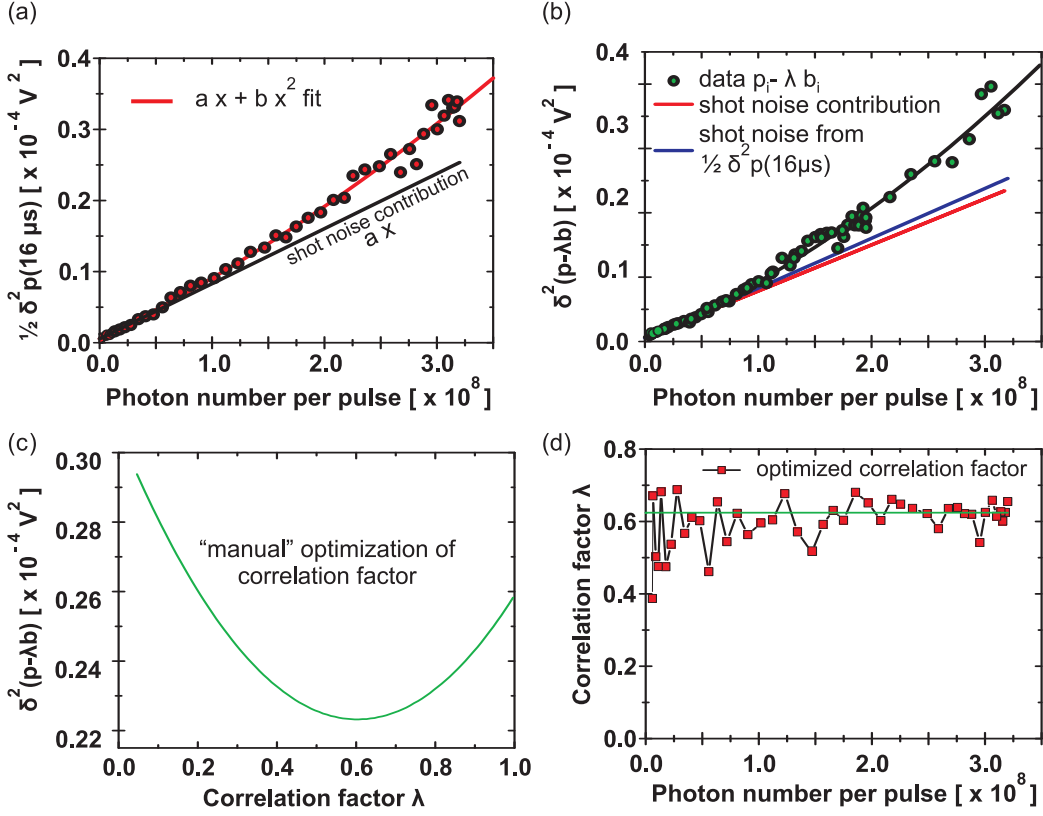


**FIGURE 6.2:** (a) Shot noise limited performance of the interferometer on a timescale of  $16 \mu\text{s}$  when using two probe pulses in the two point variance. The scaling of the variance with photon number is clearly dominated by a linear component, characteristic for shot noise. (b) Optimized two point variance  $\delta^2(p - \lambda b)$  where additional reference pulses  $b_i$  assure the knowledge of the interferometer baseline for the probe pulses  $p_i$  on a  $8 \mu\text{s}$  timescale. The linear component of the baseline corrected pulses corresponds very well to the shot noise contribution when using only probe pulses. This confirms that using a different laser to establish the baseline is a feasible method. (c) Procedure to extract the optimal correlation factor  $\lambda$ . The two point variance  $\delta^2(p - \lambda b)$  has a clear minimum for a given probe power ratio. The data is shown for  $2.4 \times 10^8$  photons in the probe pulse. (d) The minimum is stable for different probe powers, indicating that the (shot) noise contribution of the reference pulses to the data is negligible. We pick the mean value of  $\lambda$  for high probe powers as  $\lambda_{\text{opt}}$  for the data in (b).

will use photon numbers below  $10^8$  in the projection noise measurements, compare section 6.1, we can claim shot noise limited performance in the desired photon number range.

The optimization procedure of the correlation factor  $\lambda$  is illustrated in figure 6.2(c). It shows the two point variance  $\delta^2(p - \lambda b)$  for a probe pulse photon number of  $n_p = 2.4 \times 10^8$  as a function of  $\lambda$ . For  $\lambda \rightarrow 0$  the baseline subtraction is switched off and we obtain the variance on a timescale of the repetition period between two consecutive probe pulses. Since the repetition period is much larger than the timescale for shot noise limited performance, the variance grows. At the optimum value for  $\lambda \approx 0.62$ , (which we pick for the entire range of optimized data shown in figure 6.2(b)) classical correlations between the probe and reference pulses, i.e.,

the fluctuations of the interferometer, are optimally suppressed and we are left with correlations faster than the time separation between the two pulses and the shot noise contribution of both lasers. These fast fluctuations are smaller than the intrinsic measurement uncertainties and we therefore observe shot noise limited performance. Observing  $\lambda_{\text{opt}} \neq 1$  mirrors the fact that the intensities of both beams are different (compare figure 6.1). When the power in the baseline reference pulses is comparable with the probe pulses, optimizing  $\lambda$  means bargaining the knowledge on the baseline obtained with the pulses  $b_i$  against the addition of baseline pulse shot noise. Optimizing the variance in that way removes the necessity to know the power ratio of the two beams – as long as it can be assumed to be constant over the time of the measurement. Figure 6.2(d) confirms that the optimal value of  $\lambda$  is a system parameter since it stays stable for all photon numbers. Towards low photon number it becomes less well determined and the noise in  $\lambda$  increases. The mean values of  $\lambda$  for high photon numbers is a good choice for the correlation strength.

The presented data and the above discussion demonstrates that we, indeed, can claim shot noise limited performance of the interferometer on basically arbitrarily long timescales. If the power of the probe or reference beam changes dramatically, it might be necessary to adapt the correlation factor  $\lambda$  to accommodate for these changes. The important part in the procedure is that an additional beam which does not couple to the atomic ensemble is used to establish the baseline. Shot noise limited performance with reference pulses has been established for both probe colors individually and for bi-chromatic pulses. With this, the setup meets the first requirement for the probing of an atomic ensemble at the standard quantum limit.

To conclude this section on the empty interferometer noise performance, and to close the circle to the double correlated sampling technique discussed in section 4.3.2, we note that it is also possible to use baseline reference pulses before and after the actual probe pulse. This way the effective photon number in the reference pulses can be increased, which reduces the influence of reference pulse light shot noise further. This is especially important when the fluctuations of the interferometer balancing produce signal offsets which reach the saturation limit of the detector, compare 6.1(b).

## 6.2.2 Stability requirements

The above discussion relies on the assumption that all the pulses  $p_i, b_i$  are coherent light states with constant mean photon number  $\bar{n}_p, \bar{n}_b$ . The problem of classical amplitude noise of the probe lasers has been shortly mentioned in section 3.2.3 as motivation to change from the two color – single port to the two color – two port interferometer setup. The main issue of amplitude fluctuations of the probe lasers has been illustrated in figure 3.8, page 42. To take the discussion to a more formal level, let us look at the output signal of the interferometer  $S_-$ . We assume that the  $F = 3 \rightarrow F' = 4$  laser probe pulse contains  $n_3$  photons and couples with a coupling parameter  $\kappa_3 = n_3 \frac{\beta_3}{\Delta_{3,2}}$  only to the population in  $F = 3$ . Similarly, we define the values for the  $F = 4 \rightarrow F' = 5$  pulses as  $n_4$  and  $\kappa_4 = n_4 \frac{\beta_4}{\Delta_{4,5}}$ . The couplings are arranged such that  $\kappa_3 = \kappa_4$  for  $n_3 = n_4$ . For an equal atomic superposition

state of  $N$  atoms we measure a mean value of  $\bar{N}_3 = N/2$  and  $\bar{N}_4 = N/2$  of atomic population in the  $F = 3$  and  $F = 4$  level, respectively. The total interferometer output signal  $S_-$  is then built up by the two individual signals  $S_3$  and  $S_4$ :

$$S_3 = \gamma n_3 \frac{-\beta_3}{|\Delta_{3,2}|} N_3 \quad \text{and} \quad S_4 = \gamma n_4 \frac{\beta_4}{|\Delta_{4,5}|} N_4 \quad (6.9)$$

$$S_- = S_3 + S_4 = \gamma \left( n_4 \frac{\beta_4}{|\Delta_{4,5}|} N_4 - n_3 \frac{\beta_3}{|\Delta_{3,2}|} N_3 \right) \quad (6.10)$$

where  $\gamma$  parameterizes the gain of the detector. For the mean value of the signal we get  $\langle S_- \rangle = 0$ . The variance  $\delta^2 S_-$  contains several terms:

$$\begin{aligned} \frac{\delta^2 S_-}{\gamma^2} &= \delta^2(\kappa_3 N_3 + \kappa_4 N_4) \\ &= [\delta^2 \kappa_3 + \delta^2 \kappa_4] N/4 + [\delta^2 \kappa_3 + \delta^2 \kappa_4] N^2/4 + [\bar{\kappa}_3 + \bar{\kappa}_4]^2 N/4 \end{aligned} \quad (6.11)$$

where we have used that the atom numbers  $N_3$  and  $N_4$  are correlated  $N_3 + N_4 = N$ , and we have inserted the variance of a coherent atomic state  $\delta^2(N_3) = \delta^2(N_4) = N/4$ . We have omitted the electronic noise contribution from the detector since it is negligible for the photon numbers involved in the measurement, see chapter 4. The variance of the coupling strength:

$$\delta^2 \kappa_{3,4} = \frac{\beta_{3,4}^2}{\Delta_{(3,2),(4,5)}^2} \delta^2 n_{3,4} + \bar{n}_{3,4}^2 \beta_{3,4}^2 \frac{1}{\Delta_{(3,2),(4,5)}^2} \delta^2 \Delta_{(3,2),(4,5)} \quad (6.12)$$

depends on the (independent) amplitude  $\delta^2 n_3, \delta^2 n_4$  and phase  $\delta^2 \Delta_{3,2}, \delta^2 \Delta_{4,5}$  noises of the two lasers<sup>4</sup>. To first order (this has been checked experimentally) both probe lasers behave in a very similar way, so with the equal signal requirement,  $\bar{n}_4 = \bar{n}_3 \equiv \bar{n}$ , we can assume  $\delta^2 n_3 = \delta^2 n_4$  and  $\delta^2 \Delta_{3,2} = \delta^2 \Delta_{4,5}$  which leads to  $\delta^2 \kappa_3 = \delta^2 \kappa_4 \equiv \delta^2 \kappa$ . With this the variance of the signal reduces to:

$$\frac{\delta^2 S_-}{\gamma^2} = \frac{N}{2} \delta^2 \kappa + \frac{N^2}{2} \delta^2 \kappa + N \bar{\kappa}^2 \quad (6.13)$$

The first term results from the correlation of the atom numbers  $N_3 + N_4 = N$ . The second term is the noise part caused by the fluctuations of the coupling strength. These are mainly due to the probe laser amplitude and phase noise, but contain contributions from fluctuating magnetic fields, inducing Zeeman shifts, and trap laser power instabilities causing light shifts. The third term is the atomic projection noise contribution. Since the first part is dominated by the second for high atom numbers, the stability requirements for observing atomic projection noise can be reduced to:

$$\frac{\sqrt{\delta^2 \kappa}}{\bar{\kappa}} \ll \frac{\sqrt{2}}{\sqrt{N}} \quad (6.14)$$

<sup>4</sup> $\delta^2 \Delta_{3,2}$  and  $\delta^2 \Delta_{4,5}$  also accommodate for fluctuations of the atomic transition frequency due to the Zeeman effect and fluctuations in the differential light shifts of the probe transitions caused by intensity noise in the trap laser. Assuming that the bias field is stable to the level the field nulling produced  $\sqrt{\delta^2 B} \approx 35$  mGauss and that the second order Zeeman shift is of the same order of magnitude for the ground  $F = 3, 4$  and the excited levels  $F' = 2, 5$ ,  $\Delta\omega \approx 2\pi \cdot 500$  Hz/Gauss<sup>2</sup>, the influence of magnetic field fluctuation becomes negligible.

Assuming a total number of atoms of the order of  $N \sim 10^5$ , the relative power and frequency stability of the lasers become:

$$\frac{\sqrt{\delta^2 n_{3,4}}}{\bar{n}_{3,4}} \ll 3 \times 10^{-3} \quad \text{and} \quad \frac{\sqrt{\delta^2 \Delta_{(3,2),(4,5)}}}{\Delta_{(3,2),(4,5)}} \ll 3 \times 10^{-3} \quad (6.15)$$

The linewidth of the probe laser is around 250 kHz. With a probe frequency detuning  $\Delta_{4,5} \sim \Delta_{3,2} \sim 100$  MHz, the second requirement is barely met. The power stability of the lasers is a more serious problem, especially on long time scales. Although the output power of the laser diode itself is basically shot noise limited, especially the coupling into optical fibers and the use of polarization optics corrupt the power stability.

### Power stability in fibers

In the experimental setup, special care was taken to optimize the coupling efficiency into the optical fibers. This reduces the effect of coupling variations due to pointing instabilities of the lasers. In addition, the light polarization is carefully matched to the axis of the polarization maintaining fibers. At the fiber output, the fiber axis is again matched to the polarization axis of the first beam splitter. We thereby reduce power variations caused by the temperature dependent birefringence in the optical fibers. Nonetheless, the results of long term power measurements seem discouraging at first. In figure 6.3(a) we plot the relative power deviation from the start value at three positions in the setup of figure 3.6(a), page 37 – before the first fiber, after the first mode cleaning fiber and after the second fiber which transports the beams to the interferometer setup. Over a time of ten hours, the power fluctuates by several percent. On a timescale of one minute, figure 6.3(b) confirms a relative stability of  $\sqrt{\delta^2 \bar{n}} \sim 2 \times 10^{-3}$ . When we calculate the two point variance  $\delta^2 p(\tau) = \langle (p(t) - p(t+\tau))^2 \rangle_t - \langle p(t) - p(t+\tau) \rangle_t^2$  and plot the corresponding standard deviation as a function of  $\tau$ , graph 6.3(c) shows that a stability of better than  $\sqrt{\delta^2 p(\tau)} = 4 \times 10^{-4}$  can be achieved at all three measurement points for times  $\tau \lesssim 10$  s. It is thus possible to fulfil the stability requirement (6.15) on this short timescale. In principle, the power stability of the lasers especially after the optical fibers, is not good enough to perform long measurement runs. To collect sufficient statistics for projection noise measurements, we will see in the next section, several thousand repetitions of the loading cycle are necessary, each taking about 3 seconds. To circumvent this problem, we combine consecutive measurement runs  $i$  which are separated in time by only few seconds and thereby assure that the stability requirements are met. When  $p_{k,i}$  labels a set of pulses  $k$  in a single run  $i$ , we replace  $p_{k,i} - p_{k,i+1} \mapsto p_{k,i}$  and use these new “meta” pulses for the noise analysis.

### Classical noise due to laser current modulation

We are now almost ready to go for the projection noise measurements in the two color – single port interferometer setup. Before we discuss the measurements, we show an instructive example on how tiny things can cause huge effects when it comes to noise. In section 3.2.1 we have shortly discussed the locking setup for

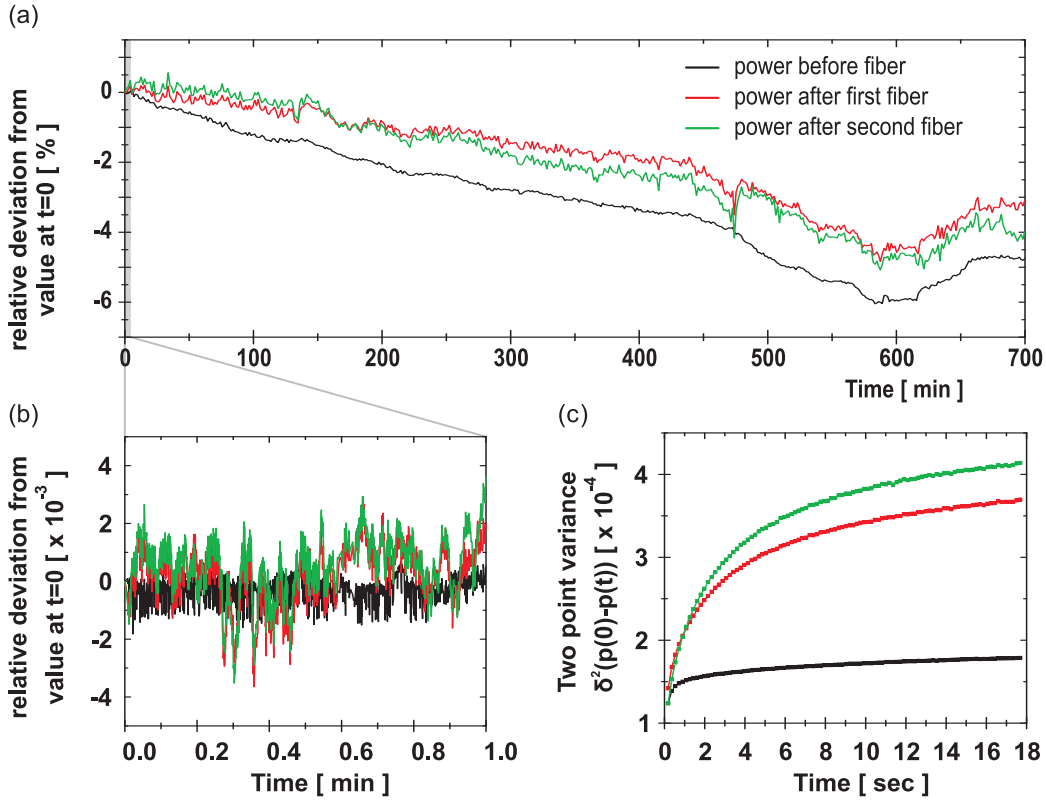


**FIGURE 6.3:** Temporal stability of probe laser power at different measurement points in the setup. (a) Over a time of several hours, the power fluctuates by few percent. (b) On a shorter timescale one can clearly observe that the fluctuations after the fibers are considerably larger than before. However, the fluctuations after the second fiber are clearly correlated with the powers after the first fiber. Pointing instability of the laser is therefore the most prominent cause of the fluctuations. (c) The two point variance  $\delta^2 p(\tau) = \langle (p(t) - p(t + \tau))^2 \rangle_t - \langle p(t) - p(t + \tau) \rangle_t^2$  of the signal in (a) shows that on a timescale below 10 s, the stability of the power is guaranteed to be better than  $\frac{\sqrt{\delta^2 n}}{n} = 4 \times 10^{-4}$ .

the probe lasers and shortly motivated the choice of beat note stabilization or external frequency sideband generation instead of direct laser current modulation. We now compare the amplitude fluctuations in a quasi pulsed measurement for a laser with frequency modulation used for locking and without the modulation. It is clear that a modulation of the injection current of the laser diode causes both frequency (which is the desired one for the locking) and amplitude modulation (which produces classical power correlations). In figure 6.4 the influence of a 4 MHz modulation on the inferred noise is shown. To obtain the data, we integrate the output of a standard dc power detector in time windows of  $\tau = 1 \mu\text{s}$  and  $\tau = 10 \mu\text{s}$  with 100  $\mu\text{s}$  repetition period and calculate the variance of these virtual pulses. For virtual pulse durations of  $\tau = 1 \mu\text{s}$ , the classical amplitude modulation of the fm lock is not averaged out and the noise is clearly dominated by a quadratic component. When we use a pulse duration of  $\tau = 10 \mu\text{s}$ , the data in the inset of figure 6.4 shows that the effect of the modulation is clearly reduced, but the classical noise contribution is still clearly visible. These observations make clear that on the timescales we are interested in, the standard frequency modulation

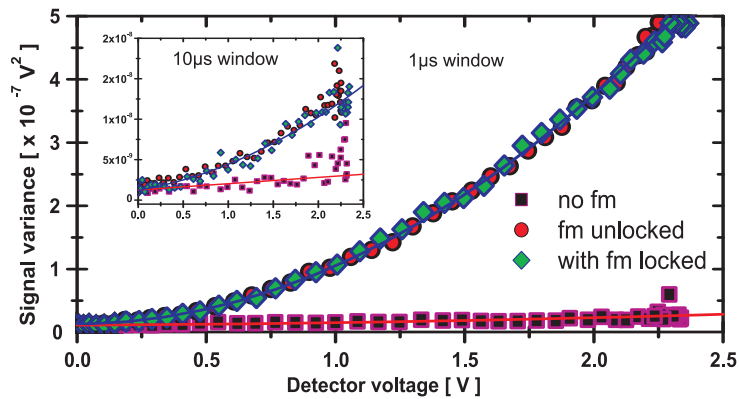


**FIGURE 6.4:** Noise introduced by diode injection current modulation for frequency modulation spectroscopy and frequency stabilization. The modulation is clearly visible as classical (quadratic) noise component compared with the linear noise scaline when no modulation is applied.  $\tau = 1 \mu\text{s}$  integration windows are too short to average out the effect of 4 MHz modulation. (inset) Using  $\tau = 10 \mu\text{s}$  long integration windows, the effect of modulation is reduced but still clearly visible. The noise level is independent on whether the stabilization loop is engaged or not. The noise observed does thus stem from the modulation and not from the frequency stabilization loop.

locking scheme as used for the MOT master lasers (compare section 3.1.2) is not usable. We therefore switch to adding sidebands with AOMs only in the part of the beam used for locking or a beat note lock setup, see section 3.2.1. Further it becomes obvious that high performance of the probe lasers in respect to amplitude and frequency noise is crucial to succeed with shot noise limited measurements.

### 6.2.3 Projection noise measurements

After this short excursion into typical challenges one runs into when attempting to measure quantities at the standard quantum limit, we shall now indulge into the fine arts of noise data analysis. The measurements as such are rather straight forward, the result of the analysis, however, crucially depends on the analysis procedures. Here we make use of the thorough understanding of the measurement apparatus we have gained throughout the preceding chapters.

#### Measurement procedure

The experimental programme for projection noise and squeezing measurements was outlined in section 2.5. Figure 6.5 presents the main principle in a nutshell. We load atoms into the dipole trap as discussed in section 3.1.2 and 3.1.3. Subsequently we initialize the atoms to one of the clock state and apply the purification procedures of section 5.3.2. A microwave  $\pi/2$ -pulse creates a coherent atomic superposition state of which we measure the population number difference in a non-destructive way using our interferometer in the two color – single input port configuration. Consider section 3.2 for the setup and the relevant sections of chapter 5 for the characterization of the non-destructive light-atom interface. For the QND measurement on the superposition state we adjust the photon numbers in the bi-chromatic probe pulses

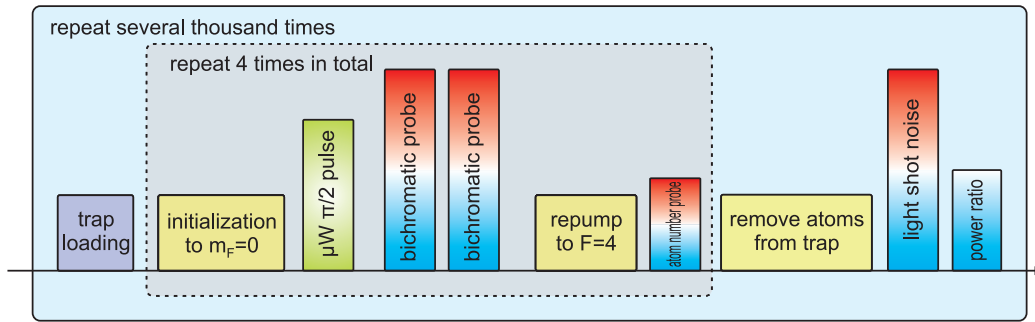


**FIGURE 6.5:** Pulse sequence for projection noise measurements. After loading atoms into the dipole trap, the sample is initialized into one of the clock states, cleaned and a coherent superposition state is produced with a microwave  $\pi/2$ -pulse. The superposition state is measured at least twice with bi-chromatic probe pulses. After the measurement the atom number is determined by repumping the sample into  $F = 4$  states and measuring the corresponding interferometer phase shift. For this measurement we reduce the probe power considerably not to saturate the detector. The initialization and measurement cycle is repeated four times within the same trap loading. After the four measurements on different atom numbers (the atom number is different for the four measurements due to the natural trap lifetime and the not perfect optical pumping efficiency, compare figure 5.11) the atoms are removed from the trap and we measure the interferometer baseline (light shot noise) and the power ratio between the two probe colors. These single experimental runs are repeated several thousand times to accumulate good statistics.

such that we obtain a decoherence parameter of the order of  $\eta = 30\%$ , as necessary for optimal squeezing, section 6.1. The decoherence parameter is measured using the spin echo techniques demonstrated in section 5.10.2. The power and frequency ratio of the two probe colors is adjusted such that the signal of an equal population superposition state shows zero interferometer phase shift as shown in figure 5.12. After two non-destructive measurements, we optically pump the atoms into the  $F = 4$  ground state and measure the total atom number equivalent interferometer phase shift. For practical reasons we also use a bi-chromatic probe pulse to determine the atom number; in principle, a light pulse coupling only to  $F = 4 \rightarrow F' = 5$  would be sufficient. Together with the known trap decay, the number of atoms in the superposition state can be extracted as discussed in connection with figure 5.11. Since a sample with all its population in the  $F = 4$  state produces a huge interferometer output signal for the photon numbers necessary in the superposition state probing, we reduce the probe power at this stage. The reference detector shown in figure 3.5 is used to monitor the power ratios. After calibrating the signal of the reference detector to the interferometer fringe amplitude measured on the differential detector, compare figure 3.7, the reference signal is also used to convert the measured signal to an actual light phase shift. To increase the data rate and to obtain measurement points at different atom numbers, we exploit the extended lifetime of the atoms in the trap<sup>5</sup>. We repeat the preparation and measurement cycle four times (compare again with figure 5.11 for confirmation that this is feasi-

<sup>5</sup>We are aware that the lifetime of few hundreds of milliseconds is not great, but taking the efficiency of  $\sim 70\%$  of the optical pumping into account, repeating the cycle for more than four times makes not too much sense. Furthermore, since we in the end record 10 data segments with the oscilloscope, we reach the limit of the data transfer speed within the loading cycle, so taking more data segments would in fact reduce the data rate.

ble) and then remove the atoms from the interaction region. At the end of a single experimental run, we measure the empty interferometer baseline and use the pulses to verify the shot noise limited performance during the measurement. The stage is also used to determine the power ratio between the two probe colors. These single experimental runs are then repeated several thousand times to gather enough statistics. During these measurements, we actively vary the atom number either by increasing or reducing the background vapor pressure by varying the dispenser current or the loading time during the MOT stage. Together with the sampling of different atom numbers in the four stages, we can obtain continuous noise data between zero and the maximum number of atoms.

For further clarification on the specifics of the measurement procedure, figures 6.6 and 6.7 should be of help. Single raw data traces from the power reference detector and from the interferometer detector are shown. The traces illustrate the power switching of the probe colors for the projection noise and the atom number measurement as discussed above. Furthermore, the interferometer reference pulses which we have discussed in section 6.2.1 are shown. Remember, these pulses were necessary to assure a light shot noise limited performance of the interferometer on the timescales in question. The power of these auxiliary light pulses has been increased as far as the dynamical range of the detector and the oscilloscope allows; the signals from the measurements on the superposition state are therefore only barely visible. Raw data for the first measurement block, i.e., superposition state measurement and corresponding atom number determination, of consecutive measurement runs  $i$  are shown in figure 6.7.

### Noise data analysis

In a first step, the acquired raw measurement data traces, i.e., the electronic signals from the detectors, are integrated with suitable window functions. The procedure to determine the optimal integration window and the necessity for the optimization has been discussed in section 4.3.2. Since the probe pulse photon numbers are of the order of  $n_{\text{ph}} \sim 4 \times 10^7$  photons, the electronic noise of the detector is negligible and a double correlated sampling window is used. From this integration we get the pulse amplitudes  $p_{k,i}$ ,  $b_{k,i}$ ,  $a_{k,i}$ ,  $s_{k,i}$  and  $r_{k,i}$  for both the interferometer and the power reference detector. The subscript  $i$  is used for the measurement run and  $k$  indicates the number of the pulse in a measurement block  $b$ . We do not distinguish between the four different measurement blocks  $b = [1 \dots 4]$  since they are associated with different atom number through the corresponding atom number measurement anyway, compare figure 6.6. We perform the analysis according to atom number later, so the pulse areas  $a_{k,i}$  are used to discriminate the segments against each other. This is equivalent to the replacements:  $p_{k,i,b} \rightsquigarrow p_{k,i+(b-1) \cdot i_{\text{max}}}$ ,  $b_{k,i,b} \rightsquigarrow b_{k,i+(b-1) \cdot i_{\text{max}}}$ ,  $a_{k,i,b} \rightsquigarrow a_{k,i+(b-1) \cdot i_{\text{max}}}$ . The data acquired with the pulses  $s_{k,i}$  corresponds to zero atom number, so we treat it in the exact same way as the pulses  $p_{k,i}$ ; we label the baseline reference pulses in that segment with  $b_{k,i}^s$ . After the pulses have been integrated, we apply a number of consistency checks to the data:

1. Data out of oscilloscope range. To reduce the influence of digitization noise,

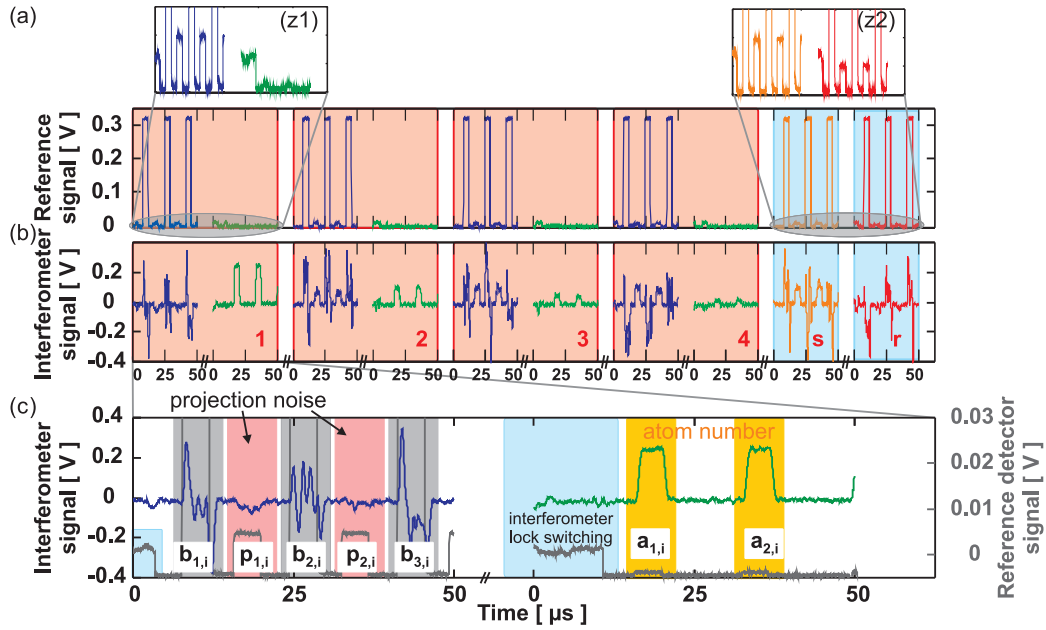


**FIGURE 6.6:** *Experimental raw data from the projection noise measurement sequence. The single experimental run shown is repeated several thousand times. (a) The signals from a reference detector represent the light pulse sequence. The insets show zooms into the traces, (z1) illustrating the power ratios between the projection noise (blue) and the atom number (green) measurement and (z2) between the two probe colors. The four measurement blocks correspond to the four consecutive measurements on the “same” trap after a single trap loading. In the segment labeled with “s”, the empty interferometer is measured. This measurement is used to make sure that the system performance is at the shot noise limit and together with segment “r” it also serves to determine the power ratio between the two colors. (b) Corresponding interferometer output signal. In the atom number signal (green) one can nicely follow the decay of the atom number due to trap loss and imperfect optical pumping. (c) Zoom into the first data block (the underlying gray trace is the reference detector signal). In the data shown, we use high power baseline reference pulses  $b_1, b_2, b_3$  before and after the actual atom projection probe pulses  $p_1, p_2$  to establish the empty interferometer baseline with the lock laser within the shot noise limited timescale of the interferometer. The atom number is determined by averaging over several probe pulses whereof only the first two  $a_1$  and  $a_2$  are shown. In the reference detector trace, the switching of the interferometer locking pulses can be seen at the left side of the traces. The lock is switched off shortly before the actual measurement starts.*

the DSO channel range is reduced as far as allowed during stable operation of the interferometer. We try to run on 100 mV/div. 200 mV/div still gives good results, when moving to the next higher scale, the DSO internally switches to a different input amplifier, which apparently has much higher noise. Acoustic noise can therefore cause the interferometer signals to lie outside the DSO range. Corresponding data is filtered out by checking the raw data for “out of range” data points.

2. Detector saturation. When several imbalanced probe pulses saturate the integration stage of the interferometer detector, the zero level of the signal does not return to anything close to zero after the applied light pulse. Applying a bound to the allowed detector offset after the pulses therefore removes

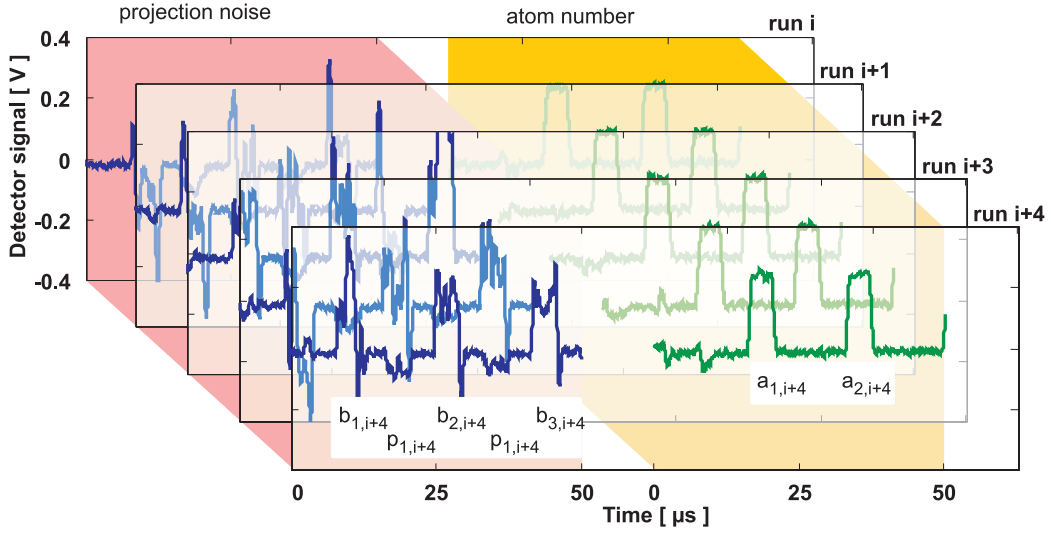


**FIGURE 6.7:** Raw data for several consecutive projection noise measurement runs  $i$ . The data shown corresponds to the interferometer output signal from the first measurement block in figure 6.6, consecutive measurement runs are stacked relative to each other.

saturation events.

3. Atom number stability and trigger failures. When the speed of data transfer between the scope and the data analysis computer is reduced (Windows can do strange things), the synchronization between the experimental sequence and the scope can fail; these trigger failures mix up the measurement segments. Sudden deviations of the atom number from its general tendency therefore serve to discriminate these events. Suboptimal performance of the dipole trap laser also induces strong shot-to-shot atom number fluctuations. In case the filters do not remove the corresponding data, we remove it manually. In figure 6.8 we show the discrimination process on the atom number signal for about 23000 consecutive measurement runs and each of the four blocks separately.
4. Probe power fluctuations. A discrimination filter is also applied to the allowed power fluctuations of the probe lasers. If the probe laser power deviates by more than a few standard deviations of the overall measurements, the corresponding data is discarded. This discrimination is applied to both the probe lasers and the reference laser powers.
5. Manual removal of data. When suboptimal performance of any of the system components is observed, we generously discard data which has been taken during these periods.

Next, we remove fast interferometer and slow general system drifts. Fast interferometer noise has been discussed in section 6.2.1 and that's what we have introduced the auxiliary reference pulses  $b_{k,i}$  for. Since the atomic population probe pulses  $p_{k,i}$  and the reference pulses  $b_{k,i}$  have different powers, we use the optimized conditional variance  $\delta^2 p_{\text{cond}}(\lambda)$  to determine the correlation factor for the subtraction

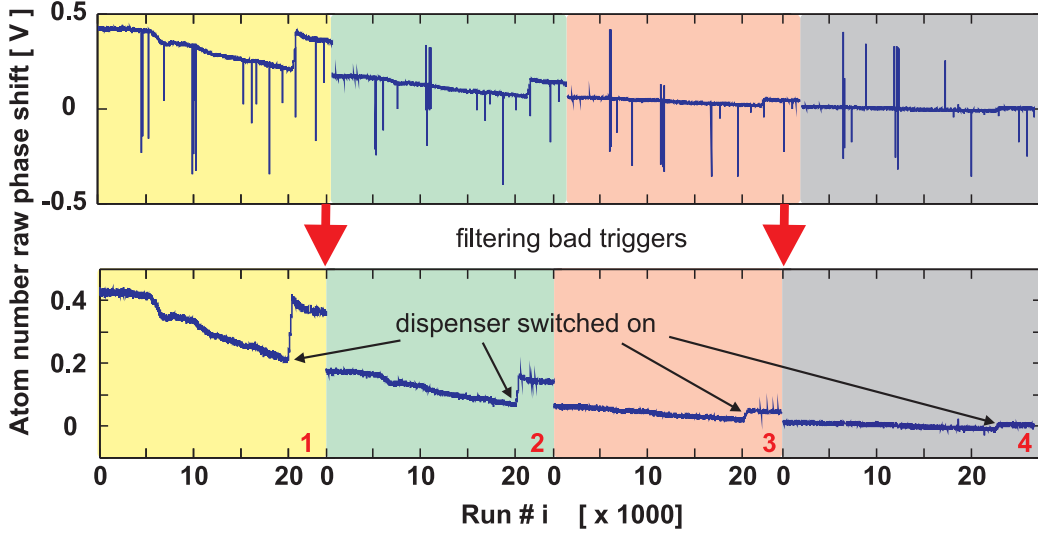


**FIGURE 6.8:** Atom number signal and filtering bad oscilloscope triggers. Data corresponding to about 23000 consecutive data runs. When the atom number deviates strongly from one run  $i$  to the next, a trigger failure can be assumed and we discard the corresponding data point. The four areas correspond to the atom numbers in the different measurement blocks. The arrows also indicate where the current of the dispensers was increased during the measurement to augment the number of atoms again and gather more data at high atom numbers.

and define the new probe pulses  $p_{k,i}$  as:

$$p_{k,i} - \lambda \frac{1}{2} (b_{k,i} + b_{k+1,i}) \rightsquigarrow p_{k,i} \quad (6.16)$$

$$s_{k,i} - \lambda \frac{1}{2} (b_{k,i}^s + b_{k+1,i}^s) \rightsquigarrow s_{k,i} \quad (6.17)$$

The optimal  $\lambda$  is determined such that it minimizes the two point variance for the empty interferometer segment  $s$ , i.e., the light shot noise measurement. It is determined globally for a long sequence of data and we follow its variation in time and adapt  $\lambda_{\text{opt}}$  in case necessary. As discussed in section 6.2.1 the optimal  $\lambda$  is supposed to be a system parameter which only depends on the powers involved and the time between the pulses.

The influence of long term drifts and especially the power instabilities induced by the optical fibers as discussed in section 6.2.2 can be removed from the data by building a two point variance of consecutive measurements. To this end, we redefine the pulses another time as:

$$p_{k,i} - p_{k,i+1} \rightsquigarrow p_{k,i}, \quad s_{k,i} - s_{k,i+1} \rightsquigarrow s_{k,i} \quad (6.18)$$

Since the repetition cycle of the experiment is few seconds, we herewith remove systematic changes on timescales much larger than these few seconds. These new “meta” pulses are associated with the mean atom number for the corresponding runs. The atom number in a single run is inferred from the mean over the measurements  $k$  in the corresponding segment:

$$\frac{1}{2} \langle a_{k,i} + a_{k,i+1} \rangle_k \rightsquigarrow a_i \quad (6.19)$$

As last preparatory step, we convert the pulse data into interferometer fringe amplitude or interferometer phase shift. To this end we normalize the pulses  $p_{k,i}$  and  $a_i$  with a fringe calibration factor extracted from data as shown in figure 3.7, page 39. The resulting data is shown in figure 6.9. We have sorted the data according

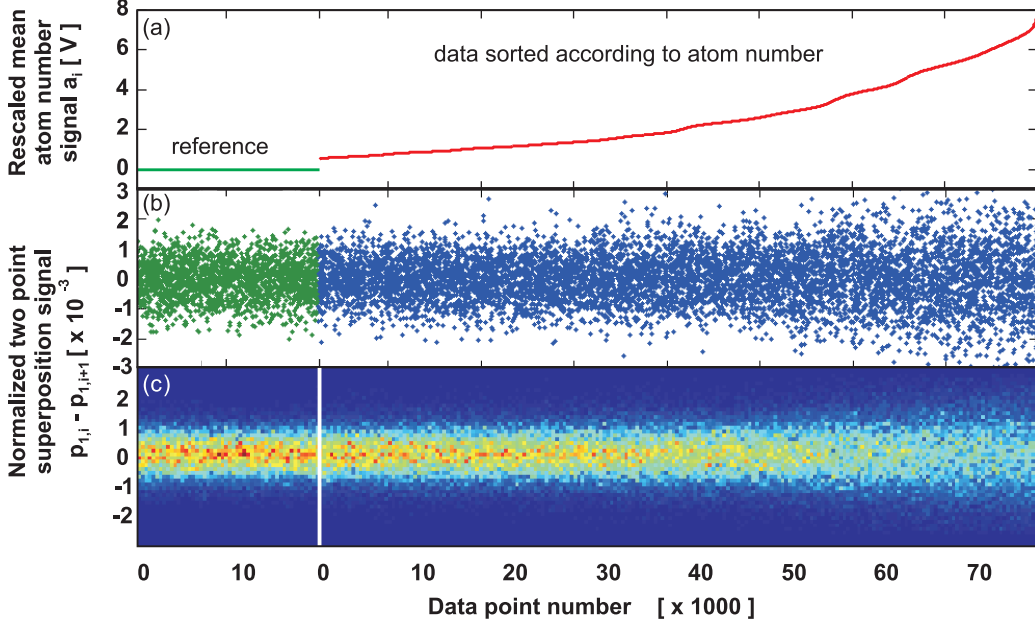


**FIGURE 6.9:** Scattering (noise) of the measurement data when sorted according to atom number. The first part of the horizontal axis corresponds to the empty interferometer reference signal. Ideally, this consists of probe light shot noise only. (a) Sorted atom number measurement signal  $\frac{1}{2}\langle a_{k,i} + a_{k,i+1} \rangle_k$ , scaled to the power of the superposition state measurement. (b) Scattering of two point superposition state data  $p_{1,i} - p_{1,i+1}$  corresponding to the rescaled mean atom number signal. (c) Density plot of the superposition state data in (b). Both graphs clearly show an increase in the signal variance with atom number.

to atom number so the horizontal axis represents a non-linear atom number scale. Sorting of the data is only necessary because we actively vary the atom number during the measurement, compare figure 6.8. Subtracting consecutive data points (equation (6.18) and (6.19)) before sorting the data according to atom number assures that the influence of slow drift issues are reduced. A clear increase of the data point scattering can be observed as the atom number increases. This is a first sign of atomic noise contributions to the signal. To confirm that it is quantum noise, a linear scaling of the signal variance with atom number has to be observed.

## 6.2.4 Experimental observation of projection noise

To extract the projection noise contribution to the scattering of the data shown in figure 6.9, we have to identify the linear component of the signal variance as function of atom number, compare section 2.1.1. We combine data corresponding to similar atom numbers and calculate the variance  $\delta^2(p_{1,i})_{i \in \text{bin}}$  inside an atom number bin. The corresponding data is shown in figure 6.10. The total noise observed is clearly dominated by the linear component of a  $f(x) = a + bx + cx^2$  fit. Since the linear part is characteristic for quantum noise, the data confirms the

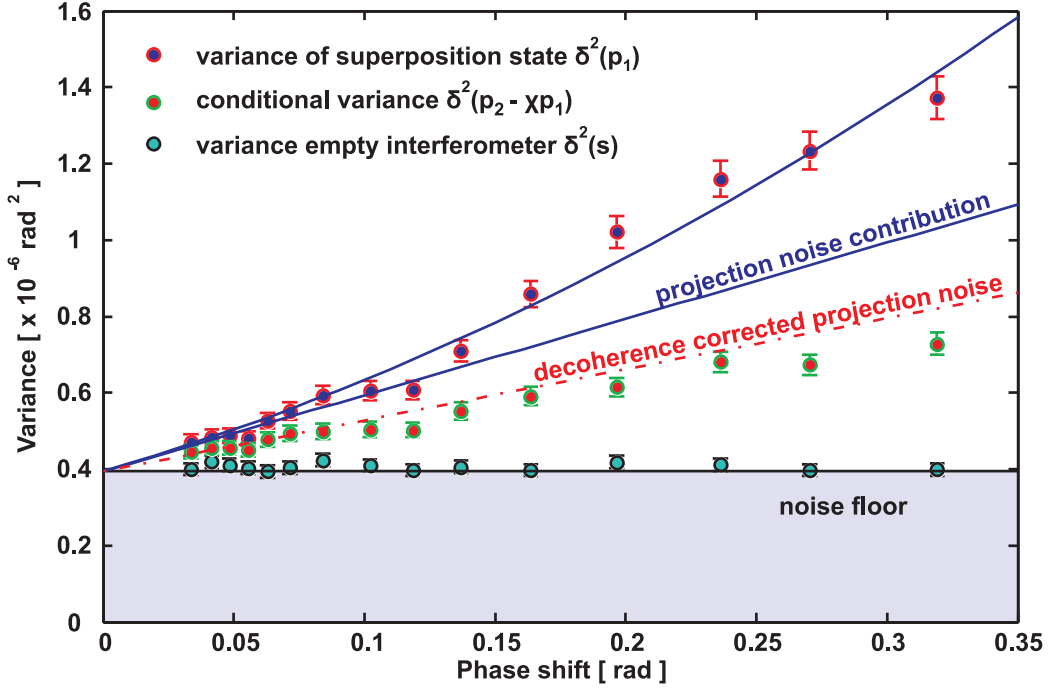


**FIGURE 6.10:** Noise scaling as function of atom number phase shift. The variance of the projection noise measurements  $\delta^2 p_1$  shows a clear quadratic contribution, which is typical for classical noise contributions. Nonetheless, the scaling is dominated by a linear part, which is due to the projection noise. The variance of the conditional variance,  $\delta^2(p_2 - \kappa p_1)$  with optimized  $\kappa$ , however, does not lie convincingly far below the decoherence corrected projection noise level, according to the Wineland squeezing criterion. The noise floor, which includes probe light shot noise, detector electronic noise and classical interferometer noise. The empty interferometer noise data points  $\delta^2 s$  are displayed at the atom number bins where the corresponding atom number runs  $i$  went. Of course, they all correspond to zero atom number. Displaying the shot noise data in this way allows us to observe drifts in the setup over time.

operation of the setup at the standard quantum limit [4]. Ideally, the noise offset  $a$  corresponds only to the light shot noise of the probe pulses.

The observed projection noise slope corresponds well to the theoretical estimate. At the maximum atomic phase shift measured,  $\Delta\phi_{\text{at}} = 0.35$  rad we extract projection noise level of  $\delta^2(\Delta\phi_{\text{at,eff}}) = 0.7 \times 10^{-6} \text{ rad}^2$ . Since the phase shift  $\Delta\phi_{\text{at,eff}} = \gamma N_{\text{at,eff}}$  is proportional to some kind of effective atom number  $N_{\text{at,eff}}$  (consider the discussion in section 3.4.3) and the variance of the phase shift is also proportional to the same atom number  $\delta^2(\Delta\phi_{\text{at,eff}}) = \gamma^2 N_{\text{at,eff}}$ , the effective atom number can be determined to be:

$$N_{\text{at,eff}} = \frac{(\Delta\phi_{\text{at,eff}})^2}{\delta^2(\Delta\phi_{\text{at,eff}})} \quad (6.20)$$

which evaluates to  $N_{\text{at,eff}} = 1.8 \times 10^5$  atoms. This is in good agreement with the value estimated directly from the phase shift  $\Delta\phi_{\text{at}} = 0.35$ , which gives  $N_{\text{at,theo}} = 2.2 \times 10^5$ . The difference can be explained by a geometrical factor which needs to be included due to the spatial inhomogeneity of the sample and the probe.

### Conditional reduction of projection noise

We have discussed the principle of squeezing with QND measurements in section 2.2.3: The first measurement  $p_1$  projects the atomic ensemble state into a subset of eigenstates. The second probe pulse  $p_2$  is used to map out the width of the probability distribution of the reduced subset. Since the initial width of the eigenvalue distribution is given by the projection noise of the atoms, a reduced width of the distribution should manifest itself in correlations between the consecutive measurements to better than the standard quantum limit would allow. The correlation between two pulses are measured with the conditional two point variance  $\delta^2(p_2 - \chi p_1)$ , where  $\chi$  is the measure for the correlation strength. To extract the degree of spin squeezing, i.e., the strength of the correlations, we optimize the conditional two point variance with respect to  $\chi$ .  $\chi$  itself is a function of the atom number (one can show that it corresponds to the ratio between the projection noise and the light shot noise level), so we find an optimal value in each atom number bin using equation (6.8).

The resulting optimized noise data is also shown in figure 6.10. The conditional variance lies considerably below the initial projection noise level. We observe a reduction of  $\frac{\delta^2(p_2 - \chi p_1)}{\delta^2 p_1} = -2.8 \text{ dB}$  with respect to the projection noise level at the highest atom number data point. However, to claim squeezing, the loss of coherence in the sample due to the first measurement  $p_1$  has to be taken into account according to the squeezing criterion in section 2.2.2.

By using the spin echo techniques discussed in section 5.10.2, we can determine the decoherence parameter  $\eta$ . Correcting the projection noise level we obtain the dash-dotted line in figure 6.10. We have applied the Wineland squeezing criterion:  $\xi = \frac{\delta^2(p_2 - \chi p_1)}{\delta^2 p_1 \cdot (1 - \eta)^2}$ . When trusting the highest atom number data point, we observe a noise reduction by 22%, which corresponds to  $\xi = -1 \text{ dB}$  of squeezing. However, especially when taking the overall scattering of the data and the possible errors in the determination of the projection noise level into account, i.e., the uncertainty in the linear component of the fit, squeezing cannot be convincingly claimed. As main issue we identify the decoherence level  $\eta$ . At the time when these measurements were done, the high power microwave amplifier was not yet available, so the decoherence is likely to be limited by the effects of atomic motion, section 5.10.1. We therefore only get an upper bound on the actual atomic state destruction by spontaneous photon scattering. By reducing the additional decoherence effects (differential light shift, trap motion), the level of decoherence would be reduced and squeezing could most likely be claimed.

The correlations between the two consecutive QND measurements  $p_1, p_2$  are shown in figure 6.11. A clear correlation between the measurement outcomes can be observed when atoms are present in the interferometer 6.11(a), while no correlations are observed in the empty interferometer case 6.11(b). This confirms that the two measurement results on the same atomic ensemble are in fact correlated. The correlations are not strong enough to overcome the decoherence caused by the first pulse.

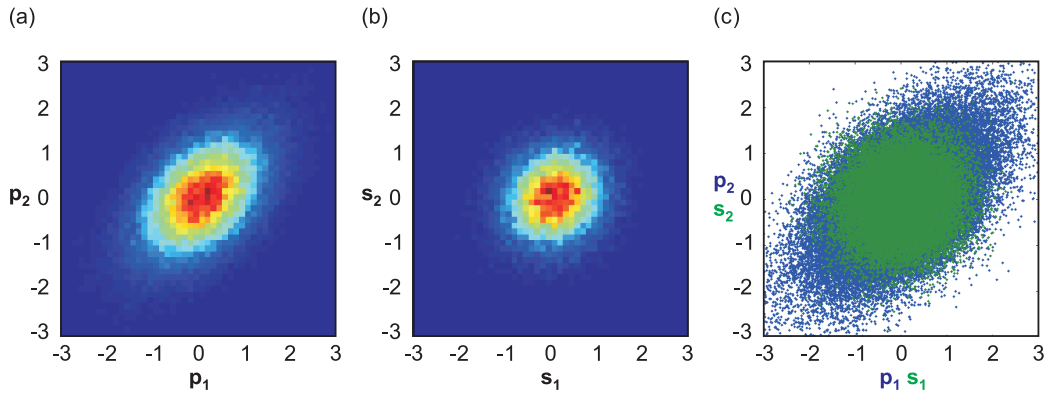


**FIGURE 6.11:** Correlation plots. (a) The two measurement results  $p_1$  and  $p_2$  are clearly correlated when atoms are present in the interferometer. (b) Removing the atoms from the interaction region reveals the empty interferometer noise. Since in the ideal case, this consists only of light shot noise, no correlations are expected. (c) The scattering of the empty interferometer measurements is clearly much smaller than with atoms present. The variance along the short axis of the correlation ellipse corresponds to the maximum achievable noise reduction. Finding the optimal correlation parameter  $\kappa$  for a certain atom number corresponds to finding the orientation of the ellipse. For perfect correlation  $\kappa \rightarrow 1$  the axis of the ellipse are oriented along the diagonals of the coordinate system.

## Discussion

In the preceding section we have demonstrated that our measurement setup is capable of resolving atomic projection noise. The noise data is undoubtedly dominated by quantum mechanical noise. Comparing the observed noise floor  $\delta^2s$  in figure 6.10 with the light shot noise level, we can also claim that the measurement is light shot noise limited. This is a very important and encouraging result.

We believe that the main reason for not being able to claim projection noise squeezing in the data presented above, is that the level of decoherence we measure with the spin echo sequence, section 5.10.2, is only an upper bound to the actual state destruction. When the data was taken, only the low power microwave amplifier was available. With about one Watt of microwave power, the Rabi frequency for microwave driving of the clock transition was limited to about 10 kHz. We therefore have to separate the light probe pulses in the spin echo sequence to determine the decoherence by at least the  $\pi$ -pulse duration of  $\tau = 50 \mu\text{s}$ . As discussed in section 5.10.1, the trap motion starts to play a crucial role on this timescale. On the timescale we look for squeezing, the separation between the two QND measurements  $\tau = 16 \mu\text{s}$ , a lower level of decoherence can be assumed. By the time the higher power amplifier had arrived, strong non-democratic forces had decided to change the interferometer to the two input port configuration. Although the advantages of the new configurations are apparent, a direct comparison between the achievable levels of squeezing in both setups under very similar experimental conditions would have been extremely helpful.

## 6.3 Noise measurements with two color – two port interferometer setup

In the previous section we have demonstrated that our experimental setup is, indeed, capable of resolving atomic projection noise. The next major goal, the quantum noise reduction below the standard quantum limit by conditioning the outcome of a second measurement on the first, however, remained elusive. For various reasons, the interferometer setup used in the previous section has been rearranged to the two input port setup, compare section 3.2.3. In the present section we will discuss the noise properties of this interferometer version. Since only the readout principle of the atomic population is slightly altered, it is clear that all the microwave spectroscopy tools demonstrated in chapter 5 can be applied. The main issue which needs to be demonstrated for the new interferometer setup is its light shot noise limited performance. We will therefore start out by discussing the corresponding procedures and then move directly to the atomic noise and squeezing measurements.

### 6.3.1 Remarks on the technical realization

The interferometer setup itself has been discussed in section 3.2.3 and it is schematically depicted in figure 6.12. The main technical difficulty when adding a beam on the second input port of the beam splitter is the spacial mode matching of the two colors in free space. In the single port scheme, this mode matching is straightforwardly obtained by coupling the two colors into one single mode fiber. The mode matching of the two colors is important for two reasons: First, both probe colors are supposed to read out the population of the same atoms with the same coupling strength. Second, perfect light shift cancelation can only be assured when the mode profiles overlap (see section 5.11). We generally achieve an interference fringe visibility between the two ports of  $> 97\%$ .

The Mach Zehnder interferometer is a differential light phase measuring device between the probe and the reference beam. At the shot noise limit, the measurement precision is limited by the light shot noise of the probe and the reference arm. By increasing the photon number in the reference arm relative to the probe arm, the influence of the reference arm light shot noise can be reduced and in the limit of  $\bar{n}_{\text{photons,reference}} \rightarrow \infty$  we obtain a perfect phase measurement for the probe beam where the uncertainty is only limited by the photon number interacting with the atoms in the probe arm. The setup then resembles a homodyning setup for one quadrature of the probe light. To get closer to this ideal situation, we use polarization optics to introduce controlled losses in the probe arm; the power split off at the polarizing beam splitter PBS1 is used for monitoring the light pulses.

### Probe laser frequency stability

In section 6.2.2 we have discussed the stability requirements for the probe lasers. *In principle*, these requirements are not altered when changing to the two port interferometer configuration. However, there are some technical advantages to the

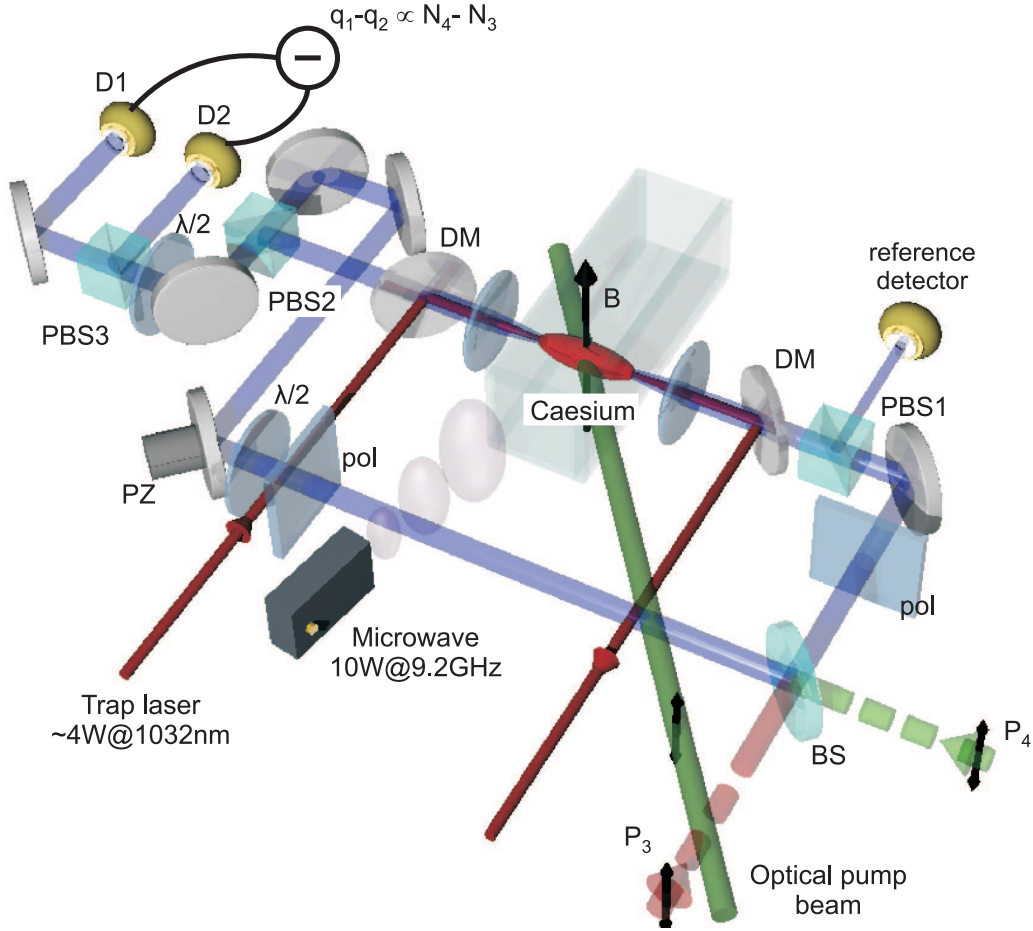


**FIGURE 6.12:** Drawing of the experimental setup in the two color – two port configuration. The arrangement has been discussed in detail in section 3.2.3. The polarization control elements inside the interferometer are used to adjust the relative power between the probe and the reference arm. The auxiliary detector in the beam split-off on PBS1 in the probe arm is used to monitor the powers.

new configuration: As discussed in section 3.2.3 and illustrated in figure 3.8, the two probe colors need to gain a phase shift with the same sign when interacting with the atoms to assure that the output signal is proportional to the population number difference. The detuning of the two lasers from the relevant transitions therefore has to have the same sign (we chose both negative  $\Delta_{4,5} = -100 \text{ MHz} < 0, \Delta_{3,2} \approx -80 \text{ MHz} < 0$ )<sup>6</sup>. In this configuration, common mode fluctuations, i.e., changes of the detuning of both lasers by the same amount and in the same direction, do not change the balancing of the output signal and are therefore of minor consideration. These fluctuations boil down to the same effect as a reduction of the effective atom number, so they enter linearly in the variance while other noise sources enter quadratically (compare equation (6.12)). By phase locking the two lasers with a beat note lock (compare section 3.2.1), anti correlated phase noise can be suppressed to few kilohertz which assures that the frequency stability

<sup>6</sup>As discussed in section 5.11 this is also the feature which makes light shift cancellation in this setup possible.

requirement is met.

### Active power stabilization

To obtain a zero mean interferometer signal for an equal atomic superposition state, both the frequencies and the powers of the two probe colors have to be matched. We decide to fix the ratio of the probe powers and find the corresponding detuning ratio by optimizing the light shift cancelation (section 5.11). The power of one of the probe lasers is actively stabilized to the other laser to maintain the fixed ratio. The error signal for the stabilization is obtained in the following way: During a stage where no atoms are present in the interferometer, we modulate the interferometer path length difference by applying short disturbing electric pulses to the piezo electric transducer which is otherwise used for the interferometer stabilization. For ideally balanced probe colors, i.e., for equal interferometer fringe amplitudes of both colors (compare figure 3.10), the output signal of the empty interferometer is independent of the path length difference. When the two probe powers are not exactly equal, the output signal of the interferometer is (in the linear part of the interference fringe) proportional to the power difference and can therefore be used to correct the power ratio. A microprocessor reads the interferometer signal during this “wiggling” process and generates an error signal for the power adjustment. The power is adjusted by turning the position of motorized waveplates which are placed in front of polarization cleaning optics at the input of the fiber which transports the beams to the interferometer table. Applying feedback to the rf power of the pulsing AOM to change the probe power instead has proven not to be a particularly good idea. High power stability of the pulsed output beam can only be assumed when the AOM is driven with optimally adjusted rf power level. This is, however, not possible if some margin for regulation is to be left open.

### Active lock point adjustment

As one of the major stability issues we have identified the power stability of the probe beams. In section 3.2.3 we have discussed the advantages of performing a balanced measurement of the interferometer output signal. Subtracting the signal from the two interferometer output ports suppresses classical amplitude fluctuations. This makes the observation of quantum effects, i.e., the observation of light shot noise in the empty interferometer case, possible in the first place. From a very basic point of view, the effective subtraction of two large and classical signals at the detector is again a two point measurement in the sense indicated in connection with the two sample variance, section 6.2.1. As discussed in section 3.2.3, the two port interferometer allows us to make use of the advantages of a balanced differential measurement also during the atomic population measurement, compare figure 3.8, page 42. The arrangement of the phase shifts allows us to shift the lock point in the presence of atoms atoms to a position where both colors are individually balanced. In this setting, the classical amplitude fluctuations of each probe laser are suppressed.

To find the optimal lock point for different atom numbers, we apply single color probe pulses to the ensemble after the superposition state measurement, see figure

6.15. When the lock point is not optimal, we observe a signal offset. The pulse amplitudes of these single color measurements are used as feedback signal to the interferometer locking circuit. We adaptively change the interferometer offset with the atom number and thereby keep the interferometer in a balanced position all the time.

### 6.3.2 Shot noise limited performance

With all the experience we have gained on performing noise measurements and demonstrating light shot noise limited performance on interferometers in chapter 4 and in section 6.2.1, not too many words need to be said on the procedures any more. Since the baseline reference pulses necessary to assure shot noise limited performance in the single port setup have become oblivious, all that needs to be done is sending trains of bi-chromatic light pulses through the setup and analyzing the signal two point variance  $\delta^2 p(\tau)$  as function of light power and pulse separation  $\tau$ . We need to achieve shot noise limited performance on a few seconds timescale such that we can apply the consecutive measurement subtraction technique (equation (6.18)) again. Longer term stability is desirable but not a requirement. Typical raw data and the confirmation of shot noise limited performance is displayed in figure 6.13. To obtain the data we send 3000 blocks of three pulses as shown in figure 6.13(a). The duration of the pulses is  $4\ \mu\text{s}$  and the repetition rate inside the block is  $16\ \mu\text{s}$ ; the blocks are separated by 2 ms in time. We can therefore compare the performance of the interferometer on a  $16\ \mu\text{s}$  timescale with the performance up to few seconds. Figure 6.13(b) shows the obtained noise levels as function of pulse separation. The almost perfect linear scaling for the three pulse separations shown confirms the shot noise limited performance of the interferometer. Hardly any additional quadratic noise contribution can be seen for pulse separations of  $\tau = 1\ \text{s}$  for mean photon numbers of  $n = 2 \times 10^8$  per bi-chromatic probe pulse. In addition, the single point variance  $\delta^2 p_1 = \langle p_{k=1,i}^2 \rangle_i - \langle p_{k=1,i} \rangle_i^2$ , where  $k = 1$  refers to the pulse number in one block and  $i$  to the number of the block, shows the same scaling and noise level as the two point variance  $\frac{1}{2}\delta^2 p(1\ \text{sec})$ .

### 6.3.3 Projection noise and squeezing measurements

Having established the shot noise limited performance of the empty two input port interferometer, we turn to the atomic projection noise measurements. The measurement sequence is illustrated in figure 6.14. In addition to the general procedure discussed in section 6.2.3 the interferometer lock point switching and necessary offset determination as discussed in section 6.3.1 is implemented as well. We initialize the ensemble in a coherent superposition state and apply the probe pulses. In contrast to the former measurements, we now use  $10\ \mu\text{s}$  long probe pulses with  $20\ \mu\text{s}$  repetition period. For reasons which will become clear later we actually apply 20 probe pulses. After the bi-chromatic probing of the ensemble we apply the two probe colors individually to determine the phase offset of the interferometer due to the atoms. This signal is used as error signal for the switching of the lock offset. We then “jump” the lock offset to the empty interferometer value and determine the atom number equivalent phase shift. After repeating this cycle

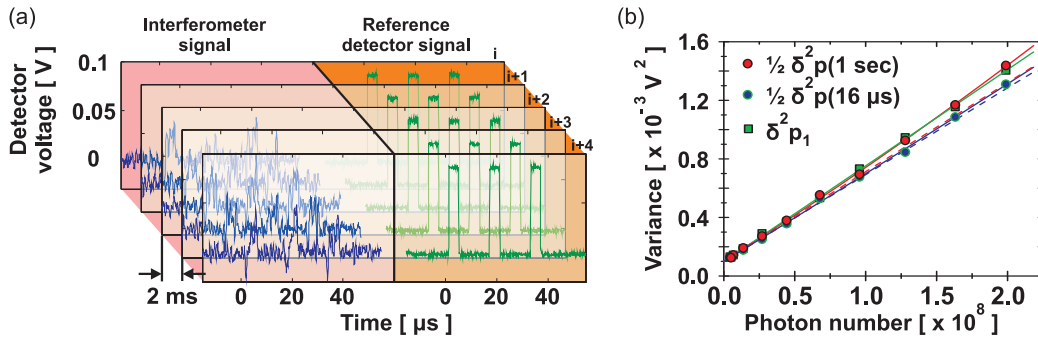


**FIGURE 6.13:** (a) Pulse sequence to determine the long term shot noise performance of the two color – two port interferometer setup. The left part of the graph shows the interferometer signal while the right data shows the corresponding reference detector signal. We send 3000 blocks  $i$  with 2 ms time spacing with 3 pulses in each block. The duration of the pulses is  $4 \mu\text{s}$  and the repetition period inside the block is  $16 \mu\text{s}$ . We label the pulses with  $p_{k,i}$  where  $k$  in addition represents the number of the pulse in the block. (b) To analyze the noise data as function of (bi-chromatic) probe pulse photon number, we calculate the two point variance  $\delta^2 p(\tau)$  on different time scales. The shortest period available is  $\tau = 16 \mu\text{s}$  and the longest one (when we assume that 6 pulses are enough to get a meaningful variance) is  $\tau = 1 \text{ s}$ . In the plot we compare these two variances with the single first pulse variance  $\delta^2 p_1$ . The two point variance contains two pulses, so it shows twice the noise level of the single pulse. We therefore chose to plot  $\frac{1}{2} \delta^2 p(\tau)$ . The two long term variances  $\delta^2 p_1$  and  $\frac{1}{2} \delta^2 p(1 \text{ s})$  deviate only marginally from  $\frac{1}{2} \delta^2 p(16 \mu\text{s})$  in the explored photon number range up to  $n = 2 \times 10^8$  photons. The linear parts of the second order fits to the three data sets coincide within the resolution of the plot.

four times we measure the empty interferometer to determine the light shot noise level and extract the ideal empty interferometer locking point. The measurement pulse sequence is further illustrated in figure 6.15. Although the figure is pretty crowded one can clearly see the 20 measurement pulses in the different measurement segments. From the trace of the reference detector the power ratio of the two probe colors and the ratio of projection noise measurement power to the level used for the atom number determination can be extracted as well. At the end of measurement segment 1 and 10 one can also see the signals caused by the individual probe colors. Their deviation from the zero level is used as feedback signal for the lock position adjustment. The fact that offsets are barely visible confirms that the lock point switching works as claimed.

### Analysis of the noise data

The analysis of the noise data acquired with the sequence shown in figures 6.14 and 6.15 follows the same steps as discussed in section 6.2.3: We apply filters to the raw data, discriminating measurement runs whose system parameters deviate considerably from the average of the neighboring values. Figure 6.16 shows the evolution of the atom number and the probe laser powers over a typical data set, in this particular case consisting of about 6900 individual runs. Areas where data has been removed manually, in the particular case due to problems with the MOT laser frequency stabilization, are indicated. The correlations in the powers of the

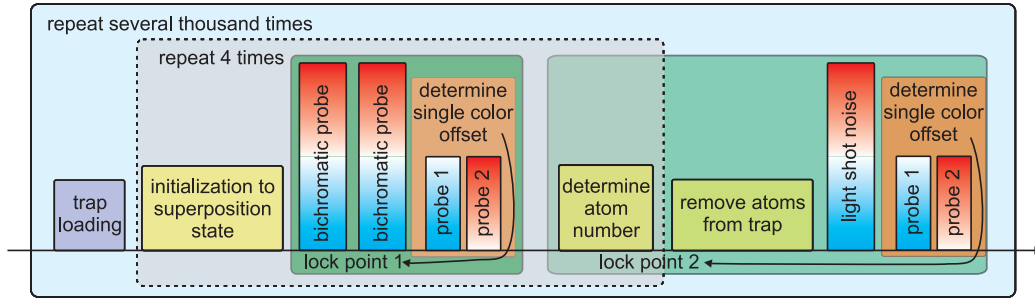


**FIGURE 6.14:** Pulse sequence for noise measurements with two color – two port interferometer setup. The main difference with respect to the sequence shown in figure 6.5 is the determination and switching of the interferometer lock points. After the projection noise measurement and when the atom have been removed from the trap, the probe lasers are applied individually. The measured phase shifts give information on the balancing of the individual colors (compare figure 3.8) and by adjusting the offset of the interferometer lock position, the imbalance can be compensated. Once the correct offset values are determined, the feedback circuit only has to follow slow drifts in the atom number. The pulse integrals are determined from the same oscilloscope signals which we use for the noise analysis.

two probe lasers shown in graph 6.16(b) confirm that the active power stabilization discussed in section 6.3.1 keeps the power ratio constant.

After the measurement pulses have been integrated with appropriate integration windows (see section 4.3.2 for details), the actual analysis is slightly simpler than in the case of the single port interferometer setup. Since we do not need auxiliary reference pulses any more<sup>7</sup>, we use the pulses directly. Again, we label the pulses according to their position  $k \in [1 \dots 20]$  in the measurement block and according to the measurement run  $i$ . The pulses  $p_{k,i,b}$  relate to the superposition state measurements,  $a_{k,i,b}$  to the corresponding atom number measurement.  $b \in [1 \dots 4]$  is the block number.  $s_{k,i}$  represent the empty interferometer shot noise measurement in block 9 and  $r_{k,i}$  corresponds to the interferometer baseline measurement in block 10. By stacking the data  $p_{k,i,b} \mapsto p_{k,i+(b-1) \cdot i_{\max}}$ ,  $a_{k,i,b} \mapsto a_{k,i+(b-1) \cdot i_{\max}}$  we can omit the number of the block  $b$ . The same interferometer baseline  $r_{k,i}$  is used for the four atom number measurements in one run:  $r_{k,i} \mapsto r_{k,i+(b-1) \cdot i_{\max}}$ . Again, we treat the empty interferometer measurements  $s_{k,i}$  in the same way as the superposition state probe pulses, assuming zero atom number.

The phase shift corresponding to the atom number of the *new* run number  $i$  is calculated according to:

$$\Delta\phi_i = (\langle a_{k,i} \rangle_k - \langle r_{k,i} \rangle_k) \cdot (\text{fringe calibration factor}) \cdot (\text{trap decay calibration factor}) \quad (6.21)$$

Both calibration factors are determined prior to and independent of the noise measurements.

<sup>7</sup>In fact, correlation measurements have shown that auxiliary reference pulses do not contain any additional information, so optimizing  $\delta^2(p - \lambda b)$  returns  $\lambda = 0$ .

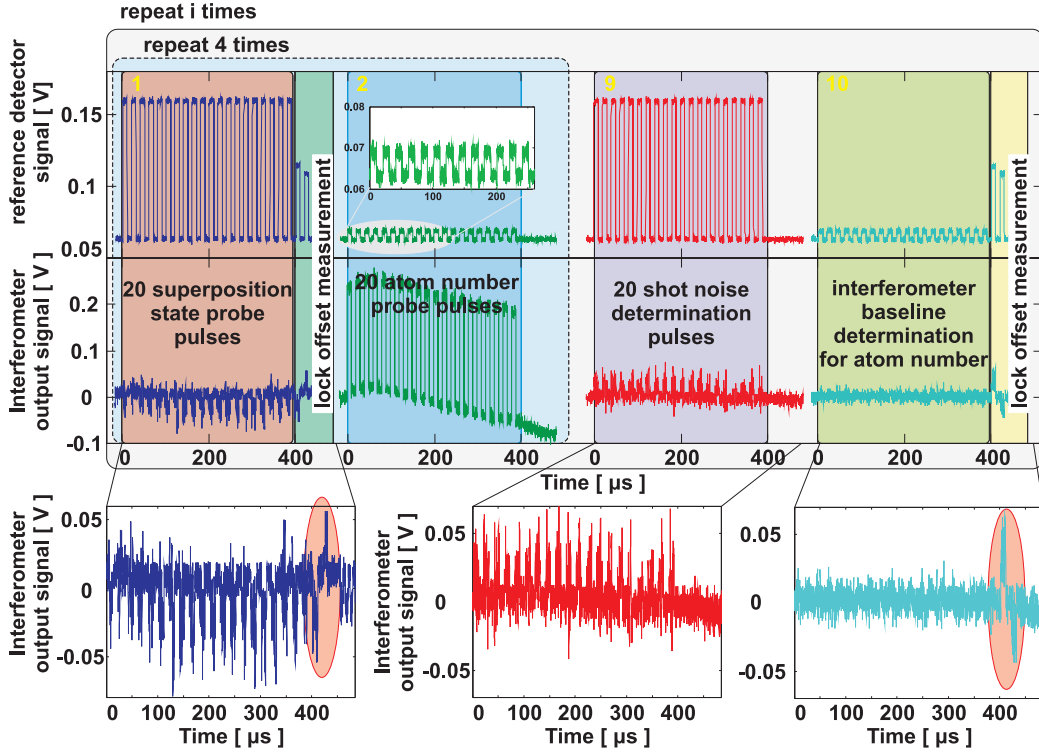


**FIGURE 6.15:** Raw data of projection noise and squeezing measurement pulse sequence. The reference detector trace illustrates the timing of the pulse sequence and the power levels involved. Measurement segment 1 corresponds to the projection noise measurement, in segment 2 we determine the corresponding atom number. Here we only use the  $F = 4 \rightarrow F' = 5$  probe laser. These two segments, building a block  $b$  are repeated four times. Segment 9 establishes the empty interferometer noise level and segment 10 measures the baseline of the empty interferometer which is used as zero level for the atom number measurement. At the end of segment 1 and 10 the two probe colors are applied individually. These pulses give information in the lock offset from balanced position and their values are used as feedback signals for the lock point “jumping” circuit. The fact that the respective interferometer signals are very well balanced confirms that the lock point switching procedure works well. The “bending” of the signal offset in segment 2 of the interferometer signal is due to detector base line pulling caused by the strong imbalance of the signal.

To evaluate the projection noise we first construct “two point pulses”:

$$p_{k,i} - p_{k,i+1} \rightsquigarrow p_{k,i} \quad (6.22)$$

$$s_{k,i} - s_{k,i+1} \rightsquigarrow s_{k,i} \quad (6.23)$$

$$\frac{1}{2} (\Delta\phi_i + \Delta\phi_{i+1}) \rightsquigarrow \Delta\phi_i \quad (6.24)$$

This subtraction of consecutive atomic projection measurements is necessary to eliminate the probe power drifts on long time scales which we observe in figure 6.16(b). Furthermore, since we have several probe pulses  $k$  available, we define

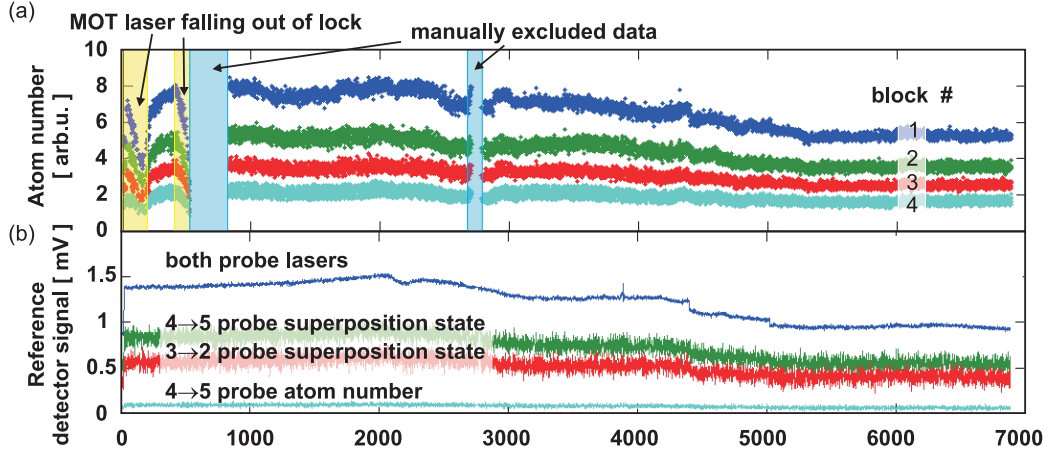


**FIGURE 6.16:** Atom number and probe laser powers of a data set consisting of  $\sim 6900$  runs of the experimental cycle. (a) The performance of the MOT lasers (and the dipole trap laser...) can be inferred from the atom number stability. Areas where the lasers perform suboptimally are either manually removed or filtered out by discriminating single runs whose atom number deviates significantly from the average of surrounding runs. (b) We observe long term drifts of the probe powers. The power drifts of the two probe colors are, however, correlated due to the active power stabilization.

“meta” pulses  $P_{1,i}^r, P_{2,i}^r$ :

$$\begin{aligned}
 P_{1,i}^r &= \sum_{k=1}^r p_{k,i}, & P_{2,i}^r &= \sum_{k=r+1}^{2r} p_{k,i} \\
 S_{1,i}^r &= \sum_{k=1}^r s_{k,i}, & S_{2,i}^r &= \sum_{k=r+1}^{2r} s_{k,i}
 \end{aligned} \tag{6.25}$$

As we have discussed in section 6.1 the degree of squeezing to expect, depends on the decoherence  $\eta$  induced by the first pulse – the squeezing pulse. The decoherence induced by single probe pulses can be extracted from spin echo measurements as shown in section 5.10.2. The  $\eta$  estimation discussed in that section actually corresponded to the probe powers and the interferometer setup and parameters used in this section. It is obvious that by combining different numbers of single probe pulses to a meta pulse, we can vary the amount of decoherence induced by the “first” measurement pulse and therefore study the effect of different coupling strengths on the observed noise reduction.

### 6.3.4 Experimental observation of projection noise

To extract the noise level for different atom numbers, we group measurements  $P_{1,i}^4$  with similar atom number together and calculate the variance of the signal  $\frac{1}{2} \left( \delta^2 P_{1,i}^4 \right)_{i \in \text{bin}}$  inside the bin.

Figure 6.17 shows the scaling of the variance of the atomic superposition state measurement  $\frac{1}{2} \delta^2 P_1^4$  with atom number. The number of atoms has been inferred from the phase shift  $\langle \Delta \phi_i \rangle_{i \in \text{bin}}$ . The scaling of the variance with atom number is clearly

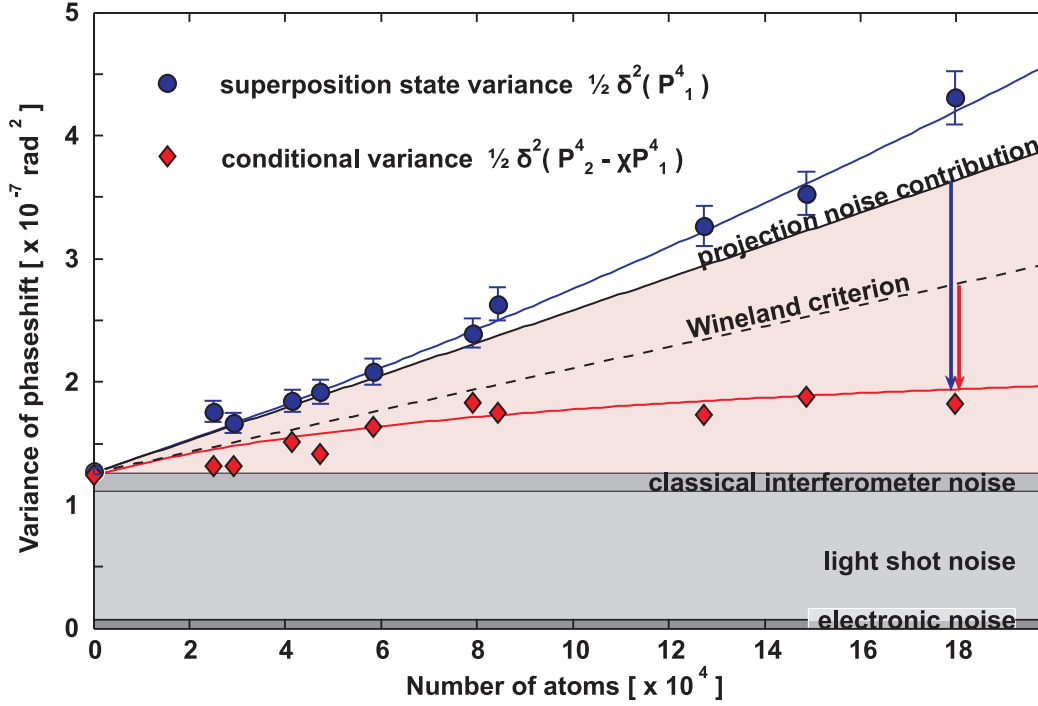


**FIGURE 6.17:** Projection noise and pseudo spin squeezing results. The scaling of the superposition state variance  $\delta^2 P_1^4$  is clearly dominated by a linear component which can only be ascribed to atomic projection noise. The optimized conditional variance  $\frac{1}{2}\delta^2(P_2^4 - \chi P_1^4)$  lies considerably below the projection noise level for all atom numbers and below the decoherence corrected projection noise level  $\delta^2 P_1^4 \cdot (1-\eta)^2$ . At the highest atom number data point, we extract a relative noise level of  $\frac{\delta^2(P_2^4 - \chi P_1^4)}{\delta^2 P_1^4} = -5.4$  dB and a spectroscopically relevant squeezing level of  $\xi = \frac{\delta^2(P_2^4 - \chi P_1^4)}{\delta^2 P_1^4 \cdot (1-\eta)^2} = -3.5$  dB. The empty interferometer noise floor has been divided into electronic noise, light shot noise and classical interferometer noise by analyzing the correlations in the pulses  $s_i$ .

dominated by a linear component, which is the signature of quantum projection noise. We can therefore also for the two port interferometer setup confidently claim projection noise limited performance.

The noise floor  $\frac{1}{2}\delta^2(S_1^4)$  on which the data rests has been analyzed and its contributions have been extracted. The analysis confirms that the projection noise measurement is also light shot noise limited. Together, the data clearly demonstrates the atomic projection noise and light shot noise limited performance of the measurement setup, i.e., the best possible measurement with the given number of photons and atoms. With respect to the data obtained in the single input port interferometer setup, figure 6.10, the quadratic noise contribution is slightly reduced. In figure 6.18 we compare the atomic noise scaling for three different data sets obtained with the two port interferometer to the data obtained for the single port setup. The projection noise slopes of the three data sets obtained in the two port interferometer agree exceptionally well with each other. Within the statistical uncertainty of the data the three slopes are basically indistinguishable. Remarkably enough, also the extracted projection noise slope of the data taken with the single port interferometer agrees well with the newer data. This adds confidence in the

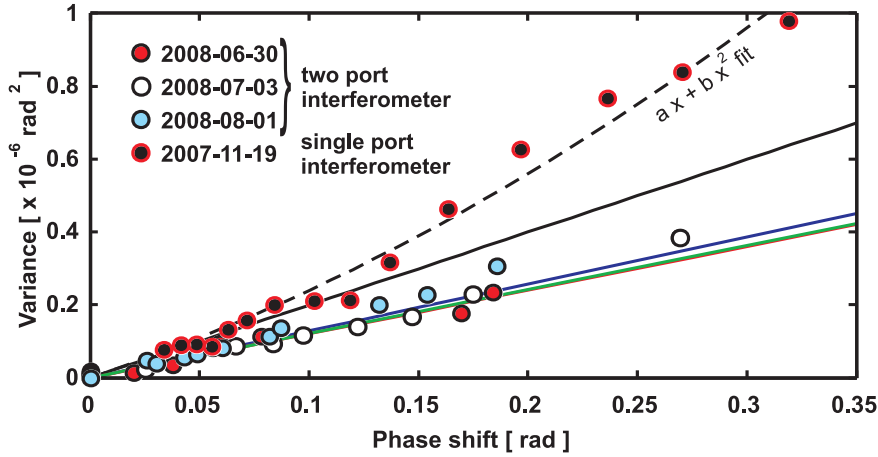


**FIGURE 6.18:** Comparison of different, independent experimental data sets. The three sets from mid 2008 were taken with the two port interferometer discussed in this section. The data and the extracted projection noise slopes (solid lines, colors association should be obvious) of the three state sets agree exceptionally well with each other. The data from 2007, which was obtained with the single input port setup discussed in section 6.2.3, fits remarkably well into the picture. For this data, both the fit  $f(x) = ax + bx^2$  is given and the linear component  $ax$  corresponding to the projection noise.

validity of our approaches and analysis procedures and backs up the claim that the single port interferometer setup is capable of projection noise limited performance and therefore of demonstrating projection noise squeezing.

### 6.3.5 Quantum noise squeezing

As for the single port interferometer setup, we evaluate the degree of conditional projection noise reduction by calculating the conditional variance of the meta pulses  $\delta^2(P_2^r - \chi P_1^r)$  with  $\chi = \frac{\text{cov}(P_1^r, P_2^r)}{\delta^2 P_1^r}$ . For  $r = 4$  the result is included in figure 6.17. As indicated in the figure, we achieve a noise reduction of 72% with respect to the initial projection noise level at the highest atom number data point. In the squeezing language it is common to express the remaining noise level in decibel, i.e., we achieve projection noise squeezing to  $\frac{\delta^2(P_2^4 - \chi P_1^4)}{\delta^2 P_1^4} = -5.4$  dB.

To evaluate the degree of spectroscopically relevant squeezing, we have to correct the observed projection noise with the decoherence induced by the squeezing pulse  $P_1^r$ . We determine the decoherence parameter  $\eta$  by using the methods discussed in section 5.10.2. From figure 5.31 we extract a decoherence parameter  $\eta_2 = 11 \pm 2\%$  for the two applied bi-chromatic probe pulses of  $10 \mu\text{s}$  duration at  $\Delta_{45} = -100$  MHz and  $\Delta_{32} = -79.19$  MHz from the  $F = 4 \rightarrow F' = 5$  and  $F = 3 \rightarrow F' = 2$  transitions, respectively. The two probe pulses contain together  $n = 7.1 \times 10^6$  photons. Since we are in the low excitation regime, the decoherence for different numbers  $r$  of combined probe pulses can be calculated:  $\eta_r = 1 - (\sqrt{1 - \eta_2})^r$ . Comparing the reduced noise level with the decoherence corrected projection noise level, we obtain a value of  $\xi = \frac{\delta^2(P_2^4 - \chi P_1^4)}{\delta^2 P_1^4 \cdot (1 - \eta)^2} = -3.5$  dB of spectroscopically relevant

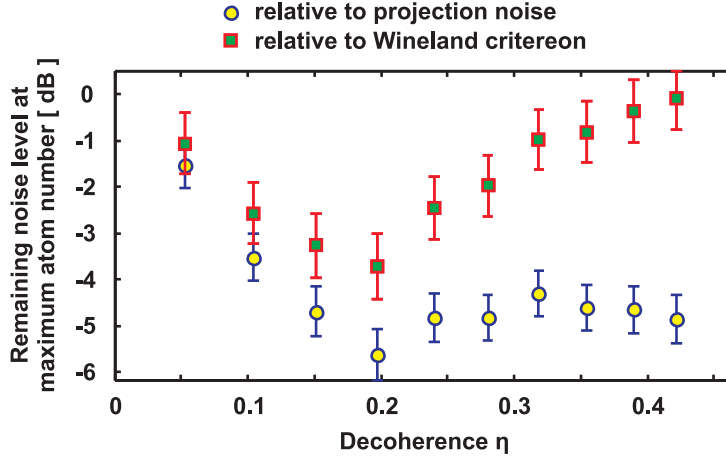


**FIGURE 6.19:** Conditional variance value at highest experimentally achieved atom number, normalized to initial projection noise level and normalized to the decoherence corrected projection noise level as function of the decoherence induced by the first probe pulse  $P_1^r$ . While the noise reduction levels off with high coupling to the atoms, the squeezing exhibits a strong optimum at  $\eta_4 \approx 0.2$  corresponding to a combination of four single probe pulses.

squeezing for the highest atom number point.

At this point the large number of probe pulses in one measurement block (compare figure 6.15) comes in handy. By combining up to  $r = 10$  probe pulses to the meta pulse  $P_i^r$  we can extract the level of projection noise reduction and degree of squeezing for different levels of probe induced decoherence. Figure 6.19 shows the projection noise reduction and the level of squeezing for the highest atom number data point in figure 6.17 as function of the decoherence  $\eta$ . The observed behavior corresponds well to the theoretically expected one. For the reduced noise level relative to the projection noise level we expect a scaling  $\frac{\delta^2 \hat{j}_z^{\text{out}}}{\delta^2 \hat{j}_z^{\text{in}}} = \frac{1}{1+\alpha_0 \eta}$ . While the noise reduction drops with the inverse of the decoherence parameter, the degree of squeezing  $\xi = \frac{1}{(1+\alpha_0 \eta)(1-\eta)^2}$  assumes an optimum where the information gain and the inflicted damage are ideally balanced. With small coupling to the ensemble (low decoherence) we get little information on the atomic state with the first probe pulse  $P_1^r$  and have only very limited abilities to predict  $P_2^r$ . For high coupling we get full information on the state, but also project the single atoms into their energy eigenstates which reduces the coherence remaining after the interaction. Experimentally, the optimal value is reached for  $\eta_4 \approx 0.2$ . Using the achieved squeezing level of  $\xi = -3.5$  dB, we calculate an effective optical depth of  $\alpha_0 = 11.8$ . For the maximum interferometer phase shift obtained in this measurement,  $\Delta\phi_{\text{at}} = 0.2$ , we obtain an optical depth of  $\alpha_0 \approx 13$  which corresponds well to the one obtained from the level of squeezing. For the observed optical depth, in return, we expect the optimal decoherence parameter  $\eta_{\text{opt}} = 0.27$  which again corresponds acceptably well to the experimentally observed value, especially when taking the simplicity of the theory into account. A more thorough analysis of the peculiarities of the two color – two port probing scheme, also taking the fact into account that inelastic Raman scattering events add noise to the final state, has been performed by a theoretically inclined subpart of the work group and can be found in [72]. It is likely that further discussions on that matter will be included in [3]. Two of the

key ingredients are:

- The detunings of the two probe colors are arranged such that they address to lowest order only cycling transitions. Cross pumping of atoms, i.e., exciting an atom off-resonantly to the  $F' = 3$  state with the  $F = 4 \rightarrow F' = 5$  probe laser and subsequent decay to a  $F = 3$  state or exciting an atom to the  $F' = 4$  state with the  $F = 3 \rightarrow F' = 2$  probe pulses and a decay into a  $f = 4$  level, is strongly suppressed by the selection rules and the far detuning. These pumping events would otherwise add noise to the output state and degrade the level of squeezing.
- The two color probing scheme does not distinguish (up to a small difference in the coupling strength) between atoms in  $m_F = 0$  and  $m_F = \pm 1$ . Raman scattering events, which remove atoms from the two-level system do therefore not add additional noise.

## Conclusion

The experiments presented in the preceding sections demonstrate the atomic projection and probe light shot noise limited population readout of an atomic ensemble. Since a measurement at the standard quantum limit gives the highest possible measurement precision for uncorrelated atoms in the ensemble and classical light states, the measurement apparatus performs optimally. This is an important step towards the applicability of our methods in state of the art atomic clocks. Together with the non-destructive nature of the interaction, our measurement can be used to increase the measurement cycle rate for example in optical clocks. This should yield a significant improvement of the signal-to-noise ratio compared to the traditional fluorescence-based destructive probing since more statistics can be collected in a given time. We have demonstrated that the standard quantum limit has been achieved in both setups, the single port and the two port interferometer configuration.

Exploiting the quantum non-demolition character of our measurement technique allows us to look for non-classical correlations between consecutive non-destructive measurements on the same ensemble. We have observed and studied these correlations and demonstrated that they obey the Wineland squeezing criterion. The observed reduction of the quantum mechanical measurement uncertainty corresponds to a population uncertainty squeezing of  $\xi = -3.5$  dB. This in return demonstrates the generation of an entangled state of few hundred thousand atoms in our sample. Although we have not been able to demonstrate squeezing in a single input port interferometer configuration, the comparison between the projection noise measurements in the two settings suggests that the single input port configuration should not perform significantly worse than the other. However, one has to admit that the advantages of the two port setup in terms of stability and light shift cancelation outbalance the additional technical complications.

At the very same time when these results became available, the group of Vladan Vuletic has made similar observations with a complementary method [13]. Other

groups have reported the observation of backaction noise [74] and smaller amounts of squeezing [75] in other atomic systems. With these observations a long standing milestone in quantum noise limited measurements has finally been achieved.

---

# Conclusion and Outlook

## 7.1 Where do we stand?

In the preceding chapters we have illustrated a good number of experimental achievements. We use the measurement of the dispersive phase shift imprinted on probe light when it interacts with an atomic ensemble to extract the population number difference of a two level quantum system. As quantum system we use the two magnetic field insensitive magnetic hyperfine substates of caesium  $6S_{1/2}(F = 3, m_F = 0)$  and  $6S_{1/2}(F = 4, m_F = 0)$ , the so-called clock states. The atomic ensemble is cooled in a magneto optical trap and further confined in an optical dipole trap. The dispersive probe light phase shift is determined with a Mach Zehnder interferometer.

In the off-resonant limit, the light-atom interaction has quantum non-demolition character. Spontaneous photon scattering events can be suppressed to a level where they do no longer dominate the atomic state evolution. In the low excitation regime, we have demonstrated that the coherent evolution of the clock state population when the ensemble is subjected to an external microwave driving field, can be followed in real time. While the results on non-destructive state readout obtained in a complimentary setup in the group of Poul Jessen [68] had been clearly dominated by the effect of probe induced decoherence, we can confidently claim that we can reduce this effect to a limit where it becomes negligible. Continuing along these lines, we have studied the effect of probe induced decoherence and realized that the most prominent effect is actually the dephasing caused by an inhomogeneous, differential light shift distribution across the atomic ensemble. We have developed a set of tools to study the effect thoroughly and a comparison of the observations with theoretical models confirms the validity of our interpretations. The obtained understanding of the dispersive light-atom interface in the particular setting of our experiment has been vital for the progress of the experiment. Together with the understanding of the decoherence effects induced by the atomic motion we have been able to establish a firm upper bound for the probe light induced spontaneous photon scattering, which is the main parameter determining the degree of observable quantum noise squeezing for a given sample density.

In a second step, we have taken the non-destructive measurement scheme to its quantum mechanical limits. We have demonstrated atomic quantum projection noise and probe light shot noise limited population readout. Projection noise limited performance has been observed in both interferometer setups discussed – two color measurement schemes where the two colors either enter through the same or through different input ports of the interferometer. Since the standard quantum limit defines the best achievable measurement precision for uncorrelated atomic and light states, the measurement setup performs optimally in that sense. While a convincing observation of projection noise squeezing could only be observed in the two port setup, we are convinced that *in principle* also the technically less demanding single port setup should be capable of demonstrating squeezing. However, the feature of inhomogeneous differential probe light shift cancelation in the two port setup is a major step forward towards the application of our techniques to a “real” atomic clock. The clock community has picked up interest in our results and is working towards the implementation of non-destructive population readout [76, 77] and projection noise squeezing in optical lattice clocks [78].

The achievements can be summarized with the following keywords:

- Non-destructive measurements on a atomic ensemble state of cold, dipole trapped caesium atoms; determination of system parameters such as lifetime in the trap, oscillation frequencies and temperature
- Creation of a highly purified ensemble in one of the clock levels
- Real time, non-destructive observation of coherent system dynamics under the influence of microwave radiation
- Microwave spectroscopy of the ensemble
- Systematic studies of probe induced decoherence, differential light shifts and influence of trap motion
- Differential light shift cancelation in bichromatic probing scheme
- Probe light shot noise and atomic projection noise limited clock state population measurement
- Quantum noise squeezing by more than 50%

## 7.2 Further developments

The experimental progress has been exceptionally satisfactory from early 2007 on. A long standing milestone, the quantum noise limited performance of our measurement setup has finally been convincingly demonstrated. This is the prerequisite for many interesting further directions of the experiment.

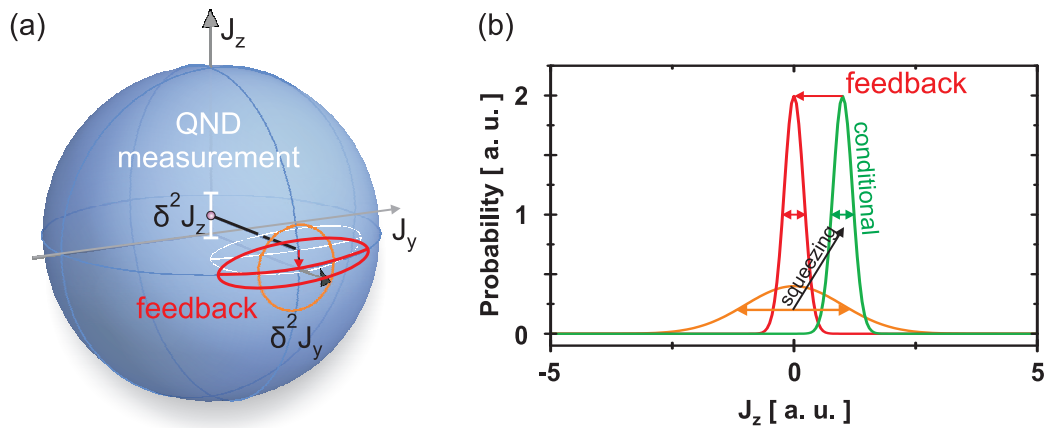


**FIGURE 7.1:** Quantum feedback to obtain unconditional noise squeezing. (a) The QND measurement produces a reduced uncertainty ellipse centered around the first measurement outcome. By feeding the outcome back onto the system with gain  $-\chi$ , the center of the ellipse is moved to the equator and squeezing without conditioning on the first measurement result can be obtained. (b) The first measurement restricts the subset of possible second measurement outcomes and thereby reduces the spread of the probability distribution around the first measurement outcome. By feeding the measurement outcome back onto the system, the center of the squeezed probability distribution overlaps with the initial one.

### Unconditional squeezing

The demonstration of squeezing relies on the knowledge of the first measurement value  $p_1$ . Squeezing is observed by finding the optimal conditional variance  $\delta^2(p_2 - \chi p_1)$ . Only when the knowledge obtained in the first measurement is actually used to predict the second measurement, a reduced uncertainty can be observed. As discussed in section 2.2.1, the first QND measurement projects the ensemble eigenstate into a decimated eigenstate subset and the second measurement can only return measurement outcomes inside this reduced space. Unless we use the measurement, we do, however, not know the boundaries of the reduced subset. When we plot the reduced noise ellipse on the Bloch sphere as in figure 7.1(a), we plot the width of the probability distribution in the reduced subset. This ellipse is centered around the first measurement result, which is not necessarily zero. Figure 7.1(b) illustrates the squeezing process in this picture. We decimate the eigenvalue spectrum in the first measurement but only the measurement itself tells us which subset we have projected into. By applying a feedback onto the atomic ensemble with gain  $-\chi$ , the subset is centered around the original mean value of the probability distribution. A second measurement will then sample a probability distribution with sub-projection noise spread and reveal an unconditionally squeezed state. From a quantum information point of view, it does not really matter in which way the information gained in the first pulse is used — by correcting the second measurement result or by correcting the system state. From a technical and quantum control point of view, however, demonstrating unconditional squeezing corresponds to sub-projection noise quantum state engineering and is therefore highly interesting.

## Quantum state tomography

In the discussion of the population uncertainty squeezing we have up to now only considered the noise reduction in the  $\hat{J}_z$  component. By applying the non-destructive measurement scheme, we have demonstrated that the variance of this component  $\delta^2 \hat{J}_z$  can be reduced below the standard quantum limit. The Heisenberg uncertainty relation predicts that the product of the variances has to be bounded by the number of atoms,  $\delta^2 \hat{J}_y \delta^2 \hat{J}_z \geq \frac{1}{4} \frac{N^2}{4}$ . Consequently, squeezing of  $\hat{J}_z$  below the standard quantum limit has to result in an increase of the variance  $\delta^2 \hat{J}_y$  above the standard quantum limit, as indicated by the noise ellipse in figure 7.1(a). Ideally, the squeezed state should remain a minimum uncertainty state. By mapping out the distribution in  $\hat{J}_y$  together with  $\hat{J}_z$ , we can determine how ideal the quantum non-demolition measurement really is.

To get access to the distribution in  $\hat{J}_y$ , we have to rotate the squeezed state around the  $\hat{J}_x$  axis. Such a rotation can, e.g., be induced by shifting the phase of the microwave field after the initial  $\pi/2$  pulse which created the superposition state and the QND interaction. The rotation axis of a resonant microwave pulse depends on the phase relation between the free atomic system and the microwave frame. Shifting the phase of the microwave field by  $\pi/2$  switches between rotations around the  $J_x$  and  $J_y$  axis. A phase shifted microwave  $\pi/2$  pulse can therefore be used to achieve the desired interchange between the  $\hat{J}_z$  and  $\hat{J}_y$  component. Rotating by variable amounts allows one to extract the dimensions of the squeezed noise ellipse in all directions for reconstruction.

## Tomography of non-Gaussian atomic states

The tomography of the squeezed state can be extended towards extracting the probability distributions of even more exotic quantum state. In principle, it is possible to create the equivalent of a single photon Fock state with atoms: We start with a coherent atomic state  $|\Psi\rangle = |3\rangle^{\otimes N}$  and excite a single atom into  $|4\rangle$ . This produces a superposition state of  $|\Psi\rangle = \frac{1}{\sqrt{N}} \sum_{i=1}^N |3\rangle^{\otimes(i-1)} |4\rangle |3\rangle^{\otimes(N-i)}$ . By rotating this state with a microwave  $\pi/2$  pulse, we obtain a superposition of superposition states  $|\Psi\rangle_{\pi/2} = \frac{1}{\sqrt{2^N N}} \sum_{i=1}^N (|3\rangle + |4\rangle)^{\otimes(i-1)} (|3\rangle - |4\rangle) (|3\rangle + |4\rangle)^{\otimes(N-i)}$ . Formally, the same output state is obtained in a homodyne setup with a strong coherent input mode with a mean photon number of  $|\alpha|^2 = N - 1$  and a single photon Fock state  $|1\rangle$  [79]. The tomography of such a state should reveal the same marginal distribution known from the Wigner function of a single photon state.

## Quantum memory

Since the work group has a long standing experience in quantum information and quantum memory experiments [80] and a non-classical light source available [79], a natural line of interesting experiments emerges: The cold, optically dense and extremely well controlled two level system at our hands can serve as storage medium for non-classical light states. The duration of, e.g., the Schrödinger kitten state of light [81] or the single photons [82] produced by the light source in the lab

next door is below one microsecond. The room temperature cells which have been used as quantum memory medium for light in [80] require typical pulse durations of several milliseconds to obtain the necessary coupling strength and temporal averaging effects due to the motion of the atoms. The cold trapped cloud promises to be a far more ideal storage medium for these states.

### **Enhancing the coupling strength**

Obviously, the amount of squeezing we observe in our experiment is limited by the number of atoms in the sample or the optical depth we achieve. The effective optical depth can easily be increased by several orders of magnitude when putting the ensemble into an optical cavity. This approach has been demonstrated to be capable of producing squeezing [13]. Although an effective optical depth of few thousand has been realized in that setup, technical difficulties and apparently fundamental limitations [83] reduce the observed squeezing to around  $\xi \approx -3$  dB. The main limitation seems to be the localization of the atoms inside the field modes of the optical cavity which also provides the trapping potential. A running wave cavity could help to circumvent this problem.

### **The Last Word**

The preceding discussion is supposed to illustrate that the experiment presented in the earlier chapters is looking ahead into a prospering future. The experiments presented in this thesis work have established a solid foundation and paved the way for various possible and highly interesting directions.



## Light atom interaction

### A.1 Atomic light phase shift and absorption

To derive the formulas (2.42,2.41) in a different way than presented in 2.3, we follow the derivation given in [84]. We start out with the definition of the atomic polarizability  $\vec{P}$  in terms of the susceptibility  $\chi$  – linear response:

$$\vec{P} = \epsilon_0 \chi \vec{E} \quad (\text{A.1})$$

When this is inserted into the Maxwell equations, assuming a wave solution, we end up with a dispersion relation:

$$(kc/\omega)^2 = 1 + \chi \quad (\text{A.2})$$

$$\chi = \chi' + i\chi'' \quad (\text{A.3})$$

$$n = \eta + i\kappa = \sqrt{1 + \chi} \approx 1 + \frac{\chi}{2} \dots \quad (\text{A.4})$$

With the complex index of refraction  $n$ , the relative phaseshift of two light beams, one traveling inside a medium of length  $l$  with refractive index  $n$  becomes:

$$E_1 = |E_1| e^{inkx - i\omega t} \quad (\text{A.5})$$

$$\rightarrow |E_1| e^{i\eta kl - \kappa kl - i\omega t} \quad (\text{A.6})$$

$$E_2 = |E_2| e^{ikx - i\omega t} \quad (\text{A.7})$$

$$\Delta\phi = kl(\eta - 1) = kl\Re(n - 1) \approx kl\frac{\chi'}{2} \quad (\text{A.8})$$

$$S = kl\kappa = kl\Im(n) \approx kl\frac{\chi''}{2} \quad (\text{A.9})$$

where  $S$  is the absorption coefficient of the amplitude of the e.m. wave. From a classical oscillator model for the valence electron:

$$m(\ddot{x} + \gamma\dot{x} + \omega_0^2 x) = -eE = -eE_0 e^{-i\omega t} \quad (\text{A.10})$$

$$\Rightarrow x = \frac{-eE}{m(\omega_0^2 - \omega^2 - i\omega\gamma)} \quad (\text{A.11})$$

$$P = -\frac{f_{1i} N e}{V} x \quad (\text{A.12})$$

we get a susceptibility of  $N$  atoms with coupling strength  $f_{1i}$  from the ground state 1 to the excited level  $i$ :

$$\chi = \frac{f_{1i}Ne^2}{\epsilon_0mV} \frac{1}{\omega_0^2 - \omega^2 - i\omega\gamma} \quad (\text{A.13})$$

$$\chi' = \frac{f_{1i}Ne^2}{\epsilon_0mV} \frac{1}{\omega_0} \frac{(\omega_0 - \omega)/2}{(\omega_0 - \omega)^2 + (\gamma/2)^2} \quad (\text{A.14})$$

$$\chi'' = \frac{f_{1i}Ne^2}{\epsilon_0mV} \frac{1}{\omega_0} \frac{\gamma/4}{(\omega_0 - \omega)^2 + (\gamma/2)^2} \quad (\text{A.15})$$

In the last two equations it has been used that the linewidth  $\gamma \ll \omega_0$  and that the absorption is only “close” to  $\omega_0$  non-negligible ( $\omega \approx \omega_0$ ), that is,  $(\omega_0^2 - \omega^2)^2$  has been expanded to  $4\omega_0^2(\omega_0 - \omega)^2$  and  $(\omega_0^2 - \omega^2) \rightarrow 2\omega_0(\omega_0 - \omega)$ .  $f_{fi} = (2m\omega_i/3\hbar)|\langle f|i\rangle|^2$  is the classical oscillator strength of the transition in question. Inserting  $f_{fi}$  into equations (A.14) and (A.15)  $\chi'$  and  $\chi''$  become:

$$\chi' = \frac{Ne^2|\langle f|i\rangle|^2}{3\epsilon_0\hbar V} \frac{\omega_0 - \omega}{(\omega_0 - \omega)^2 + (\gamma/2)^2} \quad (\text{A.16})$$

$$\chi'' = \frac{Ne^2|\langle f|i\rangle|^2}{3\epsilon_0\hbar V} \frac{\gamma/2}{(\omega_0 - \omega)^2 + (\gamma/2)^2} \quad (\text{A.17})$$

This result from a classical oscillator approach fits together with the quantum mechanical calculations. The generalization to more ground state levels and addressable excited levels reads:

$$\chi' = \frac{e^2}{3\epsilon_0\hbar V} \sum_{i,f} \frac{N_i|\langle f|i\rangle|^2(\omega_i - \omega)}{(\omega_i - \omega)^2 + (\gamma/2)^2} \quad (\text{A.18})$$

$$\chi'' = \frac{e^2}{3\epsilon_0\hbar V} \sum_{i,f} \frac{N_i|\langle f|i\rangle|^2\gamma/2}{(\omega_i - \omega)^2 + (\gamma/2)^2} \quad (\text{A.19})$$

In principle the more accurate formula for starting in one specific ground-level:

$$\chi'' = \sum_f^{\omega_f < \omega} \frac{Ne^4(\omega - \omega_f)^3}{18\pi\epsilon_0^2V\hbar^2c^3} \left| \sum_i \frac{|D_{fi}||D_{i1}|}{\omega_i - \omega - i\gamma_i(\omega)} \right|^2 \quad (\text{A.20})$$

$$\gamma_i(\omega) = \sum_j^{\omega_j < \omega} \frac{e^2|D_{ij}|^2(\omega - \omega_j)^3}{6\pi\epsilon_0\hbar c^3}$$

which takes cross-terms into account where the transition plus spontaneous decay takes the atom from state  $1 \rightarrow f$  via the excited level  $i$ . In our case where we assume only D1 or D2 transitions, the linewidth reduces to a single one, so the formula can be simplified. When we eliminate the excited states in the off-resonant limit, we can further assume that the ground state populations do not change.

In the approximation of (A.4) and using (A.8,A.9) we arrive at:

$$\Delta\phi = kl \frac{1}{2} \frac{e^2}{3\epsilon_0\hbar V} \sum_{i,f} \frac{N_i|\langle f|i\rangle|^2(\omega_i - \omega)}{(\omega_i - \omega)^2 + (\gamma/2)^2} \quad (\text{A.21})$$

$$S = kl \frac{1}{2} \frac{e^2}{3\epsilon_0\hbar V} \sum_{i,f} \frac{N_i|\langle f|i\rangle|^2\gamma/2}{(\omega_i - \omega)^2 + (\gamma/2)^2} \quad (\text{A.22})$$

for the phaseshift and the absorption. Notice that when writing the formula for the oscillator strength:

$$f_{fi} = \frac{2m\omega_i}{3\hbar} |\langle f|i \rangle|^2 \quad (\text{A.23})$$

spatial averaging over the possible atomic orientation has taken place which is not appropriate in our situation. Therefore, we have to substitute:

$$|\langle f|i \rangle|^2 \rightarrow 3|\langle f|i \rangle|^2 \quad (\text{A.24})$$

Using the dipole matrix element from equation (A.39) we end up with:

$$\Delta\phi = \frac{3l\lambda^2}{4\pi V} (2J' + 1) \sum_{F, m_F, F', m'_F} N_{F, m_F} S(F, m_F, F', m'_F) \frac{(\gamma/2)\Delta_{F, F'}}{\Delta_{F, F'}^2 + (\gamma/2)^2} \quad (\text{A.25})$$

$$S = \frac{3l\lambda^2}{4\pi V} (2J' + 1) \sum_{F, m_F, F', m'_F} N_{F, m_F} S(F, m_F, F', m'_F) \frac{(\gamma/2)^2}{\Delta_{F, F'}^2 + (\gamma/2)^2} \quad (\text{A.26})$$

$$S(F, m_F, F', m'_F) = (2F' + 1)(2F + 1) \begin{pmatrix} F' & 1 & F \\ m'_F & q & -m_F \end{pmatrix}^2 \times \left\{ \begin{matrix} J & J' & 1 \\ F' & F & I \end{matrix} \right\}^2 \quad (\text{A.27})$$

## A.2 Matrix elements

In this section we want to give a short reproduction of the derivation of the dipole matrix elements used in section 2.3.

Transition rates from an initial excited state  $|i\rangle = |J'IF'm'_F\rangle$  to a final ground state  $|f\rangle = |JIFm_F\rangle$  as function of the total decay rate  $\gamma$  are calculated from Fermis Golden rule [21]:

$$\gamma = \frac{2\pi}{\hbar} |\langle f|H_{\text{int}}|i\rangle|^2 \rho(E) \quad (\text{A.28})$$

$$\rho(E) = \frac{V\omega^2 d\Omega}{(2\pi c^3)\hbar} \quad (\text{A.29})$$

$$\gamma = |\langle f|H_{\text{int}}|i\rangle|^2 \frac{V\omega^2 d\Omega}{(2\pi)^2 c^3 \hbar^2} \quad (\text{A.30})$$

The prefactor of the interaction Hamiltonian (2.31) is:

$$H_{\text{int}} \sim e\sqrt{\frac{\hbar\omega}{2\epsilon_0 V}} \quad (\text{A.31})$$

which leads to a transition rate of:

$$\begin{aligned}\gamma &= |\langle f | \mathbf{e} \cdot \mathbf{r} | i \rangle|^2 \frac{V \omega^2 d\Omega}{(2\pi)^2 c^3 \hbar^2} e^2 \frac{\hbar \omega}{2\epsilon_0 V} \\ &= |\langle f | \mathbf{e} \cdot \mathbf{r} | i \rangle|^2 \frac{e^2 \omega^3 d\Omega}{8\pi^2 \hbar c^3 \epsilon_0}\end{aligned}\quad (\text{A.32})$$

Separating off the angle dependent parts of the dipole matrix elements and integrating over the solid angle yields  $8\pi/3$ , so the transition matrix dependent rate becomes:

$$\gamma = \frac{e^2 \omega^3}{3\pi \hbar c^3 \epsilon_0} |\langle f | \mathbf{e} \cdot \mathbf{r} | i \rangle|^2 \quad (\text{A.33})$$

The transition matrix element can be expanded using the properties of the angular momentum [40, 41, 42] (be careful with the different normalization conventions!):

$$\begin{aligned}\langle J I F m_F | r_{-q} | J' I F' m'_F \rangle &= (-1)^{\dots} \langle F m_F 1 q | F' m'_F \rangle \\ &\times \sqrt{2F+1} \left\{ \begin{matrix} F & F' & 1 \\ J' & J & I \end{matrix} \right\} \langle J' || r || J \rangle\end{aligned}\quad (\text{A.34})$$

where  $\langle F m_F 1 q | F' m'_F \rangle$  is the Clebsch – Gordan coefficient:

$$\langle F m_F 1 q | F' m'_F \rangle = (-1)^{\dots} \sqrt{2F'+1} \begin{pmatrix} F & 1 & F' \\ m_F & q & -m'_F \end{pmatrix} \quad (\text{A.35})$$

The  $\{ \dots \}$  brackets refer to the Wigner 6-j symbol and the  $( \dots )$  brackets indicate the Wigner 3-j symbol.

To calculate the reduced dipole matrix element  $\langle J' || r || J \rangle$  for the caesium D2 line, we assume a decay from  $F' = 5, m'_F = 5 \rightarrow F = 4, m_F = 4$ . Since there is only one transition possibility from this upper level, the Clebsch–Gordan coefficient is one. For  $F = 4$  and  $F' = 5$  the 6-j symbol is  $1/6$ , so the total prefactor of the reduced dipole matrix element is  $1/4$  and we obtain:

$$\frac{1}{\tau} = \gamma = 2\pi \cdot 5.21\text{MHz} = \frac{\omega^3}{3\pi\epsilon_0 \hbar c^3} \frac{e^2}{4} |\langle J' || r || J \rangle|^2 \quad (\text{A.36})$$

One can in general show that for the transitions from a given excited level to all possible ground states the following sum rule holds:

$$\sum_{F, m_F} (2J'+1)(2F+1)(2F'+1) \begin{pmatrix} F' & 1 & F \\ m'_F & m_F - m'_F & m_F \end{pmatrix}^2 \left\{ \begin{matrix} F & F' & 1 \\ J' & J & I \end{matrix} \right\}^2 = 1 \quad (\text{A.37})$$

Including all possible decay channels, the transition matrix elements (A.34) add up to  $1/(2J'+1)$  where  $J'$  is the excited state angular momentum quantum number. Ultimately end up with:

$$\gamma = \frac{\omega^3}{3\pi\epsilon_0 \hbar c^3} \frac{e^2}{2J'+1} |\langle J' || r || J \rangle|^2 \quad (\text{A.38})$$

For the full transition matrix element we now get:

$$\begin{aligned}
 |\langle JIFm_F | er_{-q} | J'IF'm'_F \rangle|^2 &= (2F+1)(2F'+1) \begin{pmatrix} F & 1 & F' \\ m_F & q & -m'_F \end{pmatrix}^2 \\
 &\times \left\{ \begin{matrix} F & F' & 1 \\ J' & J & I \end{matrix} \right\}^2 \frac{\gamma 3\pi\epsilon_0 \hbar c^3}{\omega^3} (2J'+1)
 \end{aligned}
 \tag{A.39}$$

When comparing different approaches one has to be aware that different normalization conventions exist in the Wigner Eckart theorem. All approaches [18, 22, 40, 84] yield the same result if one does not mix up the conventions.



## D1 line laser

When discussing the initialization of the trapped ensemble into the clock state by optical pumping in section 5.3.2, we have briefly mentioned the benefits from applying the pump and repump laser on different fine structure transitions. In this section we shall shortly discuss the implementation of pumping on the D1  $6S_{1/2}(F=4) \rightarrow 6P_{1/2}(F'=4)$  transition – which involves the  $F=4, m_F=0$  dark state – and keeping the repump laser on the D2  $6S_{1/2}(F=3) \rightarrow 6P_{3/2}(F'=4)$  line transition.

The mechanical setup of the laser is the same as for the external cavity diode lasers as mentioned in section 3.1.2. We also use front facette anti reflection coated diodes from Eagleyard the produce light at 894.6 nm of type number EYP-RWE-0940. These diodes have the center of their gain profile very close to 900 nm, so stable and single mode operation is rather easily obtained. To stabilize the laser frequency to the  $6S_{1/2}(F=4) \rightarrow 6P_{1/2}(F'=4)$  transition, we use a standard saturated absorption setup. The obtained signals are shown in figure B.1. The two doublets  $F=3 \rightarrow F'=3,4$  and  $F=4 \rightarrow F'=3,4$  are easily identified through the relative absorption strengths of the individual transitions. A sketch of

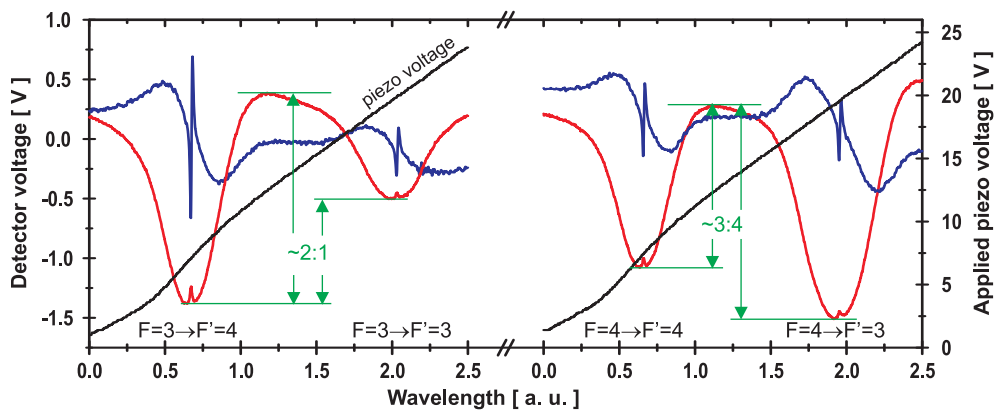


**FIGURE B.1:** Saturated absorption spectrum of the D1 transitions, error signal for frequency locking and applied piezo voltage. The ratios of the absorption dips allow one to identify the two doublets if the polarity of the piezo voltage is not known.

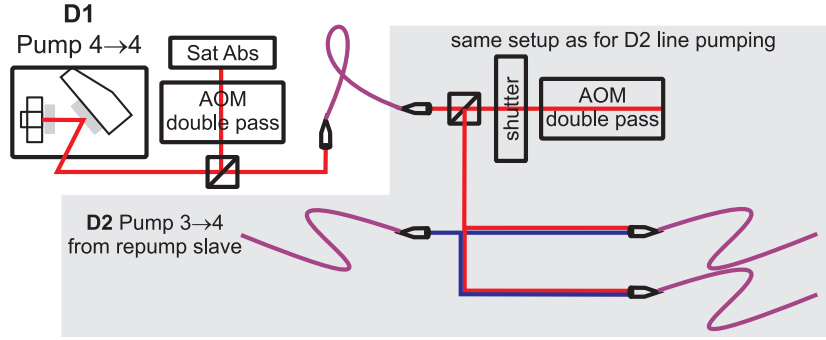


**FIGURE B.2:** Schematic laser setup for optical pumping into the clock states with one laser on the D1 line. To make the comparison between the two pumping schemes easy, the setup is designed such that only the fiber transporting the pump light originating from the different lasers need to be switched. The laser is stabilized by lock a lock-in type setup where the frequency of the double pass AOM is modulated with 100 kHz and the demodulated saturated absorption signal is used for the feedback to the laser grating.

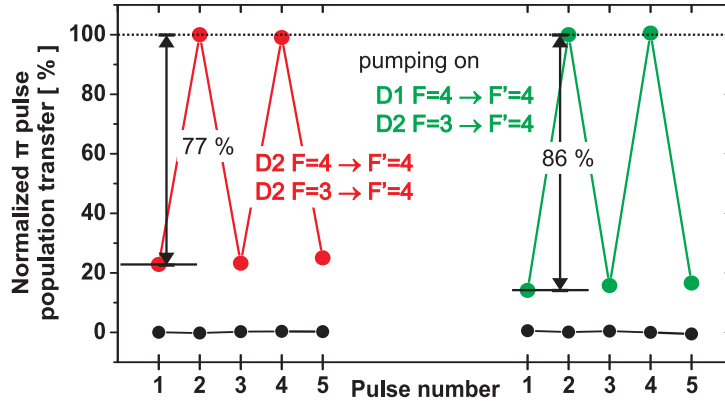


**FIGURE B.3:** Comparison between the D1 and D2 line pumping schemes. By pumping on the  $6S_{1/2}(F=4) \rightarrow 6P_{3/2}(F'=4)$  and repumping on  $6S_{1/2}(F=3) \rightarrow 6P_{3/2}(F'=4)$  we obtain a  $\pi$  pulse population transfer efficiency of 77%, while pumping on  $6S_{1/2}(F=4) \rightarrow 6P_{1/2}(F'=4)$  and repumping on  $6S_{1/2}(F=3) \rightarrow 6P_{3/2}(F'=4)$  polarizes the sample to 86%.

the laser setup is shown in figure B.2. To stabilize the laser we use the lock-in type technique as mentioned in section 3.2.1. The obtained error signals are shown in figure B.1. The stabilized light is fiber coupled and then enters the same setup as used for pumping on the D2 line. The repump light is derived in the same way as before. This way, a comparison between the two pumping schemes is very easily obtained. To compare the two pumping schemes we use the microwave  $\pi$  pulse transfer efficiency as discussed in section 5.3.2. A comparison between the D1 and the D2 line pumping with D2 repumping is shown in figure B.3. We obtain about 10% higher sample purity by pumping on the D1 line transition  $6S_{1/2}(F=4) \rightarrow 6P_{1/2}(F'=4)$  instead of the D2 transition  $6S_{1/2}(F=4) \rightarrow 6P_{3/2}(F'=4)$ . This is due to reduced magnetic substate coherences  $\Delta F=1, \Delta m_F=0$  between the  $F=3$  and  $F=4$  ground levels. In addition, off resonant excitations of the pump laser on the D2  $F=4 \rightarrow F'_{D2}=3,5$  transitions present in the D2 line pumping scheme are suppressed in the D1 line scheme, because the only possible off resonant

excitation channel  $6S_{1/2}(F = 4) \rightarrow 6P_{1/2}(F' = 3)$  is with  $\Delta_{F'_{D1}=3, F_{D1}=4} = 1.2$  GHz significantly further detuned from the desired pump transition, than in the D2 line pumping scheme. Taking also certain benefits when moving the probe light to the D1 line into consideration, it is very likely that the D1 optical pumping scheme will in the future replace the current setup. In the data presented in the experimental section only the D2 line pumping scheme has been applied.



# Wiener–Khinchin theorem and detector circuit layouts

## C.1 Wiener–Khinchin theorem

As a reminder, this chapter derives the Wiener–Khinchin theorem<sup>1</sup> which connects the spectral noise power density of a random variable to its Fourier components. The derivation follows the approach of [55].

The correlation function  $\Omega(s)$  of the stationary random variable  $o(t)$  is defined by:

$$\Omega(s) \equiv \langle o(t)o(t+s) \rangle \quad (\text{C.1})$$

where the  $\langle \dots \rangle$  denotes the ensemble average of the variable, which is equal to the time average for stationary systems. On this basis, the spectral noise power density function is defined as the correlation function's Fourier transform by:

$$\Omega(\omega) = \frac{1}{2\pi} \int_{-\infty}^{\infty} \Omega(s)e^{-i\omega s} ds = \frac{1}{2\pi} \int_{-\infty}^{\infty} \langle o(t)o(t-s) \rangle ds \quad (\text{C.2})$$

When we define the Fourier components of the random variable  $o(t)$  as:

$$o(\omega) = \frac{1}{2\pi} \int_{-\infty}^{\infty} o(t')e^{-i\omega t'} dt' \quad (\text{C.3})$$

and the inverse Fourier transform as:

$$o(t) = \int_{-\infty}^{\infty} o(\omega')e^{i\omega' t} d\omega' \quad (\text{C.4})$$

the correlation function can be written as:

$$\Omega(s) = \int \int_{-\infty}^{\infty} \langle o^*(\omega')o(\omega) \rangle e^{i(\omega-\omega')t} e^{i s \omega} d\omega' d\omega \quad (\text{C.5})$$

<sup>1</sup>The spelling of Khinchin is inconsistent in the literature. It can also be found as Chintschin or Khintchine; also the name Khinchin–Kolmogorov theorem can be found.

where we have used that  $o^*(\omega) = o(-\omega)$  because  $o(t)$  is real. Since the correlation function (C.5) has to be time independent for a stationary random process, we require:

$$\langle o^*(\omega')o(\omega) \rangle = \langle |o(\omega)|^2 \rangle \delta(\omega - \omega') \quad (\text{C.6})$$

We now obtain for the correlation function:

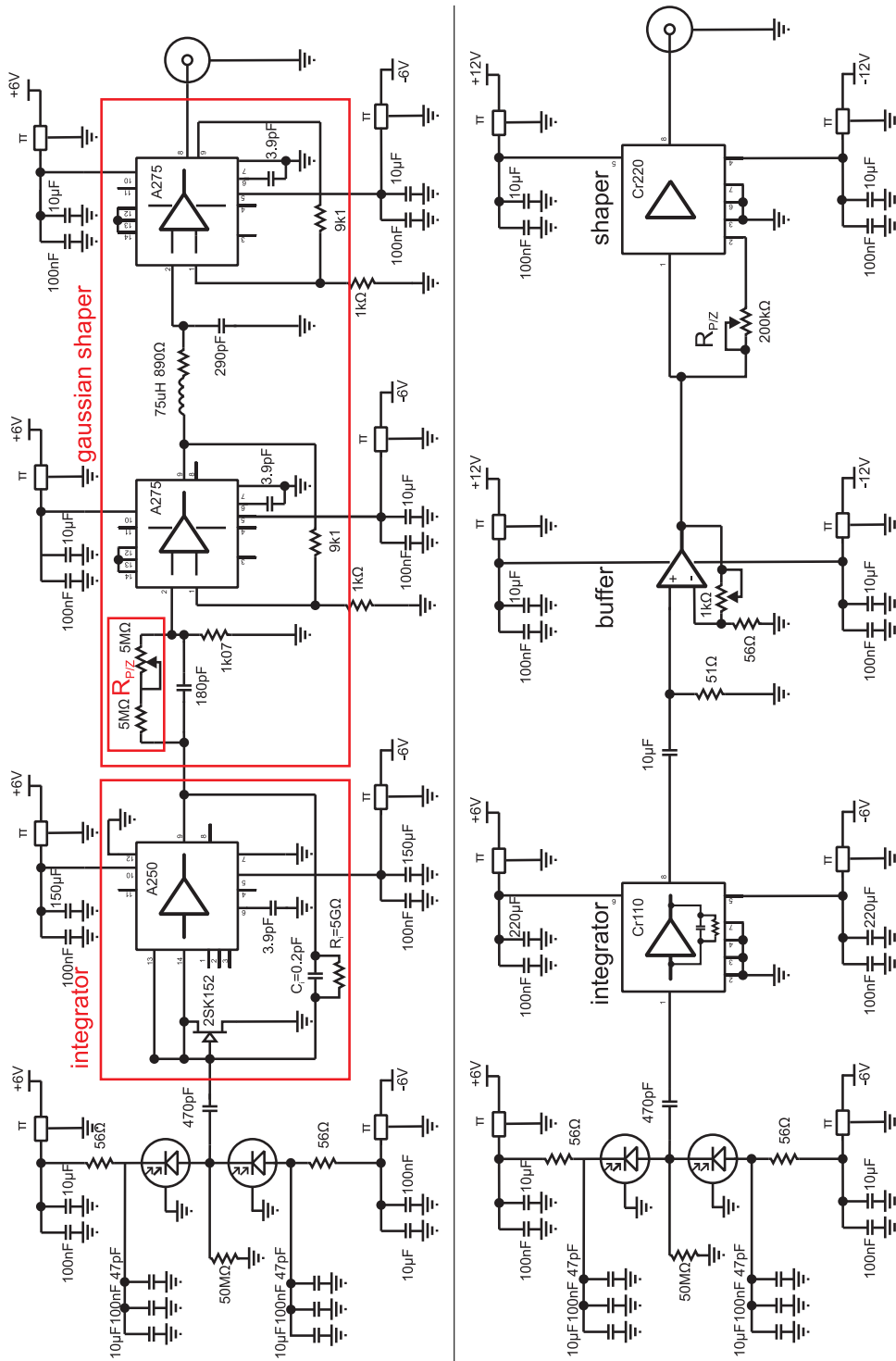
$$\Omega(s) = \int_{-\infty}^{\infty} \langle |o(\omega)|^2 \rangle e^{i\omega s} d\omega \quad (\text{C.7})$$

whereof the Fourier transform returns the spectral noise power density as:

$$\Omega(\omega) = \langle |o(\omega)|^2 \rangle \quad (\text{C.8})$$

This comprises the Wiener-Khinchin theorem: The spectral noise power density is the mean of the modulus square of the Fourier components of the random variable.

## C.2 Detector circuit layouts



Layout of the Amptek detector version and Cremat detector version



# List of publications

- [I] *Comparing Algebraic and Numerical Solutions of Classical Diffusion Process Equations in Computational Financial Mathematics*,  
A. Ruffing, P. Windpassinger, S. Panig,  
Journal of Discrete Dynamics in Nature and Society, 2001, Vol. 6, pp. 157
- [II] *Trapping of Neutral Rubidium with a Macroscopic Three-Phase Electric Trap*  
T. Rieger, P. Windpassinger, S. A. Rangwala, G. Rempe, and P. W. Pinkse  
Physical Review Letters 99, 063001 (2007)
- [III] *Quantum interface between light and atomic ensembles*  
H. Krauter, J. F. Sherson, K. Jensen, T. Fernholz, J. S. Neergaard-Nielsen, B. Melholt Nielsen, D. Oblak, P. Windpassinger, N. Kjærgaard, A. J. Hilliard, C. Olausson, J. H. Müller, and E. S. Polzik  
Proceedings of the XVIII International Conference on Laser Spectroscopy (2007)
- [IV] *Non-Destructive Probing of Rabi Oscillations on the Cesium Clock Transition near the Standard Quantum Limit*  
P. J. Windpassinger, D. Oblak, P. G. Petrov, M. Kubasik, M. Saffman, C. L. Garrido Alzar, J. Appel, J. H. Müller, N. Kjærgaard, and E. S. Polzik  
Physical Review Letters 100, 103601, (2008)
- [V] *Inhomogeneous Light Shift Effects on Atomic Quantum State Evolution in Non-Destructive Measurements*  
P. J. Windpassinger, D. Oblak, U. Busk Hoff, J. Appel, N. Kjærgaard, and E. S. Polzik  
New Journal of Physics, 10, 053032, (2008)
- [VI] *Echo Spectroscopy of Atomic Dynamics in a Gaussian Trap via Phase Imprints*  
D. Oblak, J. Appel, P. J. Windpassinger, U. Busk Hoff, N. Kjærgaard, and E. S. Polzik  
European Physical Journal D, 50, 67 (2008)
- [VII] *Quantum noise squeezing and entanglement on the atomic clock transition*  
J. Appel, P. J. Windpassinger, D. Oblak, U. B. Hoff, N. Kjærgaard, E. S. Polzik  
*submitted, preprint arXiv:0810.3545* (2008)

- [VIII] *Ultra low noise differential AC-coupled photodetector for sensitive pulse detection applications*  
P. J. Windpassinger, M. Kubasik, M. Koschorreck, A. Boisen, N. Kjærgaard, E. S. Polzik, and J. H. Müller  
*submitted* (2008)
- [IX] *Establishing the projection noise in a quantum non-demolition measurement on the clock transition*  
D. Oblak, P. J. Windpassinger, J. Appel, U. B. Hoff, N. Kjærgaard, and E. S. Polzik  
*Submitted to the Proceedings for the Central European Workshop on Quantum Optics (CEWQO 2008)*, Physica Scripta, (2008)

**Nondestructive Probing of Rabi Oscillations on the Cesium Clock Transition near the Standard Quantum Limit**

P. J. Windpassinger,<sup>1</sup> D. Oblak,<sup>1</sup> P. G. Petrov,<sup>1,\*</sup> M. Kubasik,<sup>2,1</sup> M. Saffman,<sup>3</sup> C. L. Garrido Alzar,<sup>1,†</sup> J. Appel,<sup>1</sup>  
J. H. Müller,<sup>1</sup> N. Kjørgaard,<sup>1,‡</sup> and E. S. Polzik<sup>1</sup>

<sup>1</sup>*QUANTOP, Niels Bohr Institute, University of Copenhagen, Denmark*

<sup>2</sup>*ICFO, Institut de Ciències Fotòniques, Barcelona, Spain*

<sup>3</sup>*Department of Physics, University of Wisconsin, Madison, Wisconsin 53706 USA*

(Received 9 November 2007; published 13 March 2008)

We report on the nondestructive observation of Rabi oscillations on the Cs clock transition. The internal atomic state evolution of a dipole-trapped ensemble of cold atoms is inferred from the phase shift of a probe laser beam as measured using a Mach-Zehnder interferometer. We describe a single color as well as a two-color probing scheme. Using the latter, measurements of the collective pseudospin projection of atoms in a superposition of the clock states are performed and the observed spin fluctuations are shown to be close to the standard quantum limit.

The text has been written by N. Kjørgaard. The main scientific contribution, leading to the highly non-destructive observation of Rabi oscillations on the caesium clock transition are due to P. Windpassinger. D. Oblak contributed equally to the projection noise limited data presented in figure 4.

## Inhomogeneous light shift effects on atomic quantum state evolution in non-destructive measurements

Patrick J Windpassinger<sup>1</sup>, Daniel Oblak, Ulrich Busk Hoff, Jürgen Appel, Niels Kjærgaard and Eugene S Polzik

QUANTOP, Niels Bohr Institute, University of Copenhagen, DK-2100 Copenhagen, Denmark  
E-mail: pwindpas@nbi.dk

*New Journal of Physics* **10** (2008) 053032 (15pp)

Received 28 January 2008

Published 28 May 2008

Online at <http://www.njp.org/>

doi:10.1088/1367-2630/10/5/053032

**Abstract.** Various parameters of a trapped collection of cold and ultracold atoms can be determined non-destructively by measuring the phase shift of an off-resonant probe beam, caused by the state-dependent index of refraction of the atoms. The dispersive light–atom interaction, however, gives rise to a differential light shift (ac Stark shift) between the atomic states which, for a non-uniform probe intensity distribution, causes an inhomogeneous dephasing between the atoms. In this paper, we investigate the effects of this inhomogeneous light shift in non-destructive measurement schemes in cold caesium. We interpret our experimental data on dispersively probed Rabi oscillations and Ramsey fringes in terms of a simple light shift model which is shown to describe the observed behavior well. Furthermore, we show that by using spin echo techniques, the inhomogeneous phase shift distribution between the two clock levels can be reversed.

The text has been written by P. Windpassinger with contributions on the theory by N. Kjærgaard. The analysis and interpretation of the data presented, has been performed by P. Windpassinger and N. Kjærgaard. The major experimental contributions leading to the observations discussed in the paper are due to P. Windpassinger.

## Echo spectroscopy of atomic dynamics in a Gaussian trap via phase imprints

D. Oblak, J. Appel, P.J. Windpassinger, U.B. Hoff, N. Kjærgaard<sup>a</sup>, and E.S. Polzik

QUANTOP, Danish National Research Foundation Center for Quantum Optics, Niels Bohr Institute, University of Copenhagen, Blegdamsvej 17, 2100 Copenhagen Ø, Denmark

Received 11 August 2008 / Published online 18 October 2008  
© EDP Sciences, Società Italiana di Fisica, Springer-Verlag 2008

**Abstract.** We report on the collapse and revival of Ramsey fringe visibility when a spatially dependent phase is imprinted in the coherences of a trapped ensemble of two-level atoms. The phase is imprinted via the light shift from a Gaussian laser beam which couples the dynamics of internal and external degrees of freedom for the atoms in an echo spectroscopy sequence. The observed revivals are directly linked to the oscillatory motion of atoms in the trap. An understanding of the effect is important for quantum state engineering of trapped atoms.

The manuscript has been written by N. Kjærgaard. The numerical simulation presented was performed by J. Appel and N. Kjærgaard. The presented work is a direct continuation of the work summarized in *New Journal of Physics* 10 (2008) 053032, thus based on the preceding work by N. Kjærgaard and P. Windpassinger. J. Appel, D. Oblak and P. Windpassinger contributed scientifically equally to the work.

## Quantum noise squeezing and entanglement on the atomic clock transition.

J. Appel, P. J. Windpassinger, D. Oblak, U. B. Hoff, N. Kjærgaard, and E. S. Polzik  
*Danish National Research Foundation Center for Quantum Optics – QUANTOP,  
The Niels Bohr Institute, University of Copenhagen,  
Blegdamsvej 17, DK-2100 Copenhagen Ø, Denmark.*

Squeezing of quantum fluctuations by means of entanglement is a well recognized goal in the field of quantum information science and precision measurements. In particular, squeezing the fluctuations via entanglement between two-level atoms can improve the precision of atom clocks and of spectroscopy in general [1, 2]. Here, we demonstrate 3.4 dB of metrologically relevant squeezing and entanglement for  $10^5$  cold caesium atoms via a quantum nondemolition (QND) measurement [3, 4, 5] on the atom clock levels. We demonstrate the effect of decoherence inherent to generation of entanglement via a QND measurement and present a dichromatic QND scheme which allows to minimize the effect of this decoherence in metrological applications. The spin squeezing method demonstrated here on the microwave caesium clock transition is potentially applicable to optical lattice atom clocks.

The manuscript is the product of a group effort, headed by N. Kjærgaard and E. S. Polzik. The reported achievements represent the main driving force behind the work of all subgroup members and a clear identification of the major scientific contributor is impossible. The major contributions to the experimental setup are equally ascribed to J. Appel and P. Windpassinger.

## Ultra low noise differential AC-coupled photodetector for sensitive pulse detection applications

Patrick J. Windpassinger<sup>a1</sup>, Marcin Kubasik<sup>2</sup>, Marco Koschorreck<sup>2</sup>, Axel Boisen<sup>1</sup>, Niels Kjærgaard<sup>1</sup>, Eugene S. Polzik<sup>1,2</sup>, and Jörg Helge Müller<sup>1</sup>

<sup>1</sup> QUANTOP, Niels Bohr Institute, University of Copenhagen, Denmark

<sup>2</sup> ICFO, Institut de Ciències Fotòniques, Barcelona, Spain

Dated: November 3, 2008

**Abstract.** We report on the performance of now noise differential photodetectors especially designed for probing of atomic ensembles with weak light pulses. The working principle of the detectors is discussed together with the analysis procedures employed to extract the photon shot noise of light pulses with  $\sim 1 \mu\text{s}$  duration. As opposed to frequency response peaked detectors, our approach allows for broadband quantum noise measurements. The equivalent noise charge (ENC) for two different hardware approaches is evaluated to 280 and 340 electrons per pulse, respectively which corresponds to a dark noise equivalent photon number of  $n_{3\text{dB}} = 0.8 \cdot 10^5$  and  $n_{3\text{dB}} = 1.2 \cdot 10^5$  in the two approaches. Finally, we discuss the possibility of removing classical correlations in the output signal caused by detector imperfection by using double correlated sampling methods.

The manuscript has been written by P. Windpassinger. The main scientific contributions are due to P. Windpassinger, the technical realization is based on the work of A. Boisen with input from J. H. Müller and P. Windpassinger.

# Bibliography

- [1] D. Oblak, *Non-destructive, interferometric quantum noise limited measurements on cold caesium atoms*, Master's thesis, University of Aarhus (2004).
- [2] P. G. Petrov, *Quantum noise limited light interferometry with cold atoms*, Ph.D. thesis, University of Copenhagen (2006).
- [3] D. Oblak, Ph.D. thesis, University of Copenhagen (2009-2010).
- [4] P. J. Windpassinger, D. Oblak, P. G. Petrov, M. Kubasik, M. Saffman, C. L. Garrido Alzar, J. Appel, J. Müller, N. Kjærgaard, and E. S. Polzik, *Nondestructive probing of rabi oscillations on the clock transition near the standard quantum limit*, Phys. Rev. Lett. **100**, 103601 (2008).
- [5] P. J. Windpassinger, D. Oblak, U. Busk Hoff, J. Appel, N. Kjærgaard, and E. S. Polzik, *Inhomogeneous light shift effects on atomic quantum state evolution in non-destructive measurements*, New J. Phys. **10**, 053032 (2008).
- [6] P. J. Windpassinger, M. Kubasik, M. Koschorreck, A. Boisen, N. Kjærgaard, E. S. Polzik, and J. H. Müller, *Ultra low noise differential ac-coupled photodetector for sensitive pulse detection applications*, submitted (2008).
- [7] D. Oblak, J. Appel, P. J. Windpassinger, U. Busk Hoff, N. Kjærgaard, and E. S. Polzik, *Echo spectroscopy of atomic dynamics in a gaussian trap via phase imprints*, EPJD **50**, 67 (2008).
- [8] J. Appel, P. J. Windpassinger, D. Oblak, U. Busk Hoff, N. Kjaergaard, and E. S. Polzik, *Quantum noise squeezing and entanglement on the atomic clock transition*, submitted, preprint arXiv:0810.3545 (2008).
- [9] D. Oblak, P. J. Windpassinger, J. Appel, U. Busk Hoff, N. Kjaergaard, and E. S. Polzik, *Establishing the projection noise in a quantum non-demolition measurement on the clock transition*, submitted to: Proceedings for the Central European Workshop on Quantum Optics (CEWQO 2008), Physica Scripta (2008).
- [10] G. Santarelli, P. Laurent, P. Lemonde, A. Clairon, A. G. Mann, S. Chang, A. N. Luiten, and C. Salomon, *Quantum projection noise in an atomic fountain: A high stability cesium frequency standard*, Phys. Rev. Lett. **82**, 4619 (1999).

- [11] V. Giovannetti, S. Lloyd, and L. Maccone, *Quantum-enhanced measurements: Beating the standard quantum limit*, *Science* **306**, 1330 (2004).
- [12] A. Kuzmich, N. P. Bigelow, and L. Mandel, *Atomic quantum non-demolition measurements and squeezing*, *EuroPhys. Lett.* **42**, 481 (1998).
- [13] M. H. Schleier-Smith, I. D. Leroux, and V. Vuletic, *Generating reduced-quantum-uncertainty states for an atomic clock*, (submitted, Preprint arXiv:0810.2582) (2008).
- [14] D. Oblak, P. G. Petrov, C. L. Garrido Alzar, W. Tittel, A. K. Vershovski, J. K. Mikkelsen, J. L. Sørensen, and E. S. Polzik, *Quantum-noise-limited interferometric measurement of atomic noise: Towards spin squeezing on the Cs clock transition*, *Phys. Rev. A* **71**, 043807 (2005).
- [15] P. G. Petrov, D. Oblak, C. L. Garrido Alzar, N. Kjærgaard, and E. S. Polzik, *Nondestructive interferometric characterization of an optical dipole trap*, *Phys. Rev. A* **75**, 033803 (2007).
- [16] H. Krauter, J. Sherson, K. Jensen, T. Fernholz, J. S. Neergaard-Nielsen, B. M. Nielsen, D. Oblak, P. J. Windpassinger, N. Kjaergaard, A. J. Hilliard, C. Olausson, J. H. Müller, and E. S. Polzik, *Quantum interface between light and atomic ensembles*, Proceedings of the XVIII International Conference on Laser Spectroscopy page 113 (2007).
- [17] M. O. Scully and M. S. Zubairy, *Quantum Optics* (Cambridge University Press, 1997).
- [18] D. A. Steck, *Caesium line data*, <http://steck.us/alkalidata> (2008).
- [19] F. T. Arecchi, E. Courtens, R. Gilmore, and H. Thomas, *Atomic coherent states in quantum optics*, *Phys. Rev. A* **6**, 2211 (1972).
- [20] W. M. Itano, J. C. Bergquist, J. J. Bollinger, J. M. Gilligan, D. J. Heinzen, F. L. Moore, M. G. Raizen, and D. J. Wineland, *Quantum projection noise: Population fluctuations in two-level systems*, *Phys. Rev. A* **47**, 3554 (1993).
- [21] F. Schwabl, *Quantenmechanik* (Springer, Berlin, 2002).
- [22] B. Julsgaard, *Entanglement and Quantum Interactions with Macroscopic Gas Samples*, Ph.D. thesis, University of Aarhus (2003).
- [23] F. Mandl and G. Shaw, *Quantum field theory* (Wiley, New York, 2001).
- [24] R. Glauber, *Coherent and incoherent states of the radiation field*, *Rhys. Rev.* **131**, 2766 (1963).
- [25] V. B. Braginsky and F. Y. Khalili, *Quantum measurement* (Cambridge University Press, 1992).
- [26] J.-P. Poizat, J.-F. Roch, and P. Grangier, *Characterization of quantum non-demolition measurements in optics*, *Les Editions de Physique* page 265 (1994).

- [27] C. M. Caves, K. S. Thorne, R. W. P. Drever, V. D. Sandberg, and M. Zimmermann, *On the measurement of a weak classical force coupled to a quantum-mechanical oscillator. i. issues of principles*, Rev. Mod. Phys. **52**, 342 (1980).
- [28] J. von Neumann, *Mathematische Grundlagen der Quantenmechanik* (Springer, Berlin, 1932).
- [29] Y. Aharonov, D. Z. Albert, and L. Vaidman, *How the result of a measurement of a component of the spin of a spin-1/2 particle can turn out to be 100*, Phys. Rev. Lett. **60**, 1351 (1988).
- [30] Y. Aharonov, D. Z. Albert, A. Casher, and L. Vaidman, *Surprising quantum effects*, Phys. Lett. A **124**, 199 (1987).
- [31] Y. Aharonov and A. Botero, *Quantum averages of weak values*, Phys. Rev. A **72**, 052111 (2005).
- [32] I. M. Duck, P. M. Stevenson, and E. C. G. Sudarshan, *The sense in which a "weak measurement" of a spin- $\frac{1}{2}$  particles spin component yields a value 100*, Phys. Rev. D **40**, 2112 (1989).
- [33] M. Kitagawa and M. Ueda, *Squeezed spin states*, Phys. Rev. A **47**, 5138 (1993).
- [34] D. J. Wineland, J. J. Bollinger, W. M. Itano, and D. J. Heinzen, *Squeezed atomic states and projection noise in spectroscopy*, Phys. Rev. A **50**, 67 (1994).
- [35] J. Hald, *Spin squeezing in a cold atomic ensemble*, Ph.D. thesis, University of Aarhus (2000).
- [36] D. J. Wineland, J. J. Bollinger, W. M. Itano, F. L. Moore, and D. J. Heinzen, *Spin squeezing and reduced quantum noise in spectroscopy*, Phys. Rev. A **46**, R6797 (1992).
- [37] L. Mandel and E. Wolf, *Optical Coherence and quantum optics* (Cambridge University Press, 1995).
- [38] A. Kuzmich, L. Mandel, J. Janis, Y. E. Young, R. Eijnisman, and N. P. Bigelow, *Quantum nondemolition measurements of collective atomic spin*, Phys. Rev. A **60**, 2346 (1999).
- [39] D. F. Walls and G. J. Milburn, *Quantum Optics* (Springer, Berlin, 1994).
- [40] I. I. Sobelman, *Theory of Atomic Spectra* (Alpha Science, Oxford, 2006).
- [41] D. Brink and G. Satchler, *Angular Momentum* (Oxford University Press, 1962).
- [42] A. Edmonds, *Angular Momentum in Quantum Mechanics* (Princeton University Press, 1974), 2 edition.
- [43] B. Yurke, A. L. McCall, and J. R. Klauder, *SU(2) and SU(1,1) interferometers*, Phys. Rev. A **33**, 4033 (1986).

- [44] K. Hammerer, K. Mølmer, E. S. Polzik, and J. I. Cirac, *Light-matter quantum interface*, Phys. Rev. A **70**, 044304 (2004).
- [45] C. E. Wieman, D. Pritchard, and D. Wineland, *Atom cooling, trapping, and quantum manipulation*, Rev. Mod. Phys. **71**, S253 (1999).
- [46] H. J. Metcalf and P. van der Straten, *Laser Cooling and Trapping* (Springer, Berlin, 1999).
- [47] C. E. Wieman and L. Hollberg, *Using diode lasers for atomic physics*, Rev. Sci. Instrum. **61**, 1 (1991).
- [48] L. Ricci, M. Weidemüller, T. Esslinger, A. Hemmerich, C. Zimmermann, V. Vuletic, W. König, and T. W. Hänsch, *A compact grating-stabilized diode laser system for atomic physics*, Optics Communications **117**, 541 (1995).
- [49] A. J. Hilliard, *Collective Rayleigh scattering in a Bose Einstein condensate*, Ph.D. thesis, University of Copenhagen (2008).
- [50] R. Grimm, M. Weidemüller, and Y. B. Ovchinnikov, *Optical dipole traps for neutral atoms*, Adv. At. Mol. Opt. Phys. **42**, 95 (2000).
- [51] N. Becker and J. Ravnbøl, *Investigation of rabi oscillations on the caesium clock transition and measurements using ramsey-type experiments*, Bachelor thesis, University of Copenhagen (2007).
- [52] H. Hansen, T. Aichele, C. Hettich, P. Lodahl, A. Lvovsky, J. Mlynek, and S. Schiller, *An ultra-sensitive pulsed balanced homodyne detector: Application to time-domain quantum measurements*, Optics Letters **26**, 1714 (2001).
- [53] www.amptek.com (Product data sheet A-250 and A-275).
- [54] www.cremat.com (Product data sheet CR110, CR-200).
- [55] F. Reif, *Statistische Physik und Theorie der Wärme* (de Gruyter, 1987).
- [56] M. Koschorreck (private communication).
- [57] www.hamamatsu.com (Product data sheet S3883).
- [58] I. I. Rabi, *Space quantization in a gyrating magnetic field*, Phys. Rep. **51**, 652 (1937).
- [59] F. Bloch, *Nuclear induction*, Phys. Rev. **70**, 460 (1946).
- [60] L. Allen and J. H. Eberly, *Optical resonance and two-level atoms* (Dover, New York, 1987).
- [61] J. Vanier and C. Audoin, *The Quantum Physics of Atomic Frequency Standards* (Adam Hilger, 1989).
- [62] J. José and E. Saletan, *Classical Dynamics* (Cambridge University Press, 2000).

- [63] M. Arditi, I. Hirano, and P. Tougne, *Optical pumping of a caesium beam and detection of the 0-0 'clock' transition*, J. Phys. D **11**, 2465 (1978).
- [64] G. Avila, V. Giordano, V. Candelier, E. Declercq, G. Theobald, and P. Cerez, *State selection in a cesium beam by laser-diode optical-pumping*, Phys. Rev. A **36**, 3719 (1987).
- [65] P. Tremblay and C. Jacques, *Optical pumping with two finite linewidth lasers*, Phys. Rev. A **41**, 4989 (1990).
- [66] R. Ozeri, C. Langer, J. D. Jost, B. DeMarco, A. Ben-Kish, B. R. Blakestad, J. Britton, J. Chiaverini, W. M. Itano, D. B. Hume, D. Leibfried, T. Rosenband, P. O. Schmidt, and D. J. Wineland, *Hyperfine coherence in the presence of spontaneous photon scattering*, Phys. Rev. Lett. **95**, 030403 (2005).
- [67] P. D. Featonby, C. L. Webb, G. S. Summy, C. J. Foot, and K. Burnett, *Observation of light-induced coherence loss in a caesium atomic fountain*, J. Phys. B **31**, 375 (1998).
- [68] S. Chaudhury, G. A. Smith, K. Schulz, and P. S. Jessen, *Continuous non-demolition measurement of the cs clock transition pseudospin*, Phys. Rev. Lett. **96**, 043001 (2006).
- [69] S. Kuhr, W. Alt, D. Schrader, I. Dotsenko, Y. Miroshnychenko, A. Rauschenbeutel, and D. Meschede, *Analysis of dephasing mechanisms in a standing-wave dipole trap*, Phys. Rev. A **72**, 023406 (2005).
- [70] E. Hahn, *Spin echos*, Phys. Rev. **80**, 580 (1950).
- [71] M. F. Andersen, A. Kaplan, and N. Davidson, *Echo spectroscopy and quantum stability of trapped atoms*, Phys. Rev. Lett. **90**, 023001 (2003).
- [72] M. Saffman, D. Oblak, J. Appel, and E. S. Polzik, *Spin squeezing of atomic ensembles by multi-colour quantum non-demolition measurements*, preprint arXiv:0808.0516 (2008).
- [73] D. W. Allan, *Statistics of atomic frequency standards*, Proceedings of the IEEE **54**, 221 (1966).
- [74] I. Teper, G. Vrijsen, J. Lee, and M. A. Kasevich, *Backaction noise produced via cavity-aided nondemolition measurement of an atomic clock state*, Phys. Rev. A **78**, 051803 (2008).
- [75] T. Takano, M. Fuyama, R. Namiki, and Y. Takahashi, *Spin squeezing of a cold atomic ensemble with the nuclear spin of one-half*, preprint arXiv:0808.2353 (2008).
- [76] R. Le Targat (private communication).
- [77] U. Sterr (private communication).
- [78] D. Meiser, J. Ye, and M. J. Holland, *Spin squeezing in optical lattice clocks via lattice-based QND measurements*, New J. Phys. **10**, 073014 (2008).

- 
- [79] J. S. Neergaard-Nielsen, *Generation of single photons and Schrödinger kitten states of light*, Ph.D. thesis, University of Copenhagen (2008).
- [80] B. Julsgaard, J. Sherson, J. I. Cirac, J. Fiurasek, and E. S. Polzik, *Experimental demonstration of quantum memory for light*, Nature **432**, 482 (2004).
- [81] J. S. Neergaard-Nielsen, B. M. Nielsen, C. Hettich, K. Mølmer, and E. S. Polzik, *Generation of a superposition of odd photon number states for quantum information networks*, Phys. Rev. Lett. **97**, 083604 (2006).
- [82] J. S. Neergaard-Nielsen, B. M. Nielsen, H. Takahashi, A. I. Vistnes, and E. S. Polzik, *High purity bright single photon source*, Optics Express **15**, 7940 (2007).
- [83] K. W. Murch, K. L. Moore, S. Gupta, and D. Stamper-Kurn, *Observation of quantum-measurement backaction with an ultracold atomic gas*, Nature Physics **4**, 561 (2008).
- [84] R. Loudon, *The Quantum Theory of Light* (Oxford University Press, 1973).